Effect of Milling on Microstructural Evolution in Nano ODS–18Cr Ferritic Steel and the Resultant Mechanical, Corrosion and Oxidation Properties

A thesis

Submitted by

M. Nagini

in partial fulfillment of the requirements for the award of the degree of

Doctor of Philosophy

in

Materials Engineering

School of Engineering Sciences and Technology

University of Hyderabad, Hyderabad, India

March 2017

DECLARATION

I, **M. Nagini** hereby declare that this thesis work entitled ***"Effect of Milling on Microstructural Evolution in Nano ODS–18Cr Ferritic Steel and the Resultant Mechanical, Corrosion and Oxidation Properties"*** submitted in partial fulfillment of the requirements for the award of **Doctor of Philosophy** (in **Materials Engineering**) in the School of Engineering Sciences and Technology (SEST), University of Hyderabad is a bonafide record of the work which was carried out by me under the supervision of **Dr. Koteswararao V. Rajulapati** and **Dr. R. Vijay**. I also declare that this thesis has not been submitted previously in part or in full to this University or any other University or Institution for the award of any degree or diploma.

(M. Nagini)
Reg. No.: 10ETPM07
School of Engineering Sciences and Technology
University of Hyderabad

CERTIFICATE

This is to certify that this thesis work entitled ***"Effect of Milling on Microstructural Evolution in Nano ODS–18Cr Ferritic Steel and the Resultant Mechanical, Corrosion and Oxidation Properties"***, submitted by **M. Nagini** bearing Reg. No. **10ETPM07** in partial fulfillment of the requirements for the award of the degree of **Doctor of Philosophy** in **Materials Engineering** is a bonafide record of the work that has been carried out by her under my supervision. Dr. R. Vijay, International Advanced Research Centre for Powder Metallurgy and New Materials (ARCI) has also supervised the above mentioned thesis work along with me. This thesis has not been submitted previously in part or in full to this or any other University or Institution for the award of any degree or diploma.

Thesis Supervisor

Dr. Koteswararao V. Rajulapati
Associate Professor
School of Engineering Sciences and Technology
University of Hyderabad

Approved by

Prof. M. Ghanashyam Krishna
Dean
School of Engineering Sciences and Technology
University of Hyderabad

CERTIFICATE

This is to certify that the thesis entitled ***Effect of Milling on Microstructural Evolution in Nano ODS–18Cr Ferritic Steel and the Resultant Mechanical, Corrosion and Oxidation Properties*** submitted by **M. Nagini** bearing registration number **10ETPM07** in partial fulfillment of the requirements for award of **Doctor of Philosophy** (in **Materials Engineering**) in the School of Engineering Sciences and Technology (SEST) is a bonafide work carried out by her under my supervision and guidance.

This thesis is free from plagiarism and has not been submitted previously in part or in full to this or any other University or Institution for award of any degree or diploma.

Parts of this thesis have been published in the following publications:

1. ***Metallurgical and Materials Transactions A,*** 47 A (2016) 4198–4209.
2. ***Journal of Materials Engineering and Performance***, 25 (2016) 577–586.

Further, the student has passed the following courses towards fulfillment of coursework requirement for Ph.D.

Course Code	Course Title	Credits	Pass /Fail
MT704	Thermodynamics and Phase Equilibria	4	Pass
MT710	Concepts of Materials Science	4	Pass
MT712	Metal Forming: Science and Technology	4	Pass
MT715	Characterization of Materials	4	Pass
MT724	Seminar	2	Pass
MT730	Design & Selection of Engineering Materials	4	Pass
MT731	Advanced Engineering Mathematics	2	Pass
MT735	Materials Processing and Characterization Laboratory	4	Pass
PD601	Research Methodology	4	Pass

Supervisor **Dean of School**

ACKNOWLEDGEMENTS

This thesis is the culmination of my journey of Ph.D. which was just like climbing a high peak step by step accompanied with encouragement, hardship and trust. When I found myself at top experiencing the feeling of fulfillment, I realized though only my name appears on the cover of this dissertation, a great many people including my thesis supervisors, well wishers, colleagues, family members and friends have contributed to accomplish this huge task. I would like to extend my appreciation to those people who have contributed to this long journey of Ph.D. and made it smoother and worthwhile, both directly and indirectly.

I would like to express my sincere thanks in all respects to my thesis supervisors **Dr. R. Vijay** at ARCI and **Dr. Koteswararao V. Rajulapati** at UoH for their wonderful guidance and great support at every stage of this work. I was truly fortunate to have supervisors like them who understood and supported me. I am grateful for the belief they had in me. I sincerely wish to have their guidance in all my future endeavors.

I would like to extend my deep and sincere thanks to **Dr. R. Vijay** for giving me an opportunity to work with him. It is a great pleasure to express my deep sense of gratitude for his keen attention, constant encouragement, inspiring guidance and the constant support without which this work would not have come into light. I have learned a lot from his suggestions, comments and discussions. I would like to thank him for all the efforts and valuable time he has given to me. I would also like to express my special and sincere gratitude to **Dr. A. Venugopal Reddy**, Adviser, ARCI, for his continuous advice and guidance throughout this work. **Dr. A. Venugopal Reddy** also helped to shape me and my opinions of scientific research. I express my sincere thanks to **Prof. K. Bhanu Sankara Rao** (former Dean) who has been my supervisor during his tenure at SEST for his wonderful suggestions.

I would like to express my sincere gratitude to **Dr. G. Sundararajan** (former Director) and **Dr. S.V. Joshi** (former Additional Director), **Dr. G. Padmanabham** (Director) and **Dr. Tata Narasinga Rao** (Associate Director) ARCI for permitting me to pursue my doctoral program. I would like to express my gratitude to them for providing me an excellent opportunity to carry out this research work at ARCI and for their immense

support and encouragement throughout my thesis work with all the facilities without which this work would not have been accomplished.

I also thank **Mr. R. Prabhakara Rao** (former Administrative and Personnel Officer), Mr. **R. Vijay Kumar** (Chief Finance and Accounts Officer) and **Mr. A. Srinivas** (Administrative and Personnel Officer) for their support and suggestions. I would like to render my thanks to the present Dean, **Prof. M. Ghanashyam Krishna** and former Deans of the School of Engineering Sciences and Technology, **Prof. M. Sundaraman** and **Prof. Rajender Singh** for their support and guidance. I express my sincere thanks to my Doctoral Research Committee members, **Dr–Ing. V.V.S.S. Srikanth** and **Dr. J.P. Gautam** for their valuable suggestions and encouragement during regular meetings.

I would specially acknowledge **Dr. S.B. Chandrasekhar** for his encouragement and constant support throughout my thesis work and his ever positive approach which has been a source of inspiration.

I express my sincere and hearty thanks **Dr. K. Satya Prasad** and **Mr. M. Ramakrishna** for their role in TEM analysis and for their valuable suggestions, constant encouragement and support.

I would also thank **Ms. Jyothirmayi** for her help in corrosion experiments and valuable discussions. I also thank **Dr. M. Sai Krishan Rao** (RCMA) for his help in oxidation experiments and support.

I am very thankful to **Dr**. **G. Ravi Chandra** for his help in characterization techniques, EBSD experiments. His constant support and insightful discussions were very helpful.

I also thank **Dr. Joydip Joardar** for help and valuable discussions regarding XRD characterization. I thank Dr. **B.V. Sarada** for Raman Spectroscopy analysis. I thank **Dr B. Suresh** for his help in particle size analyzer technique. I am also very thankful to **Dr. K. Radha**, **Dr. P.H. Borse**, **Dr. Malobika Karanjai**, **Dr. Neha Hebalkar, Dr. Dibyendu Chakravarty**, **Dr. Srinivasan Anandan**, **Dr. Kaliyan Hembram**, **Mr. S. Sudhakara Sarma, Ms. J. Revathi**, **Dr. K. Suresh**, **Mr. L. Venkatesh**, **Dr. P. Suresh Babu** and Dr. **Nitin P. Wasekar** of ARCI for their support with experimental and

characterization techniques during my journey of Ph.D. I thank **Mr. GVR Reddy** and **Mr. M. Laxminarayana** for his assistance in SEM lab and **Mr. K. Ramesh Reddy** for assistance with XRD.

I would like to thank **Mr. K.V.B.V. Rayudu** and **Mr. Anjan Babu** technicians of our group, as they have been very kind enough to extend their help to me at the various phases of my research. I also thank **Mr. P.V.V. Srinivas, Mr. Govind Kumar, Mr. Konda**, **Mr. P. Anjaiah, Mr. A. Praveen Kumar, Mr. J.V. Rao** and **G. Venkata Rao.** I thank them all for their support and helping me in ball milling and metallographic polishing of the samples for characterization *etc.*

I would like to thank IGCAR, Kalpakkam for funding (No. IGC/MMG/MMD/ODS/01/2010) the work and NFC, Hyderabad for carrying out hot extrusion.

I also want to acknowledge all my friends at ARCI and University of Hyderabad who made my stay pleasant and were always beside me during the happy and hard moments to push me and motivate me. I sincerely thank my friends, **Siva**, **Swapna**, **Akhila**, **Sumanth**, **Sahithi**, **Anas**, **Pramod**, **Sai Karthik**, **Pavitra**, **Archana**, **Ramya**, **Sampath**, **Pardhu**, **Sagar**, **Hari** and **Tejaswi**.

I appreciate my daughter **S. Indhu Hasitha** for abiding my ignorance and the patience she showed during my Ph.D journey. Finally, I acknowledge the people who mean a lot to me, **my parents**, **brothers**, **husband** and **sisters–in–law** for showing faith in me and giving me liberty to choose what I desire. I sincerely feel that words alone are not sufficient to express my gratitude to everyone who supported me. Thank you all!

M. Nagini

Dedicated to

my

Dear Daughter

Indhu Hasitha

LIST OF PUBLICATIONS

1. M. Nagini, R. Vijay, Koteswararao V. Rajulapati, K. Bhanu Sankara Rao, M. Ramakrishna, A.V. Reddy and G. Sundararajan, "Effect of process parameters on microstructure and hardness of oxide dispersion strengthened 18Cr ferritic steel", ***Metallurgical and Materials Transactions A,*** 47 A (2016) 4198–4209.

2. M. Nagini, A. Jyothirmayi, R. Vijay, Tata N. Rao, A.V. Reddy, Koteswararao V. Rajulapati and G. Sundararajan, "Influence of dispersoids on corrosion behaviour of oxide dispersion strengthened 18Cr steels made by high-energy milling", ***Journal of Materials Engineering and Performance***, 25 (2016) 577-586.

3. M. Nagini, R. Vijay, Koteswararao V. Rajulapati, A.V. Reddy and G. Sundararajan, "Tensile Deformation and Fracture Behaviour of Oxide Dispersion Strengthened 18Cr Ferritic Steel" communicated to ***Metallurgical and Materials Transactions A*.**

4. M. Nagini, R. Vijay, M. Sai Krishna Rao, Koteswararao V. Rajulapati, A.V. Reddy and G. Sundararajan, "Effect of dispersoids on high temperature oxidation behavior of oxide dispersion strengthened 18Cr ferritic steels", communicated to ***Oxidation of Metals***.

CONFERENCES AND WORKSHOPS ATTENDED

1. "Crystallite Size Effects in Oxide Dispersion Strengthened Iron Powders", **M. Nagini**, M. Ramakrishna, J. Joardar, R. Vijay, A.V. Reddy and G. Sundararajan, Poster Presentation at International Conference on Nanoscience and Nanotechnology (ICONSAT), Jan 21st–23rd, 2012, Hyderabad.

2. Participated in the Two–Day National Workshop on "Evaluation and Prevention of Corrosion and Failures 2012 (EFCF–2012)", Nov 29–30th, 2012, University of Hyderabad, Hyderabad.

3. Participated in the 6th International Conference on "Creep, Fatigue and Creep–Fatigue Interaction", Jan 22–25th, 2012, Mamallapuram, Tamil Nadu.

4. Participated in the "Short Term Course in Powder Metallurgy", Nov 18th–21st, 2013, ARCI, Hyderabad.

5. Participated in the Two–Day Course on "Quantitative Microscopy", Dec 12–13th, 2013, IIT, Madras.

6. "Effect of Milling on Microstructural Evolution of ODS–18Cr Nano–Ferritic Steels", **M. Nagini**, R. Vijay, M. Ramakrishna, Koteswararao. V. Rajulapati, K. Bhanu Sankara Rao, A.V. Reddy, G. Sundararajan, Oral Presentation at IUMRS, Dec 16–20th, 2013, IISc Bangalore.

7. Participated in the "APAS Golden Jubilee Science Congress" Nov 13–15th, 2014, IICT, Hyderabad.

8. Participated in "International Workshop on High Entropy Materials (IWHEM–2017)", March 11–12th, 2017, University of Hyderabad, Hyderabad.

Contents

LIST OF FIGURES ..... **i**

LIST OF TABLES ..... **vi**

LIST OF ABBREVIATIONS AND ACRONYMS ..... **viii**

LIST OF SYMBOLS ..... **ix**

ABSTRACT ..... **x**

CHAPTER 1 ..... **1**

INTRODUCTION **1**

1.1 Future generation power reactors **2**

1.1.1 Nuclear fission reactors 2

1.1.2 Nuclear fusion reactors 3

1.1.3 Thermal power plants 4

1.2 Materials requirement for the nuclear and thermal power plants **4**

1.3 Strengthening of metals **5**

1.4 Oxide dispersion strengthening **10**

1.5 Examples of oxide dispersion strengthened alloys **11**

1.6 Production methods of oxide dispersion strengthened alloys **11**

1.7 Development of oxide dispersion strengthened steels **12**

1.7.1 Iron based oxide dispersion strengthened steels 13

1.8 Mechanical alloying **15**

1.9 Objective of the present work **16**

1.10 Overview of the thesis **16**

References **18**

CHAPTER 2 ..... **21**

LITERATURE REVIEW **21**

2.1 Introduction **21**

2.2 Evolution of steels for high temperature applications **21**

2.2.1 Ferritic/Martensitic steels 21

2.2.2 Austenitic steels 26

2.2.3 Oxide dispersion strengthened steels 27

2.3 Composition design of ODS steels **27**

2.4 Production of ODS steels **30**

2.5 ODS ferritic–martensitic steels **31**

2.5.1 Microstructural evolution 31

2.5.2 Mechanical Properties 36

2.5.3 Corrosion and oxidation properties 40
2.6 ODS ferritic steels 42
2.6.1 Microstructural evolution 42
2.6.2 Mechanical properties 45
2.6.3 Corrosion and oxidation properties 47
2.7 High–Cr ferritic steels 48
2.7.1 Microstructural evolution 48
2.7.2 Mechanical properties 51
2.7.3 Corrosion and oxidation resistance 53
2.8 Mechanisms of formation of complex–oxide particles 55
2.9 Influence of process parameters on the microstructure of ODS steels 57
2.10 Present scope of work 59
References **..... 60**
CHAPTER 3 77
EXPERIMENTAL DETAILS 77
3.1 Introduction 77
3.2 Raw materials 77
3.3 High energy horizontal attritor milling (Simoloyer technology) 81
3.3.1 Process variables 81
3.4 Consolidation of milled powder 83
3.4.1 Leak check 83
3.4.2 Powder filling in cans 84
3.4.3 Canning and degassing 84
3.4.4 Upset forging and extrusion 85
3.5 Chemical analysis 86
3.6 Structural characterization 87
3.6.1 XRD analysis 87
3.6.2 High intensity X–ray diffraction 88
3.6.3 Scanning electron microscopy 88
3.6.4 Electron backscatter diffraction 89
3.6.5 Transmission electron microscopy 90
3.7 Mechanical properties 91
3.7.1 Hardness 91
3.7.2 Tensile properties 92
3.8 Corrosion studies 92
3.8.1 Sample and electrolyte preparation 92

3.8.2 Electrochemical cell 93
3.8.3 Electrochemical corrosion experiments 94
3.8.4 Immersion studies 95
3.9 Oxidation studies 95
3.10 Summary 95
***References* 96**
CHAPTER 4 97
RESULTS AND DISCUSSION 97
4.1 Effect of High Energy Ball Milling on Microstructural Development in Oxide Dispersion Strengthened 18Cr Ferritic Steel 97
4.1.1 Introduction 97
4.1.2 Characterization of milled powders 97
4.1.2.1 Effect of milling time on particle size 97
4.1.2.2 Effect of milling time on crystallite size 100
4.1.2.3 Effect of milling time on microstructural features of powders 100
4.1.3 Upset forged billets 105
4.1.4 Microstructural analysis of extruded and annealed rods 108
4.1.5 Summary 126
References* *126
4.2 Tensile Deformation and Fracture Behavior of Oxide Dispersion Strengthened 18Cr Ferritic Steel 129
4.2.1 Introduction 129
4.2.2 Microhardness of milled powders 129
4.2.3 Bulk hardness of consolidated samples 131
4.2.3.1 Upset forged samples 131
4.2.3.2 Extruded and annealed samples 131
4.2.4 Tensile properties 132
4.2.4.1 Influence of milling time 133
4.2.4.2 Influence of temperature 136
4.2.5 Prediction of flow stress 141
4.2.4.1 Based on hardness data 141
4.2.4.2 Based on tensile data 143
4.2.5 Fractographic examination 146
4.2.6 Summary 151
References* *152

4.3 Influence of Dispersoids on Corrosion Behavior of Oxide Dispersion Strengthened 18Cr Steels....154

4.3.1 Introduction....154

4.3.2 Electrochemical studies....154

4.3.2.1 Cyclic polarization....154

4.3.2.2 Electrochemical impedance spectroscopy....159

4.2.2.3 Potentiodynamic polarization....163

4.3.3 Immersion studies....164

4.3.4 Microstructural studies....164

4.3.5 Summary....167

***References*....167**

4.4 High Temperature Oxidation Behavior of Oxide Dispersion Strengthened 18Cr Ferritic Steel....169

4.4.1 Introduction....169

4.4.2 Oxidation kinetics....169

4.4.3 Characterization of surface oxide layer....173

4.4.4 Raman analysis of oxides....179

4.4.5 Characterization of oxide scale....181

4.4.6 Discussion....183

4.4.7 Summary....185

***References*....185**

CHAPTER 5....187

Conclusions and suggestions for future work....187

5.1 Conclusions....187

5.1.1 Microstructural evolution....187

5.1.2 Mechanical properties....188

5.1.3 Corrosion studies....189

5.1.4 Oxidation studies....189

5.1.2 Scope for the future work....190

LIST OF FIGURES

Chapter 1

Fig. 1.1 Evolution of nuclear fission reactor generations 3

Fig. 1.2 ITER demonstration device for the use of fusion power 4

Fig. 1.3 A dislocation cutting/shearing a particle. 9

Fig. 1.4 Orowan mechanism for dispersion strengthening. 10

Chapter 2

Fig. 2.1 Fe–Cr Phase diagram 28

Fig. 2.2 Schematic representation for the processing of ODS steels 31

Fig. 2.3 Microstructure of ODS–9Cr steel representing the ferrite embedded 32

Fig. 2.4 TEM micrographs of oxide particles in (a) residual ferritic matrix and (b) tempered martensitic matrix 34

Fig. 2.5 Schematic representation of process for oxide particle coarsening 34

Fig. 2.6. Effect of Ti, excess O and HE temperature (Te) on (a) creep 36

Fig. 2.7 Variation of (a) yield strength (b) tensile strength, (c) total elongation with temperature and (d) dependence of stress on Larson–Miller parameter 37

Fig. 2.8 Ultimate tensile strength of various ODS steels in comparison 38

Fig. 2.9 Mechanical properties of ODS–9Cr steel 39

Fig. 2.10 SEM images of the fracture surface of ODS–9Cr steel with 0.3 and 0.5 wt. % yttria at (a, c) 700 °C and (b, d) RT, respectively 40

Fig. 2.11 (a) TEM image of MA957, (b) relationship between chemical composition and size of oxides and (c) size distribution of oxide particles 43

Fig. 2.12 Variation of (a) YS and (b) UTS with temperature of experimental and commercial ODS steels 46

Fig. 2.13 SEM micrographs of tensile fracture surfaces tested at (a–b) RT indicating quasi–brittle fracture mode and at (c–d) (600 °C) indicating ductile fracture mode 47

Fig. 2.14 The effect of aging on the tensile properties at RT in high Cr–ODS steels 51

Fig. 2.15 Variation of tensile stress in ferritic steel, ODS–9Cr and ODS–19Cr steel with temperature 52

Fig. 2.16 Variation of resistances to corrosion and aging embrittlement with Cr in ODS steels 53

Fig. 2.17 Influence of Cr content on the corrosion properties of ODS steel in SCPW 54

Fig. 2.18 Variation of weight gain in high–Cr ODS ferritic steels, JLF–1LN and SUS316L in SCPW 54

Fig. 2.19 Schematic illustrations showing (a) three–stage mechanism for the formation of oxide nanoparticles during MA and consolidation and (b) size effect 57

Fig. 2.20 Variation of (a) crystallite size and (b) dispersoid size of different ODS steels. 58

Chapter 3

Fig. 3.1 Powder morphologies: (a) SEM image of pre–alloyed 18Cr steel powder produced by inert gas atomization and (b) TEM image of nano yttria powder..... 78

Fig. 3.2 Process flow sheet for the manufacturing the ODS–18Cr ferritic steel. 80

Fig. 3.3 (a) Photograph of Simoloyer CM–20, (b) with powder flow and (c) schematic of the milling container..... 83

Fig. 3.4 Photographs of (a) mild steel cans, (b) powder feeding equipment, (c) vacuum pumping system, (d) degassing furnace and (e) sealed cans. 85

Fig. 3.5 Photographs of (a) extrusion press, (b) upset billets and (c) extruded rods. 85

Fig. 3.6 Dimensions (mm) of the sample used for tensile testing. 92

Fig. 3.7 Schematic of three electrode electrochemical test cell..... 94

Chapter 4 (Section 4.1)

Fig. 4.1.1. SEM images of mechanically milled powders: a) P_1, b) P_3, c) P_6 and d) P_N. 99

Fig. 4.1.2 Variation of particle size of 18Cr and ODS–18Cr steel powders with milling time..... 99

Fig. 4.1.3 Variation of crystallite size of 18Cr and ODS–18Cr steel powders with milling time. 100

Fig. 4.1.4 TEM bright filed images of ODS–18Cr milled powders: a) P1, b) P3 and c) P6. 101

Fig. 4.1.5 TEM images of P1 powder: a) BF, b) SAED pattern, c) DF, d) EDS and e) Y_2O_3 particle. 102

Fig. 4.1.6 TEM images of P3 powder: a) BF, b) SAED pattern, c) DF and d) EDS. 103

Fig. 4.1.7 TEM images of P6 powder: (a) BF, (b) SAED pattern and (c) EDS. 104

Fig. 4.1.8 SEM microstructures of upset forged samples: a) ODS6 and b) NODS..... 106

Fig. 4.1.9 TEM bright field TEM bright field images of upset forged samples: a) ODS6 and b) NODS. 106

Fig. 4.1.10 Grain boundary character distribution of upset forged samples..... 107

Fig. 4.1.11 Grain size distribution of upset forged samples: a) ODS6 and b) NODS. 107

Fig. 4.1.12 a) TEM bright field image of upset forged ODS6 and b) dispersoid distribution..... 108

Fig. 4.1.13 SEM microstructures of extruded+annealed samples: a) ODS1, b) ODS3, c) ODS6 and d) NODS. 109

Fig. 4.1.14 Grain boundary character distribution of extruded+annealed samples: a) ODS1, b) ODS3, c) ODS6 and d) NODS. 110

Fig. 4.1.15 Grain size distribution of extruded+annealed samples: a) ODS1, b) ODS3, c) ODS6 and d) NODS. 110

Fig. 4.1.16 Variation of grain boundary length of ODS–18Cr and NODS samples with milling time. 111

Fig. 4.1.17 TEM images of extruded+annealed samples in longitudinal direction: 113

Fig. 4.1.18 TEM bright field images of extruded+annealed ODS–18Cr steel: a) ODS1, b) ODS3 and c) ODS6. 114

Fig. 4.1.19 Size distribution of dispersoids in extruded+annealed ODS–18Cr steels: a) ODS1, b) ODS3 and c) ODS6. 115

Fig. 4.1.20 Comparison of Gaussian distribution of dispersoids in ODS6 at upset forged and extruded+annealed conditions. 116

Fig. 4.1.21 HRTEM image of ODS6 taken along [100] orientation (a) $Y_2Ti_2O_7$ particle, (b) indexed FFT of (a) and (c) inverse FFT of (b) created using [222] spots of $Y_2Ti_2O_7$. 116

Fig. 4.1.22 Typical XRD–patterns of ODS–18Cr samples along with NODS. 119

Fig. 4.1.23 TEM images of $YTiO_3$ in ODS1 a) BF, b) DF, c) SAED pattern, d) simulated ICDD pattern and e) EDS. 120

Fig. 4.1.24 TEM images of Y_2O_3 in ODS1 a) BF, b) SAED pattern and c) EDS. 121

Fig. 4.1.25 TEM images of Y_2TiO_5 in ODS1 a) BF, b) SAED pattern and c) EDS 121

Fig. 4.1.26 TEM images of Y_2O_3 in ODS3 a) BF, b) SAED pattern and c) DF and d) EDS. 122

Fig. 4.1.27 TEM images of Y_2TiO_5 in ODS3 a) BF, b) DF, c) SAED pattern, d) simulated ICDD pattern and e) EDS. 123

Fig. 4.1.28 TEM images of $Y_2Ti_2O_7$ in ODS3 a) BF, b) SAED pattern and c) EDS. 123

Fig. 4.1.29 TEM images of Y_2TiO_5 in ODS6 a) BF, b) SAED pattern and c) EDS 124

Fig. 4.1.30 TEM images of $Y_2Ti_2O_7$ in ODS6 a) BF, b) SAED pattern and c) EDS. 125

Fig. 4.1.31 TEM images of TiO a) BF, b) SAED pattern and c) EDS. 125

Chapter 4 (Section 4.2)

Fig. 4.2.1 Effect of milling time on hardness of 18Cr and ODS–18Cr steel powders. 130

Fig. 4.2.2 Variation of hardness of 18Cr and ODS–18Cr steel powders with crystallite size 131

Fig. 4.2.3 Variation of hardness of annealed NODS and ODS–18Cr steels with milling time. 132

Fig. 4.2.4 Engineering stress–strain curves of NODS, ODS1, ODS3 and ODS6 samples at a) RT, b) 200 °C, c) 400 °C, d) 600 °C and e) 800 °C, respectively. 135

Fig. 4.2.5 Variation of ductility indices (a) eu and (b) et with milling time at all test temperatures. 136

Fig. 4.2.6 Engineering stress–strain curves at different test temperatures of (a) NODS (b) ODS1, (c) ODS3 and (d) ODS6 137

Fig. 4.2.7 Variation of ductility indices (a) e_u and (b) e_t of NODS and ODS samples with test temperature. 137

Fig. 4.2.8 Variation of (a) σ_y and (b) σ_u with test temperature of ODS1, ODS3 and ODS6 along with NODS. 138

Fig. 4.2.9 Variation of strain hardening exponent with milling time and test temperature. 138

Fig. 4.2.10 Calculated strengthening values of ODS–18Cr steels 143

Fig. 4.2.11 Comparison of calculated strength values along with experimental values of ODS–18Cr steels: (a) ODS1, (b) ODS3 and (c) ODS6. 145

Fig. 4.2.12 Fractographs of ODS–18Cr and 18Cr steels at RT along with the corresponding macro fractographs: (a) ODS1, (b) ODS3, (c) ODS6 and (d) NODS. 147

Fig. 4.2.13 Fractographs of ODS6 at different test temperatures: (a) RT, (b) 400, (c) 600 and (d) 800 °C. Inset shows the corresponding macro fractographs. 148

Fig. 4.2.14 Fractographs of NODS at different test temperatures: (a) RT, (b) 400, (c) 600 and (d) 800 °C. Inset shows the corresponding macro fractographs. 149

Chapter 4 (Section 4.3)

Fig. 4.3.1 CP curves of ODS–18Cr samples along with NODS sample. 155

Fig. 4.3.2 Nyquist and Bode plots of ODS and NODS samples for exposure times of 1 and 48 h. 160

Fig. 4.3.3 Nyquist and Bode plots of ODS and NODS samples with different exposure times of 1, 24, 48 and 96 h. 161

Fig. 4.3.4 Equivalent circuit used to fit the EIS data. 161

Fig. 4.3.5 SEM Morphologies of immersed samples of (a) ODS1, (b) ODS6 and (c) NODS. 164

Fig. 4.3.6 The surface morphologies of PD tested samples of (a) ODS1, (b) ODS6 and (c) NODS after 48 h exposure to the 3.5 % NaCl solution. 165

Fig. 4.3.7 The morphology of pits (a) on the surface; cross–section: (b) and (c) ODS6; (d) and (e) NODS. 165

Chapter 4 (Section 4.4)

Fig. 4.4.1 Variation of weight gain as a function of exposure time: (a) 650 °C, (b) 750 °C and (c) 850 °C 172

Fig. 4.4.2 Arrhenius plot of the parabolic oxidation rate constants of NODS and ODS–18Cr samples. 173

Fig. 4.4.3 Variation of parabolic rate constant with (a) grain size and (b) dispersoid size. 173

Fig. 4.4.4 SEM morphologies of ODS6 (a) 500 h, (b) 1000 h, (c) 2000 h and NODS (d) 500 h, (e) 1000 h, (f) 2000 h at 850 °C. 175

Fig. 4.4.5 SEM morphologies of ODS6 (a) 650 °C, (b) 750 °C, (c) 850 °C and NODS (d) 650 °C, (e) 750 °C, (f) 850 °C for exposure time of 2000 h. 176

Fig. 4.4.6 SEM morphologies of (a) ODS1, (b) ODS3, (c) ODS6 and (d) NODS exposed for 850°C and 2000 h. 177

Fig. 4.4.7 Raman spectra of NODS and ODS–18Cr samples (a, b) as a function of exposure temperature (c, d) as a function of exposure time 180

Fig. 4.4.8 (a) and (b) Cross–section images ODS6 and NODS samples exposed to 850 °C for 2000h, respectively. (c) and (d) show the EDS line–scan images of (a) and (b), respectively. (e) Raman spectra. 182

LIST OF TABLES

Chapter 1

Table 1.1 Summary of various strengthening mechanisms 6

Table 1.2 Milestones in the developments of ODS alloy processing 12

Table 1.3 Chemical compositions of commercial ODS alloys (wt. %). 13

Chapter 2

Table 2.1 Nominal chemical compositions of F/M steels 22

Table 2.2 Evolution of steels for power plant applications 24

Table 2.3 Classification of induced activity of elements 25

Table 2.4 Typical compositions of RAF/M steels 26

Table 2.5 Nominal chemical compositions of the austenitic stainless steels 27

Table 2.6 Effect of alloying additions. 30

Table 2.7 Literature review on microstructural studies of ODS–18Cr steel. 50

Chapter 3

Table 3.1 Chemical composition of the as received atomized steel powder. 78

Table 3.2 Sieve analysis of pre–alloyed 18Cr steel powder. 78

Table 3.3 Nomenclature of samples used in the present study. 86

Table 3.4 Chemical composition (wt. %) of powders and bulk samples. 87

Table 3.5 Composition of Vilella's reagent 89

Chapter 4 (Section 4.1)

Table 4.1.1 Crystallite sizes of ODS–18Cr steel milled powders. 101

Table 4.1.2 Average grain diameter of extruded and annealed ODS–18Cr and 18Cr NODS steels. 112

Table 4.1.3 Average size, number density and volume fraction of dispersoids in annealed ODS–18Cr steel 114

Chapter 4 (Section 4.2)

Table 4.2.1 Tensile properties of NODS and ODS–18Cr samples 133

Table 4.2.2 Average dispersoid size, number density and volume fraction of dispersoids in extruded+annealed ODS–18Cr steel along with the values of the various parameters used in equations (4.2.1)–(4.2.5). 142

Table 4.2.3 The calculated strength values including σ_m, $\Delta\sigma_{H-P}$ and $\Delta\sigma_{Or}$ along with experimental values of ODS1, ODS3 and ODS6 at various temperatures 146

Chapter 4 (Section 4.3)

Table 4.3.1 Data obtained from analysis of CP hysteresis curves of NODS and ODS samples. . 157

Table 4.3.2 Parameters obtained from the impedance circuit and corrosion rate calculated from potentiodynamic polarization data for ODS and NODS samples. 161

Chapter 4 (Section 4.4)

Table 4.4.1 The values of parabolic rate constant (k_p), pre–exponential factor (k_0) and activation energy 171

Table 4.4.2 Variation of composition of blisters and matrix for different exposure times at an exposure temperature of 850 °C. 177

Table 4.4.3 Variation of composition of blisters and matrix at different exposure temperatures for an exposure time of 2000 h. 178

Table 4.4.4 Variation of composition of blisters and matrix for different milling times at 850 °C and 2000 h. 178

Table 4.4.5 Raman frequencies (cm^{-1}) of oxides from present work along with the reported data. 179

LIST OF ABBREVIATIONS AND ACRONYMS

ODS	Oxide dispersion strengthened	SANS	Small angle neutron scattering
FBR	Fast breeder reactor	SAXS	Small angle X–ray scattering
VHTR	Very high temperature reactor	YS	Yield strength
GFR	Gas–cooled fast reactor	UTS	Ultimate tensile strength
SFR	Sodium–cooled fast reactor	UE	Uniform elongation
LFR	Lead–cooled fast reactor	SCPW	Super critical pressurized water
MSR	Molten salt reactor	LBE	Lead–bismuth eutectic
SCWR	Super critical water–cooled reactor	OCP	Open circuit potential
ITER	International thermonuclear experimental reactor	PUREX	Plutonium uranium extraction
F/M	Ferritic/martensitic	IGC	Intergranular corrosion
RAFM	Reduced activation ferritic/martensitic	RT	Room temperature
H–P	Hall–Petch	P/M	Powder metallurgy
SAP	Sintered aluminum product	ICP–AES	Inductively coupled plasma atomic emission spectroscopy
DBTT	ductile brittle transition temperature	FWHM	Full width at half–maximum
ODM	Oxide dispersion micro forged	SCE	Saturated calomel electrode
BCC	Body centered cubic	EIS	Electrochemical impedance spectroscopy
FCC	Face centered cubic	XRD	X–ray diffraction
MA	Mechanical alloying	EBSD	Electron backscatter diffraction
BPR	Ball to powder ratio	PIPS	Precision ion polishing system
INCO	International nickel company	CBED	Convergent beam electron diffraction
FE–SEM	Field emission scanning electron microscopy	CP	Cyclic polarization
SFR	sodium fast reactor	EIS	Electrochemical impedance spectroscopy
HE	Hot extrusion	LDA	Laser diffraction analysis
HIP	Hot isostatic pressing	BF	Bright field
SPS	Spark plasma sintering	DF	Dark field
SEM	Scanning electron microscopy	SAED	Selected area electron diffraction
TEM	Transmission electron microscopy	ICDD	International centre for diffraction data
APT	Atom probe tomography	PAH	projected area hardness

LIST OF SYMBOLS

The following notations are used in the text generally unless it is otherwise specifically stated when the letters or symbols refer to other meanings.

σ_f	Flow stress	σ_u	Ultimate tensile strength
σ_0	Strength of annealed base material	σ_y	Yield strength
σ_ρ	Strain hardening	e_u	Uniform strain
σ_{H-P}	Grain size strengthening	e_t	Total strain
σ_{or}	Orowan strengthening	σ	True stress
σ_{ss}	Solid solution strengthening	ε	True strain
σ_m	Matrix strength	n	Strain hardening exponent
τ_0	Friction stress	K_{H-P}	Hall–Petch constant
b	Magnitude of Burgers vector	d_p	Average dispersoid size
α	Proportionality constant	I_{pit}	Pitting current density
G	Matrix shear modulus	ε	Equivalent weight
σ_y	Yield stress	E_{corr}	Corrosion potential
σ_i	Friction stress	I_{corr}	Corrosion current density
d_q	Matrix grain size	E_{pp}	Primary passivation potential
C	Solute concentration	I_{crit}	Critical current density
ε	Strain exerted on the material by the solute	I_{pass}	Passive current density
r	Particle radius	E_{BP}	Breakdown/pitting potential
f	Volume fraction	E_{RP}	Repassivation potential
S	Inter–dispersoid spacing	R_s	Solution resistance
A	Numerical constant	C_{dl}	Electric double layer
Dv	Volume weighted grain size	R_{ct}	Charge transfer resistance
θ	Bragg diffraction angle	k_p	parabolic rate constant
ε_{str}	Strain factor	k_o	pre–exponential factor
λ	X–ray wavelength	E_A	activation energy

ABSTRACT

The advanced energy systems being developed to achieve economy, safety, reliability and sustainability require high performance materials that can withstand to extremely hostile service conditions. Oxide dispersion strengthened steels are being considered as potential candidate materials for high temperature applications, such as, blanket materials for fusion reactors, fuel cladding for Generation–IV fission reactors and blades for gas and ultra–super critical steam turbines due to excellent properties, such as, high temperature strength and resistance to creep, corrosion, oxidation and neutron irradiation. Many of these alloys for above mentioned applications are based on Fe–(9–18 %)Cr–2W–0.2Ti matrix with yttria as dispersoids. The performance of ODS steels depends on the composition, size and number density of dispersoids in the matrix. These steels usually contain a high number density of fine (Y–Ti–O) complex oxide particles along with fine grained structure. Addition of Ti to the yttria containing steel is known to reduce the size and increase the number density and the volume fraction of complex dispersoids. Even though ODS–9Cr ferritic–martensitic steels exhibit nearly equi–axed grain structure, they suffer from corrosion and oxidation. The resistance to corrosion and oxidation of ODS steels can be enhanced significantly by increasing the Cr content from 9 to 18 % without causing much concern from σ phase embrittlement. ODS steels are generally processed by mechanical alloying followed by consolidation either by hot extrusion or hot isostatic pressing. The emphasis of this work was aimed at developing a detailed understanding of the effect of mechanical milling duration on the microstructural evolution during various stages associated with manufacturing and the resultant mechanical, corrosion and oxidation properties of ODS–18Cr ferritic steel.

Dispersion of oxide particles in 18Cr ferritic steel (Fe–18Cr–2.33W–0.34Ti) was done by high energy ball milling of pre–alloyed powders with Y_2O_3. Simultaneously, the base steel was also processed under similar conditions without Y_2O_3 for comparative assessment. The milling was carried out for varying times up to 6 h. Consolidation of the milled powders was achieved by upset forging and hot extrusion. Microstructural evolution was studied at different stages of processing for both milled powders and consolidated rods. The changes that occur in milled powders with increasing milling time (strain accumulation) with respect to crystallite size and oxide size were examined. The

size of crystallite and Y_2O_3 progressively decreased with milling time and reached a near steady state after 5 h. The Y_2O_3 particles in powders either formed atomic clusters or dissolved in the matrix under steady state condition. In hot upset condition, the microstructure consisted of regions of unrecrystallised grains along with areas consisting of fine grains. In the case of consolidated rods, microstructural changes in grain and oxide particle sizes for different milling times were evaluated. In extruded and annealed rods, decrease in grain size, size of oxide particles and increase in the number density of dispersoids (oxide particles) observed as the time of milling is increased. The significant increase in the number density of dispersoids with milling time is due to the increase participation of titanium in the formation of oxides and decrease in size. The dispersoids were identified to be of $Y_2Ti_2O_7$ with cuboidal shape and $Fd\bar{3}m$ diamond cubic crystal structure.

The effect of mechanical milling time on microhardness of 18Cr and ODS–18Cr powders and bulk hardness of upset forged and extruded+annealed ODS–18Cr steel along with NODS steel was evaluated. The microhardness of both 18Cr and ODS–18Cr ferritic steel powders increases with increasing milling time and attaining a steady state after 5 h. The bulk hardness of ODS–18Cr steel is higher than NODS and increases with milling time. The tensile deformation and fracture behavior of ODS–18Cr ferritic steels were studied over a wide range of temperature (RT–800 °C) as a function of milling time along with the oxide–free 18Cr steel (NODS) to understand the inter–relation between microstructure and mechanical properties. At all the test temperatures, the strength of ODS–18Cr ferritic steels increased with the duration of milling time. The overall tensile deformation behavior varied significantly with milling time, but, was similar up to test temperatures below 400 °C. Beyond 400 °C, the flow stress decreased rapidly, even though the general trend of increase in strength with milling time was retained up to the maximum test temperature of 800 °C. The enhanced strength of yttria containing steels when compared to NODS is due to the development of ultra–fine grained structure along with fine dispersion of complex oxide particles. The ductility and strain hardening exponent of ODS–18Cr steels were lower than NODS steel and were found to decrease with milling time at all test temperatures. The concomitant roles of the microstructural features and oxide particles in the strengthening of ODS–18Cr steels from RT–800 °C were rationalized using root of sum of squares model. The predicted flow stress values of

ODS–18Cr steel compare well with experimentally measured values. Fractographic examination carried out on ODS–18Cr and NODS fractured tensile samples, revealed that the fracture was in the ductile fracture mode with distinct neck and shear lip formation showing dimples of varying sizes for all milling times and at all test temperatures. The role of larger inclusions and nano–sized dispersoids in dimple nucleation and growth was evident in the fracture process.

Corrosion resistance of high chromium steels, particularly in the marine environment, is of immense engineering importance. While the corrosion resistance of 18Cr steels is well studied, the corrosion behavior of the steels containing nano–sized dispersoids (ODS) is not examined in detail. The present study is aimed at understanding the influence of $Y_2Ti_2O_7$ dispersoids on the corrosion behavior in 3.5 % NaCl medium by employing electrochemical and immersion techniques. The results clearly suggest that, a) the main corrosion damage is by pitting corrosion, b) the rate of localized corrosion is higher in ODS–18Cr steel, when compared to the base steel (NODS) steel and c) the rate of corrosion increased with increased milling time. The corrosion rate initially decreased up to 48 h of exposure beyond which it increased. The higher corrosion rate at higher exposure times was attributable to the formation of the passive oxide film which is porous. Impedance analysis indicated the formation of a surface film with better corrosion resistance for NODS than ODS–18Cr steels. The corrosion behavior assessed by immersion technique was also found to be similar. The inferior corrosion resistance of ODS ferritic steel when compared to the base steel (NODS) without dispersoids was due to the action of oxide particles in promoting nucleation of pits. The study indicates that the corrosion resistance of NODS steel was marginally higher than the ODS–18Cr steels and the difference is not significant.

The high temperature oxidation behavior of 18Cr ferritic steel with and without yttria was studied by exposing the samples at different temperatures (650–850 °C) for different times (100–2000 h). The weight gain with time during the oxidation was obtained and the morphology and composition in different regions of the oxidized samples were then analyzed. The weight gain increased with exposure temperature and time, following a parabolic rate law. At any given exposure temperature, ODS–18Cr samples exhibited lower weight gain than the NODS (dispersoid–free) sample and the weight gain decreased

with grain size. In both NODS and ODS–18Cr samples, the inner most oxide layer was found to be Cr_2O_3 at all the temperatures. The outermost layer of the oxide layer mainly consists of Fe_3O_4 at lower temperatures (≤ 750 °C) and $FeCr_2O_4$ at higher temperature (850 °C). The presence of fine grained structure and uniformly distributed fine oxide particles in ODS–18Cr steel are the main reasons for enhanced oxidation resistance.

CHAPTER 1
INTRODUCTION

A brief on the current knowledge of the identified topic is provided here, highlighting the necessity for the present study.

The energy requirement of the world is increasing rapidly due to improvement in the living standards of developing nations and increase in world population (6 to 10 billion by 2050) resulting in increased consumption of the fossil fuels. Hence, the concerns regarding the energy needs of the world have become an important topic over the past several years. It also led to the development of efficient, safe, clean and long lasting energy materials [1, 2]. It is projected that the world's energy consumption shall increase to 25–60 TW by 2050 from the present 14 TW [2]. Electrical power is generated from several sources such as (a) fossil fuels (coal, petroleum and natural gas), (b) renewable (solar, wind, hydro, geothermal, biomass, tidal *etc.*) and (c) nuclear sources [3]. At present, fossil fuels contribute to more than 85 % of the total energy production of the world [4–6]. The carbon dioxide (CO_2) released during the burning of fossil fuels contributes to the greenhouse effect, causing detrimental changes in the global climate [7]. The projected increase in energy demands and associated carbon emissions have necessitated the need to increase the efficiency of the existing thermal power plants by operating at a higher temperature (>650 °C) and to identify alternative incessant energy supplies like nuclear or renewable energies. Nuclear power is an attractive source of efficient and reliable high density energy and at present its contribution is about 11 % of the total electricity produced in the world [8, 9]. It is economically viable and helps to reduce the environmental degradation due to lower CO_2 emissions (five grams of carbon dioxide is emitted for each kilowatt–hour of electricity generated by nuclear reactor when compared to emission of 900 and 365 g of CO_2 from coal and gas fired power plants respectively) [3] and also reduced the release of polluting gases (sulfur and nitrogen oxides) and particulate matter.

The efficiency of thermal power plants can be improved by increasing the operating temperature which requires materials that can withstand to such high temperatures. Understanding of operational conditions is crucial for the selection of materials for the

above mentioned applications. The advanced materials being developed for efficient, safe, reliable and sustainable nuclear and thermal power plants should have high temperature strength, good creep and irradiation induced void swelling resistance, corrosion and oxidation resistance and compatibility with sodium, fuel materials and fission products. This chapter gives a brief discussion of future power reactors, various strengthening mechanisms in materials and evolution of materials for the above stated applications.

1.1 Future generation power reactors

1.1.1 Nuclear fission reactors

Nuclear fission is a process in which atomic nuclei of heavy elements split into lighter fragments and release neutrons and huge amounts of energy. Nuclear reactors create and control fission reactions to generate heat and this heat energy is used to produce steam to generate electricity. In a fission reaction, the excellent but dangerous aspect is the chain reaction, in which, the neutrons that are released during the first fission reaction initiate consecutive fission reactions at an exponential rate. Thermal neutrons are the neutrons which have a low kinetic energy to cause fission. Fast neutrons have higher kinetic energy than thermal neutrons. A moderator is used in the nuclear reactor to slow down the fast moving neutrons to equilibrium thermal energies needed for fission. Fast reactors are designed in such a way that no moderator is required and are based on the fission caused by fast neutrons. The fast moving neutrons convert (U–238 and Th–232) into the fissionable material (Pu–239 and U–233) by using neutron capture which is called as "breeding" and each fast breeder reactor (FBR) include this process. FBRs produce more fuel from non–fissile materials than it consumes.

Nuclear fission power employs several methods for electricity generation. Fig. 1.1 shows the timeline illustration of the evolution of different nuclear reactors. For the future nuclear energy production, Generation–IV (Gen–IV) fission reactors are being developed that incorporate economics, revolutionary design features, sustainability and improved safety features than the current generation nuclear reactors [10]. Very High Temperature Reactor (VHTR), Sodium–cooled Fast Reactor (SFR), Molten Salt Reactor (MSR), Lead–cooled Fast Reactor (LFR), Gas–cooled Fast Reactor (GFR) and Super Critical Water–cooled Reactor (SCWR) are the proposed six systems that being developed.

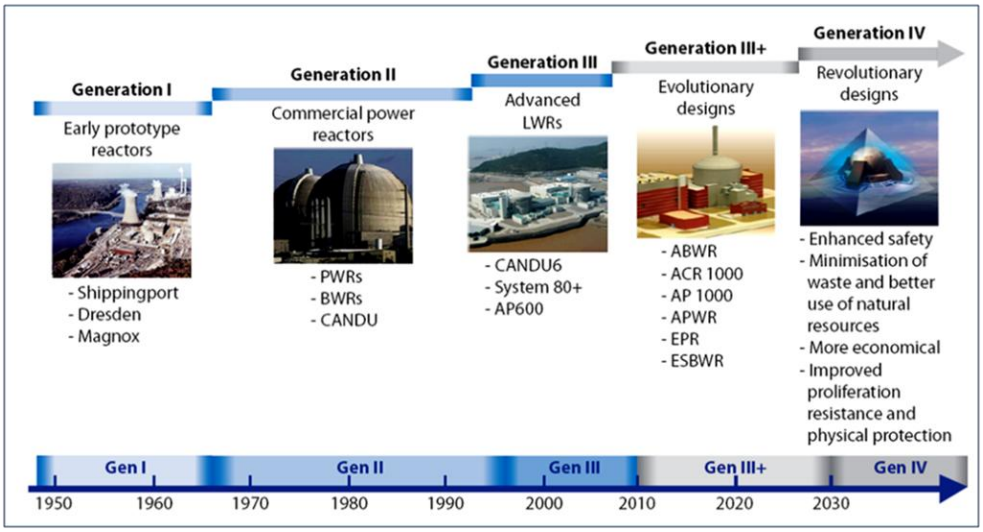

Fig. 1.1 Evolution of nuclear fission reactor generations [10].

1.1.2 Nuclear fusion reactors

Fusion power plants are being considered as potential replacements for fission power plants that can give abundant amounts of clean energy, but the design of commercial fusion reactor poses scientific, technical and industrial challenges. Fusion power is produced by combining the light atomic nuclei to heavier one at extremely high temperatures (150 million degrees centigrade). This process uses superheated hydrogen isotopes in magnetically confined plasma to produce a large amount of energy. In this system, deuterium (^{2}D) and tritium (^{3}H) fuse to form an unstable ^{5}H, which bursts into a ^{4}He with 3.5 MeV of kinetic energy and a neutron with recoil energy of 14.1 MeV [11].

$$^{2}D_{1}+^{3}T_{1}\rightarrow ^{4}He_{2}(3.5MeV)+^{1}n_{0}(14.1MeV)$$

International thermonuclear experimental reactor (ITER) project [12], envisages the setting up of experimental nuclear fusion reactor (Fig. 1.2). Many countries including, Japan, European Union, India, Korea, China, Russian Federation and the USA are part of the ITER project team.

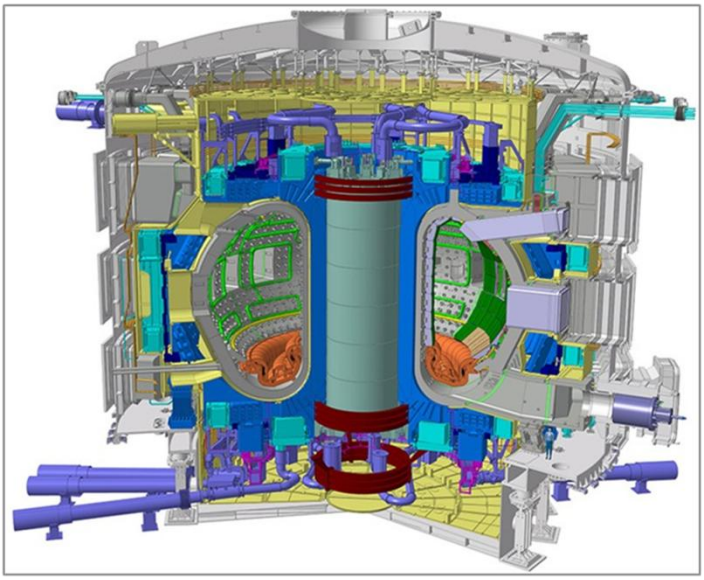

Fig. 1.2 ITER demonstration device for the use of fusion power [12].

1.1.3 Thermal power plants

Thermal power plants use fossil fuel mixed with compressed air to produce thermal energy in a boiler which converts water into steam at high temperature and pressure. The high pressure steam runs a steam turbine, by which mechanical energy is converted into electrical energy. The increase in operating temperature and pressure (700–750 °C and 35 MPa) of steam will result in increased efficiency, which results in the reduction of CO_2 emission. The improvement in efficiency can be achieved by using high performance alloys for steam turbines, boiler membrane wall, super heater and reheater tubes and thick walled headers. The gas turbine is a combustion engine and in recent times, gas turbines have become one of the most efficient machines for converting fuel energy (liquid fuels and natural gas) to electrical energy. Air is compressed to high pressures in the compressor side of gas turbine and sent into the combustion chamber along with fuel in which fuel burns and releases hot gases. These hot gases pass through the turbine. There is current need for research and development on advanced structural materials required for thermal power plant applications.

1.2 Materials requirement for the nuclear and thermal power plants

Structural materials proposed for the advanced power reactors will need to meet rigorous material requirements. The materials in nuclear and thermal reactors are exposed to chemically reactive environments, combinations of high temperatures, varied stresses and

vigorous neutron radiation fields resulting in severe material degradation. Consideration of alloy systems for the above mentioned applications is based on the thermal and mechanical properties, resistance to radiation induced damage, economical constraints and radioactive decay behavior. Various types of materials, like stainless steels (austenitic, ferritic, ferritic/martensitic (F/M) and RAFM), zirconium based alloys and vanadium (V)–based alloys. In future generation power plants, oxide dispersion strengthened (ODS) steels and Ni–based super alloys have been selected as potential candidates for high performance structural materials.

For centuries, metallurgists and material scientists have worked to produce high strength materials for the above mentioned applications without seriously sacrificing the ductility by exploiting various strengthening mechanisms.

1.3 Strengthening of metals

Strengthening of metals is needed because metals are invariably weak due to the nature of metallic bonding, which is diffuse and non–directional and also because of a large number of lattice defects. Dislocation, is an important defect, has high mobility because of the long–range periodicity of metallic lattices and the small translation vectors as compared to the spacing of the planes on which they move [13]. In crystalline metals, dislocations are the principal carriers of plastic deformation. Strength can be controlled by obstructing their dynamic motion by the addition of various microstructural obstacles through various strengthening methods. In metals, five broad categories of strengthening mechanisms exist and these are presented in Table 1.1.

Table 1.1 Summary of various strengthening mechanisms [14–16].

Strengthening mechanism	Effective temperature	Characteristics	Equation
Strain hardening	~0.3T_m	Dislocation–Dislocation strain field interaction	$\tau = \tau_0 + \alpha G b \rho^{1/2}$
Grain refinement	~0.3T_m	Grain boundaries–Dislocation interaction	$\sigma_y = \sigma_i + k d^{-1/2}$
Solid solution strengthening	~0.4T_m	Lattice strain fields–Dislocation interaction	$\Delta\tau = G b \sqrt{c}\varepsilon^{3/2}$
Precipitation strengthening	~0.6T_m	Distribution of fine precipitates, impede dislocation motion	$\Delta\sigma \approx 6G \frac{r^{1/2}}{b^{1/2}} f^{1/2}\varepsilon^{1/2}$
Dispersion strengthening	~0.9T_m	Distribution of insoluble 2nd phase particles, stabilize grain, subgrains	$\Delta\tau_{cut} = \frac{\gamma\pi d}{2b\lambda}$ $\Delta\sigma_{Orowan} = A\left(\frac{Gb}{S}\right)\ln\left(\frac{d_p}{2b}\right)$

In many engineering alloys, the combination of several important strengthening mechanisms is exploited to achieve useful strength levels. The following simplified equation 1.1 gives the flow stress of a material.

$$\sigma_f = f(\sigma_o + \sigma_\rho + \sigma_{H-P} + \sigma_{ss} + \sigma_{Or}), \tag{1.1}$$

where, σ_f is the flow stress, σ_o is the strength of annealed base material, σ_ρ is the strain hardening, σ_{H-P} is the grain size refinement strengthening, σ_{ss} is the solid solution strengthening and σ_{Or} particle strengthening.

To understand the mechanisms involved in different strengthening methods, understanding the behavior of dislocations and their interaction with various types of defects and microstructural features is important. A very brief summary of the methods employed to enhance strength of metallic materials is presented below.

(1) Strain hardening

Strain (work) hardening is the phenomenon by which ductile materials become harder and stronger when they are deformed plastically [15, 16]. The strength due to strain hardening increases with dislocation population due to cold work and the

strength increment is proportional to the dislocation density. The equation for the strength of a material due to strain proposed by Taylor is given as below:

$$\tau = \tau_0 + \alpha G b \rho^{1/2}, \tag{1.2}$$

where, τ_0 is a friction stress to move the dislocation in the absence of other dislocations in the crystal, α is a proportionality constant, G is the shear modulus and b is the Burgers vector.

(2) Grain refinement

The strength of the material increases due to grain refinement, grain boundaries being effective barriers to dislocation motion. E.O. Hall and N.J. Petch have derived the relation between yield stress (σ_y) and grain size (d) known as "Hall–Petch relation" (H–P) [15, 16].

$$\sigma_y = \sigma_i + k d^{-1/2}, \tag{1.3}$$

where, σ_i is overall resistance to dislocation movement offered by the crystal lattice which is called as the 'friction stress', k is the 'locking parameter' which measures the relative contribution of grain boundaries to hardening. The $d^{-1/2}$ term in Eq. (1.3) is small for coarse grained materials. The H–P predication was found to be in reasonable agreement when $100\ \mu m < d < 10\ nm$. In very small grains (<10 nm), grains are unable to support dislocation pile–ups and hence this mechanism is not expected to be valid. This leads to softening at low grain sizes. The inverse H–P effect observed in nanocrystalline materials shows that the H–P slope becomes negative below a critical grain size [17].

(3) Solid solution strengthening

The strength of a metal due to solid solution hardening increases by alloying with another element and the strength increment is related to the concentration of the alloying element [15, 16]. The strengthening is attributed to lattice distortion caused by solute atoms. The shear stress required to move the dislocations in a solid solution is expressed as,

$$\Delta\tau = G b \sqrt{c}\, \varepsilon^{3/2}, \tag{1.4}$$

where, c is the solute concentration and ε is the strain exerted on the material by the solute.

(4) Precipitation strengthening

The increase in flow strength is achieved by precipitation of fine coherent or semi coherent second phase particles in the matrix [15, 16]. It is produced by solution treating and quenching of an alloy in which a second phase in solid solution at the elevated temperature. For precipitation hardening to occur the second phase must be soluble at elevated temperature, but must exhibit decreasing solubility with decreasing temperature. The presence of nano–sized precipitates pin the dislocations and retard their motion, thus enhancing the flow stress.

$$\Delta\sigma \approx 6G \frac{r^{1/2}}{b^{1/2}} f^{1/2} \varepsilon^{1/2}, \tag{1.5}$$

where, $\Delta\sigma$ is an increase in yield stress, r is the particle radius, f is the volume fraction, ε is the measure of the strain field.

(5) Dispersion strengthening

The strength increase in dispersion strengthening is due to the introduction of fine semi coherent or incoherent hard and non deformable particles into the matrix [15, 16]. The dispersoids are usually Y_2O_3, Tho_2, Al_2O_3 *etc*.

In shearing process, the dispersed particles act as penetrable particles through which, dislocations can pass only when the slip plane is continuous from the matrix through the dispersed particle. At the stress levels needed to move a dislocation in dispersoid is higher than that required for dislocation motion through the matrix. Cutting is easier for small particles and the particle/matrix interfacial energy would increase due to the creation of new surfaces (Fig. 1.3). When dislocations cut through the particles, the increase in the resistance to dislocation motion occurs due to the creation of a step at the interface and other imperfections like stacking faults within the particle. The particle properties, such as, ordered structure, coherency strains, interfacial energy, stacking fault energy, morphology, lattice friction stress and modulus effect dictate the ease with which a dislocation can pass through a particle by cutting. Generally, when the size of the particle is smaller than a critical size, the particles are weak and easily

deformable and hence cutting mechanism is favored. The stress required for a dislocation to cut through a second phase particle is given by,

$$\Delta\tau_{cut} = \frac{\gamma\pi d}{2b\lambda}, \tag{1.6}$$

where, γ is the energy of the surface created by dislocation cutting, d is the particle diameter and λ is the inter particle spacing.

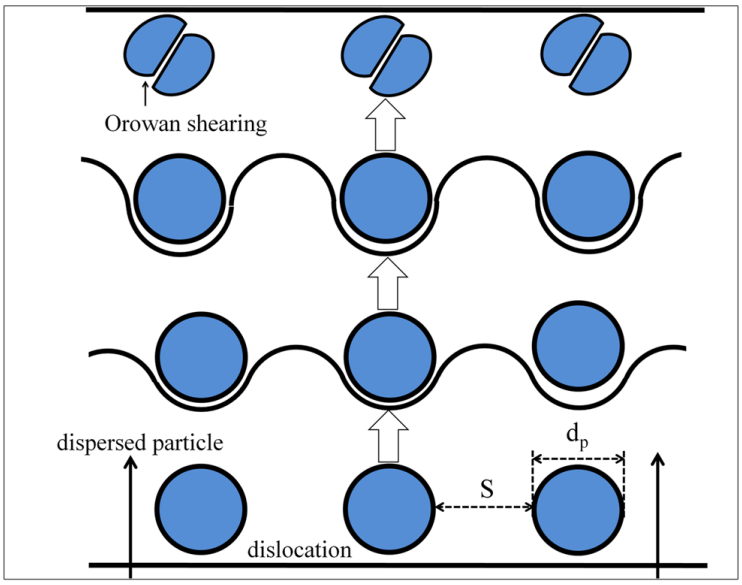

Fig. 1.3 A dislocation cutting/shearing a particle.

Under certain conditions, cutting of particles is not possible. The dislocations have to bend around the particles to bypass the particles. Such dislocation–particle interaction is named as Orowan strengthening. In this case, dispersoids force the dislocations to bypass them (Fig. 1.4) because they act as absolutely strong, impenetrable barriers. Orowan mechanism involves a) bowing of dislocations between two particles and b) dislocation exists by leaving Orowan loops after the yielding. The formation of these Orowan loops further resists the dislocation motion and leads to high work hardening. The stress required to bend a dislocation and the average inter dispersoid spacing of particles are inversely related to each other. In the matrix, uniform distribution of second phase particles plays a significant role in strengthening effect. The extent of strengthening depends on many factors, including particle size and shape, inter dispersoid spacing, volume fraction of dispersoids and the nature of bonding between the matrix and

dispersoid. An equation for the inter dispersoid spacing relating all particle related parameters is given as:

$$S = \frac{d_p}{2}\left\{\left(2\pi/3f\right)^{1/2} - 2\left(2/3\right)^{1/2}\right\}, \tag{1.7}$$

where, d_p is average dispersoid size. The strengthening effect is related to inter dispersoid spacing and the resulting increase in yield strength is given below:

$$\Delta\sigma_{Orowan} = A\left(\frac{Gb}{S}\right)\ln\left(\frac{d_p}{2b}\right), \tag{1.8}$$

where, A is a numerical constant and S is the inter dispersoid spacing.

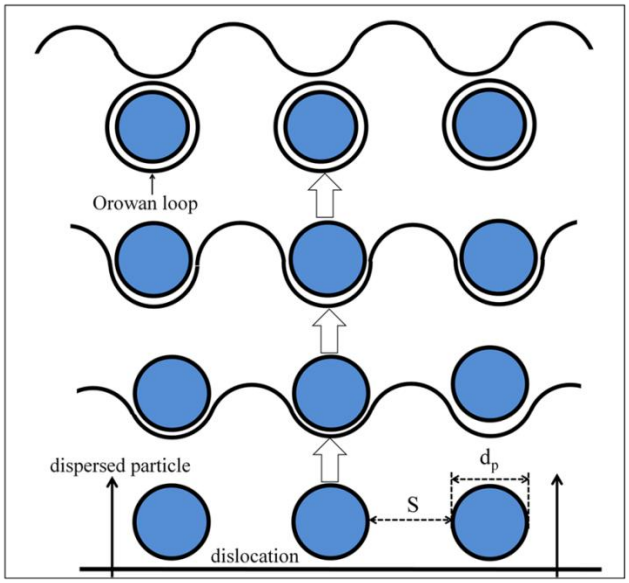

Fig. 1.4 Orowan mechanism for dispersion strengthening.

1.4 Oxide dispersion strengthening

The efficiency of retention of the strengthening effect by any of the mechanisms critically depends on the temperature of deformation [14]. It can be found that from Table 1.1, precipitation and dispersion strengthening mechanisms are the most feasible methods at temperatures greater than $0.5T_m$, for achieving the high temperature strength of a material. It is essential to retain the room temperature strength as effectively as possible for high temperature applications. But most of the strengthening mechanisms become ineffective at high temperatures because of grain growth, dislocation annihilation (recovery and recrystallization) and climb. Precipitation strengthening effect becomes less dominant if the precipitates coarsen due to high temperature exposure leading to

increased inter particle spacing and loss of coherency. The only strengthening mechanism effective at high temperature is dispersion strengthening achieved by dispersion of stable oxides in a ductile matrix. The oxides are chosen based on their chemical inertness, thermal stability and high elastic modulus. Generally, in dispersion system, dispersoids are semi coherent or incoherent with the matrix. The stable oxides not only resist the dislocation motion, but also act as sinks for neutrons, thereby increasing the irradiation resistance. For high temperature and high performance applications ODS materials are most preferred due to their high tensile strength and creep resistance at elevated temperatures.

1.5 Examples of oxide dispersion strengthened alloys

Generally, oxides make the best dispersoids due to their higher hardness, inertness or insolubility in the matrix and stability at high temperatures. Oxides of Al, Mg, Si, Be, Th, Zr and Y are preferred as dispersoids. Sintered aluminum product (SAP) and Ni strengthened with the dispersion of thoria are the initial products developed for commercial applications. The nickel base alloy (Inconel MA754) and more recently developed materials like cadmium oxide dispersed silver, platinum dispersed with thoria, yttria or zirconia and the rare earth element erbium oxide (Er_2O_3) dispersion strengthened Ti are examples of ODS materials. Efforts have been successively made to develop high performance steels with nano sized yttria dispersion. Although many oxide dispersoids have been investigated in steels, Y_2O_3 has been shown to give the most promising high temperature properties.

1.6 Production methods of oxide dispersion strengthened alloys

Several fabrication techniques were tried for the manufacture of ODS alloys, and they are (1) Mechanical alloying, (2) Internal oxidation, (3) Surface oxidation, (4) Selective oxide reduction, (5) Thermal decomposition, (6) Co–vaporization, (7) Electro combination forming, **(**8) Co–precipitation, (9) Stabilized precipitate, (10) Splat cooling, (11) Gas atomization reaction synthesis, (12) Crystallization of amorphous phases, (13) Chemical processing and (14) Ignition coating.

Internal oxidation in combination with rapid solidification processing is a potential method, but has got problems with large scale production. In a metal matrix, dispersion of oxide particles can be achieved by mixing the matrix metal powder with a fine powder of

the oxide and then consolidating the mixture. However, in the matrix, uniform oxide particle distribution with the size and inter particle spacing of dispersoids of not more than a few tens of nanometers are necessary to get the required strengthening effect. The size of the oxide particles must be extremely fine and there should be intimate mixing of oxide particle with matrix to obtain the smaller inter particle spacing. Due to this reason, conventional mixing of metal and oxide powders is not effective for producing ODS alloys. Mechanical alloying (MA) is a viable processing method to obtain the homogeneous distribution of alloying elements with a fine dispersion of oxide particles and more economical for large scale production, which has been applied initially to produce nickel based dispersion strengthened alloys and subsequently to steels and aluminum alloys.

1.7 Development of oxide dispersion strengthened steels

With the sole intention of increasing the temperature capability beyond that of conventional steels, efforts were made to exploit dispersion hardening by introducing stable oxide particles. ODS steels refer to steels that are strengthened by fine stable oxide particles. In ODS steels, the dispersion of fine stable oxide particles in crystalline matrix results in a much stronger microstructure than the matrix phase alone [18, 19]. An overview of milestones of development of ODS alloy is presented in Table 1.2. Even though, development of ODS steels dates from the 1910s, and it was pioneered in Belgium in the late 1960s and work for the above applications has still been in process. There is a huge and increasing worldwide interest in ODS steel development.

Table 1.2 Milestones in the developments of ODS alloy processing [20].

Year	Processing method	Alloy
1910	Conventional powder metallurgy	Ductile tungsten
1930	Internal oxidation	Cu, Ag and Be alloys
1946	Milling of Al powder with in–situ formation of surface oxide	Sintered aluminum product (SAP)
1958	Fine powder metallurgy	Thoria Dispersed Nickel (TD–Ni)
1970	Mechanical alloying	Ni based ODS alloy (MA 753)
2006	Gas atomization reaction synthesis	Chemical reservoir alloys

ODS steels are generally processed by powder metallurgy (P/M) route, in which mechanical alloying followed by consolidation either by hot extrusion (HE) or hot isostatic pressing (HIP). Even though, ODS steels are already available in commercial quantities, this alloy is even so special and many of the important properties are not yet understood. Iron–based ODS alloys and nickel–based ODS alloys are the two main classes of ODS alloys.

The nominal chemical compositions of some of the commercial ODS steels, such as Fe–base (MA 956 and MA 957 (INCO, Special Metals and Plansee), PM 2000 (Special Metals and Plansee) and ODM 751 (developed by Dour Metal)) and Ni–base (MA 6000, MA760 and MA 758) are given in Table 1.3. ODS steel development programs are also in progress in Europe (ODS EUROFER), Japan (F82H), United States (ODS steel) and India, each of these ODS steels has their own advantages.

Table 1.3 Chemical compositions of commercial ODS alloys (wt. %).

Fe–base	**Cr**	**Al**	**Mo**	**Ti**	**C**	**N**	**Y_2O_3**	**Fe**	**Ref**
MA 956	20	4.5	–	0.5	0.01	0.045	0.5	bal.	[21]
MA957	14	–	0.3	1	0.01	0.012	0.27	bal.	
PM 2000	20	5.5	–	0.5	<0.04	–	0.5	bal.	
ODM 751	16.5	4.5	1.5	0.6	–	–	0.5	bal.	
Ni–base	**Cr**	**Al**	**W**	**Ti**	**C**	**N**	**Y_2O_3**	**Ni**	**Ref**
MA6000	15	4.5	3.9	2.3	0.06	0.2	1.1	bal.	[21]
MA760	19.5	6	3.4	–	0.06	0.3	1.0	bal.	
MA758	30	0.3	0.5	–	0.05	–	0.6	bal.	

1.7.1 Iron based oxide dispersion strengthened steels

Fe–based ODS steels are designed to be corrosion and oxidation resistant and also possess an excellent high temperature strength compared to equivalent cast alloys due to the Y_2O_3 dispersoid particles. MA956 exhibits, excellent corrosion and oxidation resistance due to the formation of adherent, stable α–Al_2O_3 phase. Because of its high strength, corrosion resistance and formability, it is being considered for a variety of high temperature applications. This alloy was developed for the gas turbine combustors and vacuum furnace fixtures. Even though, this alloy showed better creep properties, but exhibited low impact toughness with high ductile brittle transition temperature (DBTT). The residual porosity could be a reason for the low impact toughness of the ODS steel.

MA956 is used for high temperature service applications in the form of tubes in steel making, coal and oil burning power stations and glass processing industry.

More recently MA957 and DT2203Y05 ferritic steels have been evaluated for its use at temperatures of about 700 °C in a liquid sodium environment due to their excellent swelling resistance because of body centered cubic structure of the ferritic matrix. The conventional ferritic and austenitic alloys are not suitable for this application due to the dimensional swelling caused by the high neutron fluxes [22].

Oxide dispersion micro forged (ODM) ferritic alloys are also considered for various high temperature applications, such as, heat exchangers, gas turbine combustion chambers, thermocouple shielding, resisters and diesel engine components, *etc.* The compositions of ODM 331 and ODM 751 are similar to that of MA956 steel except for little changes in the contents of Cr and Ti. ODM751 with 1.5 % Mo shows higher rupture strength than that of MA956 either due to the χ–phase or solid solution strengthening [23].

PM2000, a ferritic ODS alloy, exhibits superior mechanical properties, weldability and less pore formation during the service. It shows a lower weight gain than MA956 during the isothermal and cyclic oxidation. The applications of PM2000 are gas turbines, furnace construction as shields, ceramic industry, combustion chambers, burner tubes, thermocouple protection tubes, glass industry, high temperature testing equipment, automotive diesel engines, *etc*.

The ODS steels being developed at present are based on Fe–(9–18%)Cr–2W–0.2Ti with yttria as dispersoids. Even though, the ODS steels based on 9Cr exhibit isotropic mechanical properties, they suffer from corrosion and oxidation. The corrosion and oxidation resistance of ODS steels is improved by increasing the chromium content up to 18 % without serious incidence of σ phase embrittlement but compromising on isotropy [24].

1.8 Mechanical alloying

Mechanical alloying (MA) is an efficient and one of the best techniques to disperse fine oxide particles uniformly in the ductile metal matrix [25–27]. MA is a high energy ball milling, in which welding and fracture of powder particles occur repetitively. High energy ball mills, such as, shaker mills (SPEX 8000 mixer/mill), planetary mills (Fritsch and Retsch mills), attritor mills (Szegvari attritor) and large diameter ball mills are used to carry out MA. These mills differ from each other because of capacity, speed of the milling and temperature. Generally, SPEX shaker mills have very low capacity and arthritis have a high capacity to produce powders [26].

ODS alloys were produced through MA in 1970 by J.S. Benjamin [25]. The first alloy was a thoria dispersed nickel based superalloy developed for high strength and creep resistance at elevated temperatures. At present, MA being used to synthesize a variety of metastable phases starting from elemental powder blend stage to pre–alloyed powder stage with a combination of ductile–ductile or ductile–brittle or brittle–brittle materials [25]. Several generally accepted features of the MA are alloying of elements with high differences in their melting points, extension of the solid solubility limit, formation of metastable phases, homogeneous dispersion and grain size refinement.

During MA, the powder particles are entrapped between the balls when they collide. The impact energy exhibited on the powder particles results in work hardening and subsequent fracture of the powder particles. The newly formed surfaces enhance the welding of particles resulting in increase in particle size [26]. The particles get strain hardened and subsequently fragmented into flakes, with continued deformation. At this stage, the particles tend to fracture easily rather than cold welded [27]. The structure of the particles gets refined progressively because of the continuous impact of grinding balls and reaches a steady state beyond a particular duration milling due to the equilibrium between welding and fracture. High energy milling also induces crystal defects, such as, stacking faults, vacancies, dislocations and increased number of grain boundaries. Diffusivity of solute atoms in the matrix is enhanced due to these defects, thus the alloying effect of different elements is significant [25–27].

Various MA parameters, such as, the ball–to–powder weight ratio (BPR), size of the balls, type of equipment, milling time, milling speed, milling atmosphere, process

temperature, process control agent, fill volume *etc.*, influence the physical and chemical properties of powders.

1.9 Objective of the present work

Even though, much research work has been carried out to evaluate the size and structure of dispersoids in milled powders as well as in consolidated samples and their influence on the mechanical properties, there is an ambiguity with respect to the effect of process parameters on the evolution of microstructure at every stage of processing and their influence on mechanical, corrosion and oxidation properties. Therefore, the present research work is aimed at studying the influence of milling time on the evolution of microstructure at various stages of processing and the resultant structure–dependent properties (mechanical, corrosion and oxidation) of ODS–18Cr steel. The objectives of the present work are identified after detailed literature review and are given below:

1. To produce ODS–18Cr steel powders by high energy milling for varying times and subsequently consolidate milled powders by hot extrusion.

2. To study the effect of milling parameters on the morphological and structural changes in the matrix and dispersoids.

3. To understand the changes that occur in the microstructure and size, shape and structure of dispersoids after upset forging and extrusion at high temperatures.

4. To understand the structure and the temperature dependent deformation behavior of consolidated samples.

5. To study the influence of dispersoids on corrosion behavior of ODS–18Cr steel in 3.5 % NaCl solution.

6. To observe the effect of dispersoids on oxidation of ODS–18Cr steel at different temperatures and exposure times.

1.10 Overview of the thesis

As the present study includes all the details and analysis carried out to address the above mentioned objectives, the entire research work is divided into 5 chapters and details of these chapters are given below:

Chapter 1 presents on the need of high performance materials, various strengthening mechanisms, development of ODS steels and their applications. In addition, this chapter highlights the motivation, objectives and an overview of the present study.

Chapter 2 describes the evolution of steels for high temperature applications over a period of time with special emphasis on detailed and latest literature review on the ODS steels.

Chapter 3 deals with all the experimental details to produce ODS–18Cr steels and description of characterization tools used for evaluation of the microstructural, mechanical, corrosion and oxidation properties.

The results obtained from the present work are discussed in **Chapter 4** of the thesis. The Chapter on Results and Discussion is organized in to 4 sections.

Section 4.1 discusses the evolution of microstructure and size, shape and structure of dispersoids in ODS–18Cr steel at various stages of processing. The majority of the results discussed in this chapter has been published in a journal article; M. Nagini, R. Vijay, Koteswararao V. Rajulapati, K. Bhanu Sankara Rao, M. Ramakrishna, A.V. Reddy and G. Sundararajan, "Effect of process parameters on microstructure and hardness of oxide dispersion strengthened 18Cr ferritic steel", *Metallurgical and Materials Transactions A*, 47 A (2016) 4198–4209.

Section 4.2 presents the evaluation of mechanical properties and fracture studies of ODS–18Cr steel. This chapter deals with the influence of powder milling time (microstructural changes depend on milling time) on the tensile deformation and fracture behavior of ODS–18Cr steel at different temperatures along with oxide–free 18Cr steel. This chapter also discusses the prediction of strength values using root of sum of squares model in comparison to the experimental values. The details presented in this chapter will be communicated to *Metallurgical and Materials Transactions A*.

Section 4.3 includes the study of corrosion behavior of ODS–18Cr steels in 3.5 % NaCl solution using both the electrochemical and immersion techniques. This chapter presents the results on cyclic polarization (CP), electrochemical impedance spectroscopy (EIS), potentiodynamic polarization and immersion studies of ODS1 and ODS6 along with NODS steel. The results discussed in this chapter have been published in a journal article;

M. Nagini, A. Jyothirmayi, R. Vijay, Tata N. Rao, A.V. Reddy, Koteswararao V. Rajulapati and G. Sundararajan, "Influence of dispersoids on corrosion behavior of oxide dispersion strengthened 18Cr steels made by high–energy milling", *Journal of Materials Engineering and Performance*, 25 (2016) 577–586.

Section 4.4 discusses about the influence of dispersoids on the high temperature oxidation behavior of 18Cr ferritic steel with and without yttria. The oxidation studies were carried out at different temperatures (650–850 °C) for different times (100–2000 h). This chapter also discusses about morphology and phases present in the oxide layer. The content related to this work will be communicated to *Oxidation of Metals*.

Chapter 5 contains summary of the present work on development of ODS–18Cr steels and suggestions for the future work.

All the references that have been cited in the thesis have been listed at the end of each chapter. The style of each citation is as follows: Authors names (Initials, Last name), Title, *Journal name*, Volume number (Year) Page nos.

References

[1] J. Stringer, L.L. Horton, OSTI Document No. 811872, Office of science and technical information, (2003).

[2] U.S. DOE, A technology roadmap for generation–IV nuclear energy systems, in: GIF–002–00 OECD Nuclear Energy Agency, GIF–002–00, Washington, DC, 2002, pp. 1–90.

[3] Annual Energy Outlook 2013, U.S. Energy Information Administration (EIA), OE/EIA–0383 (2013) (Washington, D.C.: DOE, 2013).

[4] Power Reactor Information System (PRIS), (International Atomic Energy Agency, IAEA, Vienna, Austria, 2013). http:// www.iaea.org/pris/home.aspx.

[5] R.B. Rebak, Introduction to corrosion in energy production, *Journal of the Minerals, Metals & Materials Society*, 65 (2013) 1021–1023.

[6] A. Verbruggen, Renewable and nuclear power: A common future?, *Energy Policy*, 36 (2008) 4036–4047.

[7] Nuclear Energy Agency (NEA) 'Nuclear Energy Today': URL www.oecd.Nea.org/Html/Pub/Nuclearenergytoday/Welcome.html, (2005).

[8] C.T. Whitman, The case for nuclear power, 00077135, Business Week (4050), 9/17/2007.

[9] M.M. Abu–Khader, Recent advances in nuclear power: A review, *Progress in Nuclear Energy*, 51 (2009) 225–235.

[10] T. Abram, S. Ion, Generation–IV nuclear power: A review of the state of the science, *Energy Policy*, 36 (2008) 4323–4330.

[11] L.A. El–Guebaly LA, Fifty years of magnetic fusion research (1958–2008): Brief historical overview and discussion of future trends, *Energies*, 3 (2010) 1067–1086.

[12] M. Shimada, A. E. Costley, G. Federici, K. Ioki, A.S. Kukushkin, V. Mukhovatov, A. Polevoi, M. Sugihara, Overview of goals and performance of ITER and strategy for plasma wall interaction investigation, *Journal of Nuclear Materials*, 337–339 (2005) 808–815.

[13] A.H. Cottrell, The mechanical properties of matter, John Wiley, New York, 1966.

[14] M.J. Slinger, On the formation and stability of nanometer scale precipitates in ferritic alloys during processing and high temperature service, ISBN: 9780496034932. Santa Barbara, University of California, 2004.

[15] G.E. Dieter: Mechanical metallurgy, 3rd Ed., McGraw–Hill Book Co., London, 1988.

[16] T.H. Courtney, Mechanical behavior of materials, McGraw–Hill Book Co., London, 1990.

[17] C.E. Carlton, P.J. Ferreira, What is behind the inverse Hall–Petch effect in nanocrystalline materials?, *Acta Materialia*, 55 (2007) 3749–3756.

[18] G.S. Ansell, The mechanism of oxide dispersion strengthening: A review, paper presented at metallurgical society conferences on oxide dispersion strengthening, Boltan and Landing, New York, 1966.

[19] G.S. Ansell, J. Weertman, "Creep of a dispersion–hardened aluminum alloy", Transactions of the American Institute of Mining and Metallurgical Engineers 215.5 (1959) 838–843.

[20] R.F. Singer, G.H. Gessinger, Oxide dispersion strengthened superalloys, in: Powder metallurgy of superalloys, Butterworths, London, (1984) p. 213–292.

[21] H.K.D.H. Bhadeshia, Recrystallisation of practical mechanically alloyed iron–base and nickel–base superalloys, *Materials Science and Engineering A*, 223 (1997) 64–77.

[22] I.C.I. Okafor, O.N. Carlson, Equilibrium studies on a chi phase strengthened ferritic alloy, *Metallurgical and Materials Transactions A*, 9 (1978) 1651–1657.

[23] B. Kazimierzak, M. Prignon, C.L. Mertens, C. Coutsouradis, *High Temperature Materials for Power Engineering 1990*, Kluwer Academic Publishers, (1990) 131, quoted by Regle (1994).

[24] A. Kimura, H.S. Cho, N. Toda, R. Kasada, K. Yutani, H. Kishimoto, N. Iwata, S. Ukai, M. Fujiwara, High burnup fuel cladding materials R&D for advanced nuclear systems[#], nano–sized oxide dispersion strengthening steels, *Journal of Nuclear Science and Technology*, 44 (2007) 323–328.

[25] J.S. Benjamin, Dispersion strengthened superalloys by mechanical alloying, *Metallurgical Transactions*, 1 (1970) 2943–2951.

[26] C. Suryanarayana, Mechanical alloying and milling, *Progress in Materials Science*, 46 (2001) 1–184.

[27] B.S. Murty and S. Ranganathan, Novel materials synthesis by mechanical alloying/milling, *International Materials Reviews*, 43 (1998) 101–144.

CHAPTER 2
LITERATURE REVIEW

2.1 Introduction

This chapter on literature review is organized into ten sections to facilitate the co–ordination between the wide ranges of literature that is relevant to the proposed problem. Section 2.2 provides a brief on the evolution of steels for high temperature applications. Section 2.3 highlights the composition design of ODS steels. Section 2.4 highlights the production of ODS steels. Sections 2.5–2.7 review the microstructural, mechanical, corrosion and oxidation properties ODS ferritic–martensitic, ferritic and high–Cr ferritic steels. Section 2.8 deals about the mechanism of the formation of complex–oxide particles. Section 2.9 discusses the effect of process parameters on the structure and properties of ODS steels. Section 2.10 is aimed to highlight the unresolved issues and thereby describe the significance of the current work.

2.2 Evolution of steels for high temperature applications

2.2.1 Ferritic/Martensitic steels

Ferritic/martensitic (F/M) steels (9–12 % Cr) are promising clad materials in sodium fast reactor (SFR), ducts of several Generation–IV (Gen–IV) designs and structural (blanket and core) components for fusion reactors due to its high thermal conductivity, good swelling resistance and low thermal expansion relative to austenitic steels [1, 2]. Microstructure of F/M steels is usually obtained by appropriate balancing the composition in terms of Cr_{eq} and Ni_{eq} to achieve a desired fraction of ferrite and martensite on quenching. The process named as tempering (~760 °C), which transforms much of the martensite to ferrite, results in formation of tempered martensite. Initially, in 1920s, introduction of Cr–Mo steels as structural materials lead to the development of F/M steels in thermal power plants. The advantage of commercial F/M steels for fast reactors in 1970s and for fusion reactors in 1980s was established and since then, extensive research has been done on the progress and application of materials for nuclear plants [2]. In 1960s, for the power generation industry, Sandvik HT9 martensitic steel was developed in Europe and was selected as the material in the fast reactor program of the U.S. for the exploration of properties. Steels (EM–12, FV448, DIN 1.4914, PNC–FMS and JFMS) similar to HT9 were used for applications involving moderate temperature of ≅ 550 °C.

Excellent swelling resistance was exhibited by these steels with a steady–state swelling rate of ≈0.2 %/dpa up to 200 dpa [1]. When compared to conventional high Cr steels, the Japanese PNC–FMC steel has high temperature strength. At 650 ºC, this steel has the highest creep rupture strength amongst similar steels and irradiation environment could not degrade the cladding of this steel [3]. Even though, improved versions of these steels are developed; still some of these are candidates for Gen–IV reactors. Substantially, F/M steels have been developed for conventional power plants due to their high temperature creep and oxidation resistance [2, 4]. Klueh [4] provided a detailed review on various types of F/M steels that were developed during the last six decades. The nominal chemical composition of various F/M steels is shown in Table 2.1.

Table 2.1 Nominal chemical compositions of F/M steels [1–4].

Alloy/Composition (wt. %)	**C**	**Si**	**Mn**	**Cr**	**Ni**	**Mo**	**W**	**V**	**Nb**	**B**	**N**	**Other**
12Cr–1MoWV (HT9)	0.20	0.40	0.60	12.0	0.50	1.0	0.5	0.25	–	–	–	–
EM–12	0.10	0.40	0.60	9.5	–	2.0	–	0.30	0.40	–	–	–
FV448	0.10	0.46	0.86	10.7	0.65	0.6	–	0.14	0.26	–	–	–
DIN 1.4914	0.11	0.45	0.35	11.3	0.70	0.5	–	0.30	0.25	0.008	0.03	–
PNC–FMC	0.15	0.05	0.50	11.0	0.50	0.5	2.0	0.20	0.05	–	0.05	–
JFMS	0.05	0.67	0.58	9.6	0.94	2.3	–	0.12	0.06	–	–	–
2.25Cr–1Mo (T22)	0.15	0.30	0.45	2.25	–	1.0	–	–	–	–	–	–
9Cr–1Mo (EM10–T9)	0.12	0.60	0.45	9.0	0.20	1.0	–	–	–	–	–	–
12Cr–1MoV (HT91)	0.20	0.40	0.60	12.0	0.50	1.0	–	0.25	–	–	–	–
Modified 9Cr–1Mo (T91)	0.10	0.40	0.40	9.0	0.10	1.0	–	0.20	0.08	–	0.07	–
HCM12	0.10	0.30	0.55	12.0	–	1.0	1.0	0.25	0.05	–	0.03	–
NF616 (T92)	0.07	0.06	0.45	9.0	0.25	0.5	1.8	0.20	0.05	0.004	0.06	–
E911	0.11	0.40	0.40	9.0	0.20	1.0	1.0	0.20	0.08	–	0.07	
TB12	0.10	0.06	0.50	12.0	0.10	0.5	1.8	0.20	0.05	0.004	0.06	
HCM12A (T122)	0.11	0.10	0.60	12.0	0.30	0.4	2.0	0.25	0.05	0.003	0.06	1.0Cu
NF12	0.08	0.20	0.50	110.	–	0.2	2.6	0.20	0.07	0.004	0.05	2.5Co
SAVE12	0.10	0.30	0.20	11.0	–	–	3.0	0.20	0.07	–	0.04	3.0Co 0.07Ta 0.04Nd

The evolution of the F/M steels will be reviewed by considering the compositional changes that have led to improved microstructures and properties. In 1940s, T22 steel was introduced and is still extensively used. Together with T22, T9 and also Fe–9Cr–1Mo–0.6Si–0.4Mn–0.12C steels were developed for corrosion resistance. Subsequently, there has been an incessant push to enhance the operating temperatures of thermal power plants, leading to the development of various “generations” of steels with enhanced high temperature strength. Since, the introduction of T22 and T9, three generations of steels have been initiated and Gen–IV steels are in the developmental phase [5] (Table 2.2).

The two steels (T22 and T9) are called as the 'zeroth' generation steels and they had 10^5 h creep–rupture strength of 40 MPa at 600 ºC and were used up to a maximum of 538 °C [5–7]. Beyond the zeroth generation (1940s), steels mainly contained the Cr concentration of 9–12 % for high temperature corrosion and oxidation resistance.

In first generation steels, along with increased Cr, adding of carbide formers (V and Nb) to compositions of T22 and T9 also involved for precipitation hardening. To enhance the solid solution strengthening, in addition to that provided by Mo, a small amount of W was also added. In 1960s, these steels (2.25Cr–1MoV, HT91, HT9, EM12 and HCM9M) were introduced for the applications at the operating temperature of 565 º C. These steels had increased 10^5 h creep–rupture strength of 60 MPa at 600 ºC. For HT9 and HT91 steels, C is used as the most effective austenite stabilizer in addition to Ni. HT9 contains 0.2 % C, but at high temperatures, the precipitate ($M_{23}C_6$) is prone to coarsen.

Second generation steels were developed during 1970–1985. Alloying elements C, Nb, V and N were optimized and the maximum operating temperature increased to 593 ºC. These steels, which include 9Cr–1Mo (T91), HCM2S and HCM12, have 10^5 h rupture strength at 593 ºC of about 100 MPa. All over the world, among these steels, T91 has been mostly used in the power generation plants [5–7]. A noticeable increase in the creep strength was observed in T91, which was achieved by adding Nb, N and lowering the C content to promote fine MX precipitates. The optimum content of V and Nb was found to be about 0.2 % and 0.05 %, respectively.

In 1990s, third generation steels (NF616, E911, TB12 and HCM12A) were introduced and developed by the substitution of W, B and N, thus enhancing the temperature capability to 620 ºC with 10^5 h creep rupture strength of 140 MPa. The third generation 9Cr steels, NF616 (T92) and E911, are developed in Japan and Europe, respectively are simple modifications of T91. Partial replacement of W in favor of Mo and addition of B (named as T92) accomplished improvement in structural stability and creep resistance. For effective creep strengthening, the value of Mo + 0.5 W should be about 1.5 %. In stabilizing microstructure, boron is an effective addition which is being incorporated in $M_{23}C_6$. For the purpose of oxidation and corrosion resistance, Cr content shifted from 2.25 to 9–12 % as the operating temperature was increased to 600 ºC. By increasing the

chromium content from 9 to 12 %, it is required to balance the influence of the adding of ferrites stabilizer with an austenite stabilizer if total austenitization and 100 % martensitic transformation is to be attained. The reason for using low carbon 9Cr steels rather than over high Cr (> 12 % Cr) steels is due to the formation δ ferrite. To get better weldability for the third–generation 12Cr steels, usually, the carbon concentration was kept to about 0.1 %, thus requiring some other austenite–stabilizing elements to be added if δ–ferrite was to be avoided.

Finally, the next generation (fourth generation) of steels is being developed which aims to increase the operating temperatures to 650–700 ºC. An objective for the Gen–IV steels included SAVE12 and NF12 having rupture strength of 180 MPa at 600 ºC for 10^5 h life [5–7]. These two 12 % Cr compositions contain cobalt (2.5–3 %) to put down the conflicting effects of nickel on creep. For advanced fission reactors, it is not suitable to place Co–containing steels for cladding and duct materials. In these steels compared to the third–generation compositions, the amount of molybdenum has been further decreased or excluded with about 0.1 % C, and tungsten (2.6–3.0 %) has been increased. There are other issues related to the fabrication and joining linked to the formability and weldability.

Table 2.2 Evolution of steels for power plant applications [5–7].

Generation	Years	10^5 h rupture strength, 600 °C [MPa]	Steels	Operating temperature [°C]
0	1940–60	40	T22, T9	540
I	1960–70	60	EM12, HCM9M, HT9, HT91	565
II	1970–85	100	HCM12, T91, HCM2S	590
III	1985–95	140	NF616,E911, HCM12A, TB12	620
IV	Future	180	NF12, SAVE12	650–700

Reduced activation ferritic/martensitic (RAF/M) steels are tailored compositions of conventional F/M (8–12 % CrMoVNb) steels and are being considered for the fabrication of futuristic fusion reactors. These steels are being investigated by fusion materials research groups all over the world [8–11]. The damage accumulation in RAF/M steels is lower due to better thermal conductivity and higher swelling resistance [12–14]. The international fusion programs introduced the idea of low activation materials in mid–1980s [15, 16]. In radioactive environment, it is necessary to use low activation steels

which when irradiated do not become radioactive or if activated, the radioactivity decays quickly to minimize the problems in storage. The development of RAF/M steels evolved based on the replacement of undesirable elements in Cr–Mo steels to promote radioactive decay from nuclear calculations [17]. The categorization of induced activity of elements is presented in Table 2.3 [18].

Table 2.3 Classification of induced activity of elements [18].

Category	Elements
Very low activation (decays within 2 weeks)	Li, Be, B,C,O, Mg, Si, P, S
Low activation (decays in 1 month–5 years)	Ti, V, Cr, Zr, W, Pb, Y
Moderate Activation (decays in 10–30 years)	Mn, Fe, Zn, Hf
High Activation (does not decay in 100 years)	Al, Ni, Cu, Nb, Mo, Sn

Based on the developments, Cr–Mo steels with the absence of Nb, Cu, Mo, N and Ni were developed [19]. The advancement of RAF/M steels involved the replacement of Mo by W and/or V [20]. The fusion materials programs (US, EU and Japan) have advanced Ta containing Cr–V and Cr–W–V steels to which Ta is sometimes added as a substitution for Nb [21]. In addition to the judicious choice of alloying elements, RAFM steels can be quenched and tempered to develop the tempered martensitic structure. Such a structure consists of a large number of lattice defects and can act as traps for defects generated by radioactivity [22, 23]. In many RAF/M steels, the Cr concentration is limited to 7–9 % to optimize corrosion resistance and reduce DBTT [24]. Chromium levels above 12 % lead to the formation of σ–phase and δ–ferrite which lowers the impact toughness under irradiation at low temperatures [25]. Different RAF/M steels such as F82H [15, 26, 27] and JLF–I [28–30] (Japan), ORNL 9Cr–2WVTa (United States) [22, 31], CLAM (China) [11] and OPTIFER Ia, OPTIFER II and more recently EUROFER 97 (Europe) [32–35] have been developed and extensively studied. The compositions of these steels are given in Table 2.4. However, RAF/M steels are restricted to operating temperatures less than around 600 °C. Indigenous efforts at developing RAFM steel with W (1–2 %) along with Ta (0.02 to 0.18 wt. %) are in progress [35–37]. W enhances creep strength, but decreases toughness [28]. Tantalum lowers DBTT by grain size reduction [38], but the higher Ta reduces the weldability [39].

Table 2.4 Typical compositions of RAF/M steels [11, 15, 22, 26–35].

Alloy/Composition (wt. %)	C	Si	Mn	Cr	W	V	Ta	N	B	Other
F82H	0.10	0.2	0.50	8.0	2.0	0.2	0.04	<0.01	0.003	–
JLF–1	0.10	0.08	0.45	9.0	2.0	0.2	0.07	0.05	–	–
ORNL 9Cr–2WTaV	0.10	0.3	0.40	9.0	2.0	0.25	0.07	–	–	–
CLAM	0.11	–	0.40	9.0	1.6	0.21	0.15	–	–	–
OPTIFER Ia	0.10	0.06	0.50	9.3	1.0	0.25	0.07	0.015	0.006	–
OPTIFER II	0.13	0.04	0.50	9.4	–	0.25	–	0.015	0.006	1.1Ge
EUROFER97	0.11	0.05	0.50	8.5	1.0	0.25	0.08	0.03	0.005	–

2.2.2 Austenitic steels

Austenitic steels are broadly used in nuclear and conventional power plants because of their excellent mechanical properties, good corrosion and oxidation resistance, ease of fabrication and weldability [40, 41]. However, these steels have poor swelling resistance at reasonable neutron doses, which is a main performance restrictive concern [42, 43]. Addition of solute elements (Ti, Si, P, Nb, B and C), adjusting of chemical composition and applying cold work plays a major role in determining void swelling resistance [44, 45]. Till 1970's, austenitic steels (316, 316L (N) and 304) were considered as the primary materials for the fuel cladding and for the fast reactor structures of first generation reactors [2]. Austenitic steels containing B and P include PNC 316 (Japan), 15–15Ti (France), DIN 1.4970 (Gemany) and D9 (USA) [46]. For cladding, 316Ti steel has been replaced by austenitic 15/15Ti, exhibiting better swelling resistance. Influence of radiation provokes the depletion of Cr from grain boundaries, making these materials sensitive to corrosion phenomenon. To improve the void swelling resistance, D9 alloy has been designed with specifically tailored composition having carbon and titanium content with reference to the standard AISI 316. For PFBR fuel clad and fuel subassembly wrapper tubes, cold worked (20 %) D9 alloy has been selected. In cold worked D9 alloy, $M_{23}C_6$ precipitates at grain boundaries and TiC forms preferentially on the intragranular dislocations. TiC is more stable compared to $M_{23}C_6$ over longer durations and retains its finer size, thus, enhancing creep resistance beyond those of SS 316, which is strengthened by $M_{23}C_6$. Retardation of recovery and recrystallization of the cold worked structure due to the presence of fine TiC particles is the reason for elevated temperature strength of D9 [47].

To reduce the swelling behavior, 12–15Cr/20–25Ni austenitic steel was proposed as cladding material in French and Japanese reactors [46]. Compared to 15–15Ti and PNC 316 steels, these alloys exhibit better swelling resistance [48, 49]. The useful range of

these advanced austenitic steels is at around 160 dpa [50–52]. The compositions of these steels are presented in Table 2.5.

Table 2.5 Nominal chemical compositions of the austenitic stainless steels [40–52].

Alloy/Composition (wt. %)	C	Si	Mn	Cr	Ni	Mo	Ti	Nb	P	B
PNC 316	0.05	0.8	1.7	16	14	2.5	0.1	0.1	0.025	0.004
15–15Ti	0.1	0.6	1.5	15	15	1.2	0.4	–	0.03	0.005
DIN 1.4970	0.1	0.4	1.5	15	15	1.2	0.5	–	–	0.005
D9	0.05	0.9	1.7	14	15	1.5	0.23	–	–	0.005
PNC1520	0.05	0.8	1.7	15	20	2.5	0.25	0.1	0.025	0.004

2.2.3 Oxide dispersion strengthened steels

With the sole intention of increasing the temperature capability beyond that of RAFM steel, efforts were made to exploit dispersion hardening by introducing stable oxide particles into RAFM steels with minor compositional modifications. The ODS steels are evolving as potential high temperature structural materials for gas, ultra–super critical steam turbines and nuclear reactors [53–60] by virtue of their excellent high temperature strength [59–64], creep resistance [62–66] and resistance to corrosion [62, 67–69], oxidation [62, 70–72] and neutron irradiation induced void swelling [59, 62, 73]. The outstanding characteristics of ODS steels are due to the existence of the high number density of nano–sized complex oxide (Y–Ti–O) particles along with fine grained structure [74, 75]. Uniformly distributed fine stable oxide particles are multifunctional, such as, retard dislocation motion and grain boundary sliding at high temperatures leading to enhanced high temperature tensile strength and creep resistance and also act as trapping sites for both point defects and helium atoms generated during irradiation to maintain the superior resistance to irradiation damage [73].

2.3 Composition design of ODS steels

The iron–based ODS alloys intended for high temperature applications can be broadly divided into three categories [62, 66, 75, 76]. ODS steels contain different amounts of chromium concentration (9–22 wt. %), the majority of them contains Ti and W as well as other alloying elements (Mo, Ni, Mn, V, C, Ta and Al). These steels have different microstructures due to different Cr contents.

1. ODS Ferritic–Martensitic steels (9–11 % Cr)
2. ODS Ferritic steels (12–22 % Cr)
3. ODS Austenitic steels (18Cr–8Ni)

The composition of ODS steels is optimized on considerations of phase transformation kinetics, microstructure stability at operating temperature, enhanced high temperature tensile and creep strength and corrosion and oxidation resistance [77, 78]. ODS steels that contain Cr content in the range of 9–11 wt. % (Fig. 2.1) have martensitic structure. A martensitic transformation result in the formation of highly dislocated lath martensite during the quenching from austenitic to room temperature and the material is hard [79]. Ductility is imparted to martensite by tempering heat treatment. ODS steels, contain 12 wt. % Cr and above, presents a fully ferritic phase (Fig. 2.1). Both of these are commercially available in a few developed countries and the most of the investigations on ODS steels are being carried out in the USA, EU and Japan. ODS austenitic steels are based on 18Cr–8Ni and work has just started.

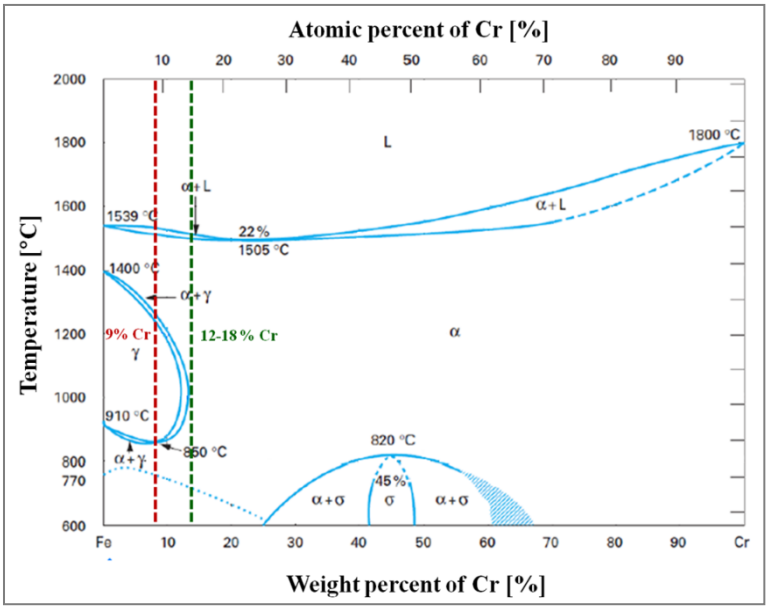

Fig. 2.1 Fe–Cr Phase diagram [80].

In the EU, there are efforts being made to develop the ODS Eurofer for fusion applications by optimizing the process conditions to improve DBTT and understanding the role of Ti in the formation of ~3 nm sized (Y–Ti–O) complex oxides [81]. Extensive studies were also carried out on a variety of experimental and MA957 ODS steels [82, 83]. Recent research in the USA has aimed mainly on the long term stability of Y–Ti–O

oxides in MA957, the consequences of low dose neutron irradiation on mechanical properties and characterization of MA957 after neutron irradiation [84]. Research in Japan has been primarily focused upon ODS–9Cr F/M and ODS–12Cr steels for the clad tubes and ducts of Gen–IV fast reactors [85]. To achieve the isotropic microstructure and properties, special efforts were made, which are necessary for fabrication of the desired shape. Two types of approaches are being employed; production of martensitic steels, that from equiaxed structures during the austenite–martensite (α–γ) phase transformation aiming at radiation resistant alloys and recrystallization processing for ferritic steels to develop equi–axed microstructures aiming at corrosion resistant alloys [86]. The current understanding of ODS steels is discussed below.

Alloying elements are added to provide a solid solution strengthening, suppress undesirable phases and for the purpose of stabilizing the phases. Cr is a ferritic stabilizer, responsible for corrosion and oxidation resistance. Cr oxidizes and a thin and tightly adherent oxide layer (Cr_2O_3) forms on the surface, thus increasing the corrosion resistance of the material. To obtain an effective passive layer, the minimum concentration of Cr is ~11 wt. % [87]. An increase of the Cr content results in further increase of corrosion resistance and hardnability. However, high Cr concentrations (14–22 wt. %) promote the σ–phase and Cr–rich phase (α'), which are cause for lower creep resistance, brittleness and corrosion [88]. In order to get the best corrosion resistance with favorable mechanical properties, concentration of Cr is the important parameter. For ODS–F/M steels, Cr level is so selected that the steel is transformable to martensite but not at very low levels, where corrosion and oxidation is sacrificed. The optimal Cr content lies in the range of 9–11 % in terms of fracture toughness, ductility and corrosion resistance based on irradiation data. Tungsten is used as a substitute to Mo, which is an undesirable element from the point of view of irradiation damage. W is partly dissolved in the matrix and partly in carbides, but its primary role is as a ferrite strengthener. In ODS steels, W of 1–3 wt. % is added in order to enhance the strength at high temperatures through solid solution strengthening [62, 73]. The other elements like Ni, Mn, Co (austenitic stabilizers) and V, Nb, Ta (carbide/nitride formers) are balanced to ensure adequate hardnability. Carbon content should be high enough to make the steel transformable in ODS F–M steels but low enough, to avoid formation of excessive $M_{23}C_6$ carbides, which reduces the Cr level in the matrix. The optimum level lies in between

0.03–0.12 wt. %. The content of C should be kept as low as possible. Titanium is an essential addition in Y_2O_3 dispersed ODS steels because of its ability to generate Y–Ti–O complex oxides [60], which leads to improved high temperature strength. If Ti is added in excess levels, it creates too much strength, which negatively impacts cold workability [62]. To achieve a balance between strength and workability, an optimum level of 0.2–1 wt. % was selected in ODS steels [62, 73]. During MA, 0.2–0.5 wt. %Y_2O_3 [82, 89–93] is added to steel powder, which in combination with Ti yields an optimum volume fraction of nano–sized complex oxides. Excess oxygen (inherited from raw materials and attained during MA) has to be carefully controlled since it is found that too much or too little affects the dispersoid and the mechanical properties. The optimum level is established to be about 0.08 % [94]. This quantity of O is predictable for the formation of Y–Ti–O oxides. Addition of small amounts of hafnium or zirconium increases the creep strength. The most commonly used alloying elements in ODS steels and their effects are summarized in Table 2.6.

Table 2.6 Effect of alloying additions.

Element	Purpose
Cr	Ferrite stabilizer, corrosion and oxidation resistance
Ti	Grain refinement, participation in solution strengthening and nanoclusters formation
W, Mo	Ferrite stabilizer and solid solution strengthening
Ni, Mn, Co	Austenite stabilizers and increase toughness
C, N	Austenite stabilizers
Si	Corrosion and oxidation resistance
P	Involved in increasing hardnability and strength

2.4 Production of ODS steels

ODS steels are invariably produced by powder metallurgy (P/M) route. Conventional metallurgical processing routes are not suitable for processing alloys containing oxide particles due to the different melting points, buoyancy and agglomeration issues in the melt [95]. MA has become an effective route for ODS alloy production.

The MA powders are canned, evacuated and sealed for obtaining useful product shapes. Consolidation is carried out either by hot extrusion (HE) [96, 97] or hot isostatic pressing (HIP) followed by conventional hot working [77, 81]. Consolidation by spark plasma sintering was also attempted [98, 99]. To produce ODS ferritic steels, at first, Fisher [100] patented MA and HE processing route, which were promoted in the 1980s as International Nickel Company (INCO) MA956 and MA957. The hot working temperature is a critical parameter. It should neither be too high to avoid microstructural coarsening nor to be too low, where high extrusion pressures are required and consolidation is incomplete. To improve the microstructure and mechanical properties, suitable heat treatment processing has to be performed. Schematic representation of the manufacturing route for ODS steels is presented in Fig. 2.2.

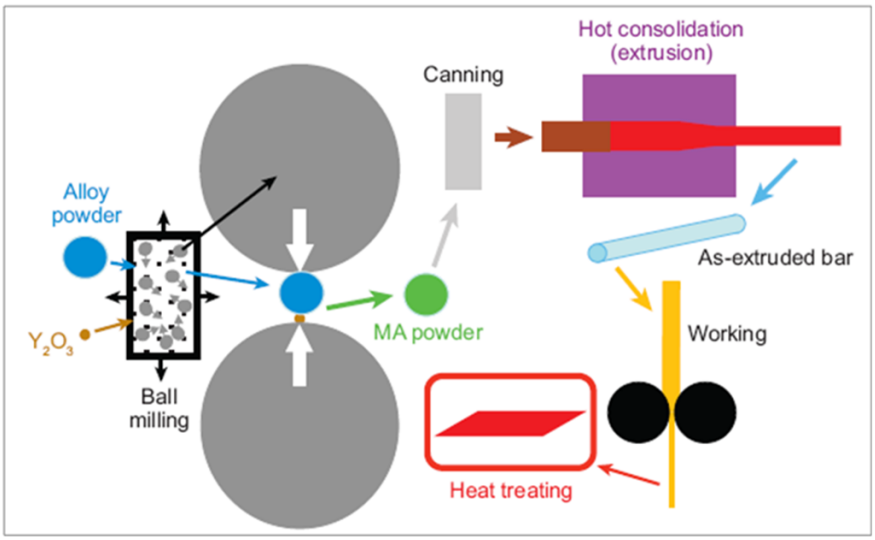

Fig. 2.2 Schematic representation for the processing of ODS steels [73].

2.5 ODS ferritic–martensitic steels

2.5.1 Microstructural evolution

The microstructure of ODS–F/M steel is tailored to transform austenite to martensite and ferrite [101]. Fig. 2.3 shows the microstructure of ODS–9Cr steel, consisting of ferrite and tempered martensite with chromium carbides [101]. The elongated ferrite phase appears smooth and white, which is indicated by arrows. Their ferrite grain size is about 30–60 μm in length and 3–10 μm in width. Both the phases were found to contain oxide particles of 2–10 nm.

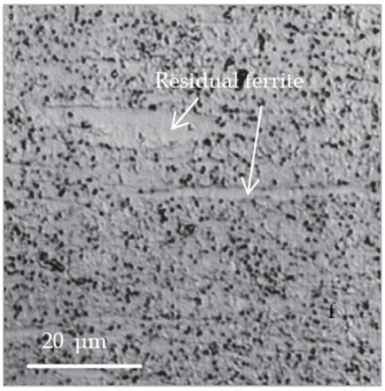

Fig. 2.3 Microstructure of ODS–9Cr steel representing the ferrite embedded by the tempered martensite [101], Arrows indicate the elongated ferrite phase.

The appropriate balance of elements like Ti and excess O is important. High Ti and O are not favorable because it increases the formation of coarser TiO_2, in preference to the fine Y–Ti–O complex oxide particles. Ohtsuka *et al.* [78, 102] examined the effect of various amounts of excess O on the nature of oxide particles in ODS–9Cr steel. When the atomic ratio of excess O and Ti is near to 1, microstructure of the hot consolidated sample consists of elongated ferrite grains with finer and denser distribution of oxides. Because of the effective pinning of the grain boundaries by the oxide particles, recrystallization is impaired even though the finishing temperature is above the recrystallization of the base steel. It is well established that ultra–fine ferrite grains established during MA are predominantly retained during heat treatment. Usually, ODS–9Cr steels show a bimodal grain distribution, some in the range of a few tens of nanometers and some others in the range of 150–250 nm [77]. The effect of heat treatment on the microstructural features of ODS–Eurofer steels in comparison to the Eurofer 97 and T92 steels was studied by Lu *et al* [103]. ODS–Eurofer steels exhibit tempered martensite structure with $M_{23}C_6$ carbides and Y_2O_3 particles. With the increase in normalizing temperature, grain size increases in conventional steels and remains same in ODS–Eurofer steels. Zilnyk *et al.* [104] discussed the microstructural stability of ODS–Eurofer steel at 800 °C for very long times (1 to 4320 h). ODS–Eurofer steel exhibits good thermal stability because of the presence of stable complex oxide particles, which are effective to retard primary recrystallization and further grain growth (Zener–Smith pinning) at this temperature. The microstructural changes of Eurofer and ODS–Eurofer steels were examined by varying the austenitizing temperatures (900–1300 °C) were investigated. In ODS–Eurofer steel, austenitic grain growth was prevented due to the fine and stable distribution of Y–based oxides [105].

Characterization of oxide particles

Even though, it is familiar that the superior properties of ODS steels results from nano–sized complex oxide particles, the knowledge regarding the characteristics (composition, size and structure) of these oxide particles is ambiguous and is still evolving [106].

Detailed study of the complex oxide particles requires advanced characterization techniques, involving Transmission Electron Microscopy (TEM), Atom Probe Tomography (APT), Small Angle Neutron Scattering (SANS) and Small Angle X–ray Scattering (SAXS) [107].

Klimiankou *et al.* [108] analyzed the structure of Y_2O_3 in ODS–Eurofer steel without Ti. High resolution TEM (HR–TEM) analysis of Y_2O_3 (12 nm) particles reveals the correlation of its crystallographic orientations with the matrix. Initially, Ukai *et al.* [55] studied the significance of Ti in the size refinement of Y_2O_3 particles in Fe–Cr matrix, attributing the complex oxide formation to Y_2O_3–TiO_2 and Y_2O_3–$2TiO_2$ reactions. The yttrium, oxygen and titanium participate to form Y–Ti–O complexes. It appears that complex–oxide particle formation follows the standard precipitation reaction involving nucleation (involving cluster formation) and growth, unlike the usual dispersion strengthening, the type of oxide that forms depend on the ratio of Y to Ti. For example, when the ratio is about 1.1–1.3, $Y_2Ti_2O_7$ forms and when it is about 2.5, Y_2TiO_5 particles are precipitated [102].

Ramar *et al.* [109] examined ODS–Eurofer 97 with and without Ti and observed the structure of oxide particles by HR–TEM. The addition of 0.3 % Ti results in fine size and high density of complex oxide particles than when yttria alone is added. These semi–coherent dispersoids are of Y–Ti–O complex oxides (7 nm) and Y_2O_3 (20 nm) with and without Ti, respectively. Studies have been performed extensively by TEM on ODS–F/M steels regarding the characterization of the nano–sized features of Y–Ti–O complex oxides [110–113] and Y_2O_3 particles [108, 109] with and without Ti, respectively. The fine complex–oxides in ODS–F/M steels are observed to be spherical in shape [102, 108, 109, 111]. Ukai *et al.* [101] analyzed the oxide particle distribution in tempered martensite and residual ferrite as seen in the TEM images in Fig. 2.4.

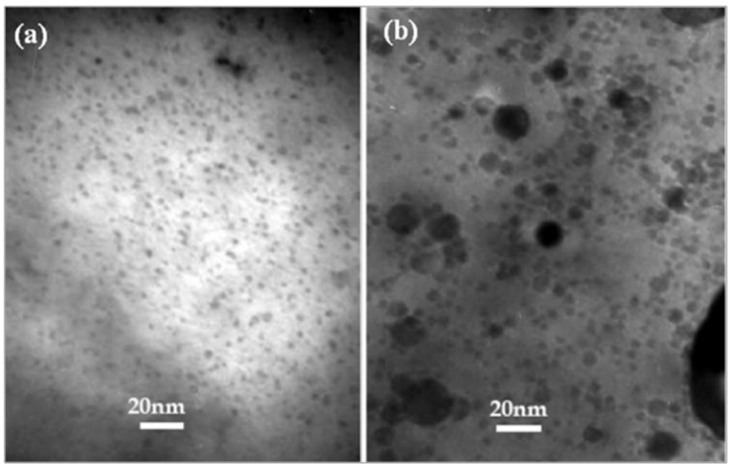

Fig. 2.4 TEM micrographs of oxide particles in (a) residual ferritic matrix and (b) tempered martensitic matrix [101].

It was observed that the dispersoids in tempered martensite are coarser (7 nm) than those in ferritic matrix (3 nm). This behavior was attributed to α–γ reverse transformation. According to Yazawa *et al.* [114], oxide precipitates sometimes coarsen during coherent to incoherent transition, which is expected in the tempered martensite as well also. Ukai *et al.* [101] explained this phenomenon through a schematic as shown in Fig 2.5. During hot consolidation, semicoherent oxide particles are formed by precipitation. Consequently, α–γ ransformation may possibly disturb the interfacial coherency; to minimize this, oxide particles get coarsened. Therefore, tempered martensite changed from γ–phase by cooling consists of coarser oxide particles, whereas the residual ferrite includes finer oxide particles for coherency.

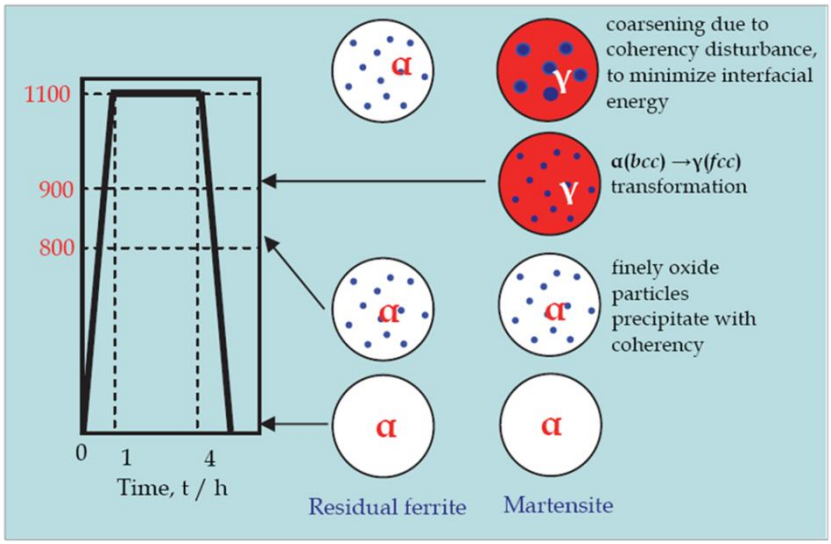

Fig. 2.5 Schematic representation of process for oxide particle coarsening in the martensite in comparison to the residual ferrite [101].

In ODS steels, analysis of nano–sized oxide particles with the size of less than 5 nm has been equally ambiguous. Generally APT analysis is focused on small oxide particles of less than very few nanometers in size. The interesting feature of oxide particles observed by APT, suggests that many of the oxide particles have a core–shell type structure [115, 116]. Marquis [115] analyzed the oxide particles of ODS–Eurofer alloy, which has the core shell structure and in which, Y_2O_3–rich core was surrounded by V and Cr–rich shell. V– and Cr–enriched shells are also observed around all investigated particles by TEM in ODS–Eurofer steels [116]. The decoration of the Y_2O_3 core with a Cr and V rich shell implies that the nano–sized oxides not only act as trapping sites for irradiation induced defects and noble gases, but also effective traps for the segregation of major alloying elements and long range diffusion. The partitioning of alloying elements hinders the particle decomposition and consequent formation of σ or χ phases [117].

Williams *et al.* [118] carried out the APT study of the ODS–Eurofer without Ti. Considerable variations in chemical composition of oxide particles (5–10 nm) were observed. Inside the oxide particle, with increasing size, the concentration of Fe decreases and at the core of coarser particles (10 nm), no Fe was found.

Aleev *et al.* [119] observed the high number density ($\sim 2\times10^{24}/m^3$) of fine nanoclusters (enriched in Y, O, N and V) in ODS–Eurofer steels using APT and compared with TEM results. Lu *et al.* [113] investigated the high density of few stoichiometric $Y_2Ti_2O_7$ particles (7 nm) by TEM studies and non–stoichiometric Y–Ti–O type nano oxide clusters (2–4 nm) using APT analysis in ODS CLAM steel.

Ohnuma *et al.* [120] quantitatively determined the size and number density of dispersoids in ODS–9Cr steels with varying amounts of Ti and excess O using SANS and SAXS. It was found that decreasing excess O and increasing Ti results in finer grain size (2.4 nm) and higher number density (1.1×10^{18}) of $Y_2Ti_2O_7$ oxide particles. Mathon *et al.* [121] found that ODS–9Cr with 0.5Ti yields the lower oxide particle size compared with the same steel with 0.3Ti using SANS studies. But as the annealing time increases oxide particle size also increases, at higher Ti contents. This is in fine agreement with the known effect of the optimum quantity of Ti addition in the reduction of the size of the oxides [60].

Ukai and Ohtsuka *et al.* [60, 78, 102] studied the influence of alloy composition on the structure, composition, number density and size distribution of nano–sized complex oxides (nanoclusters). Generally, variations in alloy compositions and processing conditions resulted in differences in the population of nanoclusters, suggestive of that they can be tailored to give best possible balance of mechanical properties and irradiation tolerance.

2.5.2 Mechanical Properties

ODS steels exhibit excellent tensile and creep strengths when compared to the same steels without oxide strengthening. The high strength of ODS steels is obtained due to the combined influence of dispersoids and their synergistic interaction with grain boundary and dislocations.

The effects of chemical compositions (Ti and O) and hot consolidation temperature on mechanical properties of ODS–9Cr steel were investigated [64]. The influence of excess O on creep and tensile properties was controlled by increasing titanium from 0.2 to 0.46 wt. % (Fig. 2.6). The creep strength of ODS–9Cr steel was enhanced by balancing the titanium content to 0.35 wt. %.

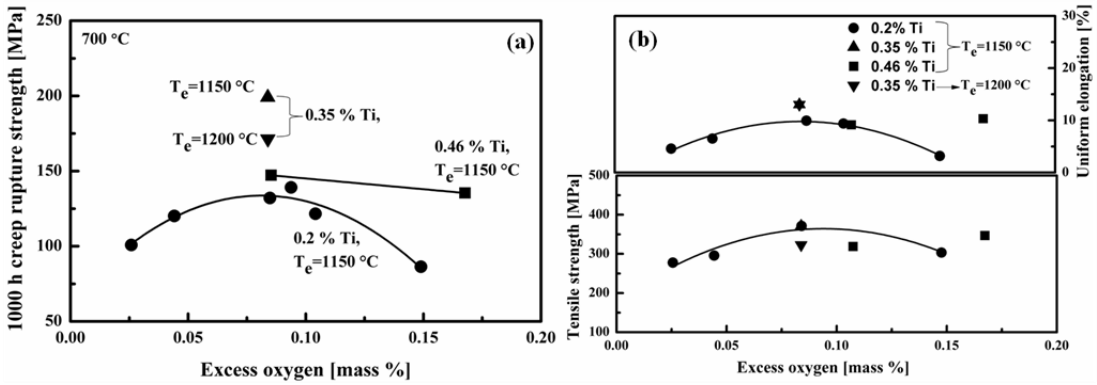

Fig. 2.6. Effect of Ti, excess O and HE temperature (Te) on (a) creep and (b) tensile properties [64].

In ODS–9Cr steels, excessive W leads to Laves phase formation. In these steels, solid solution strengthening increases with increasing the W concentration up to 2.4 mass %. by the dissolved W. To obtain the high temperature strength without Laves phase formation, the appropriate W content is around 2 mass %. The improvement in strength by the addition of W is not only due to solid solution strengthening but also due to the formation of residual α–ferrite when W content is more than 0.5 mass % [122].

Lu *et al.* [103] investigated the influence of heat treatment conditions on the hardness of ODS–Eurofer steels in compassion to the Eurofer 97 and T92 steels. With the increase of normalizing temperature, hardness increased in conventional steels and decreased in ODS–Eurofer steels. The reduction in hardness of ODS–Eurofer steels due to the enrichment of Ta in Y_2O_3 particles as evidenced by the absence of TaC. With the increase in tempering temperature, the hardness of T92 decreases, while the hardness of ODS–Eurofer decreases up to 750 °C, thereafter it increases.

The tensile strength of ODS–9Cr (Fig. 2.7) steel was almost twice that of the RAFMs up to 550 °C. The creep strength of ODS–9Cr steel was higher than RAFM steels. The dispersoid size and number density were found to remain similar even after creep testing [123].

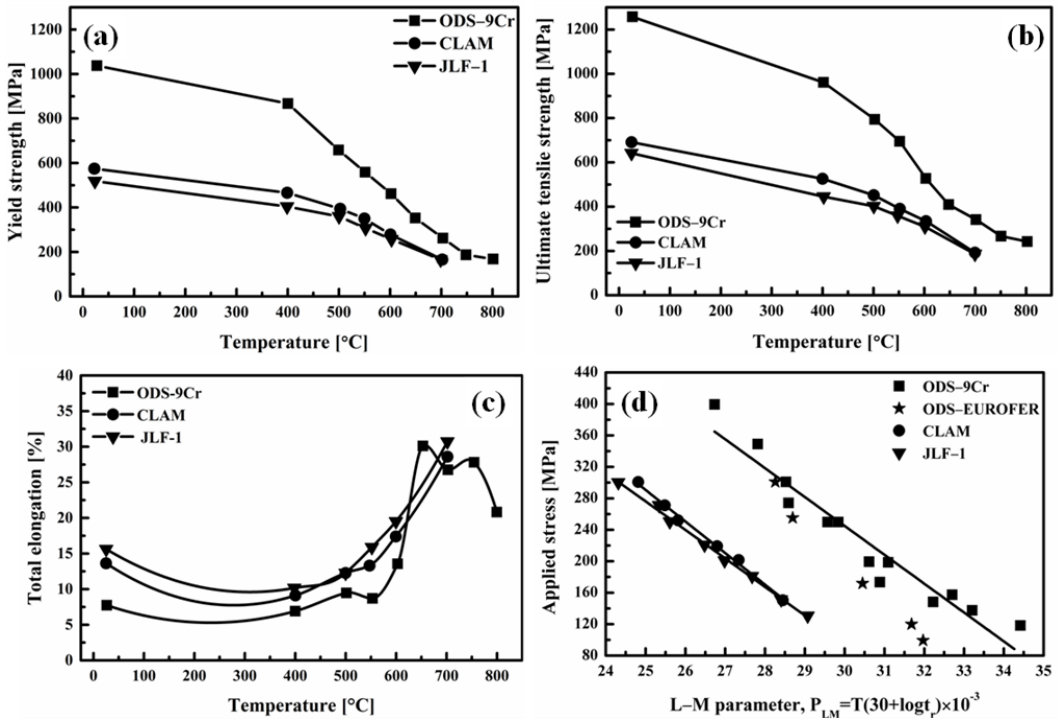

Fig. 2.7 Variation of (a) yield strength (b) tensile strength, (c) total elongation with temperature and (d) dependence of stress on Larson–Miller parameter of ODS–9Cr steel in comparison to conventional steels [123].

The tensile properties of ODS–Eurofer and commercial ODS steels are shown in Fig. 2.8 [81]. Both the yield and tensile strengths of consolidated samples are higher (about 35 %) compared to Eurofer 97 up to 700 °C (Fig. 2.8). Above 350 °C, ductility of hipped

samples was not satisfactory, where as extruded sample showed total elongation comparable to Eurofer.

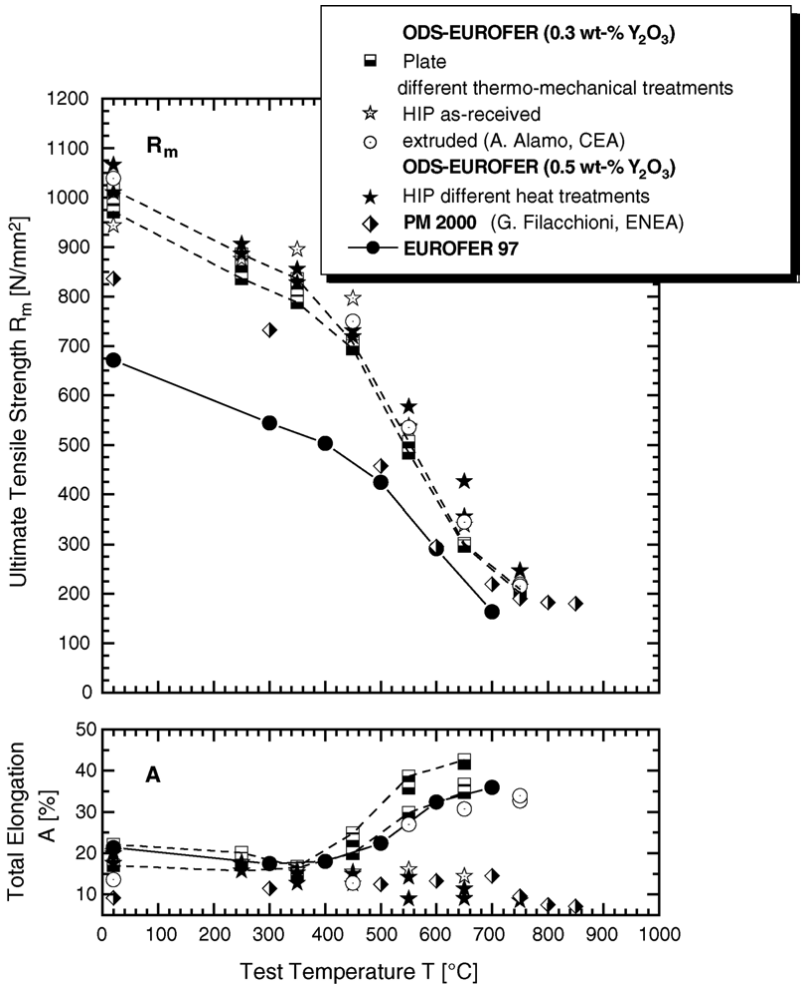

Fig. 2.8 Ultimate tensile strength of various ODS steels in comparison to the standard Eurofer with test temperature [81].

The tensile properties of ODS–9Cr in different processing conditions were estimated at 25 to 800 °C and are presented in Fig. 2.9 [60]. The properties of standard oxide free ferritic stainless steel (PNC–FMS) are also included in Fig. 2.9. ODS–9Cr steel exhibited excellent ultimate tensile strength (UTS) and uniform elongation (UE) over the entire temperature range. The ratios of UTS and UE of ODS to those of PNC–FMS are presented in Fig. 2.9 (c). The improvement in strength and ductility in the ODS–9Cr steel is significant, especially above temperatures of about 600 °C. This benefit can be attributed to dislocation pinning by oxide particles and consequent difficulty in recovery.

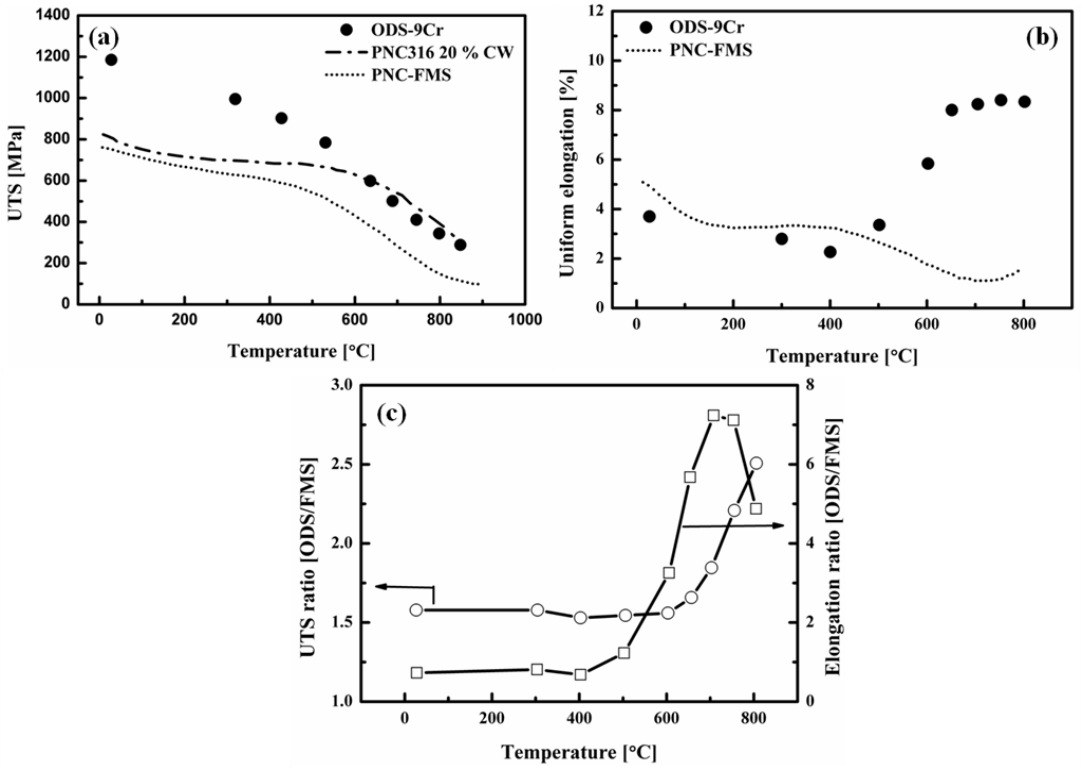

Fig. 2.9 Mechanical properties of ODS–9Cr steel [60].

Sakasegawa *et al.* [124] studied the effects of mechanically alloyed powder particle size on the microstructural parameters and creep resistance of ODS–9Cr steels. The creep cavities are reduced and creep rupture time is increased when coarser MA powder (>90 µm) was used.

The formation of residual ferrite is the superior characteristic of creep property of ODS–9Cr steels [125]. Yield strength (YS) of residual ferrite at room temperature (RT) was 1360 MPa. Minimization of the number of martensite packet boundaries is the main reason for the increase in creep strength.

Tensile tests were performed on ODS–9Cr steels with varying contents of Y_2O_3 (0.35 and 0.5 wt. %) [126]. It was observed that, the ODS steel which contains 0.3 % yttria showed better tensile properties rather than 0.5 %. Fracture surfaces shown in Fig. 2.10 exhibits the visible reduction of area with 0.3 % of yttria at 700 °C (Fig. 2.10 (a)) and at RT (Fig. 2.10 (b)). But no visible necking was observed in 0.5 % yttria, at both the test temperatures (Fig. 2.10 (c) & (d)). In both materials, there is an indication for localized ductility at higher magnifications at both temperatures. The general fracture mode, however, seems to be intergranular in nature.

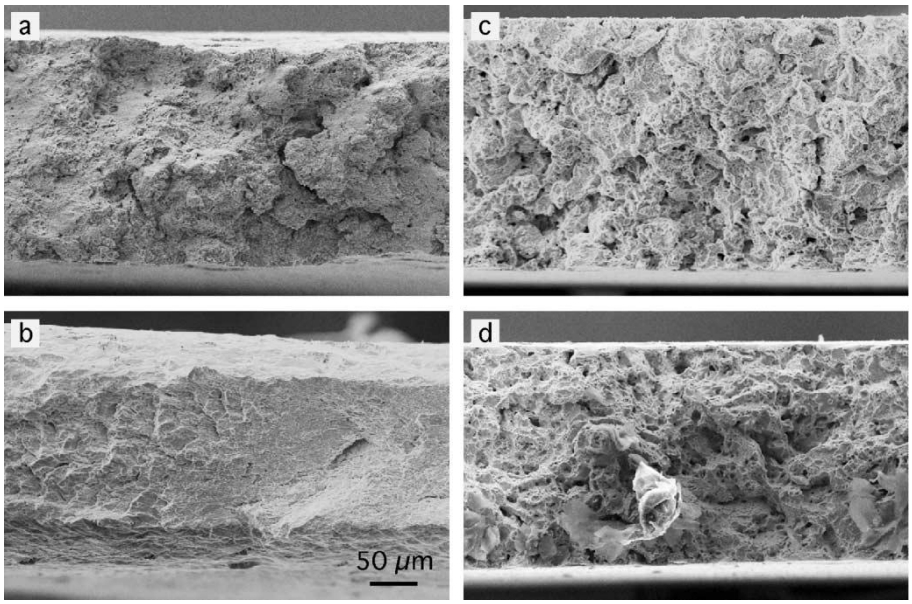

Fig. 2.10 SEM images of the fracture surface of ODS–9Cr steel with 0.3 and 0.5 wt. % yttria at (a, c) 700 °C and (b, d) RT, respectively [126].

2.5.3 Corrosion and oxidation properties

Corrosion resistance is a life limiting factor in selecting materials for SFR or fusion reactors. Since ODS steels are intended for operation at temperatures greater than 650 °C, the corrosion and oxidation behavior of these steels are to be completely understood before being used. At elevated temperatures, corrosion and oxidation resistance is highly dependent on the type of alloy. Even though, the corrosion behavior of ODS steels at high temperatures is well studied in super critical pressurized water (SCPW) [68], lead–bismuth eutectic (LBE) [127, 128], liquid lead [129] and sodium [130, 131], the general corrosion behavior of these steels at RT is not fully evaluated. The corrosion behavior of ODS–9Cr F/M steels were also observed in different chloride and acidic electrolytic solutions [132].

Cho *et al.* [68] investigated the effect of alloying elements on corrosion behaviour of ODS–9Cr steel in SCPW. The experiments of anodic polarization indicated that the passivation current in ODS steels was lower in comparison to the conventional F/M steels. ODS–9Cr F/M steels exhibited similar corrosion behavior in comparison to the F/M steels in the SCPW.

The efficacy of adding of Al for enhancement of the corrosion resistance of ODS–9Cr steel in LBE was studied [127]. Al surface coated ODS–9Cr steels exhibited superior corrosion resistance at all the experimental conditions.

The corrosion behavior of ODS–9Cr steels at 550 and 650 ºC in the static liquid Pb was investigated [129]. The observed corrosion behavior of ODS steels comparable with that of the conventional steels. However, the specific structure of ODS steels causes some variations in the corrosion process. In pure Pb, the fine–grained structure promotes intergranular corrosion (IGC) and diffusion of Pb into matrix along the grain boundaries.

An evaluation was done in different electrolytic media to find out the corrosion behavior and passive film compositions of ODS–9Cr steels [132]. The results of open circuit potential (OCP) show noble potential for measurements in 1 to 11.5 M HNO_3, and in chloride media less noble potential values were observed. The protective oxide layer has higher OCP, while the less protective passive film forms at lower OCP values. There is an influence of electrolytic media on the corrosion resistance which clearly showed in potentiodynamic polarization plots. In 0.5 M H_2SO_4 and 1 to 11.5 M HNO_3 media, higher breakdown potentials were observed. The presence of Cl^- significantly reduced the corrosion resistance despite the presence of Fe_2O_3, Cr_2O_3, and Y_2O_3 layers on the passive film. In the acidified chloride and chloride only media, pitting corrosion was prominently observed. The morphology of pits appeared in SEM were hemispherical and globular.

The corrosion behavior of Eurofer and ODS–Eurofer steels was tested at RT in NaCl and H_2SO_4. The results were compared with conventional ferritic stainless steel grades AISI 430 ferritic and AISI 410 martensitic grade [133]. The corrosion resistance of Eurofer was better than ODS–Eurofer 97 but lower than AISI 430 and AISI 410 stainless steels. The addition of Y_2O_3 did not improve the corrosion resistance of ODS–Eurofer.

The oxidation behavior of ODS F/M steels is well studied in SCPW [71, 134, 135], LBE [72] and liquid lead [136] but literature exists on the oxidation behavior at high temperatures of ODS steels in air is limited. Kaito *et al*. [137] reported that ODS–9Cr F/M and ODS–12Cr ferritic steels exhibited higher oxidation resistance when compared to the conventional steels, which is due to the presence of finer grains in ODS steels. The

detailed mechanism, however, is not yet clear, even though ODS steels exhibit better oxidation resistance than conventional steels.

2.6 ODS ferritic steels

2.6.1 Microstructural evolution

Usually, the microstructure of ODS ferritic steels is ferrite. In ODS ferritic steels, extrusion results in anisotropic and textured grains. A recrystallization process is generally used to decrease the degree of anisotropy in an extrusion direction [55]. All worldwide efforts are directed to overcome the anisotropy induced by fibrous grain structure observed after hot extrusion [138]. In MA957, grains with the dimensions of ≈ 0.5 μm in transverse direction, whereas in the extrusion direction that are elongated with a <110> texture and the aspect ratio of 10:1 [67, 139–141]. In ODS ferritic steels, dislocation densities in as–extruded condition are reasonable to high, usually forming polygonized subgrain structures [67, 83, 142, 143]. Compared with MA957, J12YWT has smaller grains with higher dislocation densities [142, 144].

Characterization of oxide particles

Sakasegawa *et al.* [145] observed different type of particles, such as, TiO_2 (>35 nm), $Y_2Ti_2O_7$ (15–35 nm) and non–stoichiometric Y–Ti–O complex oxides (2–15 nm) in MA957 (Fig. 2.11 (a)) and also shown that the chemical composition of oxide particles depends on their size (Fig. 2.11 (b & c)).

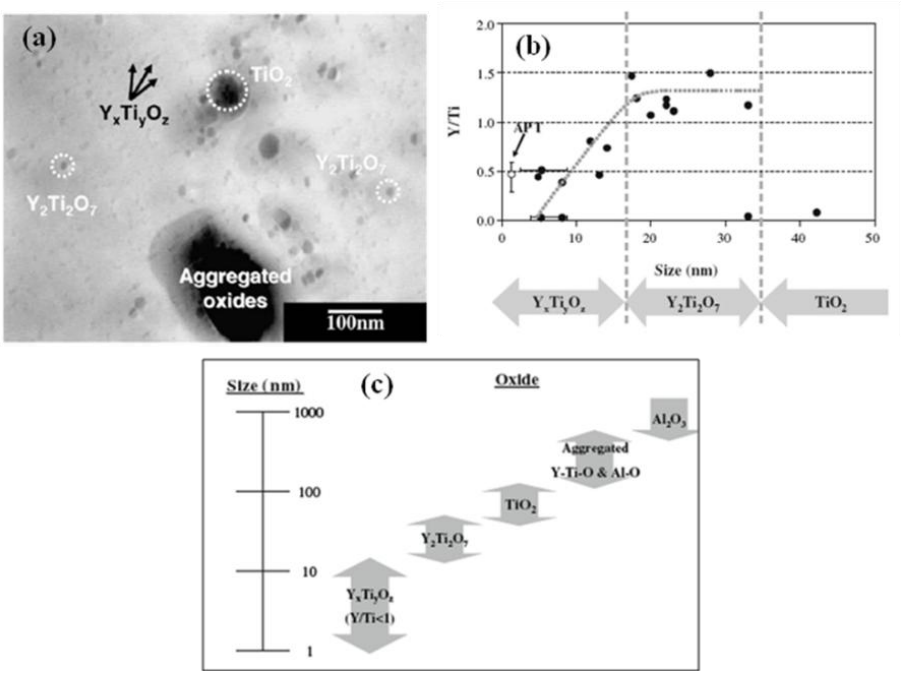

Fig. 2.11 (a) TEM image of MA957, (b) relationship between chemical composition and size of oxides and (c) size distribution of oxide particles [145].

A recent study [106] by Hirata *et al.* provided the imperative evidence that a defective NaCl type structure is possessed by the higher lattice coherency nanoclusters with the ferrite matrix in 14YWT. The remarkable high temperature stability of these nanoclusters in exhaustive neutron irradiation fields was found to be due to the abundance of point defects. Wu *et al*. [146], studied the near stoichiometric $Y_2Ti_2O_7$ nanoparticles and Ribis *et al.* [147] also observed $Y_2Ti_2O_7$ structure particles after annealing at 1300 °C for 1 h. Brandes *et al.* [148] confirmed the presence of amorphous nanoparticles. Bhattacharyya *et al.* [149] analyzed a new phase in ODS–14Cr steel. HRTEM–FFT indexing analyzed this phase to be orthorhombic Y_2TiO_5, with Y/Ti ratios calculated by energy dispersive spectroscopy (EDS) between 1 and 2. In adding together, HRTEM–FFT indexing showed that small $Y_2Ti_2O_7$ (<5 nm) oxides form in the ODS–14Cr steel with the similar alloy composition following HIP process at 850 °C.

Miller *et al*. [150] observed the distribution of oxides in ODS–12Cr steels with and without Ti using APT. ODS–12Cr steels with Ti results in finer size and high number density (4 nm and $1.4\times10^{24}/m^3$) of Y–Ti–O enriched particles compared to ODS–12Cr without Ti samples (5 nm and $3.9\times10^{23}/m^3$). In MA 957, oxide particles were appeared as Y–Ti–O clusters and also containing significant amount of Fe and Cr. The measured compositions were differing from complex oxides like $YTiO_3$, Y_2TiO_5 and $Y_2Ti_2O_7$ [151]

as indicated by APT analysis. The range of (Ti+Y)/O ratios of Y–Ti–O clusters were between 1.1 and 1.3. Using APT, Miller *et al*. [89, 152] analyzed the ratio of Y:Ti, considerably lesser than 1 (0.25–0.5), when the Ti:O ratio was about 1:1. This was in conformity with the results of Hirata *et al*. [106]. During APT data acquisition, general analysis of the sub–stoichiometric oxygen concentration measured is that not all the oxygen is identified [146].

The core shell/structure of nanoparticles is observed by different research groups in different ODS materials and by different techniques (APT and HRTEM, *etc.*). The theory behind the formation of oxide particles is that the shell acts as a wetting layer for the nucleation of the particles [118], and it was proposed by Sakasegawa *et al*. [153] that the formation mechanism is strongly dependent on the diffusion of Y. Marquis [115] analyzed the oxide particles of Fe–12Cr model alloy and MA957 with core shell structure. The core is composed of Y and O while the shell is enriched with Cr in Fe–12Cr model alloy and in MA 957 oxide particles consist of Y, Ti, Al and O with core and also a Cr–enrich shell. The presence of a shell is observed of the size (4–8 nm) of these oxides. However, for the larger particles (8 nm and more), the shell structure is visible all around the core. Since the structure of oxide nanoparticles is similar in three of the studied ODS steels (Y–rich core with solute–rich shells), it is suggested that the structures of oxides are governed by the interfacial energy between oxide particle and matrix.

Similarly, ODS–12Cr model alloy also have Cr–rich shell (thickness: 1–3 nm) confirmed by TEM (STEM, EELS, EFTEM) analysis [154, 155]. In addition, this shell structure still exists even after prolonged annealing times (during 24 and 96 h at 750 °C). EFTEM analyses performed on ODS steel annealed for 96 h, do not reveal any significant difference in thickness of Cr–rich shell in comparison to the particles after annealing for 4 h.

SANS measurements, revealed that processing conditions dictate the formation of Y–Ti–O oxides [73, 156, 157]. SANS and APT results suggest that Y–Ti–O complexes are maybe GP zone–type transition phases.

While it is well established that the dispersoids are of spherical shape in ODS–F/M steels, there exists an ambiguity in the shape of dispersoids (spherical or cuboidal) in ODS–

ferritic steels. Recent studies, however, indicate that the dispersoids are of both spherical [106, 158, 159] and cuboidal [147, 148, 160, 161] in ODS–14Cr ferritic steel. Thus, there is uncertainty in the process dependent shape evolution of the dispersoids in ferritic steels.

2.6.2 Mechanical properties

The effect of yttria concentration (up to 0.56 wt. %) on the strength and ductility of ODS–13Cr steels consolidated by HE was studied [55]. Tensile strength and creep rupture strength increased with Y_2O_3 content in the extrusion direction, while total elongation decreases. At about 0.4 wt. % of Y_2O_3, the creep rupture strength got saturated.

A study of the influence of milling type was carried out on the hardness of ODS–14Cr steels [156]. SPEX–milled powders were extremely hard (Fe–14Cr≈750 kg/mm^2 and 14YWT ≈1000 kg/mm^2), with the crystallite size of 30 nm with very high dislocation densities. Compared to lower energy attritor milling, SPEX milling resulted in higher hardness as a result of fine grained structure with high dislocation densities. After annealing at 850 °C for 1 h, hardness of the SPEX–milled 14Cr powders (without Ti or Y) recovered completely to the unmilled level (750 to 150 kg/mm^2).Hardness of 14Cr milled powders (without Ti or Y) after annealing for 1 h at 850 °C was similar. At all annealing temperatures up to 1150 °C, the powders with yttrium and powders with both titanium and yttrium showed much higher hardness.

The experimental steel 12YWT (Fig. 2.12) has a better tensile properties compared to MA956, MA957 and PM2000 and the strength levels of all these steels are the same at temperatures of about 900 °C. Small differences were observed in total elongation of both experimental and commercial steels. At RT, both 12Y1 and 12YWT had the lowest values. Highest values were attainted in 12Y1 in the range of 600–800 °C. Otherwise, the elongations of the commercial steels and 12YWT were comparable [61].

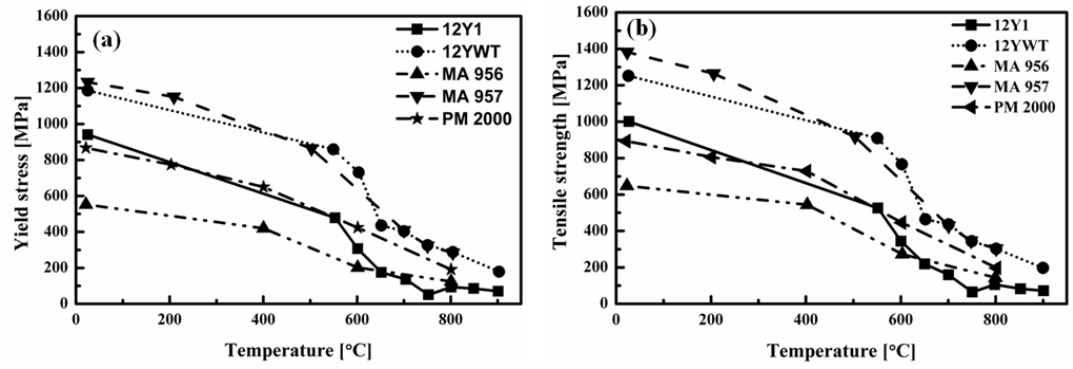

Fig. 2.12 Variation of (a) YS and (b) UTS with temperature of experimental and commercial ODS steels [61].

Alamo *et al.* [66] investigated the mechanical behavior of MA957 alloy for fine grains and intermediate recrystallized conditions. The fine grained structure exhibits high tensile strength and very low DBTT while recrystallized structure presents a higher ductility and better creep behavior.

The relative contributions of various strengthening mechanisms at different temperatures in ODS–14Cr steel were estimated [162]. While the linear summation method results in overestimation, the root mean square method was found to predict the YS closer to experimental values. In this particular study, the dispersed barrier hardening model shows a better estimation than Orowan hardening. Among the proposed mechanisms, the Hall–Petch component has the highest contribution over a wide range of test temperature.

Anisotropy in extruded ODS–14Cr alloy was examined in the longitudinal (LT) and transverse directions (TT) [163]. While there was no significant change in the strength, the ductility in TT direction was about 50 % lower than that in LT direction. There were differences in the macroscopic appearance of the fracture surfaces.

Rahmanifard *et al.* [164] described the tensile and fracture studies of ODS–12Cr steel (Fig. 2.13). HE at 850 °C resulted in nearly equiaxed ultrafine grain structure with YS of 1390 MPa and UTS of 1470 MPa and total elongation (e_t) of 13 % at RT. Maximum e_t was found at 600 °C where a fully ductile dimple feature was revealed in the fractography of the tensile specimen as compared to the very fine dimpled and split crack structure that were observed at RT. The presence of very small particles on the wall of dimples at 800 °C with the nearly chemical composition of the matrix was attributed to the activation of the decohesion of boundaries mechanism as a result of diffusion of solute atoms.

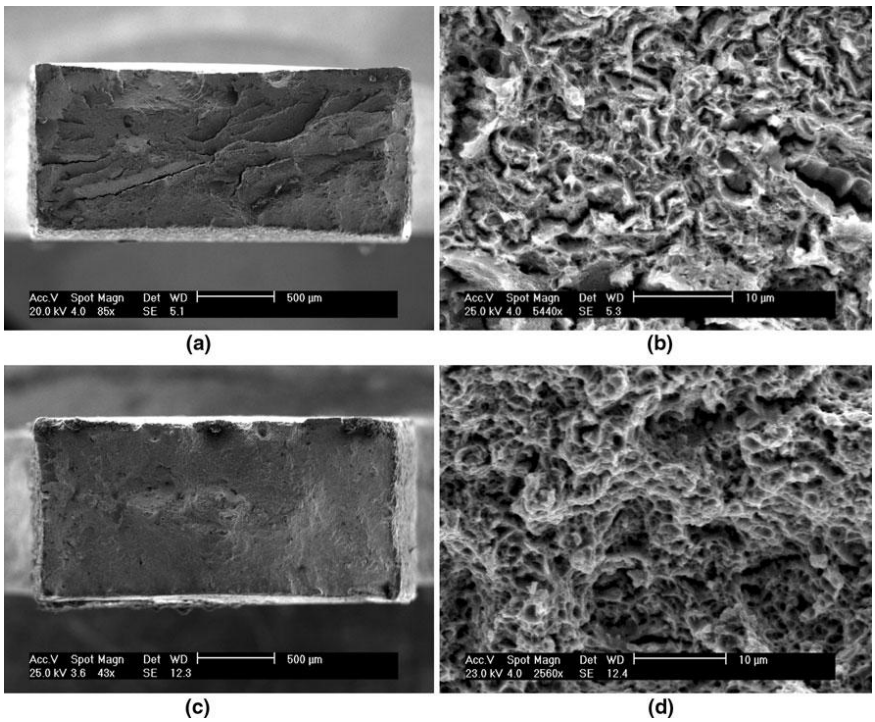

Fig. 2.13 SEM micrographs of tensile fracture surfaces tested at (a–b) RT indicating quasi–brittle fracture mode and at (c–d) (600 °C) indicating ductile fracture mode [164].

2.6.3 Corrosion and oxidation properties

Even though, ODS–9Cr steels have excellent high–temperature strength, low void swelling, high resistance to creep and neutron irradiation embrittlement, the corrosion resistance of these materials is poor due to the reduced Cr content (<13 %). For better corrosion resistance it is imperative to use high Cr steels. The primary aspect of recycling the old fuel is to recover the uranium and plutonium and thus close the fuel cycle. The PUREX (plutonium, uranium extraction) process is the standard method of extraction for the reprocessing of most commercial reprocessing plants. During different stages of spent fuel dissolution of PUREX process, HNO_3 is used at various contents (1–14 M) and in

boiling conditions [165]. However, severe IGC was found to be a serious problem [166]. The corrosion behavior of ODS ferritic steels at high temperatures is well studied in SCPW, LBE, liquid lead and sodium [69, 129–131]. The corrosion behavior of ODS ferritic steels was also observed in different chloride and acidic electrolytic solutions [167–170].

The corrosion behavior and passive film composition of ODS 9–15 % Cr in various concentrations of nitric acid were studied. The OCP is shifted towards more noble potential as the concentrations increased from 1 to 9 M HNO_3 in all the experimental steels. No IGC attack was noticed in the above mentioned HNO_3 contents [167–169]. The passive film compositions and corrosion resistance of ODS–12Cr and ODS–15Cr in 3 to 9 M HNO_3 was evaluated. Potentiodynamic polarization plots exhibited a shift in corrosion potential and high passive current density with increasing HNO_3 contents. In ODS–12Cr steel, the higher corrosion rate was noticed in all HNO_3 conditions. Nevertheless, low corrosion rate noticed in ODS–15Cr steel was recognized to Al_2O_3 enrichment. TEM studies indicated a formation of complex $Y_2Hf_2O_7$ in ODS–15Cr steel and this might have a role in suppressing the IGC [170].

The influence of yttrium and nano complex oxides on the high temperature oxidation behavior of ODS ferritic steels was investigated [171, 172]. The study of conventional stainless steels with the same chemical composition was done for comparison purposes. Long term oxidation experiments were carried out at 800 °C up to 2000 h under air. The results exhibited that an adding of yttrium to ODS–14Cr steel sufficiently reduced the oxidation rate. Therefore, ODS processing to precipitate nanoclusters is a more effective means of improving high temperature oxidation rather than a simple yttrium addition [171].

2.7 High–Cr ferritic steels

2.7.1 Microstructural evolution

Hsiung *et al*. [173–175] carried out the HRTEM analysis to observe the interfacial structure of oxide particles (1.7 to 30 nm) in ODS–16Cr–4Al steel. A structure with a $Y_4Al_2O_9$ core associated with a shell was observed in both small and large oxide particles. The shell was found to be amorphous in contrast to the previously reported core–shells

structures [115, 116]. The authors suggested that the amorphous shell results in a partial crystallization of amorphous nanoparticles during consolidation, whereas amorphization of these oxides particles appear during the MA process. This structure vanishes after prolonged heat treatment (900 °C/168 h) for particles with diameter larger than 20 nm, indicating that these core/shell structures are far from chemical equilibrium.

MA 956 also exhibits the same structure of crystalline core and amorphous shell with more thickness compared to ODS–16Cr steel. By comparing the HRTEM studies of MA 956 and ODS–16Cr steels with the results of Marquis [115], the content of these solute–enriched shells may differ and depends on the initial composition of the ODS steel. The author suggests that $Y_4Al_2O_9$ and $YAlO_3$ core forms in ODS–16Cr and MA 956 materials and Y_2TiO_5 and $Y_2Ti_2O_7$ forms in the case of Ti–containing ODS–12Cr steel. It is supposed that shell forms as a result of solute depletion from the core during crystallization of the particles upon annealing. However, there is no clear understanding about the origin and the nature of these core/shell structures.

The phase and metal–oxide interface structure of oxide particle in ODS–15.5Cr–4Al steel, extruded at 1050 and 1150 °C were analysed by HRTEM and diffraction contrast techniques [176]. After 1050 °C, almost all the particles are yttrium–aluminum–hexagonal ($YAlO_3$) phase with 86.5% (diameter <4.5 nm) and was found to be coherent with the matrix. After extrusion at 1150 °C, both Y–Al–perovskite oxides and Y–Al–hexagonal with 78 % (diameter 4.5–10 nm) and were found to be are semi–coherent with the matrix.

The microstructure of ODS–16Cr and ODS–16Cr–5Al ferritic steels produced by sol–gel method together with hydrogen reduction, MA and SPS methods showed the typical ferritic structure with the homogeneous distribution of complex oxides in Al–free (Y–Ti–O:10–30 nm) and Al–contained samples (Y–Al–O: 20–100 nm), respectively [177].

The microstructural evolution of ODS–18Cr steels is limited and the details of the work carried out by various research groups is given in Table 2.7 [75, 178–186].

Table 2.7 Literature review on microstructural studies of ODS–18Cr steel.

Composition	Processing stage	Salient features	Ref
Fe–18Cr–1W–0.8Ti–0.3 Y_2O_3	Milled powders (1–48 h) Heat treated (850, 1100 and 1300°C for 1 h) powders SANS study	Particles less than 10 nm were found in powders even after 48 h milling. At 850°C, nanoclusters and Y–Ti–O oxides were present. At 1100°C, these nanoclusters completely precipitated as Y–Ti–O oxides of 2 nm. At 1300°C, particle coarsening (10 nm) occurred.	[178]
Fe–18Cr–W–Ti–Y_2O_3	Milled powders Heat treated (850, 1100 and 1300°C for 1 h) powders FESEM and TEM studies	Ferritic nano grain structure. Oxides are not present in milled powders. Bimodal grain structure at all annealing temperatures and the fraction of fine grains decreased with increase in temperature. At 850°C, oxide particles are not found by TEM. At 1100°C, fine oxide particles could not be resolved by TEM. At 1300°C, Y_2O_3, $Y_2Ti_2O_7$ and new pyrOrtho Y–Ti–O phase along with hexagonal Y_2TiO_5 plates (0.5–2µm) present. Shape: spherical and facetted.	[179]
Fe–18Cr–1W–0.26Ti–0.56Y_2O_3	Hot extruded (1100°C), hot rolled (20% at 650°C) and annealed (1050 °C for 1 h), TEM study	Very fine elongated grains along HE direction. Spherical dispersoids of 10 nm to few hundred nm were observed. Structure: Not reported.	[180]
Fe–18Cr–1W–0.4Ti–0.56Y_2O_3	Hot extruded (1100°C), hot rolled (20% at 700°C) and annealed (1050 °C and 1300°C for 1 h) TEM, TXRD and XAS studies	Elongated grains along the extrusion direction at both 1050 and 1300°C. Annealing at 1050°C revealed the presence of $Y_2Ti_2O_7$ along with $M_{23}C_6$, TiO_2 and Y_2O_3 (bcc & fcc) particles. Annealing at 1300°C, $Y_2Ti_2O_7$ particles coarsened to 15 nm and only fcc Y_2O_3 is present along with $M_{23}C_6$.	[181]
Fe–18Cr–1W–0.4Ti–0.5Y2O3	Hot extruded (1150°C) TEM and SANS studies	Elongated grains in extrusion direction. spherical nanoclusters of < 3 nm with high number density were observed along with coarser particles of few hundreds of nm	[182]
Fe–18Cr–1W–0.3Ti–0.6Y2O3	Hot extruded (1100°C), hot rolled (20% at 650°C) and annealed (1050 °C for 1 h) TEM study	Elongated grains in extrusion direction Nanoclusters (3 nm) of $Y_2Ti_2O_7$ were observed.	[183]
Fe–18Cr–1W–0.3Ti–0.5Y2O3	Hot extruded (1150°C) TEM study	Spherical oxide particles of 2–25 nm were present.	[184]
(a)Fe–18Cr–1W–0.14N–0.5TiH_2 (b)Fe–18Cr–1W–0.8Ti–0.16N_2	Mechanically milled (10 h), Annealed (600–1000°C) Hot extruded (800°C). Composition in (b) was plasma nitrided prior to annealing and hot extrusion	There is no presence of nano–nitrides in both milled and plasma nitrided powders. Precipitation of nano nitrides of ≅ 2 nm occurs on annealing at (600–1000°C).	[185]
Fe–18Cr–0.2Ti–0.35Y_2O_3 without Al and with 5Al	Hot extruded (1150°C) and annealed (1050°C for 1 h) FESEM and TEM studies	Bamboo–like grain structure parallel to extrusion direction. Both Y_2TiO_5 and $Y_2Ti_2O_7$ of size <12 nm were present in which <5 nm particles are coherent and 5–12 nm particles are semicoherent. Four fold increases in number fraction of 5–12 nm particles was observed in ODS–18Cr–5Al due to the formation of $YAlO_3$ and $Y_3Al_5O_{12}$.	[75, 186]

2.7.2 Mechanical properties

Kimura *et al*. [67] studied the ODS steels having high Cr with the addition of aluminum for high temperature tensile properties. As the increase in Cr content often causes the aging embrittlement due to the formation of Cr–rich phases, the consequences of aging (at 500 °C for 1,000 h) on the mechanical properties were examined. Fig. 2.14 presents the effect of aging on the UTS and total elongation of various ODS steels. The ODS steels having 19 wt. % Cr, both with and without Al addition exhibited age hardening, while ODS steels having 14 and 16 wt. % Cr, did not exhibit any age hardening. It is obvious that the aging does not cause for the decrease of total elongation in all the high Cr–ODS alloys. After aging, both ODS–19Cr alloys exhibited a large shift of DBTT. However, no embrittlement was noticed in 14Cr and ODS–16Cr alloys even after aging up to 1000 h.

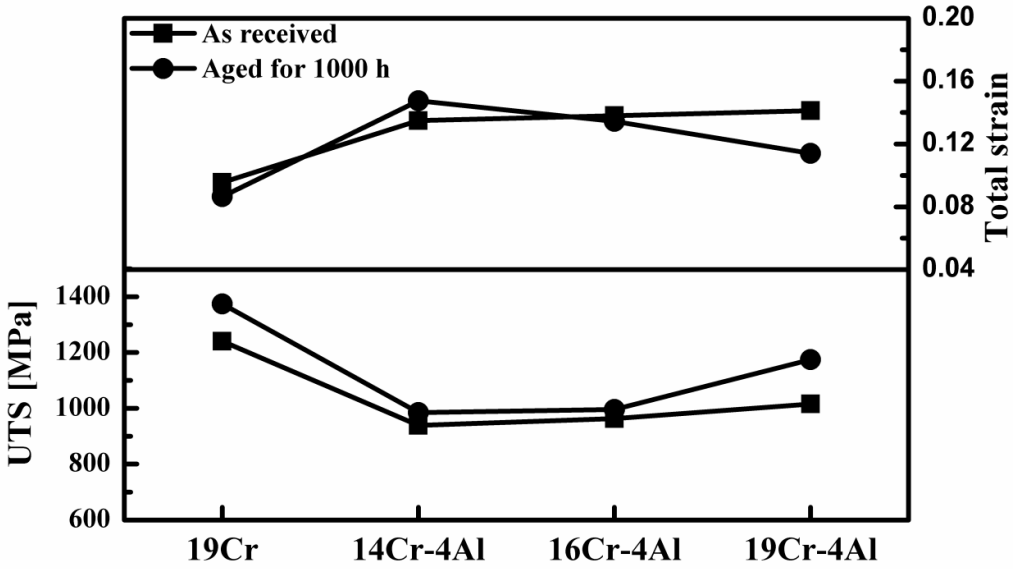

Fig. 2.14 The effect of aging on the tensile properties at RT in high Cr–ODS steels [67].

The tensile stress increases with the increase in Cr concentration due to the solid solution strengthening effect of chromium (Fig. 2.15). The variation in the tensile stress by increasing Cr is slightly smaller than the difference in the tensile stress among ODS–9C steel and ferritic steel. In which, the only difference is the presence of high number density of nano–sized complex oxide particles in ODS–9Cr steel [67].

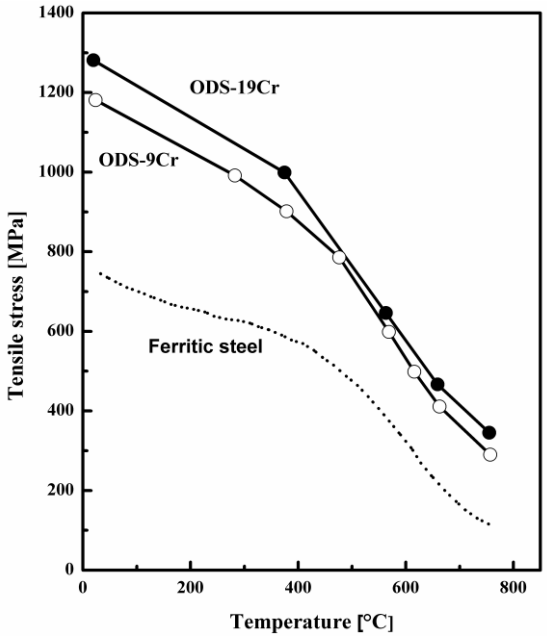

Fig. 2.15 Variation of tensile stress in ferritic steel, ODS–9Cr and ODS–19Cr steel with temperature [67].

The high chromium content in steel decreases the corrosion rate, but enhances the thermal aging embrittlement (Fig. 2.16). To improve the corrosion resistance and to avoid aging embrittlement, aluminum is added to lower chromium containing steels [67]. But the addition of aluminum reduces the strength (Fig. 2.17). Research work is being carried out to increase the strength of Al containing ODS steels by small additions of Zr or Hf. The presence of Zr results in the precipitation of carbides and oxides at the grain boundary, which strengthens creep. The ODS steel containing Zr or Hf is designated as "Super ODS steel" and the work is being carried out in Japan [187].

The literature available on mechanical properties of ODS–18Cr ferritic steels is scanty, when compared to the ODS–14Cr ferritic steels [75, 180, 182, 189–193]. The UTS of ODS steel without Al is superior to Al containing ODS steel, at all temperatures up to 700 °C. The primary reason was that there were relatively fewer and coarser oxide particles when ODS steel contains Al. There was mechanical property anisotropy even in ODS steels with Al [189].

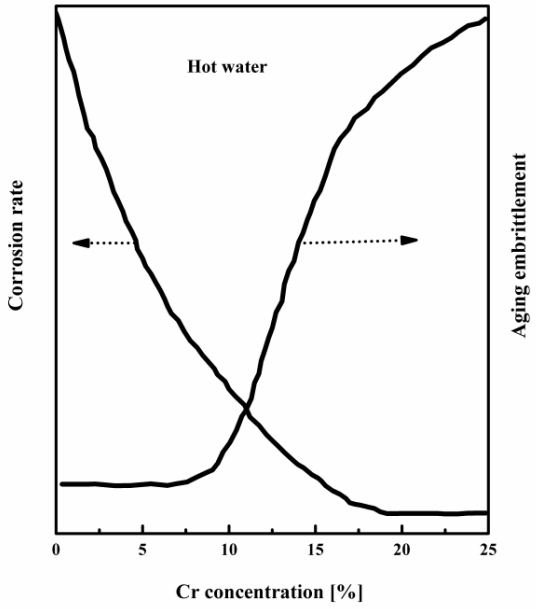

Fig. 2.16 Variation of resistances to corrosion and aging embrittlement with Cr in ODS steels [188].

The high temperature tensile properties of ODS–18Cr steel were estimated and compared with MA957 alloy [180]. The behavior of the both steels is similar. The effect of thermal ageing at 400–600 °C during 5000 h on the mechanical properties of ODS–18Cr ferritic steel was examined [190]. Embrittlement was observed when aged at 400 and 500 °C due to the formation of α' particles. The ductility and impact strength were significantly lower in aged condition. The brittle failure was characterized by cleavage fracture [189].

2.7.3 Corrosion and oxidation resistance

Kimura *et al*. [188] studied aluminum addition to the ODS steels having high Cr for corrosion properties. The influence of Cr content on the corrosion behavior of ODS steels in SCW is presented in Figs. 2.17 and 2.18. These results indicated that, all ODS steels having higher Cr gained lower weight gain than SUS316L. It is observed that the corrosion resistance of the ODS–14Cr is high compared to SUS316L. The ODS alloys having a high Cr content exhibit improved corrosion properties. ODS–12Cr steel without Al exhibits comparable corrosion behavior as ODS–9Cr steel. In steels containing Al, both corrosion and oxidation resistance increased in addition to the inherent improvement with enhanced Cr concentration.

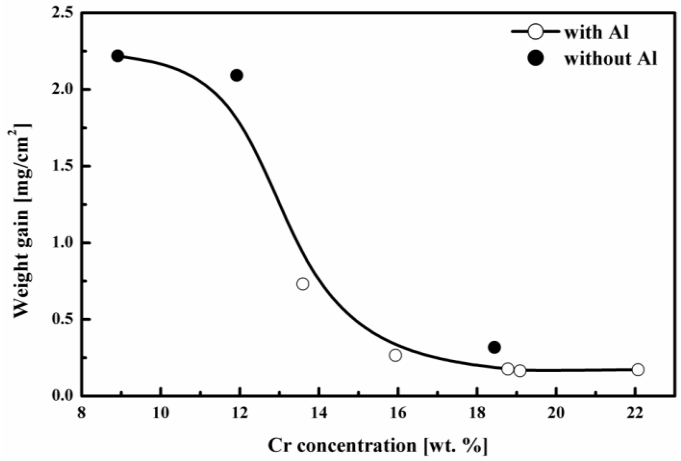

Fig. 2.17 Influence of Cr content on the corrosion properties of ODS steel in SCPW [68].

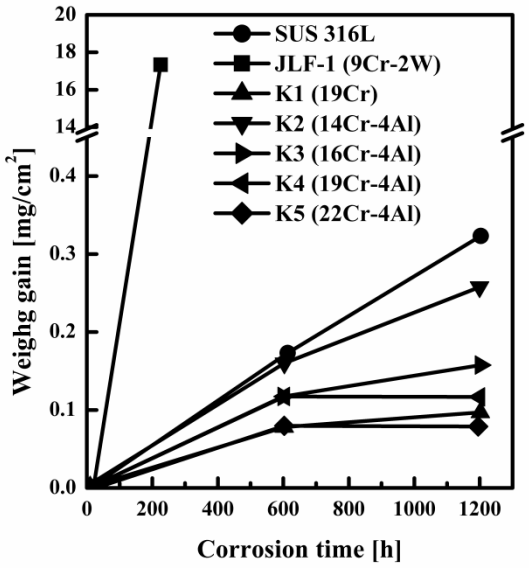

Fig. 2.18 Variation of weight gain in high–Cr ODS ferritic steels, JLF–1LN and SUS316L in SCPW [188].

ODS–16Cr–5Al steel has higher oxidation resistance in comparison to the ODS–16Cr and conventional SS 304 steel due to the formation of continuous and dense Al_2O_3 film on the surface. The outstanding oxidation resistance of ODS–16Cr–5Al makes it capable to be used as advanced structural alloys in severe corrosion environments [177].

The ODS–18Cr steel exposed in SCW showed that weight gain increases with increasing time. The corrosion behavior follows a parabolic law. The corrosion product consists of Fe_2O_3 as an outer layer, $(FeCr)_3O_4$ as inner layer and Cr_2O_3 in the diffusion layer above the substrate [194].

The effects of temperature and alloying elements on corrosion performance of ODS ferritic steels were investigated in SCW. Addition of 4 wt. % Al is efficient in improving the corrosion resistance of ODS–16Cr steel. Addition of rare earth elements like Ce, Y, La was found to be beneficial in addition to Al addition [195].

2.8 Mechanisms of formation of complex–oxide particles

The microstructural evolution in ODS steels consists of the changes that occur to the Y_2O_3 particles during MA and its subsequent hot consolidation. Different research groups have widely studied the formation of complex–oxide particles. However, still there are contradictory reports on the mechanism of formation of oxide particles.

Some of the groups show that the formation mechanism of oxide particles in ODS steels happens in a two stage process whether the,

1. Y_2O_3 particles fragment to a size of < 2 nm and exist either in crystalline state [108, 196] or in amorphous state [197–199] or (b) Y_2O_3 particles fragment, dissociate and dissolve in the matrix during MA [74, 152, 200, 201]. The matrix is the homogeneous solid solution of Fe, Cr, Ti, Y and O;
2. Precipitation of nano–sized Y–Ti–O complex oxide particles takes place during hot consolidation by the participation of Ti existing in steel [74, 152, 199, 200–204].

Studies on as milled pure iron with Y_2O_3 and Y_2O_3+Ti postulated the presence of 2–5 nm sized Y_2O_3/$Y_2Ti_2O_7$ particles in the milled powder [205]. Recent studies on as milled ODS steels indicated the presence of Y, Ti, O atomic clusters and also Y and O enrichment in the matrix [147, 158].

The recent work by Brocq *et al*. [206] reported that the role of MA process appears to be more complex for the formation of complex–oxide particles. The initially formed oxide particles in MA powder are the basis for the distribution of oxides noticed in consolidated samples. The formation of oxides in this way can be controlled by varying the milling parameters (temperature, atmosphere and intensity) and annealing parameters (duration and temperature). However, the specific conditions of ball milling (reactive ball milling: Fe_2O_3 and YFe_3 are used as reactants) that are used for this study should be mentioned. This mechanism can be summarized as follows:

1. Dissolution of Y_2O_3 and nucleation of first complex–oxide particles occurs during ball milling;
2. Nucleation and growth of these complex–oxide particles continue after subsequent annealing.

Hsiung *et al.* [173–175] also suggested another mechanism for the complex–oxide particle formation. HRTEM studies of ODS–16Cr and MA956 steels revealed that oxides contain core–shell structure, in which some of the oxide particles are surrounded by an amorphous shell. The proposed formation mechanism of these oxide particles (Fig. 19) based on the HRTEM analysis includes the following stages:

1. During the initial stages of MA, Y_2O_3 particles fragment and get dispersed in the powder;
2. During the later stages of MA process, dissolution and formation of oxide clusters occurs;
3. The subsequent consolidation process leads to the formation of distinct oxide particles of about 2 nm.

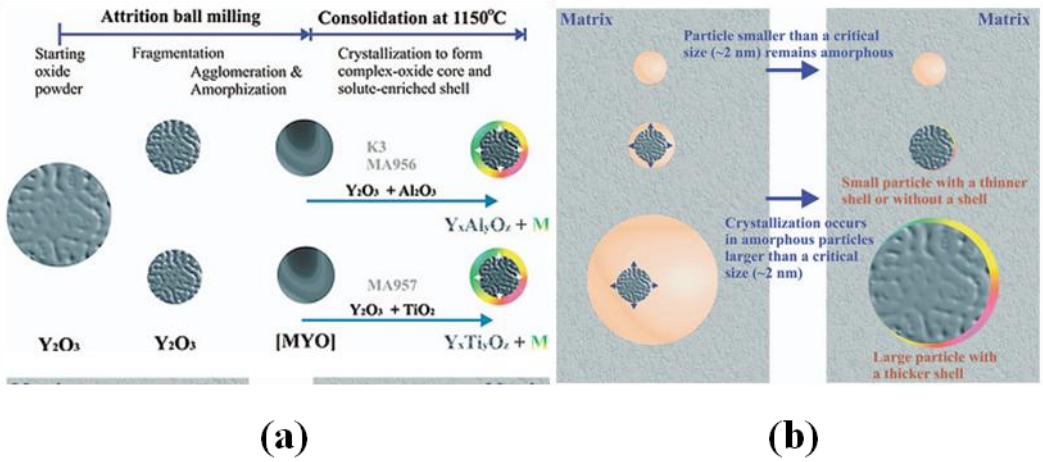

Fig. 2.19 Schematic illustrations showing (a) three–stage mechanism for the formation of oxide nanoparticles during MA and consolidation and (b) size effect on the formation of core/shell structures in oxide particles [175].

2.9 Influence of process parameters on the microstructure of ODS steels

The process parameters employed in the manufacture of ODS steels have a strong influence on the development of microstructure of the matrix and size and number density of oxide particles, which affect the mechanical properties and performance of the material.

Ohtsuka *et al.* [78] studied the effects of MA conditions on oxygen contamination of ODS–9Cr F/M steel. It was mentioned that excess oxygen (whole oxygen content in the steel minus the oxygen content in Y_2O_3) is an important parameter for the fine and homogeneous dispersion of oxides in the matrix. Use of high purity Ar atmosphere during the MA process drastically reduces the excess oxygen content.

Miller *et al*. [151] studied the influence of milling time (40 and 80 h) on the microstructure of ODS–14Cr steel by APT. As, no residual parts of Y_2O_3 powder are observed in the as–milled state, it is an indicative that these particles have fully dissolved in Fe–Cr matrix during the milling. No significant difference is observed between 40 and 80 h of milling time.

Alinger *et al*. [74] performed a systematic study to understand the influence of consolidation temperatures (850, 1000 and 1150 °C) on number density, nanoclusters size, volume fraction and hardness of ODS–14Cr steel using SANS. The size of nanoclusters increases with an increase in consolidation temperature, whereas number

density, volume fraction as well as hardness decreases. He also compared the effects of consolidation by HIP and HE. The size of nanoclusters remains the same in both the processes, whereas, HE processed alloy exhibits high number density (3.5×10^{24} /m^3) than HIP (1.2×10^{24}/m^3) processed alloy.

The effect of HE at 850 and 1175 °C on the characteristics of nanoclusters was studied in ODS–14Cr steel. HE at 850 °C yields a high number density Y–Ti–O (2 nm) complex oxide particles, while HE at 1175 °C results in low number density of mostly $Y_2Ti_2O_7$ oxide particles [207].

Dou *et al.* [96] also studied the effect of consolidation temperature in ODS–15.5Cr steel (4Al). The decrease in HE temperature from 1150 to 1050 °C leads to considerable reduction in grain size. The size of oxide particles decreases to about half (from 6.7 to 3.2 nm) and number density increases (from 1.72×10^{23} to 9.2×10^{23}/m^3). Therefore, higher consolidation temperature results in larger size and lower number density of oxides. The variations of crystallite size and dispersoid size of different ODS steels are presented in Fig. 2.20.

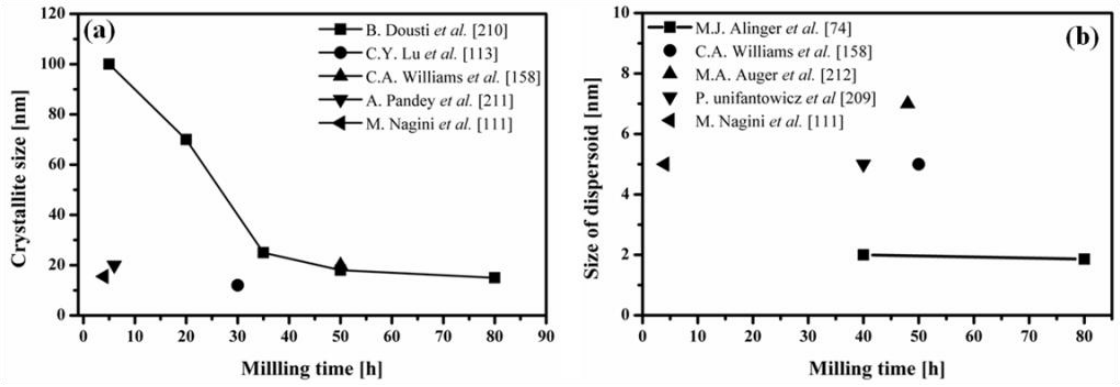

Fig. 2.20 Variation of (a) crystallite size and (b) dispersoid size of different ODS steels.

Influence of HE (1100 °C) and HIP (1150 °C) on final microstructure of ODS–14Cr was studied by Unifantowicz *et al* [208]. MA of powder is performed in planetary ball mill under hydrogen atmosphere. After consolidation, both ODS–14Cr steels are heat treated at 850 °C for 1 h. TEM analysis revealed that both the samples exhibited fairly equiaxed grain structure with a size of 40–80 nm along with the high number density of nanoclusters. In comparison to HIP sample (4 nm, 9.3×10^{23}/m^3), hot extruded sample results in higher oxide particle size (8 nm) with higher number density (17.4×10^{23}/m^3).

ODS–14Cr steel developed by HE shows high tensile strength and hardness at low to reasonable temperatures in comparison to the same steel processed by HIP. The higher strength levels in hot extruded materials are due to the existence of higher number density of fine oxides and work hardening effects compared to HIP processed samples [208].

Oksiuta *et al.* [209] investigated the mechanical properties of ODS–14Cr steel at high temperatures consolidated by HIP at 1150 °C under various pressure conditions in the range of 185–300 MPa for 3 h. The HIP pressure shows insignificant effect on the tensile strength and hardness, although it improves the ductility of the alloy.

2.10 Present scope of work

As evident from the foregoing literature survey covered in chapter 2, it is amply evident that the high temperature capabilities of Cr containing steels are enhanced by the Y_2O_3 dispersion. It is also well established that the addition of small quantities of Ti reduces the dispersoid size from 20–40 nm in Y_2O_3 alone to about 5–10 nm and the oxide changes to Y–Ti–O complex oxides. ODS steels are produced by MA, using Y_2O_3 powder milled with Fe–Cr matrix, followed by hot consolidation. However, there is ambiguity on the formation of nano–sized oxide complexes, in which, one group advocates that fragmentation of Y_2O_3 during MA is responsible for size reduction, another supports formation of nano oxide complexes by dissociation of Y_2O_3 and precipitation during the hot consolidation process. It can be expected that the dissolution and nucleation mechanism may vary with sample chemistry and processing parameters. Microstructural features have individual and synergistic effects on the resulting mechanical properties. However, the limited amount of work was performed in order to characterize ODS–18Cr steels. The present work, therefore, is aimed at understanding of the following effects:

1. The influence of milling time in a high energy ball mill,
2. The effect of mechanical alloying on Y_2O_3,
3. The role played by various hot working operations and
4. The correlation between structure and properties of ODS–18Cr steels.

References

[1] F.A. Garner, M.B. Toloczko, B.H. Sencer, Comparison of swelling and irradiation creep behavior of fcc–austenitic and bcc–ferritic/martensitic alloys at high neutron exposure, *Journal of Nuclear Materials*, 276 (2000) 123–142.

[2] R.L. Klueh, A.T. Nelson, Ferritic/martensitic steels for next–generation reactors, *Journal of Nuclear Materials*, 371 (2007) 37–52.

[3] S. Ukai, M. Harada, S. Nomura, S. Shikakura, I. Shibahara, in: Proceedings of an international symposium on material chemistry in nuclear environment, Tsukuba, Japan, 12 and 13th March 1992.

[4] R.L. Klueh, Elevated temperature ferritic and martensitic steels and their application to future nuclear reactors, *International Materials Reviews*, 50 (2005) 287–310.

[5] F. Masuyama, Advanced heat resistant steel for power generation, eds. R. Viswanathan and J. Nutting, The Institute of Materials, London, 33–48, 1999.

[6] R. Viswanathan, W. Bakker, Materials for ultra supercritical coal power plants–Boiler materials: Part 1, *Journal of Materials Engineering and Performance*, 10 (2001) 81–95.

[7] R. Viswanathan, W. Bakker, Materials for ultra supercritical coal power plants–Turbine materials: Part II, *Journal of Materials Engineering and Performance*, 10 (2001) 96–101.

[8] L. Tan, Y. Katoh, A.A.F. Tavassoli, J. Henry, M. Rieth, H. Sakasegawa, H. Tanigawa, Q. Huang, Recent status and improvement of reduced activation ferritic martensitic steels for high temperature service, *Journal of Nuclear Materials*, 479 (2016) 515–523.

[9] A. Kohyama, A. Hishinuma, D.S. Gelles, R.L. Klueh, W. Dietz, K. Ehrlich, Low activation ferritic and martensitic steels for fusion application, *Journal of Nuclear Materials*, 233–237 (1996) 138–147.

[10] A. Kimura, M. Narui, T. Misawa, H. Matsui, A. Kohyama, Dependence of impact properties on irradiation temperature in reduced–activation martensitic steels, *Journal of Nuclear Materials*, 258–263 (1998) 1340–1344.

[11] N. Baluc, D.S. Gelles, S. Jitsukawa, A. Kimura, R.L. Klueh, G.R. Odette, B. van der Schaaf, J. Yu, Status of reduced activation ferritic/martensitic steel development, *Journal of Nuclear Materials*, 367–370 (2007) 33–41.

[12] D.S. Gelles, Microstructural examination of commercial ferritic alloys at 200 dpa, *Journal of Nuclear Materials*, 233–237 (1996) 293–298.

[13] H. Kurishita, H. Kayano, M. Narui, A. Kimura, M.L. Hamilton, D.S. Gelles, Tensile properties of reduced activation Fe–9Cr–2W steels after FFTF irradiation, *Journal of Nuclear Materials*, 212–215 (1994) 730–735.

[14] A. Kimura, H. Kayano, S. Ohta, Effects of neutron irradiation on hydrogen–induced intergranular fracture in a low activation 9%Cr–2%W steel, *Journal of Nuclear Materials*, 179–181 (1991) 741–744.

[15] M. Tamura, H. Hayakawa, M. Tanimura, A. Hishinuma, T. Kondo, Development of potential low activation ferritic and austenitic steels, *Journal of Nuclear Materials*, 141–143 (1986) 1067–1073.

[16] R.L. Klueh, D.S. Gelles, T.A. Lechtenberg, Development of ferritic steels for reduced activation: The US program, *Journal of Nuclear Materials*, 141–143 (1986) 1081–1087.

[17] G.J. Butterworth, O. N. Jarvis, Comparison of transmutation and activation effects in five ferritic alloys and AISI 316 stainless steel in a fusion neutron spectrum, *Journal of Nuclear Materials*, 123 (1994) 982–988.

[18] J.Ch. Sublet, G.J. Butterworth, The neutronic basis for elemental substitution in martensitic steels, *Journal of Nuclear Materials*, 212–215 (1994) 695–700.

[19] R.W. Conn, E.E. Bloom, J.W. Davis, R.E. Gold, R. Little, K.R. Schultz, D.L. Smith, F.W. Wiffen, Panel report on low activation materials for fusion applications, Nuclear Technology/Fusion, 5 (1984) 291.

[20] D. Dulieu, K.W. Tupholme, G.J. Butterworth, Development of low activation martensitic stainless steels, *Journal of Nuclear Materials*, 141–143 (1986) 1097–1101.

[21] R.L. Klueh, P.J. Maziasz, Microstructure of Cr–W steels, *Metallurgical and Materials Transactions A*, 20A (1989) 373–381.

[22] A. Kimura, R. Kasada, K. Morishita, R. Sugano, A. Hasegawa, K. Abe, T. Yamamoto, H. Matsui, N. Yoshida, B.D. Wirth, T.D. Rubia, High resistance to helium embrittlement in reduced activation martensitic steels, *Journal of Nuclear Materials*, 307–311 (2002) 521–526.

[23] A. Kimura, Current status of reduced activation ferritic/martensitic steels R&D for fusion energy, *Materials Transactions*, 46 (2005) 394–404.

[24] R.L. Klueh, D.J. Alexander, Impact toughness of irradiated reduced activation ferritic steels, *Journal of Nuclear Materials*, 212–215 (1994) 736–740.

[25] D.S. Gelles, Microstructural examination of several commercial ferritic alloys irradiated to high fluence, *Journal of Nuclear Materials*, 104 (1981) 975–979.

[26] M. Tamura, H. Hayakawa, A. Yoshitake, A. Hishinuma, T. Kondo, Phase stability of reduced activation ferritic steel 8Cr–2W–0.2V–0.04–Ta–Fe, *Journal of Nuclear Materials*, 155–157 (1988) 620–625.

[27] M. Yamanouchi, M. Tamura, H. Hayakawa, A. Hishinuma, T. Kondo, Accumulation of engineering data for practical use of reduced activation ferritic steel 8Cr–2W–0.2V–0.04–Ta–Fe, *Journal of Nuclear Materials*, 191–194 (1992) 822–826.

[28] F. Abe, T. Noda, H. Araki, S. Nakazawa, Alloy composition selection for improving strength and toughness of reduced activation 9Cr–W steels, *Journal of Nuclear Materials*, 171–181 (1991) 663–666.

[29] A. Kohyama, Y. Kohno, K. Asakura, H. Kayano, R&D of low activation ferritic steels for fusion in japanese universities, *Journal of Nuclear Materials*, 212–215 (1994) 684–689.

[30] H. Kayano, A. Kimura, M. Narui, T. Kikuchi, S. Ohta, Effects of small changes in alloy composition on the mechanical properties of low activation 9 %Cr–2 %W steel, *Journal of Nuclear Materials*, 179–181 (1991) 671–674.

[31] R.L. Klueh, Heat treatment behavior and tensile behavior of Cr–W steels, *Metallurgical and Materials Transactions A*, 20A (1989) 463–469.

[32] K. Ehrlich, S. Kelzenberg, H.D. Rohrig, L. Schafer, M. Schirra, The development of ferritic–martensitic steels with reduced long term activation, *Journal of Nuclear Materials*, 212–215 (1994) 678–683.

[33] B. Vander Schaaf, D.S. Gelles, S. Jitsukawa, A. Kimura, R.L. Klueh, A. Moslang, G.R. Odette, Progress and critical issues of reduced activation ferritic/martensitic steel development, *Journal of Nuclear Materials*, 283–287 (2000) 52–59.

[34] P. Fernandez, M. Lancha, J. Lapena, M. Hernandez–Mayoral, Metallurgical characterization of the reduced activation ferritic/martensitic steel Eurofer 97 on as– received condition, *Fusion Engineering and Design*, 58–59 (2001) 787–792.

[35] R. Lindau, M. Schirra, First results on the characterisation of the reduced activation ferritic martensitic steel EUROFER, *Fusion Engineering and Design*, 58–59 (2001) 781–785.

[36] A. Alamo, J.C. Brachet, A. Castaing, C. Lepoittevin, F. Barcelo, Physical metallurgy and mechanical behaviour of FeCrWTaV low activation martensitic steels: Effects of chemical composition, *Journal of Nuclear Materials*, 258–263 (1998)1228–1235.

[37] Y. Li, Q. Huang, Y. Wu, T. Nagasaka, T. Muroga, Mechanical properties and microstructures of China low activation martensitic steel compared with JLF–1, *Journal of Nuclear Materials*, 376–370 (2007)117–121.

[38] L. Schaefer, M. Schirra, Influence of thermal aging on tensile and impact bending properties of the steel grades OPTIFER and F82H mod, *Journal of Nuclear Materials*, 271–272 (1999) 455–458.

[39] T. Hasegawa, Y. Tomita, A. Kohyama, Influence of tantalum and nitrogen contents, normalizing condition and TMCP process on the mechanical properties of low–activation 9Cr–2W–0.2V–Ta steels for fusion application, *Journal of Nuclear Materials*, 258–263 (1998) 1153–1157.

[40] K.L. Murty, I. Charit, Structural materials for Gen–IV nuclear reactors: Challenges and opportunities, *Journal of Nuclear Materials*, 383 (2008) 189–195.

[41] A.F. Rowcliffe, S.J. Zinkle, J.F. Stubbins, D.J. Edwards, D.J. Alexander, Austenitic stainless steels and high strength copper alloys for fusion components, *Journal of Nuclear Materials*, 258–263 (1998) 183–192.

[42] W.R. Corwin, U.S. generation IV reactor integrated materials technology program, Nuclear Engineering and Technology, 38 (2006) 591–618.

[43] S.J. Zinkle, P.J. Maziasz, R.E. Stoller, Dose dependence of the microstructural evolution in neutron–irradiated austenitic stainless steel, *Journal of Nuclear Materials*, 206 (1993) 266–286.

[44] G.S.Was, Fundamentals of radiation materials science: metals and alloys, Springer–Verlag, Berlin, Heidelberg, 2007.

[45] F.A. Garner, Irradiation performance of cladding and structural steels in liquid metal reactors, Materials Science and Technology: A Comprehensive Treatment, VCH publishers, 10A (1994) 419–543.

[46] J.S. Cheon, C.B. Lee, B.O. Lee, J.P. Raison, T. Mizuno, F. Delage, J. Carmack, Sodium fast reactor evaluation: core materials, *Journal of Nuclear Materials*, 392 (2009) 324–330.

[47] M.D. Mathew, S. Latha, G. Sasikala, S.L. Mannan, P.Rodriguez, Creep properties of three heats of type 316 stainless steel for elevated temperature nuclear applications, *Nuclear Technology*, 81 (1988)114–121.

[48] Status of liquid metal cooled fast reactor technology, IAEA–TECDOC–1083, International Atomic Energy Agency, 1999.

[49] I. Shibahara, N. Akasaka, S. Onose, H. Okada, S. Ukai, Swellling of advanced austenitic stainless steels developed for the environment of heavy neutron exposure, *Journal of Nuclear Materials*, 212–215 (1994) 487–491.

[50] P. Billot, J.L. Seran, in: Materials for Generation IV Nuclear Reactors, NATO Advanced Study Institute, Cargese, France, September 24–October 6, 2007.

[51] M. Katsuragawa, H. Kashihara, M. Akebi, Status of liquid–metal fast breeder reactor–fuel development in Japan, *Journal of Nuclear Materials*, 204 (1993) 14–22.

[52] A. Uehira, S. Mizuta, S. Ukai, R.J. Puigh, Irradiation creep of 11Cr–0.5Mo–2W,V,Nb ferritic–martensitic, modified 316, and 15Cr–20Ni austenitic S.S. irradiated in FFTF to 103–206 dpa, *Journal of Nuclear Materials*, 283–287 (1993) 396–399.

[53] T. Jayakumar, M.D. Mathew, K. Laha, High temperature materials for nuclear fast fission and fusion reactors and advanced fossil power plants, *Procedia Engineering*, 55 (2013) 259–270.

[54] C. Capdevila, M. Serrano, M. Campos, High strength oxide dispersion strengthened steels: fundamentals and applications, *Materials Science and Technology*, 30 (2014) 1655–1657.

[55] S. Ukai, M, Harada, H. Okada, M. Inoue, T. Nishida M. Fujiwara, Alloying design of oxide dispersion strengthened ferritic steel for long life FBRs core materials, *Journal of Nuclear Materials*, 204 (1993) 65–73.

[56] H. Zhu, T. Wei, R. Harrison, L. Edwards, K. Maruyama, Development of oxide dispersion strengthened steels for high temperature nuclear structural applications, Engineering Asset Management and Infrastructure Sustainability, Springer, London, pp. 1147–1160, 2012.

[57] D.K. Mukhopadhyay, F.H. Froes, D.S. Gelles, Development of oxide dispersion strengthened ferritic steels for fusion, *Journal of Nuclear Materials*, 258–263 (1998) 1209–1215.

[58] J.P. Hurely, Applications for dispersion strengthened alloys in thermal power systems, Proceedings of the twenty first annual conference on fossil energy materials, Tennessee, 2007.

[59] G.R. Odette, Recent progress in developing and qualifying nanostructured ferritic alloys for advanced fission and fusion applications, *Journal of the Minerals, Metals & Materials*, 66 (2014) 2427–2441.

[60] S. Ukai, M. Fujiwara, Perspective of ODS alloys application in nuclear environments, *Journal of Nuclear Materials*, 307–311 (2002) 749–757.

[61] R.L. Klueh, J.P. Shingledecker, R.W. Swindeman, D.T. Hoelzer, Oxide dispersion strengthened steels: A comparison of some commercial and experimental alloys, *Journal of Nuclear Materials*, 341 (2005) 103–114.

[62] S. Ukai, Oxide dispersion strengthened steels, *Comprehensive Nuclear Materials*, 4 (2012) 241–271.

[63] R.L. Klueh, P.J. Maziasz, I.S. Kim, L. Heatherly, D.T. Hoelzer, N. Hashimoto, E.A. Kenik, K. Miyahara, Tensile and creep properties of an oxide dispersion strengthened ferritic steel, *Journal of Nuclear Materials* 307–311 (2002) 773–777.

[64] S. Ohtsuka, S. Ukai, M. Fujiwara, T. Kaito, T. Narita, Improvement of creep strength of 9Cr ODS martensitic steel by controlling excess oxygen and titanium concentrations, *Materials Transactions*, 46 (2005) 487–492.

[65] S. Ukai, S. Mizuta, T. Yoshitake, T. Okuda, M. Fujiwara, S. Hagi, T. Kobayashi, Tube manufacturing and characterization of oxide dispersion strengthened ferritic steels, *Journal of Nuclear Materials*, 283–287 (2000) 702–706.

[66] A. Alamo, V. Lambard, X. Averty, M.H. Mathon, Assessment of ODS–14%Cr ferritic alloy for high temperature applications, *Journal of Nuclear Materials*, 329–333 (2004) 333–337.

[67] A. Kimura, H.–S. Cho, N. Toda, R. Kasada, K. Yutani, H. Kishimoto, N. Iwata, S. Ukai, M. Fujiwara, High burnup fuel cladding materials R&D for advanced nuclear systems, nano–sized oxide dispersion strengthening steels, *Journal of Nuclear Science and Technology*, 44 (2007) 323–328.

[68] H.S. Cho, A. Kimura, S. Ukai, M. Fujiwara, Corrosion properties of oxide dispersion strengthened steels in super–critical water environment, *Journal of Nuclear Materials*, 329–333 (2004) 387–391.

[69] H.L. Hu, Z.J. Zhou, L. Liao, L.F. Zhang, M. Wang, S.F. Li, C.C. Ge, Corrosion behavior of a 14Cr–ODS steel in supercritical water, *Journal of Nuclear Materials* 437 (2013) 196–200.

[70] B.A. Pint, I.G. Wright, Long–term high temperature oxidation behavior of ODS ferritic steels, *Journal of Nuclear Materials*, 307–311 (2002) 763–768.

[71] Y. Chen, Kumar Sridharan, S. Ukai, T.R. Allen, Oxidation of 9Cr oxide dispersion strengthened steel exposed in supercritical water, *Journal of Nuclear Materials*, 371 (2007) 118–128.

[72] C. Schroer, J. Konys, T. Furukawa, K. Aoto, Oxidation behaviour of P122 and a 9Cr–2W ODS steel at 550 °C in oxygen–containing flowing lead–bismuth eutectic, *Journal of Nuclear Materials***,** 398 (2010) 109–115.

[73] G.R. Odette, M.J. Alinger, B.D Wirth, Recent developments in irradiation–resistant steels, *Annual Review of Materials Research*, 38 (2008) 471–503.

[74] M.J. Alinger, G.R. Odette, D.T. Hoelzer, On the role of alloy composition and processing parameters in nanocluster formation and dispersion strengthening in nanostructured ferritic alloys, *Acta Materialia*, 57 (2009) 392–406.

[75] J.H. Lee, Development of oxide dispersion strengthened ferritic steels with and without aluminum, *Frontier Energy*, 6 (2012) 29–34.

[76] Z. Zhou, S. Yang, W. Chen, L. Liao, Y. Xu, Processing and characterization of a hipped oxide dispersion strengthened austenitic steel, *Journal of Nuclear Materials* 428 (2012) 31–34.

[77] C. Cayron, E. Rath, I. Chu, S. Launois, Microstructural evolution of Y_2O_3 and $MgAl_2O_4$ ODS EUROFER steels during their elaboration by mechanical milling and hot isostatic pressing, *Journal of Nuclear Materials*, 335 (2004) 83–102.

[78] S. Ohtsuka, S. Ukai, M. Fujiwara, T. Kaito, T. Narita, Nano–structure control in ODS martensitic steels by means of selecting titanium and oxygen contents, *Journal of Physics and Chemistry of Solids*, 66 (2005) 571–575.

[79] L. Schafer, M. Schirra, K. Ehrlich, Mechanical properties of low activating martensitic 8–10% CrWVTa steels of type OPTIFER, *Journal of Nuclear Materials*, 233–237 (1996) 264–269.

[80] Binary alloy phase diagrams, edited by T.B. Massalski, ASM International, Materials Park, Ohio, 1986.

[81] R. Lindau, A. Moslang, M. Rieth, M. Klimiankou, E. Materna–Morris, A. Alamo, A.A.F. Tavassoli, C. Cayron, A.M. Lancha, P. Fernandez, N. Baluc, R. Schaublin, E. Diegele, G. Filacchioni, J.W. Rensman, B.V.D. Schaaf, E. Lucon, W. Dietz,

Present development status of EUROFER and ODS–EUROFER for application in blanket concepts, *Fusion Engineering and Design*, 75–79 (2005) 989–996.

[82] A. Alamo A, J.L. Bertin, V.K. Shamardin, P. Wident, Mechanical properties of 9Cr martensitic steels and ODS–FeCr alloys after neutron irradiation at 325 °C up to 42 dpa, *Journal of Nuclear Materials*, 367–370 (2007) 54–59.

[83] T.S. Chou, H.K.D.H. Bhadeshia, Crystallographic texture in mechanically alloyed oxide dispersion strengthened MA956 and MA957 steels, *Metallurgical and Materials Transactions A*, 24A (1993) 773–779.

[84] R.J. Kurtz, A. Alamo, E. Lucon, Q. Huang, S. Jitsukawa, A. Kimura, R.L. Klueh, G.R. Odette, C. Petersen, M.A. Sokolov, P. Spatig, J.W. Rensman, Recent progress toward development of reduced activation ferritic/martensitic steels for fusion structural applications, *Journal of Nuclear Materials*, 386–388 (2009) 411–417.

[85] S. Ukai, S. Ohtsuka, Nano–mesoscopic structure control in 9Cr–ODS ferritic steels, *Energy Materials*, 2 (2009) 26–35.

[86] T. Kaito, S. Ukai, S. Ohtsuka, T. Narita, Development of ODS ferritic steel cladding for the advanced fast reactor fuels, Proceedings of GLOBAL 2005, Tsukuba, Japan, 2005.

[87] M. Durand–Charre, Microstructure of steels and cast irons, Springer, 2004.

[88] C. Capdevila, M.K. Miller, I. Toda, J. Chao, C. Capdevila, α–α′ phase separation on the tensile properties of Fe–base ODS PM 2000 alloy, *Materials Science and Engineering A*, 527 (2010) 7931–7938.

[89] M.K. Miller, D.T. Hoelzer, E.A. Kenik, K.F. Russell, Stability of ferritic MA/ODS alloys at high temperatures, *Intermetallics*, 13 (2005) 387–392.

[90] R. Lindau, A. Moslang, M. Schirra, P. Schlossmacher, M. Klimenkov, Mechanical and microstructural properties of a hipped RAFM ODSsteel, *Journal of Nuclear Materials*, 307–311 (2002) 769–772.

[91] M. Klimenkov, R. Lindau, A. Moslang, TEM study of internal oxidation in an ODS–Eurofer alloy, *Journal of Nuclear Materials*, 386–388 (2009) 557–560.

[92] I. Monnet, P. Dubuisson, Y. Serruys, M.O. Ruault, O. Kaitasov, B. Jouffrey, Microstructural investigation of the stability under irradiation of oxide dispersion strengthened ferritic steels, *Journal of Nuclear Materials*, 335 (2004) 311–321.

[93] C. Capdevila, M.K. Miller, K.F. Russell, J. Chao, J.L. Gonzalez–Carrasco, Phase separation in PM 2000™ Fe–base ODS alloy: Experimental study at the atomic level, *Materials Science and Engineering A*, 490 (2008) 277–288.

[94] S. Ohtsuka, S. Ukai, M. Fujiwara, Nano–mesoscopic structural control in 9Cr ODS ferritic/martensitic steels, *Journal of Nuclear Materials*, 351 (2006) 241–246.

[95] J.H. Schneibel, S. Shim, Nano–scale oxide dispersoids by internal oxidation of Fe–Ti–Y intermetallics, *Materials Science and Engineering A*, 488 (2008) 134–138.

[96] P. Dou, A. Kimura, T. Okuda, M. Inoue, S. Ukai, S. Ohnuki, T. Fujisawa, F. Abe, Effects of extrusion temperature on the nano mesoscopic structure and mechanical properties of an Al alloyed high Cr ODS ferritic steel, *Journal of Nuclear Materials*, 417 (2011) 166–170.

[97] S. Ukai, T. Nishida, H. Okada, T. Okuda, M. Fujiwara, K. Asabe, Development of oxide dispersion strengthened ferritic steels for FBR core application (I), *Journal of Nuclear Science and Technology*, 34 (1997) 256–263.

[98] X. Boulnat, D. Fabregue, M. Perez, M.H. Mathon, Y. de Carlan, High temperature tensile properties of nano oxide dispersion strengthened ferritic steels produced by mechanical alloying and spark plasma sintering, *Metallurgical and Materials Transactions A*, 44 (2013) 2461–2465.

[99] S. Pasebani, I. Charit, Effect of alloying elements on the microstructure and mechanical properties of nanostructured ferritic steels produced by spark plasma sintering, *Journal of Alloys and Compounds*, 599 (2014) 206–211.

[100] J.J. Fisher, Dispersion strengthened ferritic alloy for use in liquid metal fast breeder reactors, *U.S. Patent No. 4,075,010*, 1978.

[101] S. Ukai, Microstructure and high temperature strength of 9Cr ODS ferritic steel, 2011, Ch. 14.

[102] S. Ohtsuka, S. Ukai, M. Fujiwara, T. Kaito, T. Narita, Improvement of 9Cr–ODS martensitic steel properties by controlling excess oxygen and titanium contents, *Journal of Nuclear Materials*, 329–333 (2004) 372–376.

[103] Z. Lu, R.G. Faulkner, N. Riddle, F.D. Martino, K. Yang, Effect of heat treatment on microstructure and hardness of Eurofer 97, Eurofer ODS and T92 steels, *Journal of Nuclear Materials*, 386–388 (2009) 445–488.

[104] K.D. Zilnyk, H.R.Z. Sandim, R.E. Bolmaro, R.Lindau, A. Moslang, A. Kostka, D. Raabe, Long term microstructural stability of oxide dispersion strengthened Eurofer steel annealed at 800 °C, *Journal of Nuclear Materials*, 448 (2014) 33–42.

[105] K.D. Zilnyk, V.B. Oliveira, H.R.Z. Sandim, A. Moslang, D. Raabe, Martensitic transformation in Eurofer–97 and ODS–Eurofer steels: A comparative study, *Journal of Nuclear Materials*, 462 (2015) 360–367.

[106] A. Hirata, T. Fujita, Y.R. Wen, J.H. Schneibel, C.T. Liu, M.W. Chen, Atomic structure of nanoclusters in oxide dispersion strengthened steels, *Nature Materials*, 10 (2011) 922–926.

[107] S.J. Zinkle, G.E. Ice, M.K. Miller, S.J. Pennycook, X.L. Wang, Advances in microstructural characterization, *Journal of Nuclear Materials*, 8 (2009) 386–388.

[108] M. Klimiankou, R. Lindau, A. Moslang, HRTEM Study of yttrium oxide particles in ODS steels for fusion reactor application, *Journal of Crystal Growth*, 249 (2003) 381–387.

[109] A. Ramar, N. Baluc, R. Schaublin, On the lattice coherency of oxide particles dispersed in EUROFER97, *Journal of Nuclear Materials*, 386–388 (2009) 515–519.

[110] S. Saroja, A. Dasgupta, R. Divakar, S. Raju, E. Mohandas, M. Vijayalakshmi, K. Bhanu Sankara Rao, Baldev Raj, Development and characterization of advanced 9Cr ferritic/martensitic steels for fission and fusion reactors, *Journal of Nuclear Materials*, 409 (2011) 131–139.

[111] M. Nagini, R. Vijay, M. Ramakrishna, A.V. Reddy, G. Sundararajan, Influence of the duration of high energy ball milling on the microstructure and mechanical properties of a 9Cr oxide dispersion strengthened ferritic–martensitic steel, *Materials Science and Engineering A*, 620 (2015) 490–499.

[112] M. Klimiankou, R. Lindau, A. Moslang, Energy–filtered TEM imaging and EELS study of ODS particles and Argon filled cavities in ferritic–martensitic steels, *Micron*, 36 (2005) 1–8.

[113] C.Y. Lu, Z. Lu, C.M. Liu, Microstructure of nano structured ODS CLAM steel by mechanical alloying and hot isostatic pressing, *Journal of Nuclear Materials*, 442 (2013) S148–S152.

[114] Y. Yazawa, T. Furuhara, T. Maki, Effect of matrix recrystallisation on morphology, crystallography and coarsening behavior of vanadium carbide in austenite, *Acta Materialia*, 52 (2004) 3727–3736.

[115] E.A. Marquis, Core/shell structures of oxygen–rich nanofeatures in oxide dispersion strengthened Fe–Cr alloys, *Applied Physics Letters*, 93 (2008) 181904 (1–3).

[116] M. Klimenkov, R. Lindau, A. Moslang, New insights into the structure of ODS particles in the ODS–Eurofer alloy, *Journal of Nuclear Materials*, 386–388 (2009) 553–556.

[117] A. Moslang, C. Adelhelm, R. Heidinger, Innovative materials for energy technology, *International Journal of Materials Research*, 99 (2008) 1045–1054.

[118] C.A. Williams, E.A. Marquis, A. Cerezo A, G.D.W Smith, Nanoscale characterization of ODS–Eurofer 97 steel: An atom probe tomography study, *Journal of Nuclear Materials*, 400 (2010) 37–45.

[119] A.A. Aleev, N.A. Iskandarov, M. Klimenkov, R. Lindau, A. Moslang, A.A. Nikitin, S.V. Rogozhkin, P. Vladimirov, A.G. Zaluzhnyi, Investigation of oxide particles in unirradiated ODS Eurofer by tomographic atom probe, *Journal of Nuclear Materials*, 409 (2011) 65–71.

[120] M. Ohnuma, J. Suzuki, S. Ohtsuka, S.W. Kim, T. Kaito, M. Inoue, H. Kitazawa, A new method for the quantitative analysis of the scale and composition of nano–sized oxide in 9Cr–ODS steel, *Acta Materialia*, 57 (2009) 5571–5581.

[121] M.H. Mathon, M. Perrut, S.Y. Zhong, Y.de Carlan, Small angle neutron scattering study of martensitic/ferritic ODS alloys, *Journal of Nuclear Materials*, 428 (2012) 147–153

[122] T. Narita, S.Ukai, S. Ohtsuka, M. Inoue, Effect of tungsten addition on microstructure and high temperature strength of 9CrODS ferritic steel , *Journal of Nuclear Materials*, 417 (2011) 158–161.

[123] Y. Li, T. Nagasaka, T. Muroga, A. Kimura, S. Ukai, High temperature mechanical properties and microstructure of 9Cr oxide dispersion strengthened steel compared with RAFMs, *Fusion Engineering and Design*, 86 (2011) 2495–2499.

[124] H. Sakasegawa, S. Ohtsuka, S. Ukai, H. Tanigawa, M. Fujiwara, H. Ogiwara, A. Kohyama, Particle size effects in mechanically alloyed 9Cr ODS steel powder, *Journal of Nuclear Materials*, 367–370 (2007) 185–190.

[125] S. Ukai, S.Ohtsuka, T.Kaito, H. Sakasegawa, N. Chikata, S. Hayashi, S. Ohnuki, High temperature strength characterization of advanced 9Cr–ODS ferritic steels, *Materials Science and Engineering A*, 510–511 (2009) 115–120.

[126] R. Schaeublin, T. Leguey, P. Spatig, N. Baluc, M. Victoria, Microstructure and mechanical properties of two ODS ferritic/martensitic steels, *Journal of Nuclear Materials*, 307–311 (2002) 778–782.

[127] K. Lambrinou, V. Koch, G. Coen, J. Van den Bosch, C. Schroer, **C**orrosion scales on various steels after exposure to liquid lead–bismuth eutectic, *Journal of Nuclear Materials*, 450 (2014) 244–255.

[128] S. Takaya, T. Furukawa, G. Muller , A. Heinzel, A. Jianu, A. Weisenburger, K. Aoto, M. Inoue, T. Okuda, F. Abe, S. Ohnuki, T. Fujisawa, A. Kimura, Al–containing ODS steels with improved corrosion resistance to liquid lead–bismuth, *Journal of Nuclear Materials*, 428 (2012) 125–130.

[129] O. Yeliseyeva, V. Tsisar, Z. Zhou, Corrosion behavior of Fe–14Cr–2W and Fe–9Cr–2W ODS steels in stagnant liquid pb with different oxygen concentration at 550 and 650 °C, *Journal of Nuclear Materials*, 442 (2013) 434–443.

[130] T. Furukawa, S. Kato, E. Yoshida, Compatibility of FBR materials with sodium, *Journal of Nuclear Materials*, 392 (2009) 249–254.

[131] E. Yoshida, S. Kato, Sodium compatibility of ODS steel at elevated temperature, *Journal of Nuclear Materials*, 329–333 (2004)1393–1397.

[132] S. Ningshen, M. Sakairi, K. Suzuki, S. Ukai, Corrosion resistance of 9% Cr oxide dispersion strengthened steel in different electrolytic media, *Corrosion*, 69 (2013) 863–874.

[133] M. Terada, A.J.O. Zimmermann, H.R.Z. Sandim, I. Costa, A.F. Padilha, Corrosion behavior of Eurofer 97 and ODS–Eurofer alloys compared to traditional stainless steels, *Journal of Applied Electrochemistry*, 41 (2011) 951–959.

[134] Y. Chen, K. Sridharan, T.R. Allen, S. Ukai, Microstructural examination of oxide layers formed on an oxide dispersion strengthened ferritic steel exposed to supercritical water, *Journal of Nuclear Materials*, 359 (2006) 50–58.

[135] J. Bischoff, A.T. Motta, Oxidation behavior of ferritic–martensitic and ODS steels in supercritical water, *Journal of Nuclear Materials*, 424 (2012) 261–276.

[136] O.I. Yaskiv, V.M. Fedirko, Oxidation/corrosion behaviour of ODS ferritic/martensitic steels in Pb melt at elevated temperature, *International Journal of Nuclear Energy*, 2014 (2014)1–8.

[137] T. Kaito, T. Narita, S. Ukai, Y. Matsuda, High temperature oxidation behavior of ODS steels, *Journal of Nuclear Materials*, 329–333 (2004) 1388–1392.

[138] J.S. Lee, C.H. Jang, I.S. Kim, A. Kimura, Embrittlement and hardening during thermal aging of high Cr oxide dispersion strengthened alloys, *Journal of Nuclear Materials*, 367–370 (2007) 229–233.

[139] S. Ukai, T. Nishida, T. Okuda, T. Yoshitake, R&D of oxide dispersion strengthened ferritic martensitic steels for FBR, *Journal of Nuclear Materials*, 258–263 (1998) 1745–1749.

[140] S. Yamashita, N. Akasaka, S. Ukai, S. Ohnuki, Microstructural development of a heavily neutron irradiated ODS ferritic steel (MA957) at elevated temperature, *Journal of Nuclear Materials*, 367–370 (2007) 202–207.

[141] K. Yutani, H. Kishimoto, R. Kasada, A. Kimura, Evaluation of Helium effects on swelling behavior of oxide dispersion strengthened ferritic steels under ion irradiation, *Journal of Nuclear Materials*, 367–370 (2007) 423–427.

[142] J. Bottcher, S. Ukai, M. Inoue, ODS steel clad MOX fuel pin fabrication and irradiation performance in EBR–II, *Nuclear Technology*, 138 (2002) 238–245.

[143] S. Ukai, T. Kaito, M. Seki, A. Mayorshin, O. Shishalov, Oxide dispersion strengthened (ODS) fuel pins for BOR–60 irradiation test, *Journal of Nuclear Science and Technology*, 42 (2005)109–122.

[144] C. Capdevila, H.K.D.H. Bhadeshia, Manufacturing and microstructural evolution of mechanically alloyed oxide dispersion strengthened superalloys, *Advanced Engineering Materials*, 3 (2001) 647–656.

[145] H. Sakasegawa, L. Chaffron, F. Legendre, L. Boulanger, T. Cozzika, M. Brocq, Y. de Carlan, Correlation between chemical composition and size of very small oxide particles in the MA957 ODS ferritic alloy, *Journal of Nuclear Materials*, 384 (2009) 115–118.

[146] Y. Wu, E.M. Haney, N.J. Cunningham, G.R. Odette, Transmission electron microscopy characterization of the nanofeatures in nanostructured ferritic alloy MA957, *Acta Materialia*, 60 (2012) 3456–3468.

[147] J. Ribis, Y. de Carlan, Interfacial strained structure and orientation relationships of the nanosized oxide particles deduced from elasticity driven morphology in oxide dispersion strengthened materials, *Acta Materialia*, 60 (2012) 238–252.

[148] M.C. Brandes, L. Kovarik, M.K. Miller, M.J. Mills, Morphology, structure and chemistry of nanoclusters in a mechanically alloyed nanostructured ferritic steel, *Journal of Materials Science*, 47 (2012) 3913–3923.

[149] D. Bhattacharyya, P. Dickerson, S.A. Maloy, M. Misra, M.A. Nastasi, G.R. Odette, On the structure and chemistry of complex oxide nanofeatures in nanostructured ferritic alloy U14YWT (2011), DOE/ER–0313/50.

[150] M.K. Miller, E.A. Kenik, K.F. Russell, L. Heatherly, D.T. Hoelzer, P.J. Maziasz, Atom probe tomography of nanoscale particles in ODS ferritic alloys, *Materials Science and Engineering A*, 353 (2003) 140–145.

[151] M.K. Miller, K.F. Russell, D.T. Hoelzer, Characterization of precipitates in MA/ODS ferritic alloys, *Journal of Nuclear Materials*, 351 (2006) 261–268.

[152] M.K. Miller, D.T. Hoelzer, E.A. Kenik, K.F. Russell, Nanometer scale precipitation in ferritic MA/ODS alloy MA957, *Journal of Nuclear Materials*, 329–333 (2004) 338–341.

[153] H. Sakasegawa, F. Legendre, L. Boulanger, M. Brocq, L. Chaffron, T. Cozzika, Stability of non stoichiometric clusters in the MA957 ODS ferrtic alloy, *Journal of Nuclear Materials*, 417 (2011) 229–232.

[154] S. Lozano–Perez, V. de Castro Bernal, R.J. Nicholls, Achieving sub–nanometre particle mapping with energy–filtered TEM, *Ultramicroscopy*, 109 (2009) 1217–1228.

[155] V. de Castro, E.A. Marquis, S. Lozano–Perez, R. Pareja, M.L. Jenkins, Stability of nanoscale secondary phases in an oxide dispersion strengthened Fe–12Cr alloy, *Acta Materialia*, 59 (2011) 3927–3936.

[156] M.J. Alinger, G.R. Odette, D.T. Hoelzer, The development and stability of Y–Ti–O nanoclusters in mechanically alloyed Fe–Cr based ferritic alloys, *Journal of Nuclear Materials*, 329–333 (2004) 382–386.

[157] M.J. Alinger, On the formation and stability of nanometre scale precipitates in ferritic alloys during processing and high temperature service, ISBN: 9780496034932. Santa Barbara, University of California, 2004.

[158] C.A. Williams, P. Unifantowicz, N. Baluc, G.D.W. Smith, E.A. Marquis, The formation and evolution of oxide particles in oxide dispersion strengthened ferritic steels during processing, *Acta Materialia*, 61 (2013) 2219–2235.

[159] P. Olier, J. Malaplate, M.H. Mathon, D. Nunes, D. Hamon, L. Toualbi, Y. de Carlan, L. Chaffron, Chemical and microstructural evolution on ODS Fe–14CrWTi steel during manufacturing stages, *Journal of Nuclear Materials*, 428 (2012) 40–46.

[160] J. Ribis, M.L. Lescoat, S.Y. Zhong, M.H. Mathon, Y. de Carlan, Influence of the low interfacial density energy on the coarsening resistivity of the nano oxide particles in Ti–added ODS material, *Journal of Nuclear Materials*, 442 (2013) S101–S105.

[161] Z. Oksiuta, M. Lewandowska, K.J. Kurzydłowski, Mechanical properties and thermal stability of nanostructured ODS RAF steels, *Mechanics of Materials*, 67 (2013) 15–24.

[162] J.H. Kim, T.S Byun, D.T. Hoelzer, C.H. Park, J.T. Yeom, J.K. Hong, Temperature dependence of strengthening mechanisms in the nanostructured ferritic alloy 14YWT: Part II–Mechanistic models and predictions, *Materials Science & Engineering A*, 559 (2013) 111–118.

[163] A. Steckmeyer, M. Praud, B. Fournier, J. Malaplate, J. Garnier, J.L. Bechade, I. Tournie, A. Tancray, A. Bougault, P. Bonnaillie, Tensile properties and deformation mechanisms of a 14Cr ODS ferritic steel, *Journal of Nuclear Materials* 405 (2010) 95–100.

[164] R. Rahmanifard, H. Farhangi, A.J. Novinrooz, S. Moniri, Development of a high strength ultrafine grained ferritic steel nanocomposite, *Metallurgical and Materials Transactions A*, 44A (2013) 990–998.

[165] J.P. Glatz, Spent fuel dissolution and reprocessing processes, *Comprehensive Nuclear Materials*, 5 (2012) 345–366.

[166] Baldev Raj, U. Kamachi Mudali, Materials development and corrosion problems in nuclear fuel reprocessing plants, *Progress in Nuclear Energy*, 48 (2006) 283–313.

[167] S. Ningshen, M. Sakairi, K. Suzuki, S. Ukai, The passive film characterization and anodic polarization behavior of 11% Cr ferritic/martensitic and 15% Cr oxide dispersion strengthened steels in different electrolytic solutions, *Applied Surface Science*, 274 (2013) 345–355.

[168] M. Sakairi, S. Ningshen, K. Suzuki K, and S. Ukai, Corrosion study and passive film characterization of 11% Cr F/M and 15% Cr ODS steels, *Journal of Civil Engineering and Architecture*, 7 (2013) 940–955.

[169] S. Ningshen, M. Sakairi, K. Suzuki, and S. Ukai, The surface characterization and corrosion resistance of 11% Cr ferritic/martensitic and 9%–15% Cr ODS steels for nuclear fuel reprocessing application, *Journal of Solid State Electrochemistry*, 8 (2014) 411–425.

[170] S. Ningshen, M. Sakairi, K. Suzuki, and S.Ukai, The corrosion resistance and passive film compositions of 12% Cr and 15% Cr oxide dispersion strengthened steels in nitric acid media, *Corrosion Science*, 78 (2014) 322–334.

[171] J.H. Kim, K.M. Kim, T.S Byun, D.W. Lee, C.H. Park, High temperature oxidation behavior of nano structured ferritic oxide dispersion strengthened alloys, *Thermochemica Acta*, 579 (2014) 1–8.

[172] Z. Oksiuta, High temperature oxidation resistance of ultrafine–grained 14 %Cr ODS ferritic steel, *Journal of Materials Science*, 48 (2013) 4801–4805.

[173] L. Hsiung, M. Fluss, S. Tumey, J. Kuntz, B. El–Dasher, M. Wall, B. Choi, A. Kimura, F. Willaime, Y. Serruys, HRTEM study of oxide nanoparticles in K3–ODS ferritic steel developed for radiation tolerance, *Journal of Nuclear Materials*, 409 (2011) 72–79.

[174] L.L. Hsiung, M.J. Fluss, S.J. Tumey, B.W. Choi, Y. Serruys, F. Willaime, A. Kimura, Formation mechanism and the role of nanoparticles in Fe–Cr ODS steels developed for radiation tolerance, *Physical Review B*, 82 (2010) 184103.

[175] L.L. Hsiung, M.J. Fluss, A. Kimura, Structure of oxide nanoparticles in Fe–16Cr MA/ODS ferritic steel, *Materials Letters*, 64 (2010) 1782–1785.

[176] P. Dou, A. Kimura, T. Okuda, M. Inoue, S. Ukai, S. Ohnuki, T. Fujisawa, F. Abe, Polymorphic and coherency transition of Y–Al complex oxide particles with extrusion temperature in an Al–alloyed high–Cr oxide dispersion strengthened ferritic steel, *Acta Materialia*, 59 (2011) 992–1002.

[177] Y.P. Xia, X.P. Wang, Z. Zhuang, Q.X. Sun, T. Zhang, Q.F. Fang , T. Hao, C.S. Liu, Microstructure and oxidation properties of 16Cr–5Al–ODS steel prepared by sol–gel and spark plasma sintering methods, *Journal of Nuclear Materials*, 432 (2013) 198–204.

[178] M. Ratti, D. Leuvrey, M.H. Mathon, Y. de Carlan, Influence of titanium on nano–cluster (Y, Ti, O) stability in ODS ferritic materials, *Journal of Nuclear Materials*, 386–388 (2009) 540–543.

[179] C. Cayron, A. Montani, D. Venet, Y. de Carlan, Identification of new phases in annealed Fe–18CrWTi ODS powders, *Journal of Nuclear Materials*, 399 (2010) 219–224.

[180] Y. de Carlan, J.L. Bechade, P. Dubuisson, J.L Seran, P. Billot, A. Bougault, T. Cozzika, S. Doriot, D. Hamon, J. Henry, M. Ratti, N. Lochet, D. Nunes, P. Olier, T. Leblond, M.H. Mathon, CEA developments of new ferritic ODS alloys for nuclear applications, *Journal of Nuclear Materials*, 386–388 (2009) 430–432.

[181] J.L. Bechade, D. Menut, M.L. Lescoat, B. Sitaud , S. Schlutig , P.L. Solari, I. Llorens, H. Hermange, Y. de Carlan, J. Ribis, L. Toualbi, Application of synchrotron radiation to analyze the precipitation in ODS materials before irradiation in Fe–9%Cr single grain of powder and consolidated Fe–18%Cr, *Journal of Nuclear Materials*, 428 (2012) 183–191.

[182] P. Dubuisson, Y. de Carlan, V. Garat, M. Blat, ODS Ferritic/martensitic alloys for sodium fast reactor fuel pin cladding, *Journal of Nuclear Materials*, 428 (2012) 6–12.

[183] M.L. Lescoat, J. Ribis, A. Gentils, O. Kaitasov, Y. de Carlan, A. Legris, In situ TEM study of the stability of nano oxides in ODS steels under ion–irradiation, *Journal of Nuclear Materials*, 428 (2012) 176–182.

[184] J. Ribis, M.L. Lescoat, Y. de Carlan, J.M. Costantini, I. Monnet, T. Cozzika, F. Delabrouille, J. Malaplate, Stability of nano oxides upon heavy ion irradiation of an ODS material, *Journal of Nuclear Materials*, 417 (2011) 262–265.

[185] M.H. Mathon, M. Perrut, L. Poirier, M. Ratti, N. Herve, Y. de Carlan, Development of new ferritic alloys reinforced by nano titanium nitrides, *Journal of Nuclear Materials*, 456 (2015) 449–454.

[186] J.H. Lee, J.H. Kim, Characterization of oxide nanoparticles in Al–Free and Al–containing oxide dispersion strengthened ferritic steels, *Journal of Nanoscience and Nanotechnology*, 13 (2013) 6169–6173.

[187] J. Isselin, R. Kasada, A. Kimura, Effects of aluminum on the corrosion behavior of 16% Cr ODS ferritic steels in a nitric acid solution, *Journal of Nuclear Science and Technology*, 48 (2010) 169–171.

[188] A. Kimura, H. Cho, N. Toda, R. Kasada, H. Kishimoto, N. Iwata, S. Ukai, S. Ohtsuka, M. Fujiwara, Super ODS Steels R&D for Cladding of Highly Efficient Nuclear Plants, in: Proceedings of the International Congress on Advances in Nuclear Power Plants (ICAPP–2007), 2007, 7374.

[189] A.L. Rouffie, J. Crepin, M. Sennour, B. Tanguy, A. Pineau, D. Hamon, P. Wident, S. Vincent, V. Garat, B. Fournier, Effect of the thermal ageing on the tensile and impact properties of a 18% Cr ferritic steel, *Journal of Nuclear Materials*, 445 (2014) 37–42.

[190] B. Fournier, A. Steckmeyer, A.L. Rouffie, J. Malaplate, J. Garnier, M. Ratti, P. Wident, L. Ziolek, I. Tournie, V. Rabeau, J.M. Gentzbittel, T. Kruml, I. Kubena, Mechanical behaviour of ferritic ODS steels–Temperature dependency and anisotropy, *Journal of Nuclear Materials*, 430 (2012) 142–149.

[191] S. Li, Z. Zhou, M. Li, M. Wang, G. Zhang, Microstructure characterization and tensile properties of 18Cr–4Al oxide dispersion strengthened ferritic steel, *Journal of Alloys and Compounds*, 648 (2015) 39–45.

[192] S. Li, Z. Zhou, J. Jang, M. Wang, H. Hu, H. Sun, L. Zou, G. Zhang, L. Zhang, The influence of Cr content on the mechanical properties of ODS ferritic steels, *Journal of Nuclear Materials*, 455 (2014) 194–200.

[193] H. Hadraba, B. Fournier, L. Stratil, J. Malaplate, A.L. Rouffie, P. Wident, L. Ziolek, J.L. Bechade, Influence of microstructure on impact properties of 9–18%Cr ODS steels for fusion/fission applications, *Journal of Nuclear Materials*, 411 (2011) 112–118.

[194] H. Hu, Z. Zhou, M. Li, L. Zhang, M. Wang, S. Li, C. Ge, Study of the corrosion behavior of a 18Cr–oxide dispersion strengthened steel in supercritical water, *Corrosion Science*, 65 (2012) 209–213.

[195] J.H. Lee, R. Kasada, A. Kimura, T. Okuda, M. Inoue, S. Ukai, S. Ohnuki, T. Fujisawa, F. Abe, Influence of alloy composition and temperature on corrosion behavior of ODS ferritic steels, *Journal of Nuclear Materials*, 417 (2011) 1225–1228.

[196] V de Castro, T. Leguey, M.A. Monge, M. Munoz, R. Pareja, D.R. Amador, J.M. Torralba, M. Victoria, Mechanical dispersion of Y_2O_3 nanoparticles in steel EUROFER 97: process and optimisation, *Journal of Nuclear Materials*, 322 (2003) 228–234.

[197] S.W. Kim, T. Shobu, S. Ohtsuka, T. Kaito, M. Inoue, M. Ohnuma, Kinetic approach for growth and coalescence of nano–size oxide particles in ODS–9Cr steel using high energy synchrotron radiation X–rays in Spring–8, *Materials Transactions*, 50 (2009) 917–921.

[198] I. Hilger, M. Tegel, M.J. Gorley, P.S. Grant, T. Weissgarber, B. Kieback, The structural changes of Y_2O_3 in ferritic alloys during milling, *Journal of Nuclear Materials*, 447 (2014) 242–247.

[199] L. Dai, Y. Liu, Z. Ma, Z. Dong, L.Yu, Microstructural evolution of oxide dispersion strengthened Fe–Cr model steels during mechanical milling and subsequent hot pressing, *Journal of Materials Science*, 48 (2013) 1826–1836.

[200] A. Ramar, Z. Oksiuta, N. Baluc, R. Schaublin, Effect of mechanical alloying on the mechanical and microstructural properties of ODS EUROFER 97, *Fusion Engeening Design*, 82 (2007) 2543–2549.

[201] M.J. Alinger, S.C. Glade, B.D. Wirth, G.R. Odette, T. Toyama, Y. Nagai Y, M. Hasegawa, Positron annihilation characterization of nanostructured ferritic alloys, *Materials Science & Engineering A*, 518 (2009) 150–157.

[202] D. Larson, P. Maziasz, I.S Kim, K. Miyahara, Three–dimensional atom probe observation of nanoscale titanium–oxygen clustering in an oxide dispersion strengthened Fe–12Cr–3W–0.4Ti+Y_2O_3 ferritic alloy, *Scripta Materialia*, 44 (2001) 359–364.

[203] T. Okuda, M. Fujiwara, Dispersion behavior of oxide particles in mechanically alloyed ODS Steel, *Journal of Materials Science Letters*, 14 (1995) 1600–1603.

[204] S. Yamashita, S. Ohtsuka, N. Akasaka, S. Ukai, S. Ohnuki, Formation of nanoscale complex oxide particles in mechanically alloyed ferritic steel, *Philosophical Magazine Letters*, 84 (2004) 525.

[205] R. Vijay, M. Nagini, J. Joardar, M. Ramakrishna, A.V. Reddy, G. Sundararajan, Strengthening mechanisms in mechanically milled oxide dispersed iron powders, *Metallurgical and Materials Transactions A*, 44A (2013) 1611–1620.

[206] M. Brocq, B. Radiguet, S. Poissonnet, F. Cuvilly, P. Pareige, F. Legendre, Nanoscale characterization and formation mechanism of nanoclusters in an ODS steel elaborated by reactive inspired ball milling and annealing, *Journal of Nuclear Materials*, 409 (2011) 80–85.

[207] D.T. Hoelzer, J. Bentley, M.A. Sokolov, M.K. Miller, G.R. Odette, M.J. Alinger, Influence of particle dispersions on the high–temperature strength of ferritic alloys, *Journal of Nuclear Materials*, 367–370 (2007) 166–172.

[208] P. Unifantowicz, Z. Oksiuta, P. Olier, Y. de Carlan, N. Baluc, Microstructure and mechanical properties of an ODS RAF steel fabricated by hot extrusion or hot isostatic pressing, *Fusion Engineering and Design*, 86 (2011) 2413–2416.

[209] Z. Oksiuta, A. Ozieblo, K. Perkowski, M. Osuchowsk, M. Lewandowska, Influence of HIP pressure on tensile properties of a 14Cr ODS ferritic steel, *Fusion Engineering and Design*, 89 (2014) 137–141.

[210] B. Dousti, R. Mojaver, H.R. Shahverdi, R.S. Mamoory, Microstructural evolution and chemical redistribution in Fe–Cr–W–Ti–Y_2O_3 nanostructured powders prepared by ball milling, *Journal of Alloys and Compounds*, 577 (2013) 409–416.

[211] Abhishek Pandey, K. Jayasankar, P. Parida, M. Debata, B.K. Mishra, S. Saroja, Optimization of milling parameters, processing and characterization of nano–crystalline oxide dispersion strengthened ferritic steel, *Powder technology*, 262 (2014) 162–169.

[212] M.A. Auger, V. de Castro, T. Leguey, M.A. Monge, A. Munoz, R. Pareja, Microstructure and tensile properties of oxide dispersion strengthened Fe–14Cr–0.3Y_2O_3 and Fe–14Cr–2W–0.3Ti–0.3Y_2O_3, *Journal of Nuclear Materials*, 442 (2013) S142–S147.

CHAPTER 3
EXPERIMENTAL DETAILS

3.1 Introduction

This chapter presents various experimental conditions used to produce oxide dispersion strengthened (ODS)–18Cr ferritic steels and different characterization techniques employed to evaluate these materials. Powder metallurgy (P/M) technique was employed to produce ODS–18Cr ferritic steels. The dispersion of Y_2O_3 in 18Cr ferritic steels was achieved by mechanical alloying (MA) and consolidation of these ODS steels involved processes like canning, degassing and hot extrusion. The parameters used for these processes including MA play an important role in the determining the final properties like density, hardness and strength of the consolidated ODS–18Cr ferritic steels. Microstructural and mechanical property characterizations were carried out by X–ray diffraction, scanning electron microscopy and transmission electron microscopy, vickers hardness testing (micro and macro) and universal testing machine. Electrochemical corrosion and high temperature oxidation experiments were also carried out. In the following sections, the details of each process are described.

3.2 Raw materials

In the present study, raw materials used for manufacturing the ODS–18Cr ferritic steel were argon gas atomized iron based pre–alloyed steel powder with a nominal composition by weight percent of Fe–18Cr–2.33W–0.34Ti and 0.35 % nano yttria powder. The pre–alloyed steel powder with 99.95 % purity and having an average particle size of 100 µm produced at M/s ARCI, India by inert gas atomization. Yttrium oxide (Y_2O_3) nano powder (purity: 99.95 %, particle size: 30–50 nm) was supplied by M/s Inframat Advanced Materials, USA. SEM image of pre–alloyed 18Cr steel powder produced by argon gas atomization is shown in Fig 3.1 (a). The chemical composition of atomized pre–alloyed 18Cr steel powder is given in Table 3.1. The sieve analysis of the powder is presented in Table 3.2. The powder particles are spherical and the size variation is observed. The TEM image of as received nano yttria powder is shown in Fig. 3.1 (b). The Y_2O_3 powder constituted of small crystallites with an average size of 40 nm. The particles of as received nano yttria are in the range of 30–50 nm.

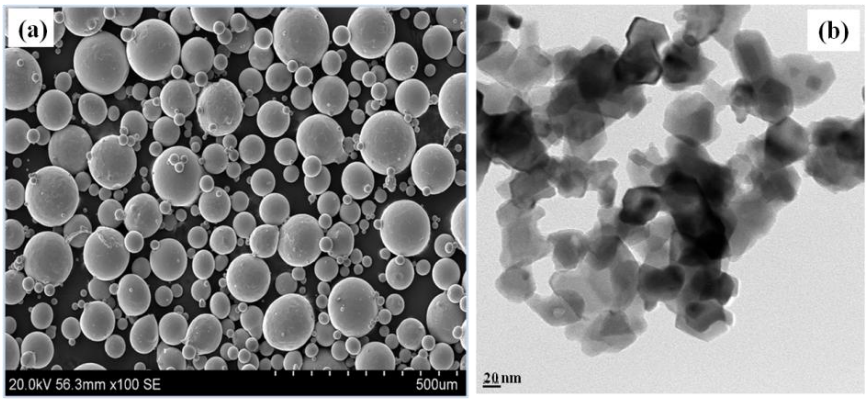

Fig. 3.1 Powder morphologies: (a) SEM image of pre–alloyed 18Cr steel powder produced by inert gas atomization and (b) TEM image of nano yttria powder

Table 3.1 Chemical composition of the as received atomized steel powder.

Sample/Composition (wt. %)	Fe	Cr	W	Ti	Mn	Al	P	C	O	N
Pre–alloyed powder	bal.	17.8	2.33	0.34	0.014	0.016	0.008	<0.03	0.006	0.003

Table 3.2 Sieve analysis of pre–alloyed 18Cr steel powder.

Size fraction [µm]	Weight [%]
–150+106	30.8
–106+75	25.1
–75+44	27.4
–44	16.7

The basic chemical composition of ODS–18Cr ferritic steel was designed through a combination of basic thermodynamic principles as well as experience gained from the prior research efforts. In the present work, the main aim is to produce an alloy suitable for fast breeder clad tube applications subjected to elevated temperatures and intense irradiation. In the development of ODS–18Cr ferritic steels, the body centered cubic (BCC) ferritic crystal structure must be preserved to reduce the void swelling under neutron irradiation. This implies that austenitic stabilizers (carbon and nitrogen) must be omitted or minimized to the least levels. As corrosion resistance (against Na) is a primary concern in this alloy, hence Cr content of 18 % is adequate to ensure the fully ferritic structure with good corrosion and oxidation resistance. The quantity of 0.35 % yttria was added to achieve the desired nano–sized complex oxide dispersoids. 0.34 % Ti was also added to produce a fine distribution of nano–sized complex oxides. The quantity of 2.33

% W was added in the matrix for the purpose of solid solution strengthening. The process flow sheet for manufacturing the ODS–18Cr steel is shown in Fig. 3.2.

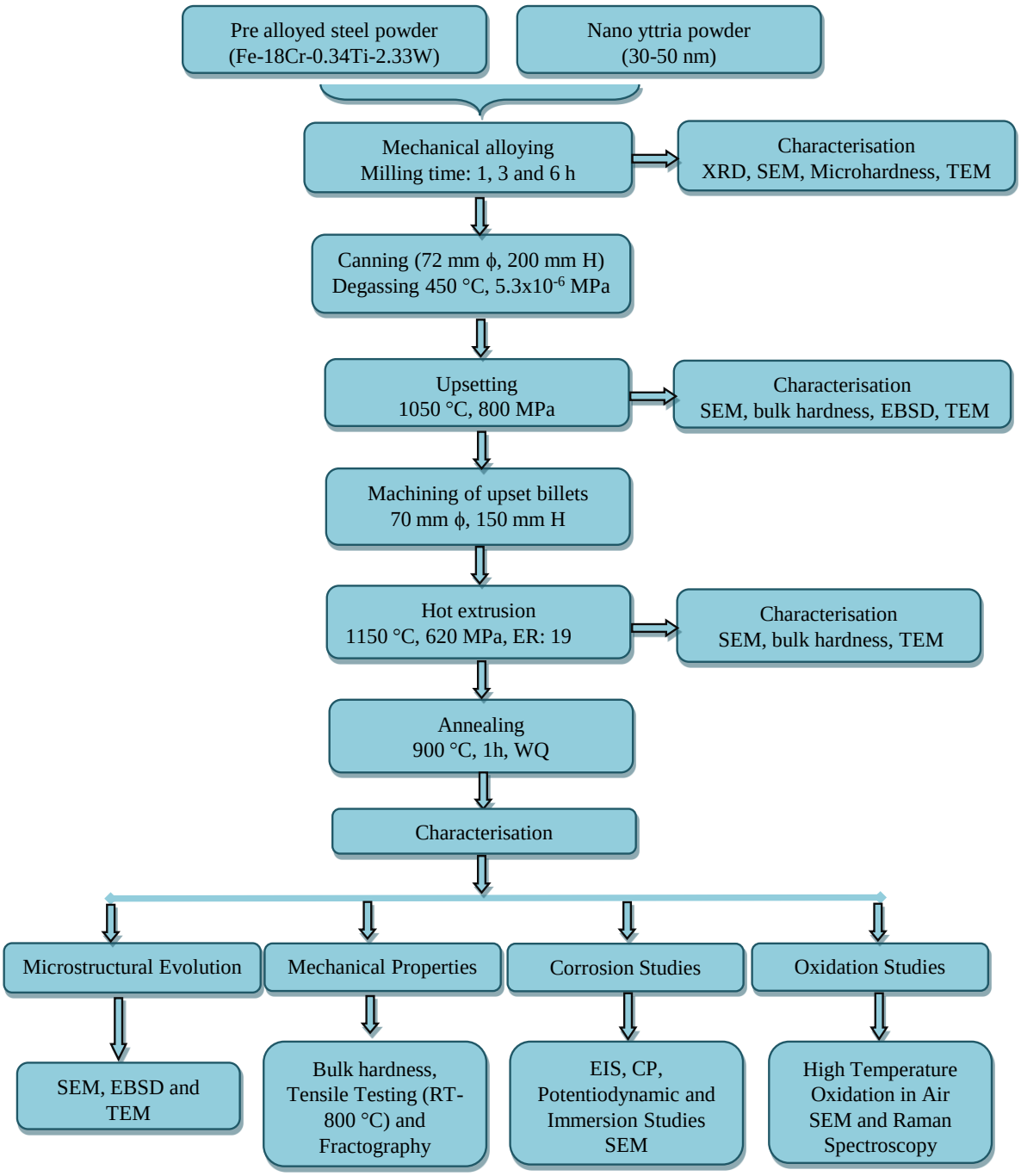

Fig. 3.2 Process flow sheet for the manufacturing the ODS–18Cr ferritic steel.

3.3 High energy horizontal attritor milling (Simoloyer technology)

In the present work, MA of the pre–alloyed 18Cr steel powder with and without nano yttria was carried out in a horizontal attrition mill (Simoloyer CM–20, Zoz GmbH, Germany). The high energy horizontal attritor mill is an advanced device based on simoloyer technology and is widely used for MA, reactive and high energy milling in research as well as in industrial applications [1]. Simoloyer CM–20 consists of fixed double walled horizontal vial, hardened 100Cr6 steel balls of diameter 5 mm, high speed rotor with fourteen arms that promote balls motion and cooling system. Simoloyer CM–20 is connected to computer with Maltoz software for system operation, system control and partially controls the process. The high performance system control allows computer protection of the device, controllable process temperature, full record of milling history and milling power. The processing principle of simoloyer is high and homogeneous kinetic energy transfer to the powder particles by collisions of balls. During milling, the energy which is transferred from the balls to the powder controls the kinetics of alloying and other phase transformations induced during MA. The high kinetic energy process in these mills is due to the collisions of the grinding media instead of shear and friction interactions [1]. It allows processing without negative gravity influence and dead zones. The energy transfer is governed by many parameters.

3.3.1 Process variables

Milling time

Milling time is the most important parameter. Usually, milling time is chosen in order to attain a steady state between the cold welding and fracturing of the powder particles. The time required depends on the many factors, such as, type of mill used, ball–to–powder ratio, milling intensity and milling temperature. If the milling of the powder is carried out for longer times than required, not only the contamination levels increase but some undesirable phases also form. In Simoloyer CM–20, 6 h is the optimal milling time for the fabrication of ODS–18Cr ferritic steels.

Milling speed

Higher rotational speed of the mill results in the high energy input to the powder particles. The powder refining process is often hindered by the increased temperature due to high milling speed. This mill (Simoloyer) generates the highest relative velocity of grinding media (>14 m/s, three times higher than the conventional devices), results in shorter

processing times because of high kinetic energy supply to the powder particles and lower contamination levels of the processed powders than the other ball mills. In the present case, Simoloyer mill was operated by rotation cycles with each cycle includes 300 rpm for 1 min and 500 rpm for 4 min (total cycle time of 5 min) until the desired milling time was reached.

Charge ratio

Charge ratio is an essential variable in milling procedure which can be also called as the ratio of the weight of ball to powder (BPR). The time required for achieving a particular phase in the milled powder, BPR has a major effect. Hence, the higher the BPR, the time required for milling is shorter. Due to the impact forces exerted on powder particles, alloying occurs between the powder particles. Too dense packing of balls decreases the mean free path of the ball, while loose packing minimizes the collision frequency. The availability of free space for free movement of the balls after any impact is performed by a total filling of 40 % and below [2]. In the present case, BPR of 7.5:1 was maintained for all the milling operations. Quantity of the powder used for each run was 4 kg.

Milling atmosphere

The major effect of the milling atmosphere is on the contamination of the powder. Prior to milling, the atmosphere inside the container was evacuated and filled with argon gas to prevent contamination during milling and all the powder handling was carried out in a glove box under protective argon atmosphere to avoid oxygen pickup.

The photographs of Simoloyer CM–20 with the principle of powder flow during processing in a Simoloyer and schematic of milling container are shown in Fig. 3.3 (a–c) respectively.

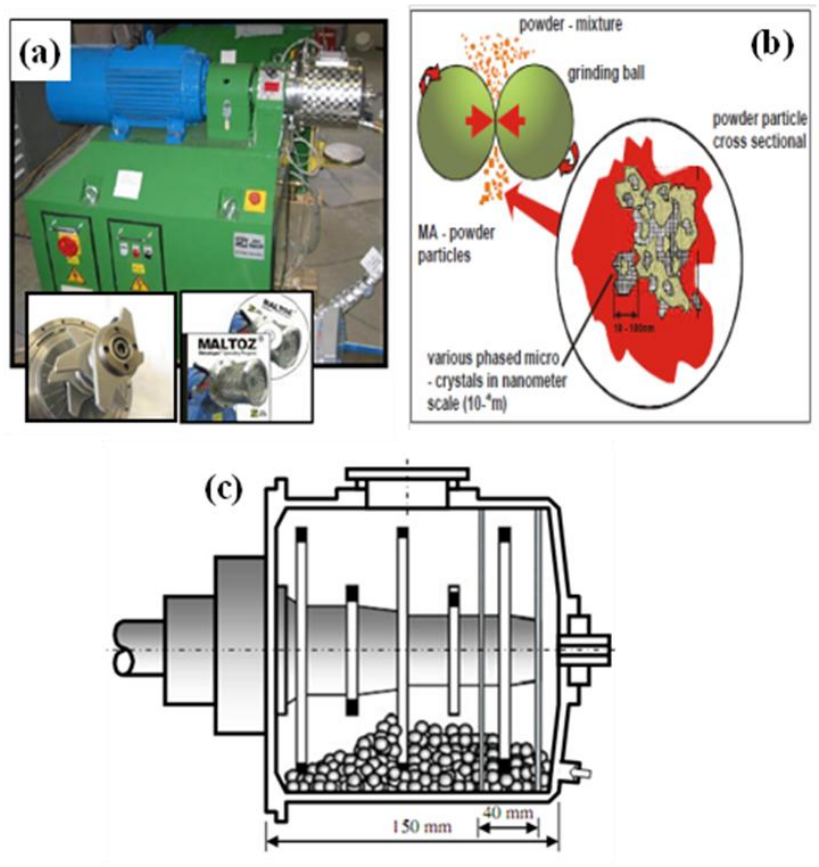

Fig. 3.3 (a) Photograph of Simoloyer CM–20, (b) with powder flow and (c) schematic of the milling container.

3.4 Consolidation of milled powder

As the milled powder contains strain, it is difficult to achieve good density (>90 %) by conventional compaction and sintering. In order to achieve the required density, hot consolidation techniques like hot extrusion (HE) or hot isostatic pressing (HIP) are employed to consolidate the milled powder. HE was selected in the present work. The procedure for the HE of milled powder is to fill the powder in a hollow can, degas the powder, seal the can and compact the sealed can to get billet. This billet is used for extrusion. Degassing temperature and evacuation time are the important parameters to get good density in the extruded rod. Cans of 72 mm ϕ and 200 mm height were used for consolidation of milled powder.

3.4.1 Leak check

The cans were tested for leaks before filling with milled powder. The cans were cleaned by ultrasonic cleaning with acetone for removing the oxide layer on the surface of the

cans. The cans were dried and checked for leaks by connecting to vacuum pumping system using acetone. The photograph of sealed cans is shown in Fig. 3.4 (a).

3.4.2 Powder filling in cans

The can was fixed to a pneumatic vibrator and the powder was poured into the can under vibration to achieve good packing of powder in the can almost reach the tap density of the powder. About 2.8 kg of milled powder was filled in each can with the above mentioned dimensions. After powder filling, a 44–micron sieve stainless steel cloth was pushed down to the powder level to avoid powder getting into the vacuum system while degassing. The photograph of powder filling equipment is shown in Fig. 3.4 (b).

3.4.3 Canning and degassing

Prior to HE, degassing of powder filled cans is essential to make sure that the cans are free off air pockets and adsorbed gases from the powder particles to promote densification. If the adsorbed gases are not removed, there will be pressure build–up in cans during heating for consolidation leading to poor densification and even bursting. The powder filled cans were connected to diffusion vacuum pumping system and heated in a furnace to 450 °C. The vacuum pump was continued to run till a steady state vacuum of 5.3×10^{-6} kPa reached. At this stage the cans were crimped and sealed with tungsten inert gas welding. The photographs of vacuum pumping system and degassing furnace are shown in Fig. 3.4 (c, d). The sealed cans were tested for any seal leaks by a non destructive testing method with dye penetrate test using developer, cleaner and penetrator. The photograph of sealed cans is shown in Fig. 3.4 (e).

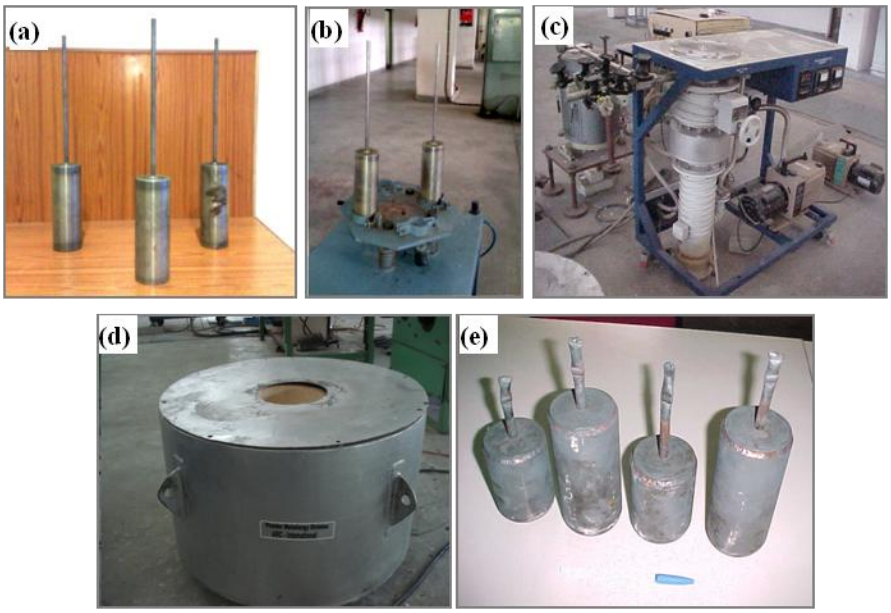

Fig. 3.4 Photographs of (a) mild steel cans, (b) powder feeding equipment, (c) vacuum pumping system, (d) degassing furnace and (e) sealed cans.

3.4.4 Upset forging and extrusion

The sealed cans were upset forged at 1050 °C and at a pressure of 800 MPa. The upset billets were surface machined. A rod of 17.4 mm diameter was obtained by extruding the machined billets at 1150 ºC by applying a pressure of 620 MPa at an extrusion ratio of 19. The photographs extrusion press, upset billets and extruded rods are shown in Fig. 3.5 (a–c), respectively. All the extruded rods were annealed at 900 °C for 1 h and then water quenched to remove the residual strain.

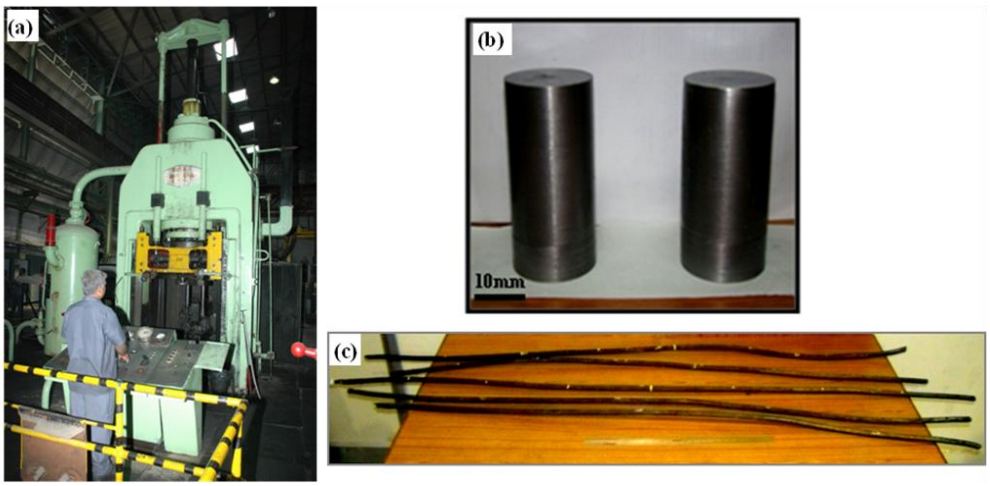

Fig. 3.5 Photographs of (a) extrusion press, (b) upset billets and (c) extruded rods.

For ease of presentation, the ODS steel powder samples are identified as P_1, P_2, P_3, P_4, P_5 and P_6 with the subscript indicating the number of hours of milling and the extruded+annealed rods as ODS1, ODS3 and ODS6 for milling times of 1, 3 and 6 h, respectively. The base pre–alloyed steel powder milled for 6 h and subsequently extruded and annealed rods are referenced as P_N and NODS, respectively. Table 3.3 gives the designation and the description of various samples used in this study.

Table 3.3 Nomenclature of samples used in the present study.

Designation	Description
P_o	Pre–alloyed steel powder (Fe–18Cr–2.3W–0.3Ti)
P_N	Pre–alloyed steel powder milled for 6 h
P_1	Pre–alloyed steel powder + 0.35% Y_2O_3 milled for 1h
P_3	Pre–alloyed steel powder + 0.35% Y_2O_3 milled for 3h
P_6	Pre–alloyed steel powder + 0.35% Y_2O_3 milled for 6h
NODS	Extruded + annealed sample of P_N
ODS1	Extruded + annealed sample of P_1
ODS3	Extruded + annealed sample of P_3
ODS6	Extruded + annealed sample of P_6

3.5 Chemical analysis

The structure and properties of ODS–18Cr ferritic steels can be attributed to the chemical composition during the fabrication process. During fabrication, precautions should be taken at each step to control the pickup of impurities. Pre–alloyed steel powder, milled powders and extruded+annealed samples were subjected to various chemical analyses, including metallic elements like iron, chromium, tungsten and titanium and also non–metallic elements like carbon, oxygen and nitrogen, *etc*.

The chemical composition including C, O and N of powder as well as bulk samples were evaluated using inductively coupled plasma–atomic emission spectrometer (ICP–AES) (Jobin–Yuon, France, Model: Ultima–2CHR), nitrogen/oxygen (Leco, Model: TC436) and carbon–sulfur (Leco, Model: CS444) analyzers. The total carbon content was determined by using an inert gas fusion method based on the principle of the infrared absorption of the carbon dioxide and/or carbon monoxide produced by the combustion of

1 g of sample in an induction furnace in a current of pure oxygen. The principle for the evaluation of total oxygen content using oxygen–nitrogen analyzer is to fuse the sample in a high purity graphite crucible in the furnace in inert gas helium at a very high temperature of 2000 °C. The carbon crucibles supply the necessary heat for fusing the sample of 1 g, and also carbon for reducing the oxygen in the sample. Infrared detector measures the CO and CO_2 in the crucible which are formed by reacting with the oxygen present in the sample.

The chemical compositions of pre–alloyed steel powder (P_0), ODS–18Cr steel powder milled for 6 h (P_6) and bulk samples of NODS and ODS6 are given in Table 3.4.

Table 3.4 Chemical composition (wt. %) of powders and bulk samples.

Sample/Composition (wt. %)	Fe	Cr	W	Ti	C	Total O	N	Y_2O_3	Excess O
P_0	Bal.	17.8	2.3	0.34	<0.03	0.006	0.003	–	–
P_6	Bal.	17.5	2.4	0.33	<0.03	0.12	0.012	0.36	0.04
NODS	Bal.	17.6	2.3	0.34	<0.03	0.05	0.012	–	–
ODS6	Bal.	17.4	2.2	0.31	<0.03	0.14	0.012	0.36	0.06

The chemical analysis indicated that the oxygen and nitrogen contents in both ODS and NODS steels increased slightly when compared to the pre–alloyed steel powder. This is due to minor leakages during milling under argon atmosphere.

3.6 Structural characterization

The particle shape, size, crystallite size and phases were analyzed using X–ray diffraction (XRD) and scanning electron microscopy (SEM). Transmission electron microscopy (TEM) was used to characterize the size, shape, distribution and structure of the dispersoids in ODS–18Cr ferritic steel.

3.6.1 XRD analysis

XRD studies were carried out on the milled powders in a Bruker D8 Advance system fitted with Lynx Eye detector (Bruker Axs GmbH, Germany) using Cu K_α radiation with a scan rate of 5 s per step of 0.05° (2θ) and the 2θ range of all the measurements was restricted to 20–110°. The X–ray generator was operated at 45 kV at an anode current of

40 mA. The crystallite sizes were calculated from the XRD data using full width half maxima (FWHM) of the most intense line Bragg peak of the sample using Scherrer formula after subtracting the widths due to instrumental broadening and strain effects using the equation [3].

$$FWHM_{sample} - FWHM_{LaB6} = (\frac{\lambda}{(D_v \cos\theta)} + 4\varepsilon_{str} \tan\theta), \quad (3.1)$$

where, λ is the wave length of X–ray beam (1.541 Å), *Dv* is the volume weighted grain size, θ is the Bragg angle, and ε_{str} is a strain factor. The crystallite size was calculated after subtracting the contribution from instrumental broadening, which was determined from X–ray measurements on LaB_6 powder.

3.6.2 High intensity X–ray diffraction

High intensity XRD studies were carried out in Rigaku Rapid–IID/MAX using chromium target with X–ray beam spot size of 100 µm diameter to obtain different phases present in NODS and ODS–18Cr samples. This system is equipped with a very high intensity micro focus X–ray source *viz.* Rigaku MicroMax 007HF, which is a high flux rotating anode system with excellent beam stability and brightness close to a second generation synchrotron. The system also has a highly sensitive and very large image plate–based two dimensional (2D) detector, which collects the diffraction Debye rings in 2D and ensures a full scans from 0 to 150° or 10 to 160° for 2θ in a single exposure of very small duration making it a rapid system.

3.6.3 Scanning electron microscopy

Sample preparation

Standard metallographic procedures were used to prepare samples for microstructural examination. Samples were sectioned with a low–speed diamond saw (Buehler: Isomet 1000 precision saw) at 200 rpm. This sectioning method was selected as to minimize the damage introduced during cutting. A cutting lubricant was used to improve cutting rates and minimize the frictional heat generated. After sectioning, the samples were then mounted in a conductive mounting powder using a mounting press (Bianmount, Metco, India) at a temperature of 180 °C for 15 min duration of time under a pressure of 4 bar. The samples were grounded on 120, 220, 320, 400, 600, 800, 1000, 1200 and 2000 grit silicon carbide impregnated emery paper and subsequently, samples were polished with

diamond suspensions of 9, 6, 3 and 1 μm to a bright, smooth mirror–like finish. Grain morphology and other intrinsic microstructural features were revealed using an etchant of Vilella's reagent whose composition is given in Table 3.5.

Table 3.5 Composition of Vilella's reagent.

Content	Quantity
Glycerol	3 parts
Hydrochloric acid	2 parts
Nitric acid	1 part

The size, shape and morphology of milled powders, microstructures of upset forged and extruded+annealed samples were analyzed using SEM (Hitachi, model: S–3400N) equipped with secondary electron and backscattered electron detectors. The composition analysis was carried out using electron dispersion spectroscopy (EDS). Sputter coater is used to coat the powder samples with a thin layer of gold to improve conductivity. The particle size of the milled powder was estimated by using the laser diffraction particle size analyzer (Malvern, Model: MS2000) and standard image analysis software (Olympus, Model: GX51). Feret mean diameter of the particle was calculated by analysis of SEM images of the powder particles as per ASTM F1877–05 standard. About 1000 particles are used in each sample to estimate the particle size.

3.6.4 Electron backscatter diffraction

Electron backscatter diffraction (EBSD) also called as orientation imaging microscopy is a SEM based powerful and adaptable technique for the study of microstructure. With crystallographic data of the phase under study as the input, microstructural information such as the crystallographic orientation of the individual grains, grain boundary character distribution and micro texture can be obtained. In EBSD, the specimen is first tilted to 70° and the electron beam is scanned across the region of interest with a fixed step size. The backscattered electrons that are generated undergo diffraction, the effect of which is detected as bands on a phosphor screen. By moving the source beam along a regular grid of discrete points on the sample surface, the diffraction pattern at each point is recorded and analyzed to determine the orientation at that point.

EBSD patterns are generated within a small interaction volume located at the surface of a sample with a penetration depth typically less than 50–100 nm. As a result of this, quality of the EBSD pattern is extremely sensitive to the integrity of the crystallographic lattice order at the surface of the sample. The specimen preparation for EBSD is same as that mentioned above, except that in EBSD there is a final polishing step with 0.05 micron colloidal silica (CS), which has a pH of 9.8. For EBSD analysis, an excellent surface finish is provided by the chemical–mechanical polishing. Samples were polished for 30 minutes and cleaned with ethanol by ultrasonication.

In the present study, EBSD scans were recorded using a Digiview EBSD camera in the field emission SEM (Hitachi, S–4300 SE/N). The orientation data analysis was carried out using OIM analysis 5.0 software.

3.6.5 Transmission electron microscopy

Powder sample preparation

For TEM examination, powders were mixed properly in a conductive Gatan G1 epoxy and filled in a 3 mm inner diameter brass tube followed by curing at 120 °C for period of 20 min and cooling to room temperature. This was subsequently cut, ground, polished and dimpled in a dimpling grinder (Fischione; Model 200) and ion–milled in precision ion polishing system (PIPS) (Gatan, Model 691) as per the standard procedure.

Bulk sample preparation

Bulk samples for TEM study were mechanically thinned down to the thickness of about 100 µm and discs of 3 mm in diameter. These discs were electro polished using 10% $HClO_4$ and 90% CH_3COOH solution as electrolyte at room temperature and 30 V in a twin jet electro polisher (Fischione, Model 110). The electro polished samples were cleaned further with an Ar ion beam at a low angle in PIPS.

TEM observations of powder, upset forged and extruded+annealed samples were carried out by using FEI Tecnai G^2 200 kV (LaB_6) microscope equipped with Olympus (SIS mega view III) wide angle camera. High resolution imaging was carried out using Tecnai F30 300 kV FEG system equipped with a Gatan image filter (Tridiem 863). To observe the TEM foils, a low background double tilt specimen holder was used. By using an EDAX silicon detector with an ultra thin window the EDS spectra were collected. Once

the dispersoid diameter was obtained for each sample, the corresponding volume fraction of dispersoids (*f*) was estimated using the equation given below [4]:

$$f = \frac{\pi \sum N_i d_i^3}{6At} \tag{3.2}$$

In Eq. (3.2), N_i is the number of dispersoids having a diameter of d_i, t is the foil thickness and A is the total projection area. The foil thickness was estimated by *K-M* patterns from using convergent beam electron diffraction (CBED) [5].

3.7 Mechanical properties

Mechanical characterization techniques such as micro, macro hardness and tensile tests were employed on the samples. They are described below.

3.7.1 Hardness

The powder and the bulk samples were sectioned, hot mounted and polished to a mirror surface finish using standard metallographic techniques prior to indentation testing. A flat surface enables the formation of the symmetrical indentation and minimizes the testing error. A minimum of 100 measurements on powder particles and 30 measurements on bulk samples were made on each sample and an average hardness value was calculated after eliminating the erroneous values obtained because of the low residual thickness of the polished particles.

Vickers hardness

Vickers hardness (micro and macro) is a measure of the materials resistance to a localized plastic deformation, applied mostly in materials characterization. Micro hardness of the powders was measured at 50 g load and bulk hardness of the upset forged and extruded+annealed samples were measured with 5 kg load using Vickers micro (Walters UHL, Model: VMH– I04) and macro hardness testing machines (Leco, Model: LV–700AT) under standard test conditions. The load on the Vickers micro–hardness indenter usually ranges from a few grams to a kilogram. In contrast, in ‘Macro’ Vickers hardness test the applied loads vary from 1 to 120 kg. The actual indenters used are Vickers (a square base diamond pyramid with an apical angle of 136°) or Knoop (a narrow rhombus shaped indenter).

3.7.2 Tensile properties

The tensile properties of the annealed samples were evaluated as per ASTM E21 standard from room temperature (RT) to 800 °C at a strain rate of 7.5×10^{-4} s^{-1} using a universal testing machine (Instron, Model: 4507, 200 kN) with a furnace capable of heating the sample up to 1000 °C. Round tensile test specimens of 3.99 mm Ø and 22 mm gauge length were used [6] and for each test condition, the average results obtained on two specimens are reported. Fractographic examination was carried out on fractured tensile samples using SEM. The drawing of a tensile specimen used is given in Fig: 3.6.

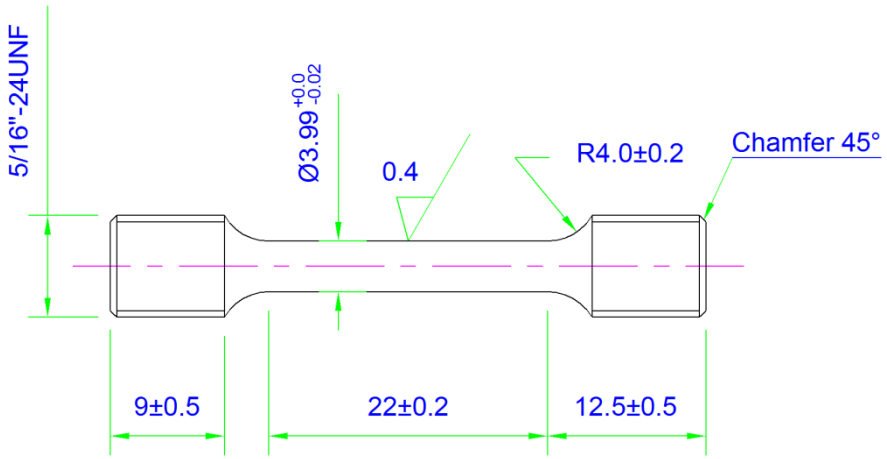

Fig. 3.6 Dimensions (mm) of the sample used for tensile testing.

3.8 Corrosion studies

To determine the corrosion behavior of NODS and ODS–18Cr samples, electrochemical experiments (cyclic polarization, electrochemical impedance spectroscopy and potentiodynamic polarization) and immersion tests were carried out in 3.5% NaCl solution at room temperature. In each experimental condition, three sets of tests were carried out and all the results were reproducible.

3.8.1 Sample and electrolyte preparation

Transverse sections of extruded+annealed samples with the dimensions of 12 mm ϕ and 5 mm thickness were mounted and polished by standard polishing techniques, ultrasonically cleaned with distilled water and then by acetone to avoid the surface contaminants and are air dried. The exposed area of the sample in the mount for corrosion studies is 1.33 cm^2. The electrolyte solution (3.5 % NaCl solution) was prepared using

analytical grade reagent and distilled water. The as prepared 3.5 % NaCl solution was purged with N_2 gas in order to remove the dissolved oxygen.

3.8.2 Electrochemical cell

A typical three electrode electrochemical test cell used for electrochemical experiments is schematically shown in Fig. 3.7. The corrosion cell had the classic configuration of three electrodes, sample as a working electrode, a saturated calomel electrode (SCE) as a reference electrode and platinum as counter electrode. The potential in the electrolyte of the metal under study the working electrode is measured against that of a reference electrode by means of a voltmeter. The SCE, which is the most widely used reference electrode, which consists of mercury covered with a paste of mercurous chloride and mercury in a chloride solution. The potential depends on the saturated solution of potassium chloride and the concentration of chloride ions and this is used to minimize the junction potential between the electrolyte and the solution in the reference electrode in the cell. To minimize the mutual contamination of the two solutions, contact is usually made through a porous ceramic plug between the test solution and the saturated potassium chloride solution of the calomel electrode. The potential difference across this cell gives the potential of the metal in the test solution against the SCE. A standard three–electrode cell assembly was connected to the computer controlled Solartron Electrochemical Interface (Model SI 1287) with Corrware and Corrview–2 softwares and Solartron (Model SI 1260) Impedance/Gain Phase analyzer with Z–plot, Z–view softwares to obtain and analyze the corrosion data.

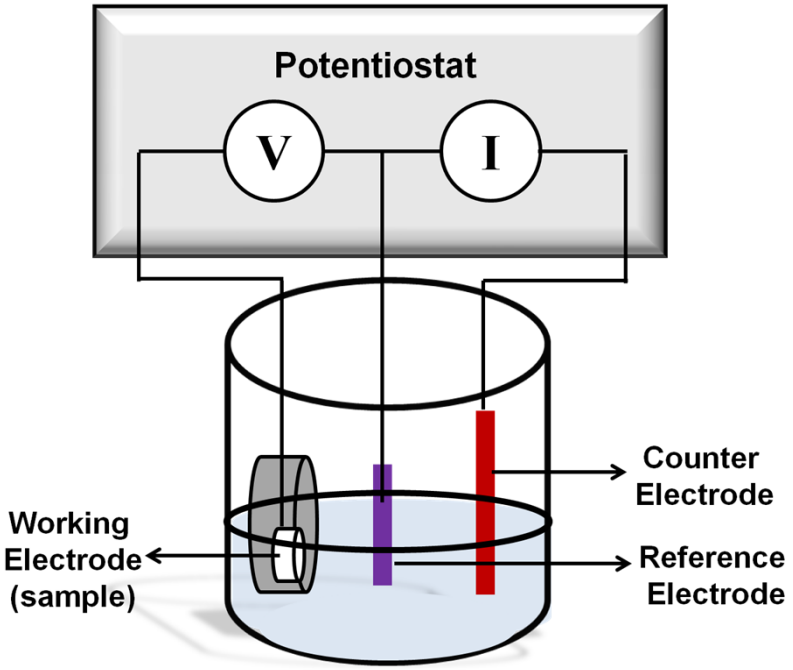

Fig. 3.7 Schematic of three electrode electrochemical test cell.

3.8.3 Electrochemical corrosion experiments

Cyclic polarization (CP) experiments were performed to evaluate the pitting resistance of the alloys and carried out from a potential of -0.8 V relative to the reference electrode potential with a scan rate of 1 mV/sec up to 1 V and the scan was reversed back to the potential of -0.85 V.

Electrochemical impedance spectroscopy (EIS) and potentiodynamic polarization experiments were carried out on samples exposed to 3.5 % NaCl for different exposure times of 1, 24, 48 and 96 h. By applying an AC signal with 10 mV amplitude, EIS spectra were recorded prior to polarization scan and a frequency range of 25 kHz–0.02 Hz at open circuit potential (OCP). After EIS scans, potentiodynamic scan was performed from cathodic to anodic region stating with a potential of -0.8 V up to 1.2 V relative to the reference electrode potential at a scan rate of 1 mV/s. Prior to the start of the scans, OCP of the samples was stabilized in the test solution. Since the passivation started immediately on immersion, polarization resistance (R_p) fit method (linear polarization technique) is used to analyze the data obtained in the present work. In this method, applied potential (E) is plotted with the measured current (i), which is linear within ±20 mV of corrosion potential and R_p is obtained from the slope of the plot ($\Delta E/\Delta i$) [7].

3.8.4 Immersion studies

To study the corrosion behavior of samples for a long time, immersion tests have been carried out by dipping all samples in 3.5 % NaCl solution for 365 days.

After the samples were removed from the cell, they were immediately rinsed with alcohol and dried, then stored in a desiccator. Characterization of the surface and cross–section morphology of the samples was done by SEM. The surface and cross–section morphology of the samples were characterized by SEM.

3.9 Oxidation studies

High temperature oxidation studies of NODS and ODS–18Cr samples were carried out by exposing the samples to 650, 750 and 850 °C in air for 100, 500, 1000, 1500 and 2000 h. Specimens with a size of 11 mm diameter and 5 mm thickness were used for carrying out oxidation studies. Prior to oxidation experiments, all the samples were polished by standard polishing techniques, cleaned and dried. The weight of the samples before and after oxidation experiments was measured using semi micro balance (Presica ES 225SM–DR) with an accuracy of 0.01 mg. Four measurements were taken and the average value was reported for each specimen.

The morphology and cross–sectional observations of the oxidized samples were carried out using SEM with EDS. Raman spectrometry (Horiba, Jobin–Yvon Lab Ram HR 800) was performed on the oxidized samples to find out the phases in the oxide layer. The source of optical excitations was Ar–ion (514 nm, 20 mW) laser. The baseline correction and calibration were based on 520 cm^{-1} Raman peak of polycrystalline Si.

3.10 Summary

ODS–18Cr and 18Cr steels were produced by mechanical alloying followed by hot extrusion. Various processing conditions like milling, upset forging and extrusion were explained. The characterization procedures pertaining to microstructural, mechanical, corrosion and oxidation are explained.

References

[1] H. Zoz, D. Ernst, R. Reichardt, High energy milling/Mechanical alloying/ Reactive milling, 3rd international symposium of school of chemical engineering, University of Mexico city, 1998.

[2] C. Suryanarayana, Mechanical alloying and milling, *Progress in Materials Science*, 46 (2001) 1–184.

[3] R. Delhez, T.H. Keijser, J.I. Langford, D. Louer, E.J. Mittemeijer, E.J. Snneveld, Crystal imperfection broadening and peak shape in the reitveld method, Oxford University press, Oxford, 1993.

[4] J. Wosik, B. Dubial, A. Kruk, H.J. Penkalla, F. Schubert, C.F. Filemonowicz Stereological estimation of microstructural parameters of nikel–based superalloy Waspaloy using TEM methods, *Materials Characterization*, 46 (2001) 119–123.

[5] D.B. Williams, C.B. Carter: *Transmission Electron Microscopy*, Plenum press, New York, London, 1996.

[6] R. Vijay, M. Nagini, S.S. Sarma, M. Ramakrishna, A.V. Reddy, G. Sundararajan, Structure and properties of nano–scale oxide dispersed iron, *Metallurgical and Materials Transactions A*, 45A (2014) 777–784.

[7] G. Sundararajan, P. Sudharshan Phani, A. Jyothirmayi, Ravi.C. Gundakaram, The influence of heat treatment on the microstructural, mechanical and corrosion behaviour of cold sprayed SS 316L coatings, *Journal of Materials Science*, 2009, 44 (2009) 2320–2326.

CHAPTER 4
RESULTS AND DISCUSSION

The experimental details about the processing of 18Cr and ODS–18Cr steels and related microstructural, mechanical, corrosion and oxidation characterization procedures were discussed in the previous chapter. The results obtained and the discussions based on the results are presented in the present chapter.

4.1 Effect of High Energy Ball Milling on Microstructural Development in Oxide Dispersion Strengthened 18Cr Ferritic Steel

4.1.1 Introduction

The microstructure of metallic materials depends on the chemical composition, processing stages, phase transformations and final heat treatment. The Fe–18Cr–2.33W–0.34Ti base steel used in this study, when processed by conventional ingot metallurgy route, consists of equi–axed ferrite grains and $M_{23}C_6$ type carbides in conformity with the predicted phases in Fe–Cr phase diagram. The microstructural evolution in ODS–18Cr steel (Fe–18Cr–2.33W–0.34Ti–0.35Y_2O_3) made by consolidation of mechanical milled powder is quite a complex phenomenon. The severe deformation induced changes in milled powders along with formation of unusual meta–stable solid solutions lays the foundation for the formation of stable structure during hot consolidation. The sequence of structural development during milling and hot consolidation lead to the formation of stable nano structured ferrite with nano–sized Y–Ti–O particles is presented in this chapter.

4.1.2 Characterization of milled powders

4.1.2.1 Effect of milling time on particle size

The morphologies of ODS–18Cr steel powders milled for 1, 3 and 6 h (P_1, P_3 and P_6) along with non ODS powder milled for 6 h (P_N) are shown in Figs. 4.1.1 (a–d) respectively. The spherical particles were deformed into flattened and rounded discs. During the early stages of milling, particles tend to flatten with wide size distribution due to the dominance of deformation and at larger milling times, become nearly uniform sized faceted shapes with narrow size distribution as a result of complex interplay between plastic deformation, welding and fracture. The variation of particle size of ODS

milled powders estimated from SEM micrographs by image analysis and by laser diffraction analysis (LDA) as per ASTM F 1877–05 and ASTM E 2651–13 standards respectively, is shown in Fig. 4.1.2 for different milling times along with P_N particle size. The particle sizes of the ODS steel powders estimated by both techniques (image analysis and LDA) were found to be comparable. Feret mean diameter of the particle was calculated with standard image analysis software using images of the powder particles (about 1000 particles in each sample) obtained from SEM. During high energy milling, the ductile particles get cold deformed, welded to particles in close contact and fragment when fracture strain is accumulated. While plastic deformation and welding are dominant during the initial stages of milling, fracture occurs subsequently. Since cold welding and fragmentation are competitive processes and the steady state can be reached only when particle coarsening due to welding is matched by size decrease due to fragmentation [1, 2]. The steady state particle size (139 μm) of ODS–18Cr steel powder attained after 5 h of milling signifies a balance between particle coarsening caused by deformation and welding and decrease in size by fragmentation. In the case of P_N, the size estimated by image analysis (314 μm) was lower than the measurement made by LDA (415 μm). The lower size by image analysis is because of the difficulty in spreading and retaining coarser particles during sample preparation for SEM examination. The particle size of P_6 is much finer than P_N because of the fact that the fracture strain is expected to be lower in ODS steels as a result of the solid solution hardening and/or hardening caused by Y, Ti, O atomic clusters formed at steady state milling conditions.

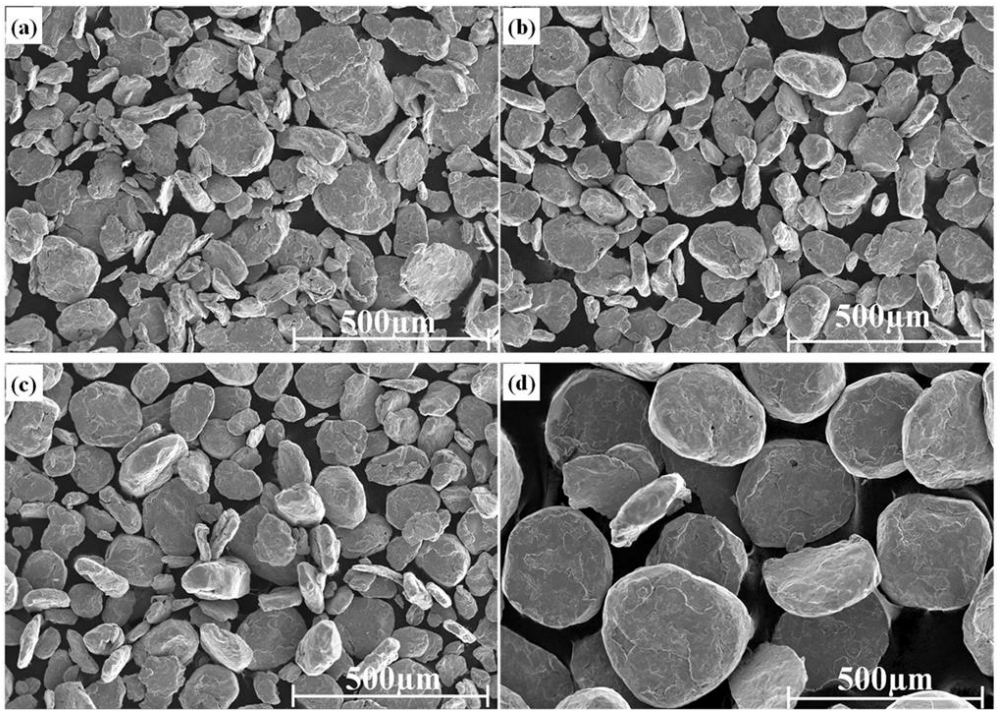

Fig. 4.1.1. SEM images of mechanically milled powders: a) P_1, b) P_3, c) P_6 and d) P_N.

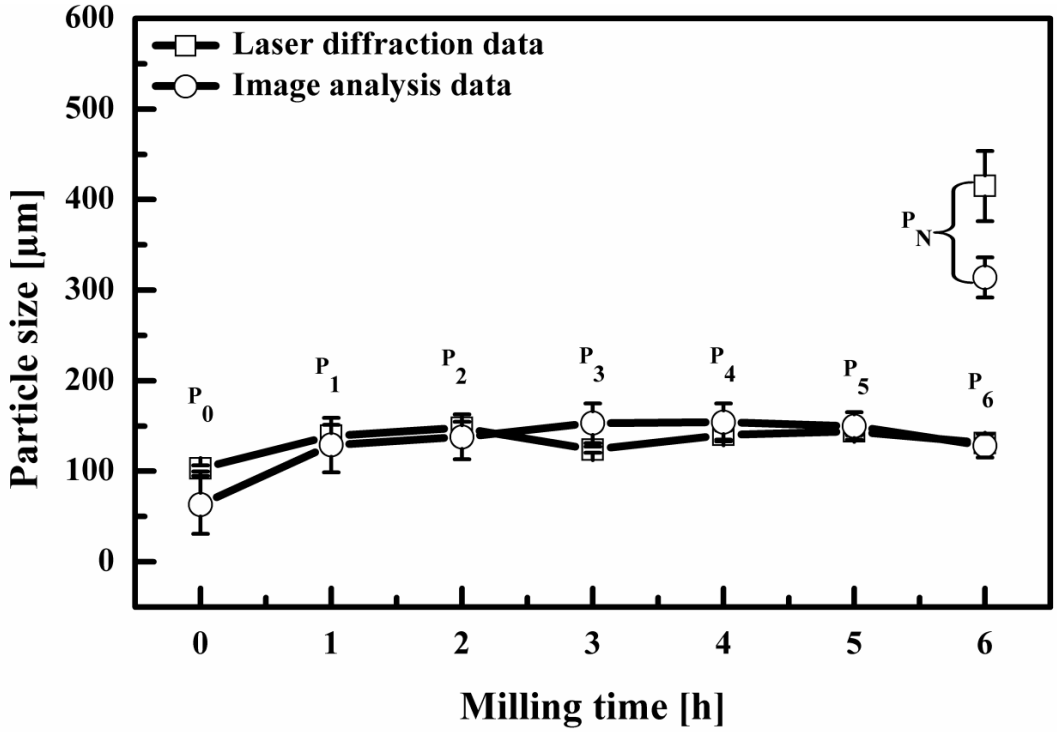

Fig. 4.1.2 Variation of particle size of 18Cr and ODS–18Cr steel powders with milling time.

4.1.2.2 Effect of milling time on crystallite size

The variation of average crystalline size estimated from the XRD analysis of 18Cr and ODS–18Cr steel powders as a function of milling time is shown in Fig. 4.1.3. The results indicated that the crystallite sizes of both the powders decrease continuously with increasing milling time and reach a steady state size of about 16 nm beyond 5 h milling and the crystallite size of P_N is comparable to P_6. At identical milling times, ODS–18Cr steel powder exhibited higher crystallite size than 18Cr steel powder. The presence of oxide particles retards the dislocation motion substantially, thereby, delaying the formation of cell structure to higher strains. This results in larger crystallite size in ODS–18Cr steel powders for a given strain [3].

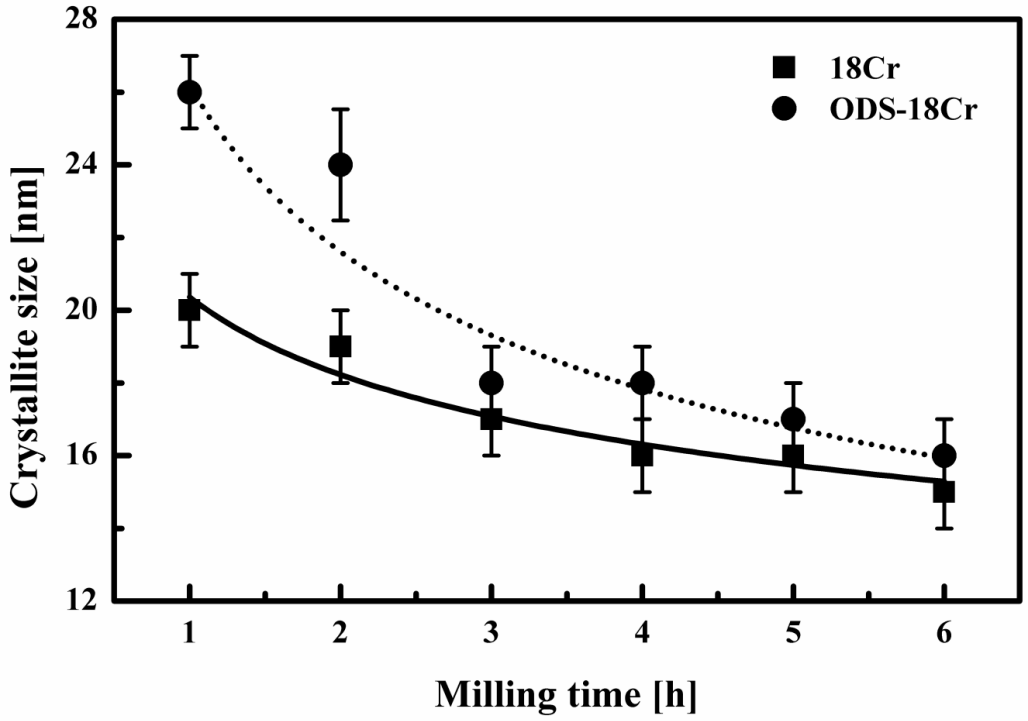

Fig. 4.1.3 Variation of crystallite size of 18Cr and ODS–18Cr steel powders with milling time.

4.1.2.3 Effect of milling time on microstructural features of powders

TEM examination was carried out on P_1, P_3 and P_6 representing the whole range of milling time. Typical TEM bright field (BF) images are shown in Fig. 4.1.4. While P_1 revealed banded structure containing cell structure within the bands, P_3 and P_6 showed nearly equiaxed cells. The cell size was found to decrease from P_1 to P_6. The crystallite sizes for P_1, P_3 and P_6 powders estimated by XRD and TEM analysis (average of a minimum of 400 cells) are given in Table 4.1.1. The results are consistent with the

milling time dependent decrease in crystallite size and both the techniques yielded comparable crystallite size. The estimated crystallite sizes are comparable to the steady state crystallite sizes reported for ODS–14Cr steel [4, 5]. The progressive decrease in cell size with increasing strain is caused by dislocation generation and cell multiplication. The decrease in cell size with increasing strain is in conformity with the well established sub structural changes that occur during plastic deformation of BCC metals. The attainment of steady state is due to the balance between cell multiplication and cell annihilation [6].

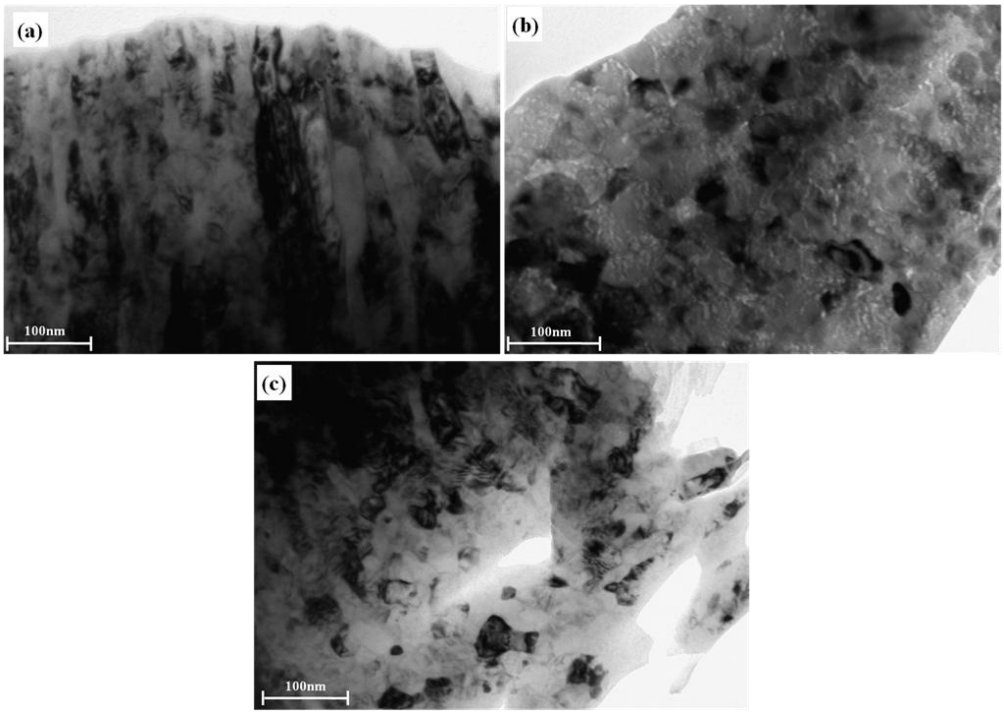

Fig. 4.1.4 TEM bright filed images of ODS–18Cr milled powders: a) P1, b) P3 and c) P6.

Table 4.1.1 Crystallite sizes of ODS–18Cr steel milled powders.

Sample name	Crystallite size [nm]	
	XRD	TEM
P_1	26 (±1)	23(±13.25)
P_3	18(±1)	22(±15.26)
P_6	16(±1)	18(±7.83)

To understand the influence of milling time on Y_2O_3 particles, detailed TEM examination was also carried out on the as milled powders. Typical TEM images obtained on P_1 are shown in Figs. 4.1.5 (a–e) respectively. The BF image (Fig. 4.1.5 (a)) revealed the substructure and clusters of Y_2O_3 particles located along the boundaries of lamellar structure formed due to plastic deformation during milling. The selected area electron diffraction (SAED) pattern obtained from the entire area shown in Fig. 4.1.5 (a) is presented in Fig. 4.1.5 (b). Analysis of the SAED pattern indicated that all the rings correspond to the matrix BCC phase except for the two extra spots marked by arrows. The d spacing corresponding to the extra spots was found to be 3.05 Å, which matches with the interplanar spacing (3.06 Å) of {222} of Y_2O_3 particles [ICDD No: 00–041–1105]. The dark field (DF) image obtained on the extra spot, shown in Fig. 4.1.5 (c) indicated the presence of both coarse (≈10nm) and fine (<5nm) Y_2O_3 particles suggestive of size refinement of Y_2O_3 particles by fragmentation during milling. EDS pattern obtained from the particles (Fig. 4.1.5 (d)), indicated the presence of the Fe, Cr from the matrix and Y from the Y_2O_3 particles. Fig. 4.1.5 (e) shows the lattice resolution image from one of the Y_2O_3 particles. The interplanar spacing estimated from the lattice image is 2.7 Å which closely matches with {400} inter planar spacing (2.65 Å) of Y_2O_3 [ICDD No: 00–041–1105].

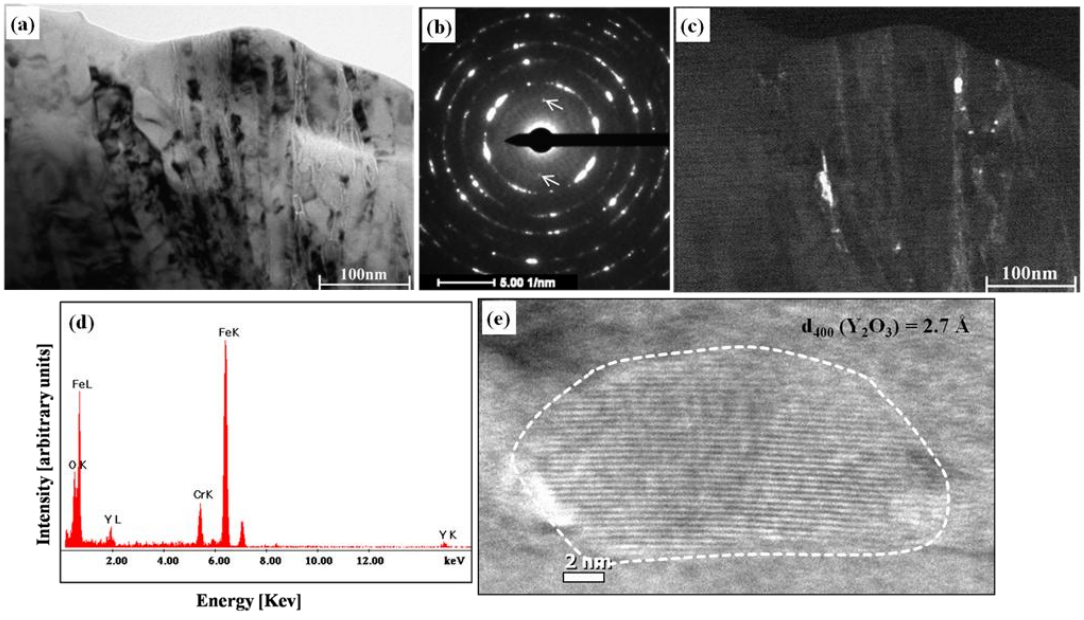

Fig. 4.1.5 TEM images of P1 powder: a) BF, b) SAED pattern, c) DF, d) EDS and e) Y_2O_3 particle.

Similar TEM studies were also made on P_3 and P_6 powders. Fig. 4.1.6 shows the typical TEM images obtained on P_3. The microstructure of P_3 was similar to P_1, except that the cell size was relatively finer; Y_2O_3 particles were further fragmented to less than 5 nm size and were more uniformly distributed. The SAED pattern presented in Fig. 4.1.6 (b) taken from the entire region shown in Fig. 4.1.6 (a) revealed extra spots (indicated by arrows) in addition to the spots corresponding to the matrix. The calculated interplanar spacings were matching to that of Y_2O_3 phase. The DF image obtained from the extra spot is shown in Fig. 4.1.6 (c), which indicates the presence of finer Y_2O_3 particles when compared to P_1. The presence of these fine Y_2O_3 particles suggests the occurrence of further fragmentation after 1 h of milling. The EDS pattern obtained from the bright region of Fig. 4.1.6 (c) is shown in Fig. 4.1.6 (d). The presence of only Y further confirms the presence of Y_2O_3. There was no evidence of Y–Ti–O complex oxide formation in both P_1 and P_3 powders.

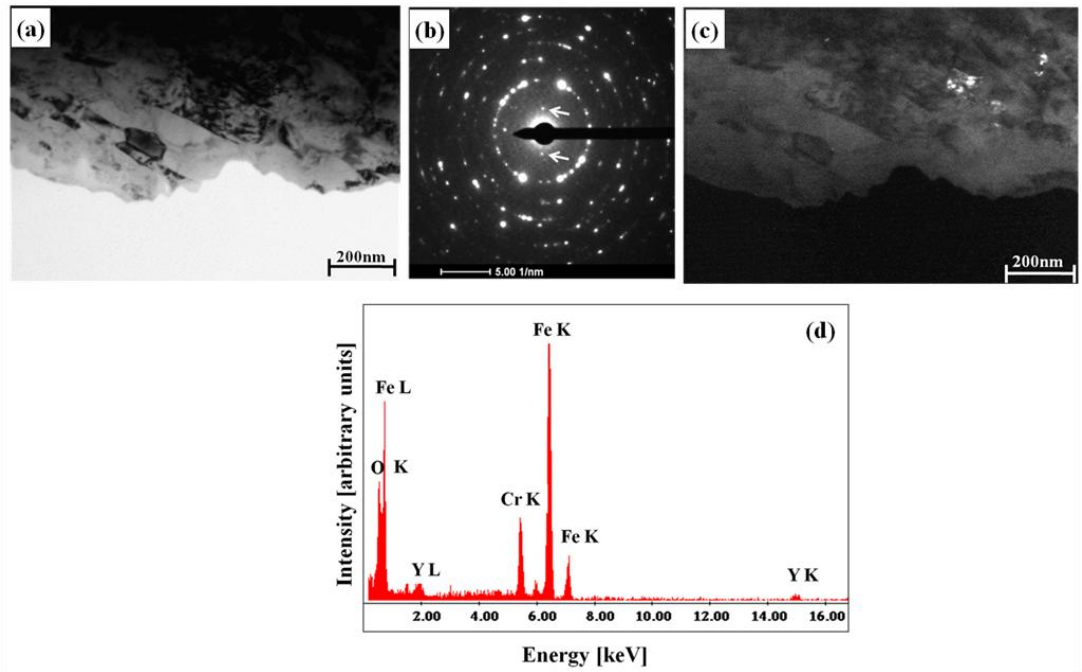

Fig. 4.1.6 TEM images of P3 powder: a) BF, b) SAED pattern, c) DF and d) EDS.

Typical BF image showing much finer cell structure, SAED and EDS pattern of P_6 powder are shown in Figs. 4.1.7 (a–c) respectively. It was observed that extra spots were not present in the diffraction pattern (Fig. 4.1.7 (b)) which implies the absence of Y_2O_3 phase. EDS pattern (Fig. 4.1.7 (c)), indicated the presence of the Fe, Cr from the matrix and nonexistence of Y. An examination of several SAED patterns taken on larger number of thin foils did not reveal the presence of any type of yttrium–based oxide particles. The

microstructural development during milling, thus, involves large strain deformation and development of cell structure due to dynamic recovery. As expected, the cell size decreases with increasing milling time. Fragmentation of Y_2O_3 particles occurs progressively with attendant reduction in size and improved uniformity in distribution. At larger milling times representing near steady state crystallite size, Y_2O_3 particles are not resolvable at the resolutions employed in TEM. The finding is in agreement with the proposition that, at larger milling times, the fragmented Y_2O_3 particles dissociate and dissolve in the matrix [7].

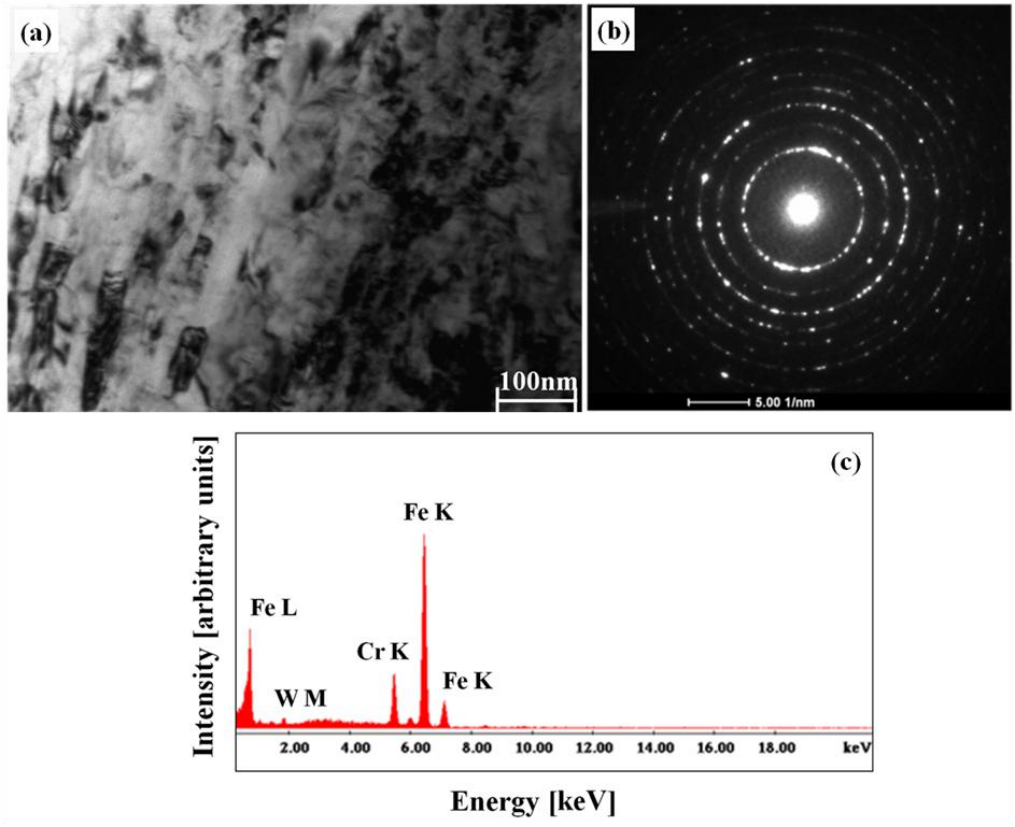

Fig. 4.1.7 TEM images of P6 powder: (a) BF, (b) SAED pattern and (c) EDS.

The microstructural evolution critically depended on the milling time. During mechanical milling, many dynamic events would be occurring concurrently resulting in intense plastic deformation of the ductile matrix and fragmentation of the fragile Y_2O_3 particles with associated changes. During the early stages of mechanical milling, the matrix undergoes severe shear deformation with the attendant increase in the population of dislocations and vacancies. With increasing milling time, the dislocations tend to rearrange themselves as crystallites whose size decreases and misorientation angle increases progressively. A steady–state is finally reached when the increase in dislocation

density due to further deformation is negated by dynamic recovery effects, thus stabilizing the crystallite size (Fig. 4.1.3). The Y_2O_3 particles, being friable and stronger, fragment and get embedded in the matrix. Even though, SAED patterns of P_1 and P_3 indicated the presence of Y_2O_3 particles, the possibility of some of them dissociating and dissolving in the matrix cannot be discounted. In P_6, which represents the steady state with respect to crystallite size, there was no evidence of the presence of Y_2O_3 or any of the Y–Ti–O complexes suggesting that either Y and O are completely dissolved in the steel matrix forming metastable solid solution or exist as non crystalline atomic clusters of such size which cannot be resolved with the capabilities of TEM used in this study. Recent studies by neutron diffraction have suggested that Y and O dissolution occurs during mechanical milling [4]. Atom probe studies indicated the formation of approximately 2 nm sized atomic clusters consisting of Y, Ti and O atoms [8]. The cluster formation has been reported to occur due to the enhanced diffusivity aided by a large number of vacancies and the relative chemical affinities of O, Ti and Y [7, 9]. The experimental results on P_6 powder (absence of Y_2O_3 or Y–Ti–O complex oxide particles) tend to support the hypothesis that dissolution of Y and O occur during milling, which probably lead to the formation of Y–Ti–O nano clusters under steady state milling conditions.

4.1.3 Upset forged billets

Since upset forging is first high temperature exposure followed by hot extrusion, it is useful to examine the matrix microstructure and size and shape of dispersoids. Since ODS6 corresponds to steady state condition, detailed examination was carried out at upset forging stage and compared with NODS. SEM and TEM images showing the microstructures of upset forged samples of ODS6 and NODS are shown in Figs. 4.1.8 (a–b) and 4.1.9 (a–b) respectively. Grain boundary character distribution maps for ODS6 and NODS are shown in Figs. 4.1.10 (a–c) respectively. Essentially grain boundary distribution indicates the subgrain (1–5°), low angle (5–15°) and high angle (15–180°) grain boundaries in red, green and blue respectively. To obtain the grain size distribution, the area fraction of the grains in the EBSD maps was plotted as a function of grain diameter for ODS6 and NODS and is shown in Figs. 4.1.11 (a–b) respectively. The average grain sizes of ODS6, NODS were 1.21 and 2.53 μm respectively. From the microstructural analysis, it is evident that, ODS6 showed heterogeneous structure

consisting of unrecrystallised regions along with a few pockets of very fine recrystallized grains. Due to the existence of combination of recrystallized, unrecrystallized grain structure, ODS6 exhibits bimodal grain size distribution. Unlike ODS6, NODS revealed fully recrystallized ferrite grains with uniform grain size distribution. There is a distinct difference in recrystallization behavior of ODS6 and NODS. While recrystallization has set in uniformly at all locations in NODS, it is localized at prior particle boundaries in ODS6. The retarded recrystallization in ODS6 when compared to NODS is due to the presence of dispersoids.

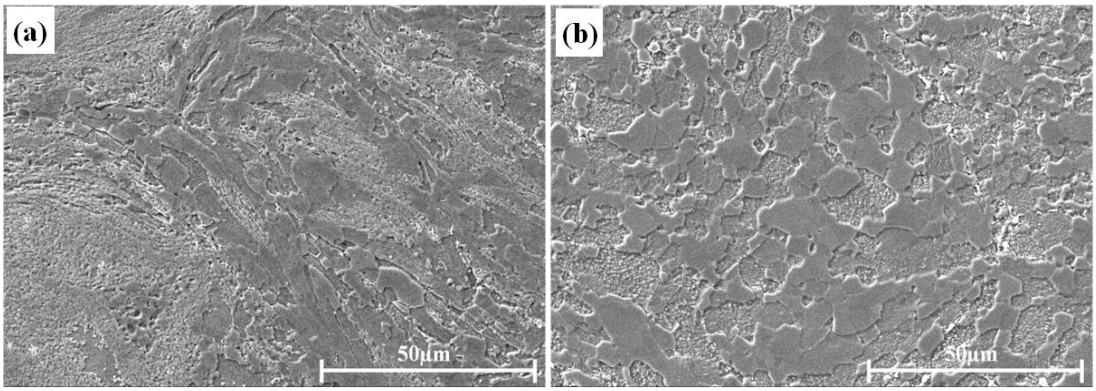

Fig. 4.1.8 SEM microstructures of upset forged samples: a) ODS6 and b) NODS.

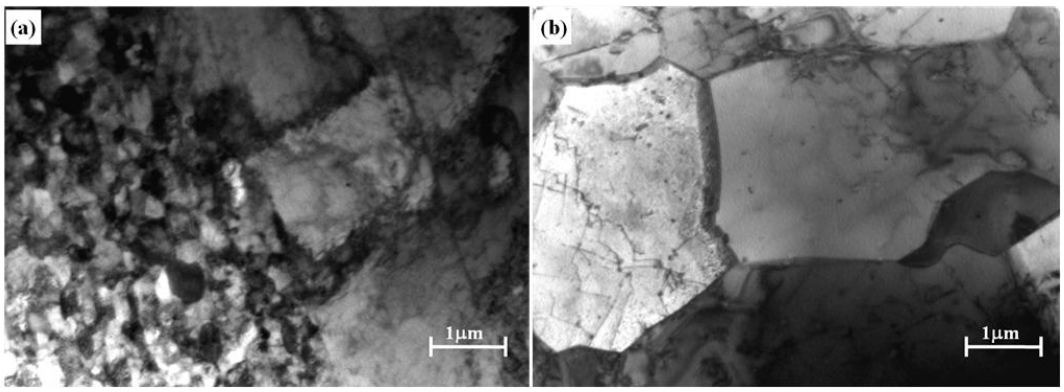

Fig. 4.1.9 TEM bright field TEM bright field images of upset forged samples: a) ODS6 and b) NODS.

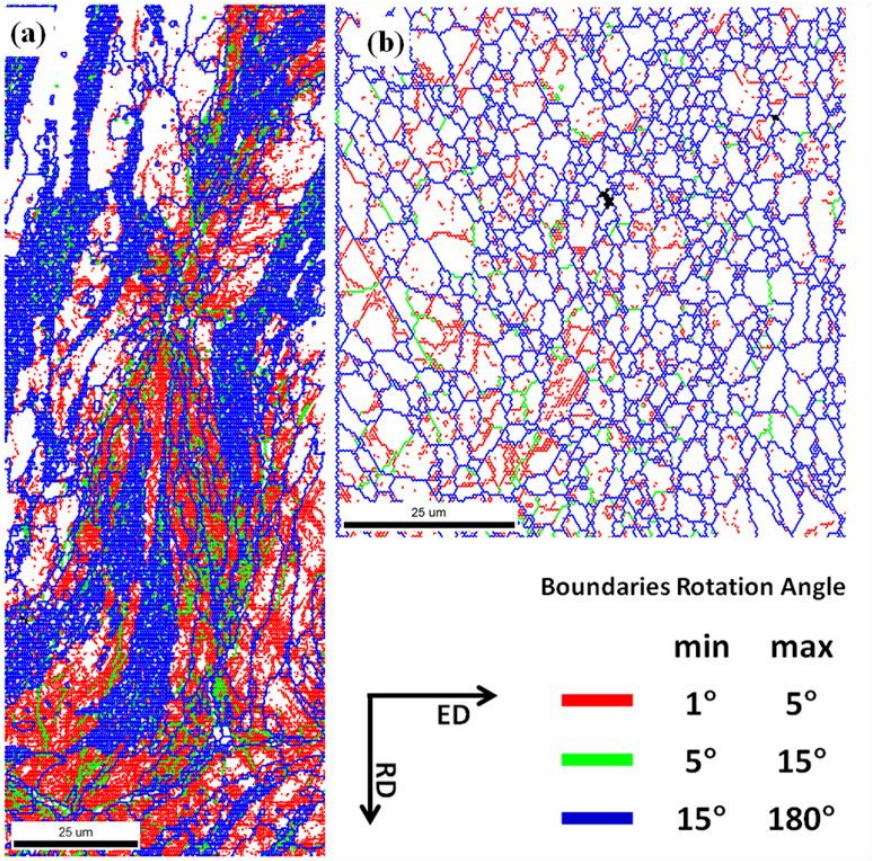

Fig. 4.1.10 Grain boundary character distribution of upset forged samples of a) ODS6 and b) NODS.

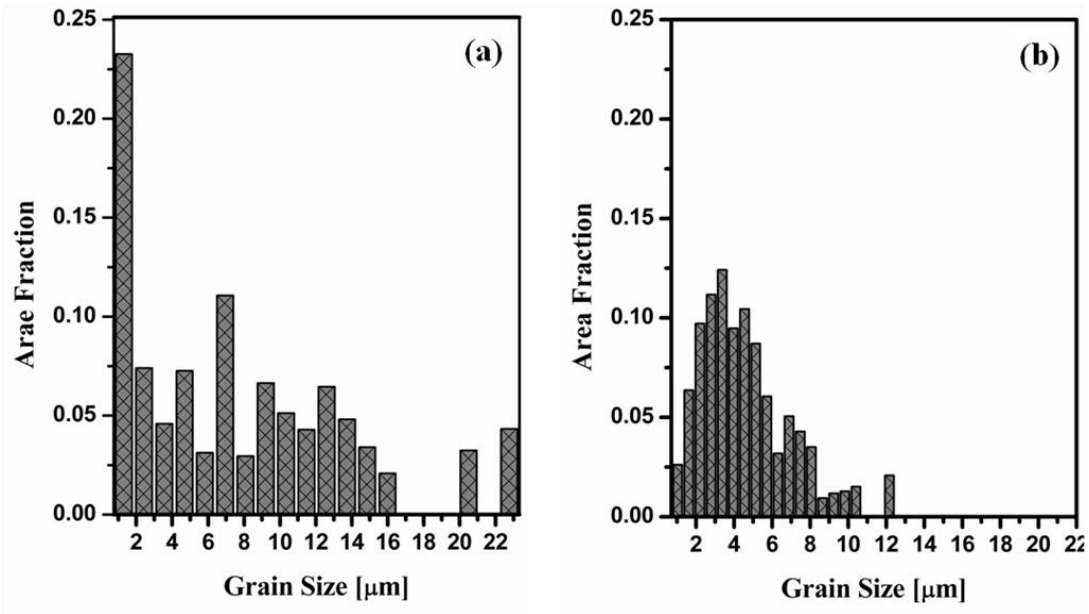

Fig. 4.1.11 Grain size distribution of upset forged samples: a) ODS6 and b) NODS.

Upset forging led to the formation of the complex dispersoid particles of stochiometry $Y_2Ti_2O_7$. The TEM bright field image of upset forged sample of ODS6 showing dispersoids along with the size distribution and are shown in Figs. 4.1.12 (a–b) respectively. The dispersoids are of cuboidal shape and are in the size range of 2–5 nm with an average size of 3 nm. While the coarser particles could be identified as $Y_2Ti_2O_7$ particles, the finer (≤2 nm) particles did not yield conclusive evidence to correctly label them and are considered to be nano clusters of Y–Ti–O which are still in the transition stage enroute to the formation of $Y_2Ti_2O_7$ particles [10]. Further work is needed to understand the influence of upset temperature on the nucleation and growth of Y–Ti–O complex oxide particles.

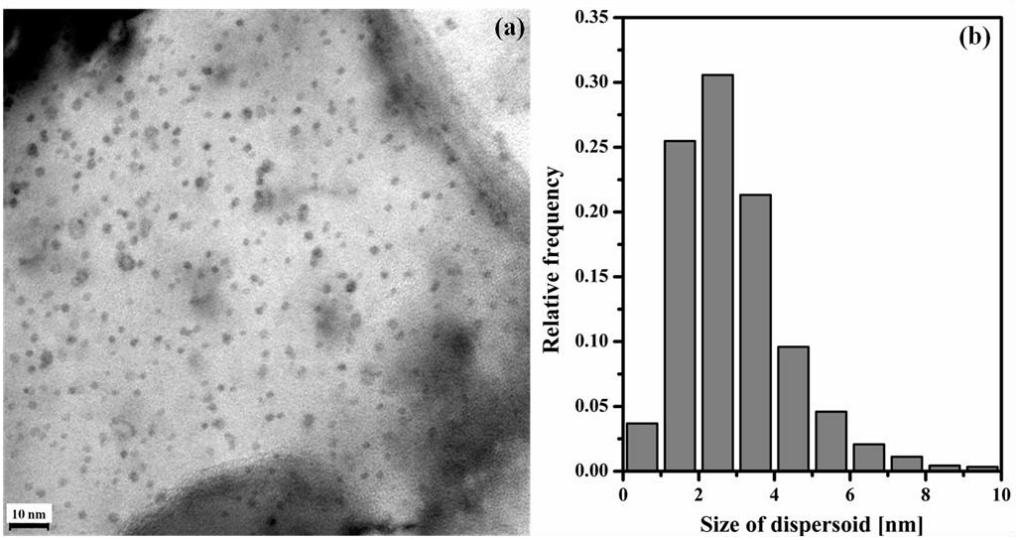

Fig. 4.1.12 a) TEM bright field image of upset forged ODS6 and b) dispersoid distribution.

4.1.4 Microstructural analysis of extruded and annealed rods

Typical SEM microstructures taken on longitudinal sections of ODS1, ODS3, ODS6 and NODS are shown in Figs. 4.1.13 (a–d) respectively. From the SEM micrographs, it is clear that a) ODS1 revealed nearly equiaxed grain structure with slight fibrosity, b) ODS3 and ODS6 contained fibrous grain structure, the grain fibers being thinner in ODS6 when compared to ODS3 and c) NODS showed equiaxed grain structure. Fine grains were observed within each fibrous grain in ODS3 and ODS6 which could not be clearly resolved in SEM examination.

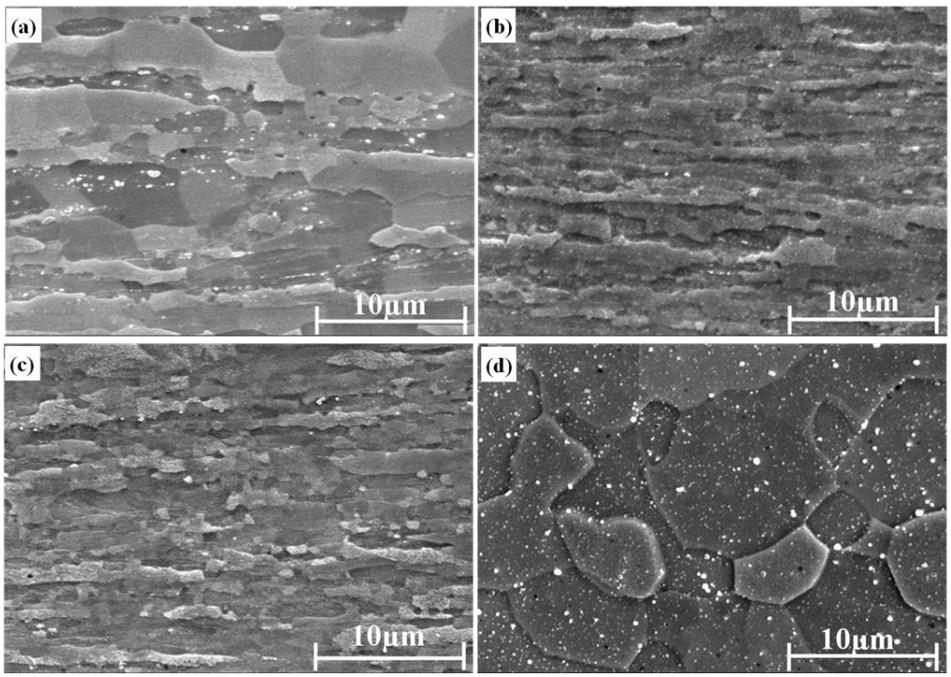

Fig. 4.1.13 SEM microstructures of extruded+annealed samples: a) ODS1, b) ODS3, c) ODS6 and d) NODS.

EBSD analysis was carried out to obtain more details of the grain morphology and grain size distribution of ODS–18Cr and NODS samples. The grain boundary character distribution for ODS1, ODS3, ODS6 and NODS are shown in Figs. 4.1.14 (a–d) respectively. The grain size distribution of ODS–18Cr and NODS samples in the longitudinal direction are shown in Figs. 4.1.15 (a–d) respectively. The average grain sizes of ODS1, ODS3, ODS6 and NODS were 1.17, 0.73, 0.48 and 13 µm respectively (Table. 4.1.2). At lower milling times (ODS1), elongated grains are relatively strain–free (lack of subgrain boundaries). The total length of the subgrain boundaries enhanced with increased milling time (Fig. 4.1.16).

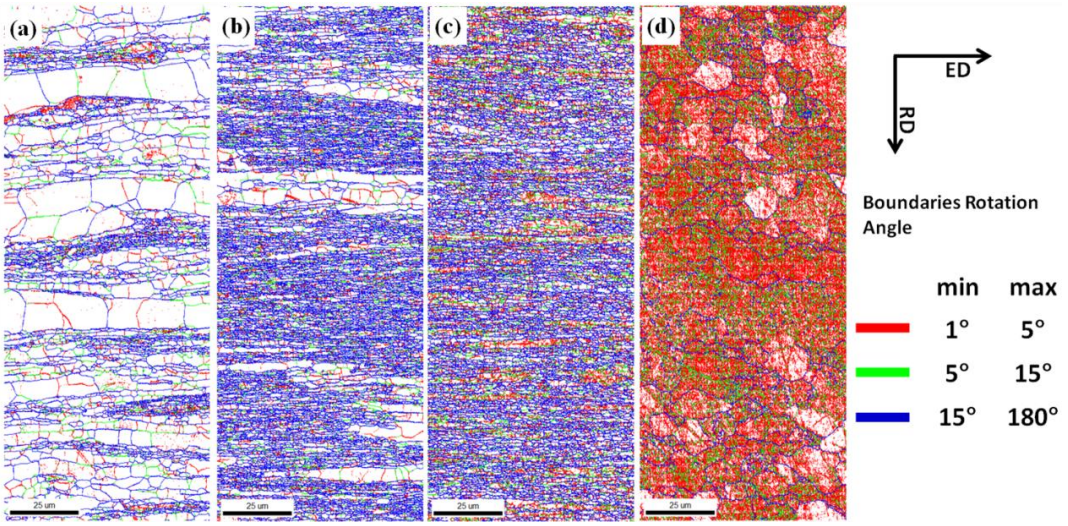

Fig. 4.1.14 Grain boundary character distribution of extruded+annealed samples: a) ODS1, b) ODS3, c) ODS6 and d) NODS.

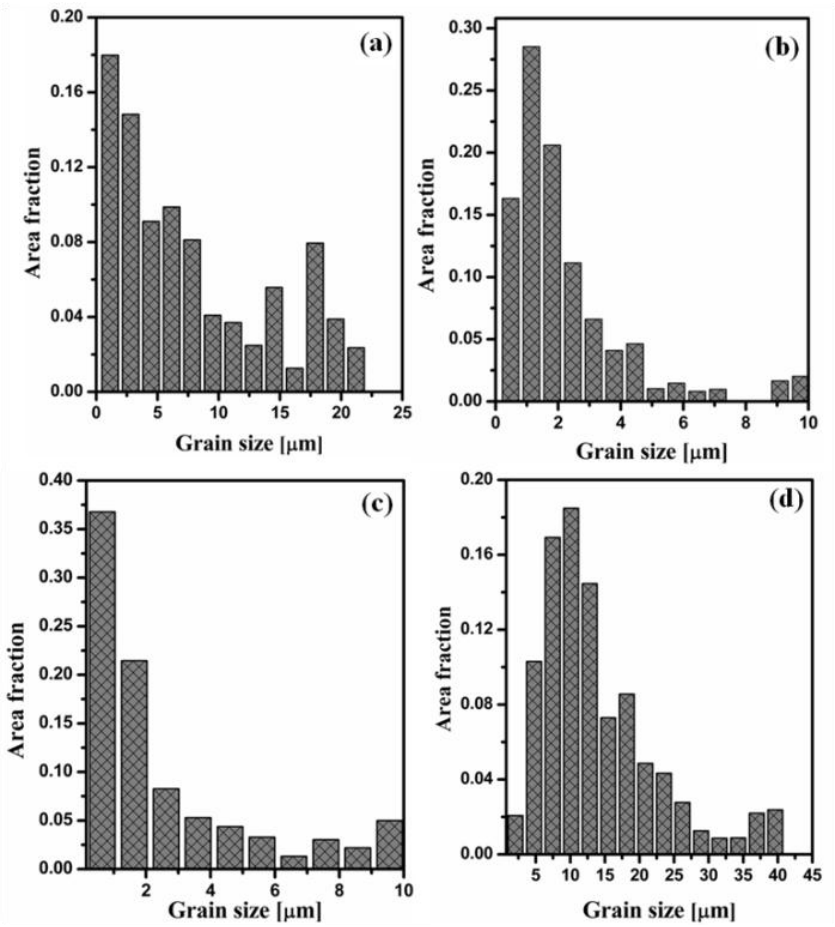

Fig. 4.1.15 Grain size distribution of extruded+annealed samples: a) ODS1, b) ODS3, c) ODS6 and d) NODS.

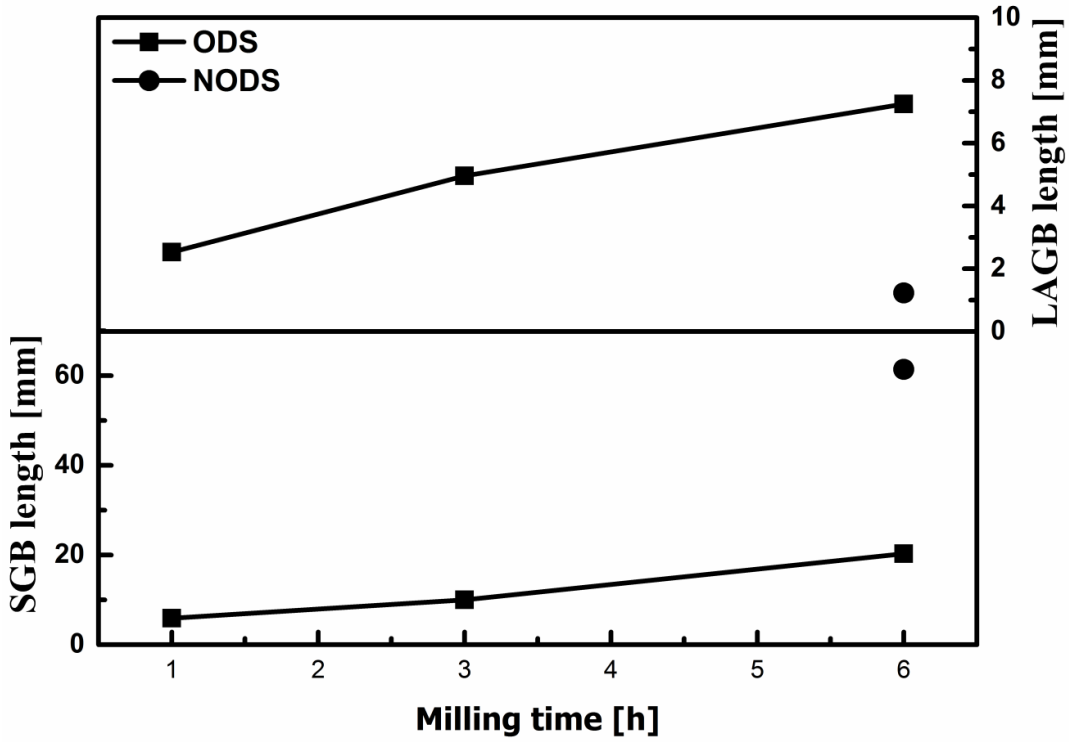

Fig. 4.1.16 Variation of grain boundary length of ODS–18Cr and NODS samples with milling time.

The experimental EBSD results clearly suggest that ODS1 consists of bands with larger grains interspersed with regions of fine grains. The deformed grains have elongated shape parallel to the longitudinal direction in ODS3 and ODS6, grain structure becomes fine and uniform with increasing milling time. Grain size of NODS is an order of magnitude coarser than all ODS samples and it decreases with increasing milling time in ODS samples. There is a dramatic decrease in grain size in ODS6 when compared to NODS which was also milled for 6 h. In general, the fibrous structure tends to become finer in rods made from powders with increasing milling time. The progressive refinement of the fibrous structure with increasing milling time is caused by the decreased size and increased number density of the dispersoids, which retard recrystallization by effectively pinning the grain boundaries during hot working and subsequent annealing. The absence of these stable grain boundary pinning oxide particles is the reason for the observed coarser recrystallized grains in NODS.

Detailed TEM studies were performed on ODS1, ODS3, ODS6 and NODS samples for analyzing the size and morphology of the grains and size, shape and distribution of dispersoids. Typical micrographs obtained on the longitudinal sections are shown in Fig.

4.1.17. While bimodal grain distribution consisting of a large number of elongated grains with few nearly equiaxed grains was observed in all the ODS samples. NODS sample showed large equiaxed grains. The estimated aspect ratios (length/diameter) of the grains (average of a minimum of 250 grains) were 1.99, 1.60 and 1.53 in ODS1, ODS3 and ODS6 respectively. The grain sizes estimated from EBSD and TEM (Table 4.1.2) are comparable. The experimental results suggest that the grains tend to become finer and nearly equiaxed with increasing milling time. The microstructural refinement is considered to be the result of the higher number of finer dispersoids in samples milled for longer milling times.

Table 4.1.2 Average grain diameter of extruded and annealed ODS–18Cr and 18Cr NODS steels.

Sample name	Grain size (d_g), [μm]	
	TEM	EBSD
ODS1	0.51	1.17
ODS3	0.46	0.73
ODS6	0.37	0.48
NODS	10.0	13.0

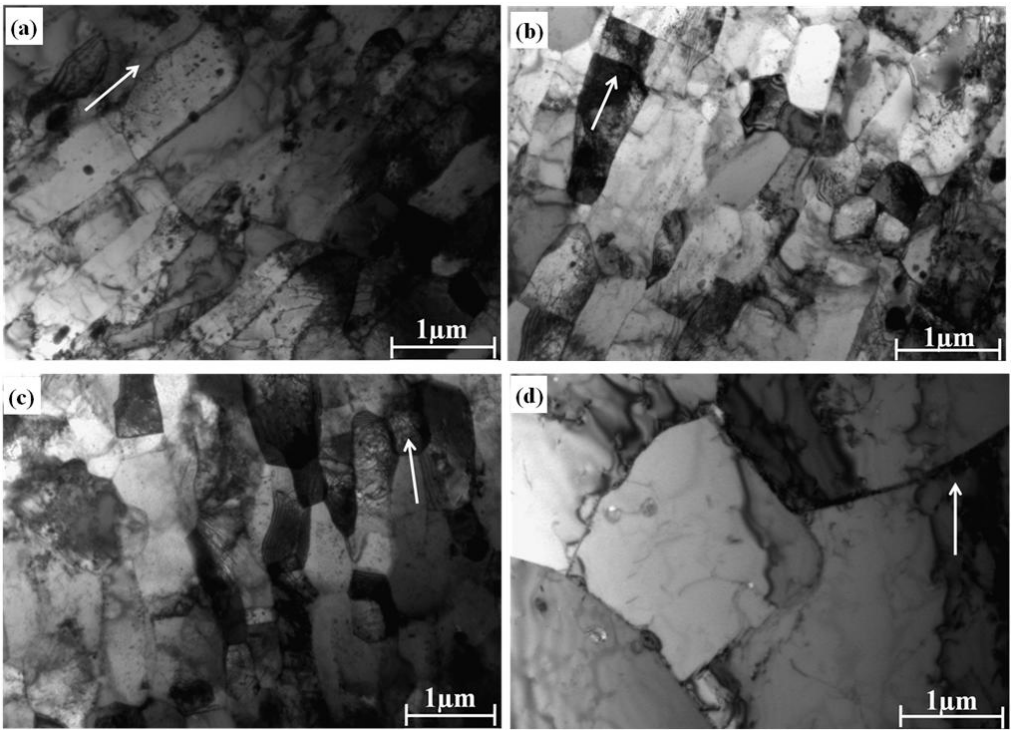

Fig. 4.1.17 TEM images of extruded+annealed samples in longitudinal direction: a) ODS1, b) ODS3, c) ODS6 and d) NODS. (Arrow indicates extrusion direction)

Varieties of oxide particles of varying sizes (2–300 nm) were observed in ODS1 to ODS6. The coarse particles (15–300 nm) were in general, less in number density and therefore were considered only for the purpose of identification. The principle strengthening dispersoids, which are in the size range 2 to 7 nm, were characterized extensively. Typical micrographs of TEM bright field images showing the dispersoids in ODS1, ODS3 and ODS6 are presented in Figs. 4.1.18. The average dispersoid size, number density and volume fraction in ODS1, ODS3 and ODS6 are given in Table 4.1.3. The size distribution of dispersoids in ODS1, ODS3 and ODS6 are shown in Fig. 4.1.19. Comparison of Gaussian distribution of dispersoids in ODS6 at upset forged and extruded+annealed conditions is shown in Fig. 4.1.20. A high resolution lattice image of one of the particles observed in ODS6 along with corresponding Fast Fourier Transformation (FFT) image are shown in Figs. 4.1.21. Critical analysis of the microstructures indicated that: (a) the dispersoids are coarse (size range 4–24 nm) and non uniformly distributed in ODS1, (b) the particles become finer (size range 4–14 nm) and more uniformly distributed in ODS3, (c) the oxide particles are significantly finer with narrow size range (2–7 nm) in ODS6 when compared to ODS1 and ODS3, (d) with increase in milling time the average dispersoids size decreased, the volume fraction was

nearly constant and the number density increased by an order of magnitude, (e) the particles were predominantly of cuboidal shape and (f) high resolution and FFT analysis suggested that the particles in ODS6 are $Y_2Ti_2O_7$ with diamond cubic crystal structure $Fd\bar{3}$m having a lattice parameter of 10.1 Å and the particles are semicoherent with the matrix (Fig. 4.1.21 (b)).

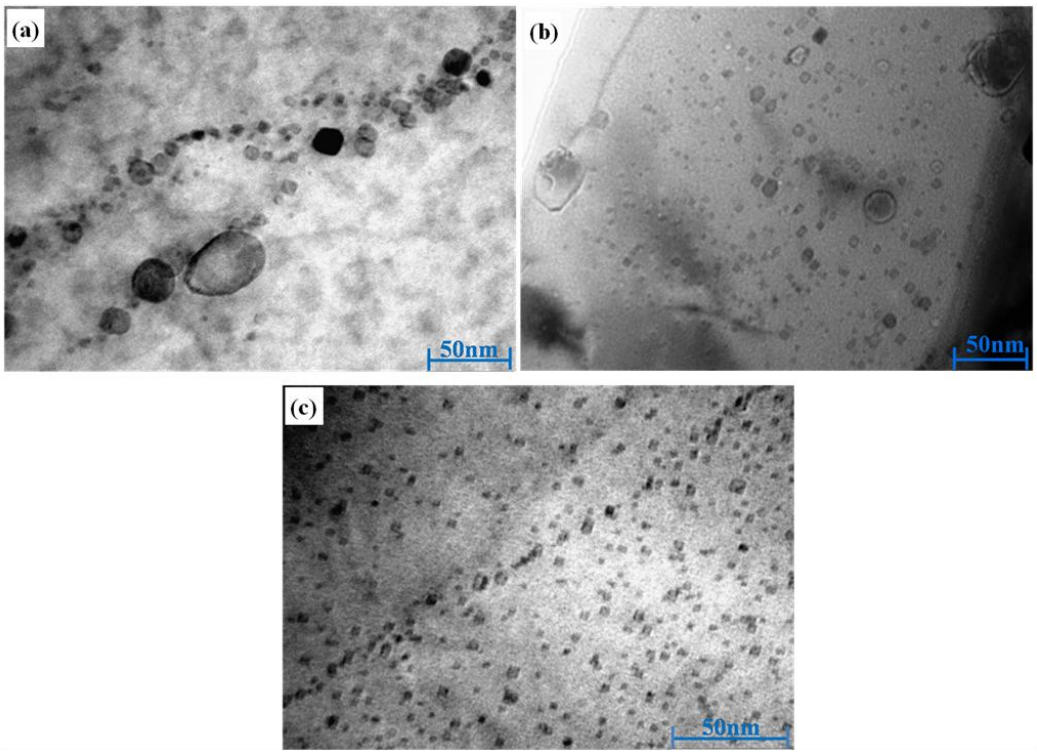

Fig. 4.1.18 TEM bright field images of extruded+annealed ODS–18Cr steel: a) ODS1, b) ODS3 and c) ODS6.

Table 4.1.3 Average size, number density and volume fraction of dispersoids in annealed ODS–18Cr steel.

Name	Average dispersoid size [nm]	Number density (m^{-3})	Volume fraction
ODS1	15 (± 11.76)	$6.21x10^{21}$	0.0092
ODS3	10 (± 7.03)	$1.82x10^{22}$	0.0094
ODS6	5 (±2.35)	$1.24x10^{23}$	0.0096

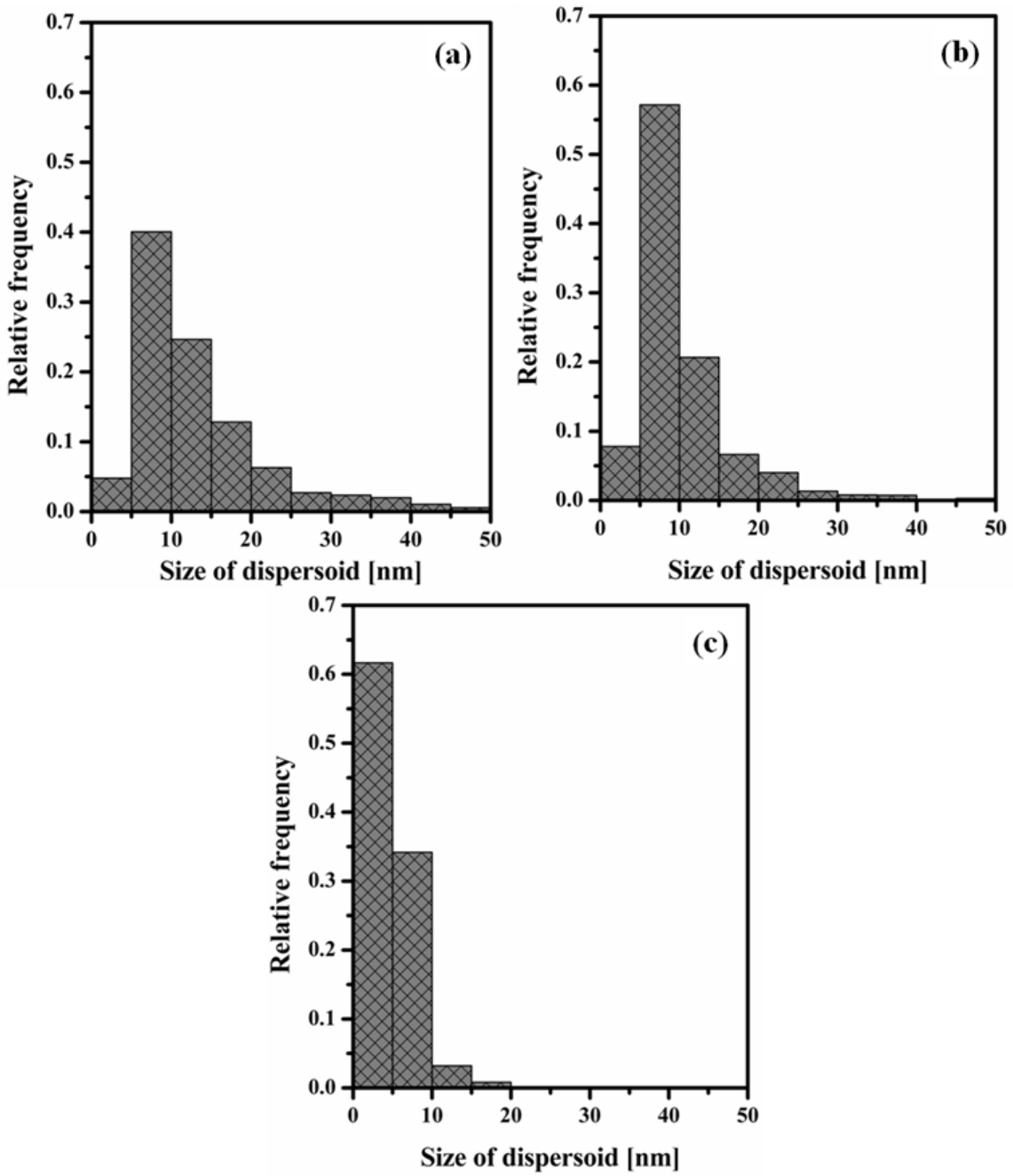

Fig. 4.1.19 Size distribution of dispersoids in extruded+annealed ODS–18Cr steels: a) ODS1, b) ODS3 and c) ODS6.

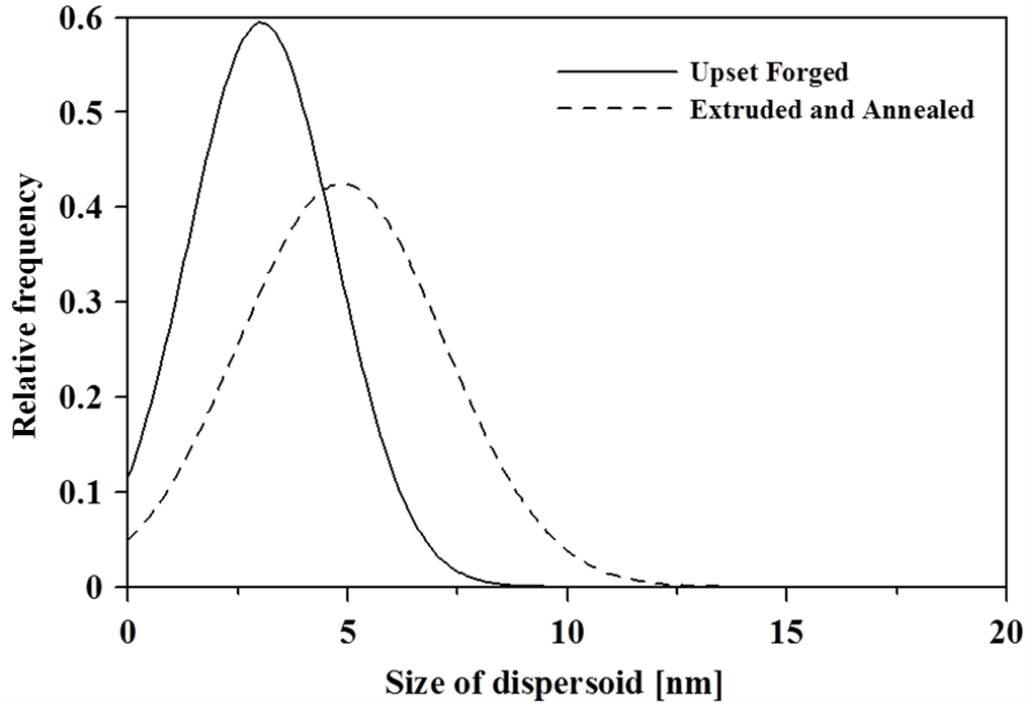

Fig. 4.1.20 Comparison of Gaussian distribution of dispersoids in ODS6 at upset forged and extruded+annealed conditions.

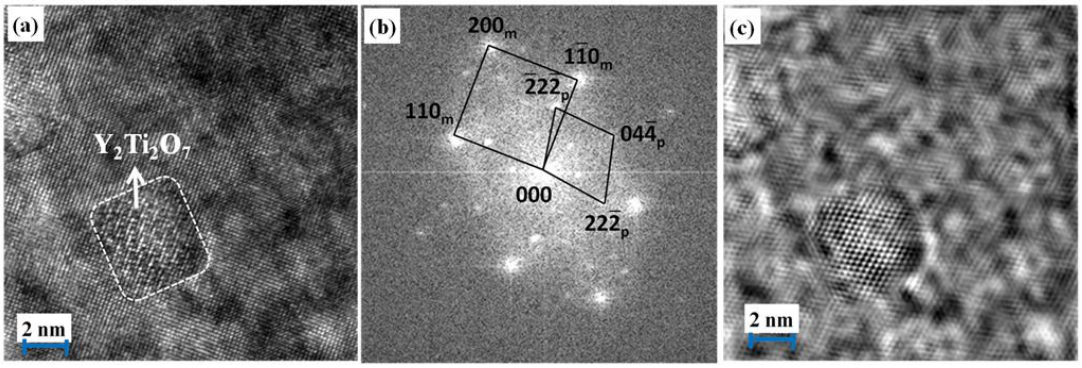

Fig. 4.1.21 HRTEM image of ODS6 taken along [100] orientation (a) $Y_2Ti_2O_7$ particle, (b) indexed FFT of (a) and (c) inverse FFT of (b) created using [222] spots of $Y_2Ti_2O_7$.

The microstructure of the final product (annealed rod) has its origins in the structure of the milled powders and critically depends on the temperature and time of exposure to high temperature during upset forging, extrusion and final annealing. Thermal recovery and recrystallization occurs at each stage of high temperature exposure leading to replacement of low angle cell boundaries in milled powders by subgrain boundaries with relatively higher misorientation angle, which coarsen due to boundary migration or coalescence during each high temperature exposure. The presence of 2–7 nm sized dispersoids effectively retard boundary migration and therefore subgrains can coarsen

only when higher thermal energies are imparted. Since primary recrystallization involves growth of subgrains with high angle boundaries, recrystallization can occur in ODS steels only at temperatures far higher than those for NODS steels of similar compositions. The final microstructure of annealed ODS steels depends on the balance between the driving force (reduction in the elastic energy of stored dislocations) and the dragging force (grain boundary surface energy minimization being retarded by the pinning effect of particles). The gradual decrease in grain size from ODS1 (0.5 μm) to ODS6 (0.37 μm) is the direct consequence of increased efficiency of the drag exerted by a larger number of finer particles in ODS6. Recent studies on ODS ferritic steels supported the fact that complete recrystallization does not occur even after annealing at 1200 °C [11, 12].

Along with matrix microstructure development, evolution of oxide particles occurs during high temperature exposure starting from the state in which these particles exist in milled powders. The experimental results indicate that the oxide particles are of $Y_2Ti_2O_7$ type and that the average dispersoid size decreases gradually (with increasing milling time of powders) and stabilize at the observed size range of 2–7 nm in ODS6. The coarser $Y_2Ti_2O_7$ particles in ODS1 and ODS3 are considered to have been formed due to the diffusion of Ti in some of the preexisting Y_2O_3 particles unlike the formation of finer $Y_2Ti_2O_7$ particles in ODS6 from the metastable solid solution containing Y, O and Ti by classical nucleation and growth process. When exposed to high temperatures, $Y_2Ti_2O_7$ type oxide particles are expected to nucleate and grow because of the accelerated diffusivity. However, in spite of repeated exposure of the samples to high temperatures 900–1150 °C, the dispersoids did not grow significantly (3 nm in upset forged and 5 nm in annealed state, Fig. 4.1.20) because of lower Y diffusivity and retarded coarsening due to low interfacial energy. The higher shear modulus and microstructural complexity of $Y_2Ti_2O_7$ also contribute to the retarded growth of dispersoids [16]. The finer nano–sized (2–7 nm) dispersoids observed in ODS6 is in broad agreement with the retarded growth of $Y_2Ti_2O_7$ particles. The shape of $Y_2Ti_2O_7$ is reported to be spherical in ODS–9Cr steels [14–16] and both spherical [8, 17, 18] and cuboidal [10, 13, 19, 20] in ODS–14Cr ferritic steel. In the present study, the $Y_2Ti_2O_7$ particles were found to be of cuboidal shape even at particle sizes of about 2 nm in both upset forged and extruded+annealed conditions. Recently Ribis *et al*. [13] have analyzed various factors influencing the shape and size of dispersoids in detail and concluded that the parameters such as size of the dispersoids, interfacial energy and elastic strain energy between the particle and the matrix determine

the shape of the particle. The experimental results of the present work indicated that the semicoherent $Y_2Ti_2O_7$ particles are of cuboidal shape at all sizes. This finding is in agreement with the postulation that cuboidal particles are formed directly without any intermediate shape change.

High intensity micro focus XRD technique was employed to obtain the different phases present in experimental steels. Fig. 4.1.22 shows the typical XRD patterns of NODS, ODS1, ODS3 and ODS6 samples. Despite of very a small fraction (~0.35 wt. %) of the second phase, major reflections developed from these nano scale oxide particles were recognized. Diffraction peaks from various phases, including the ones developed from the small volume fraction of nano–scale complex oxide particles, were identified and indexed. The main peak corresponds to the metallic matrix, which is ferrite phase with the BCC crystal structure. Strong peaks of TiO were observed in all the samples. In addition, peaks from the complex oxide particles were also found in all ODS–18Cr samples. These oxide particles were identified as $YTiO_3$, Y_2O_3 and Y_2TiO_5 in ODS1. After 3 h of milling, peaks of Y_2O_3, Y_2TiO_5 and $Y_2Ti_2O_7$ were found. $YTiO_3$ was not found in ODS3. In ODS6, Y_2TiO_5 and $Y_2Ti_2O_7$ peaks were observed.

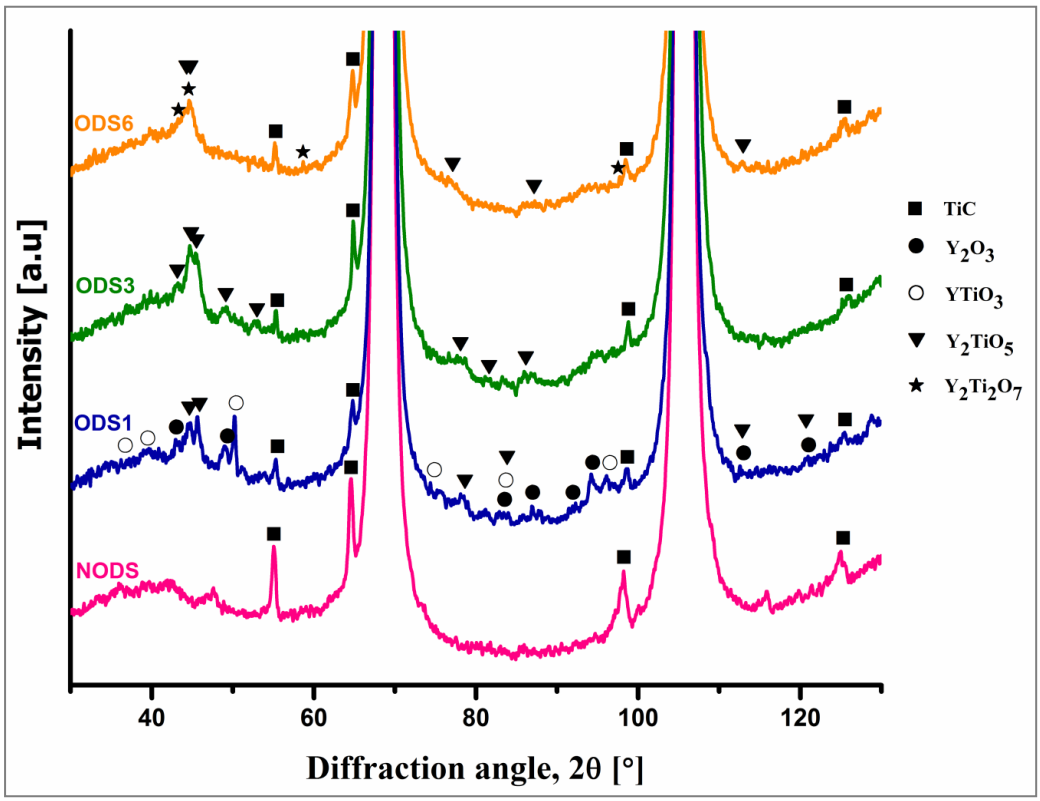

Fig. 4.1.22 Typical XRD–patterns of ODS–18Cr samples along with NODS.

From the detailed TEM analysis, it is evident that different types of oxide particles were present in the matrix and can be classified into two divisions depending on the size range. The prominent type and densely populated ones are the very fine ones and are in the size range of 2–5 nm. They are extensively studied using HRTEM and imaging and are reported as $Y_2Ti_2O_7$. Other than this, coarse oxide particles were also observed in all the samples. To investigate the crystal structure and chemistry of oxide particles in ODS1, ODS3 and ODS6 samples, SAED and EDS techniques respectively were carried out and the phase was determined. In ODS1, it was observed that the oxides of $YTiO_3$ type are predominant along with Y_2O_3 and Y_2TiO_5 and the corresponding BF, SAED and EDS images are shown in Figs. 4.1.23–4.1.25 respectively. As the milling time was increased to 3 h (ODS3), oxides of Y_2O_3, Y_2TiO_5 and $Y_2Ti_2O_7$ were found and the results are shown in Figs. 4.1.26–4.1.28 respectively. In ODS6, it was found that the oxide particles of Y_2TiO_5 (Fig: 4.1.29) and $Y_2Ti_2O_7$ (Fig: 4.1.30) were found and these particles have finer size when compared to that of in ODS1 and ODS3. Ti–enrich particles were also present in all the samples, which have face centered cubic (FCC) crystal structure with a = 4.3 Å matches with TiO and the evidence is shown in Fig. 4.1.31. The major phases observed by X–ray diffraction were also confirmed by electron microscopic studies.

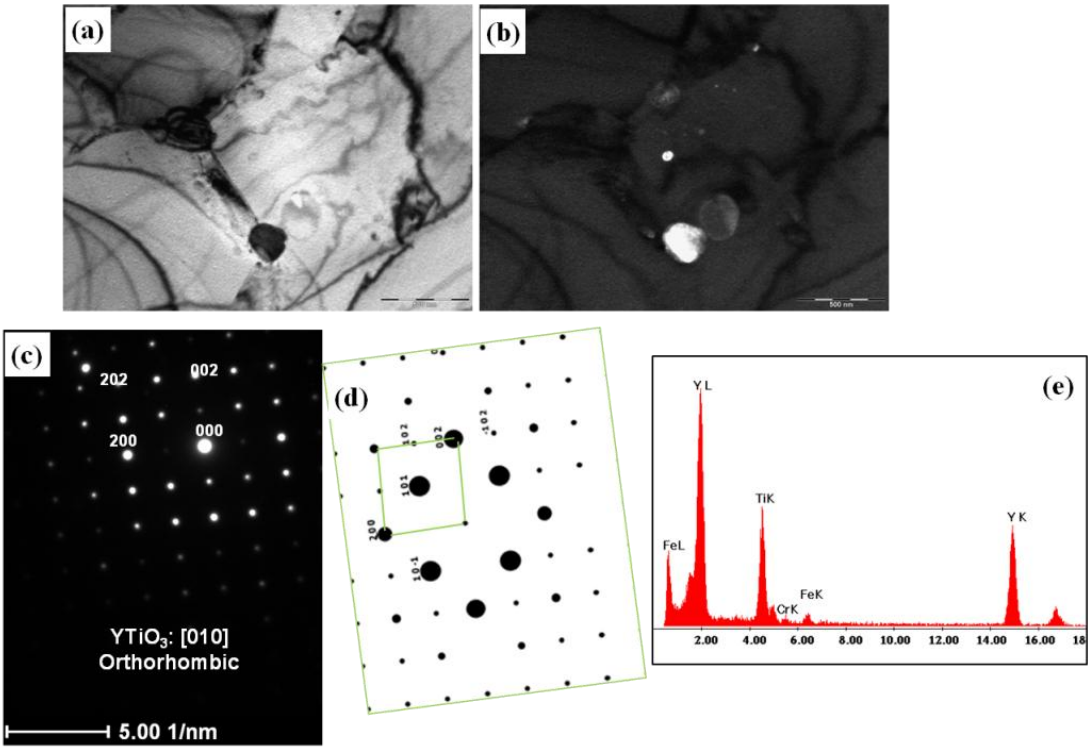

Fig. 4.1.23 TEM images of $YTiO_3$ in ODS1 a) BF, b) DF, c) SAED pattern, d) simulated ICDD pattern and e) EDS.

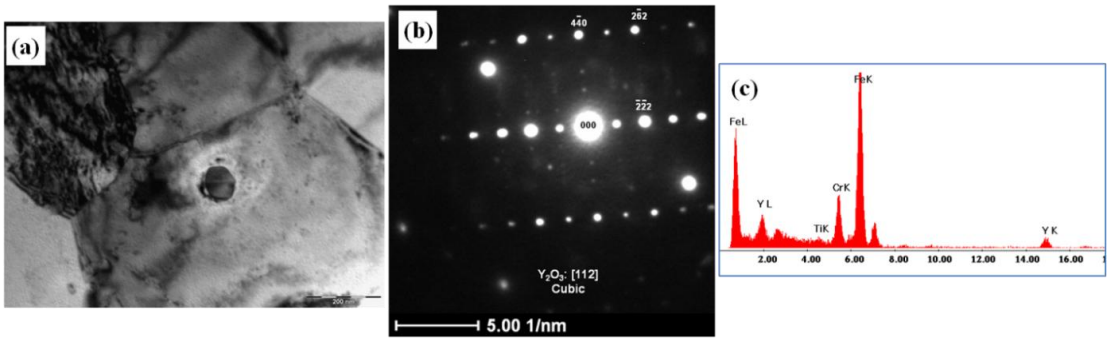

Fig. 4.1.24 TEM images of Y_2O_3 in ODS1 a) BF, b) SAED pattern and c) EDS.

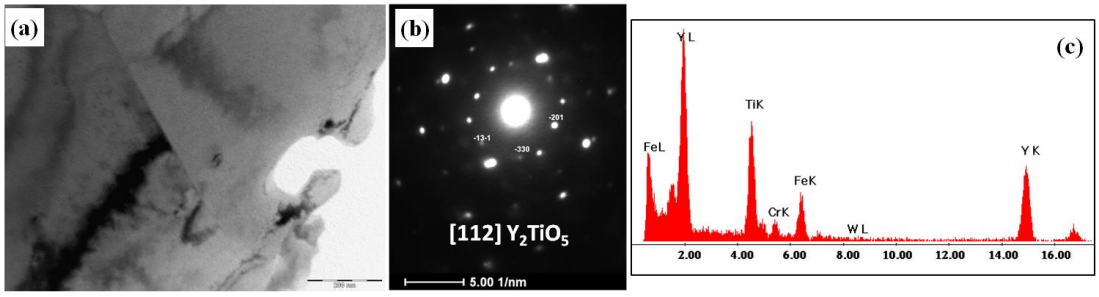

Fig. 4.1.25 TEM images of Y_2TiO_5 in ODS1 a) BF, b) SAED pattern and c) EDS.

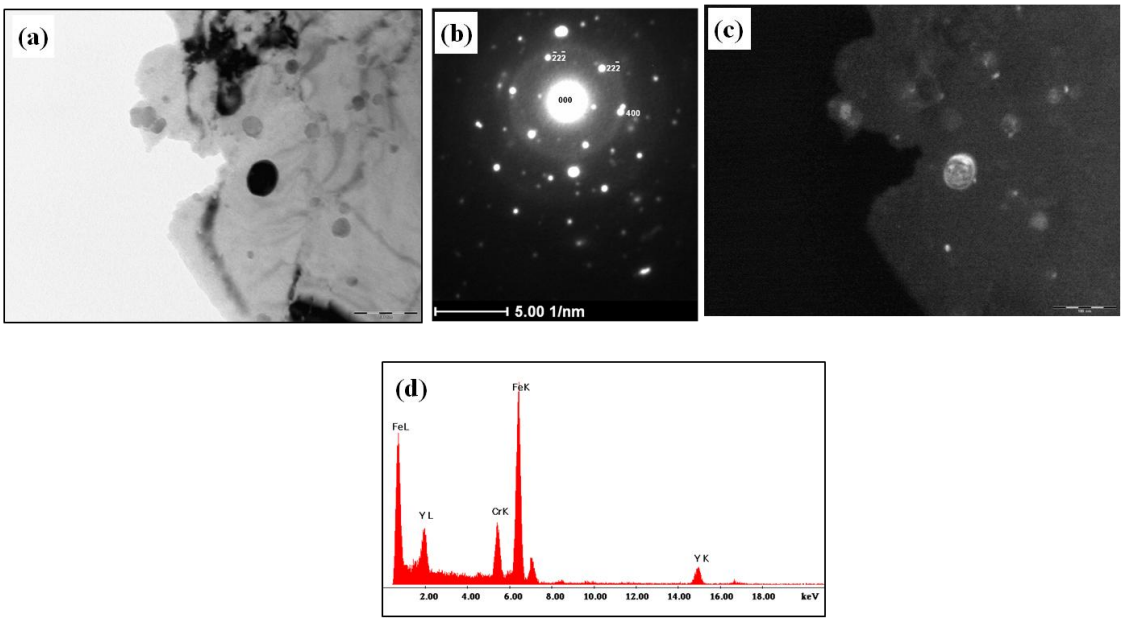

Fig. 4.1.26 TEM images of Y_2O_3 in ODS3 a) BF, b) SAED pattern and c) DF and d) EDS.

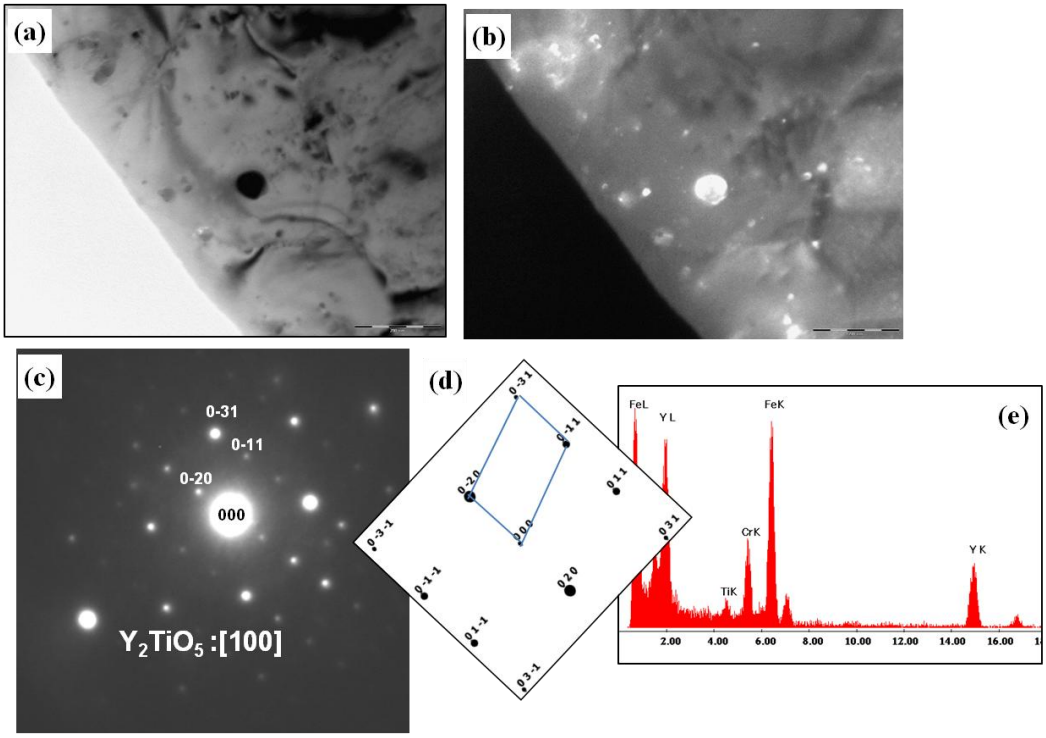

Fig. 4.1.27 TEM images of Y_2TiO_5 in ODS3 a) BF, b) DF, c) SAED pattern, d) simulated ICDD pattern and e) EDS.

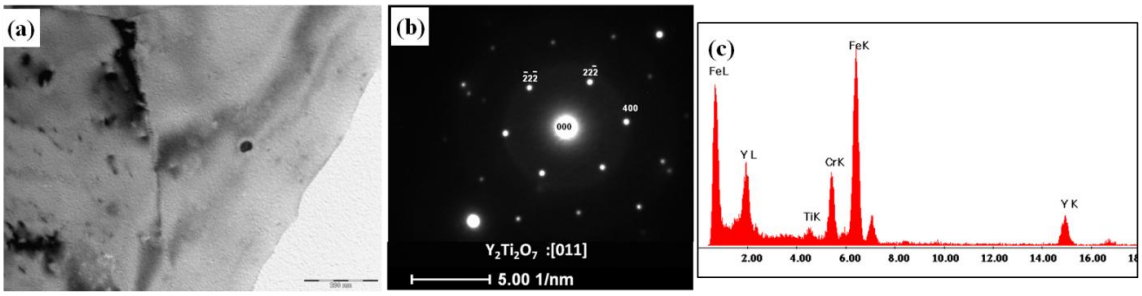

Fig. 4.1.28 TEM images of $Y_2Ti_2O_7$ in ODS3 a) BF, b) SAED pattern and c) EDS.

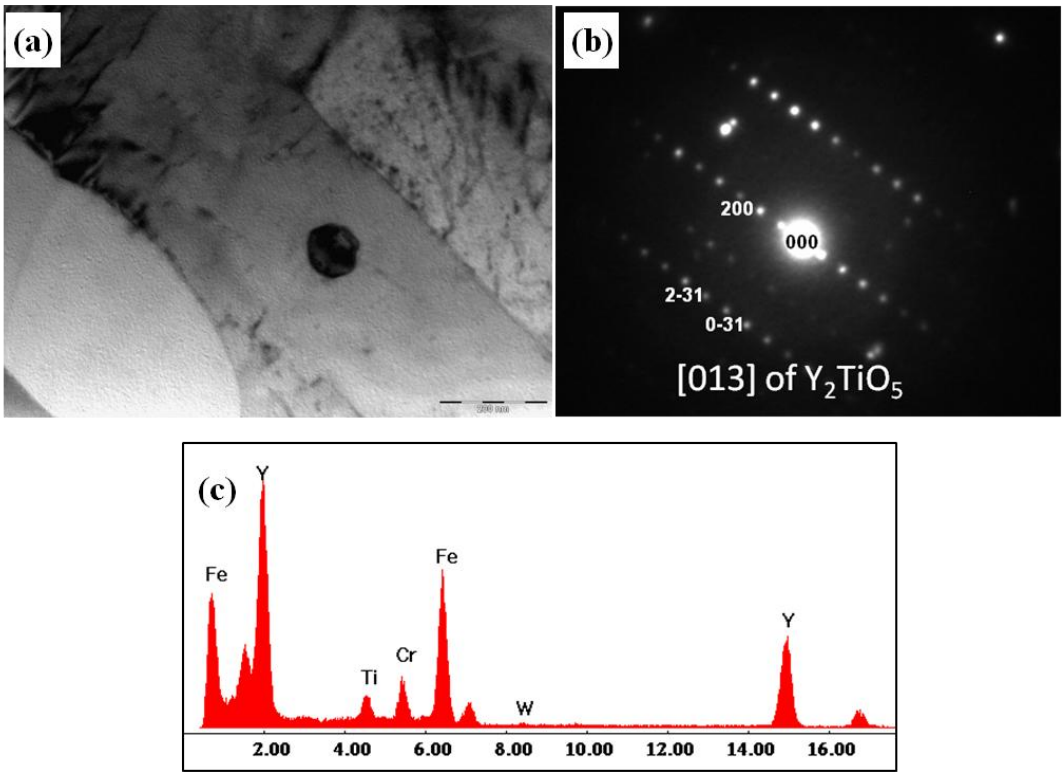

Fig. 4.1.29 TEM images of Y_2TiO_5 in ODS6 a) BF, b) SAED pattern and c) EDS.

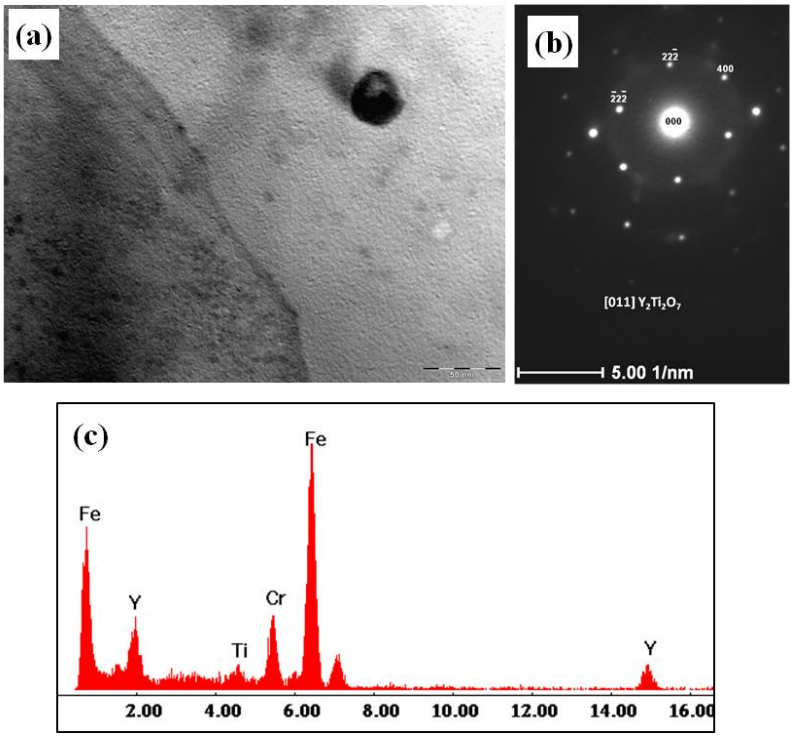

Fig. 4.1.30 TEM images of $Y_2Ti_2O_7$ in ODS6 a) BF, b) SAED pattern and c) EDS.

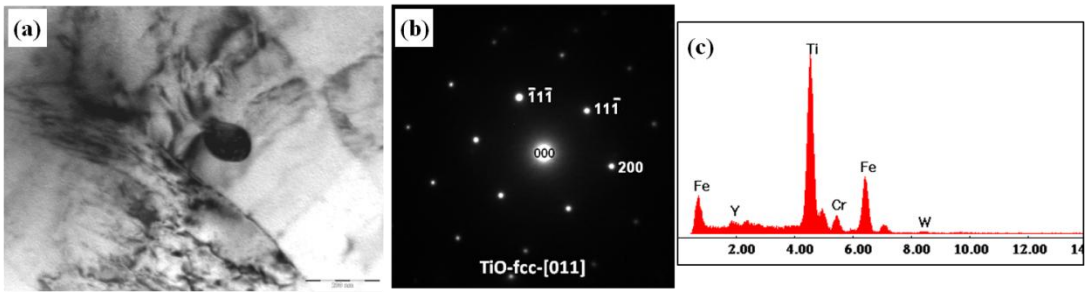

Fig. 4.1.31 TEM images of TiO a) BF, b) SAED pattern and c) EDS.

4.1.5 Summary

Influence of milling time on the microstructural changes that occur in ODS–18Cr ferritic steel during milling and subsequent hot consolidation of the milled powders was investigated. Particle size of ODS–18Cr steel milled powders decreased with milling time reaching a steady state value of 139 μm after 5 h of milling and is finer than 18Cr steel milled powder without yttria. Crystallite size of ODS–18Cr steel milled powders also decreased with milling time reaching a steady value of 16 nm after 5 h of milling. The size of yttria particles decreases during the initial stages of milling and the oxide particles are not resolvable at longer milling times (6 h). The microstructure of the extruded and annealed ODS–18Cr steel indicated the presence of fibrous grain structure and the structure being finer in ODS6. On the contrary, NODS showed coarse equi–axed grain structure. Coarse and non–uniformly distributed oxide particles were observed in ODS1 and ODS3 and the particles are finer (2–7 nm) and uniformly distributed in ODS6. The semi coherent oxide particles in ODS6 are of cuboidal $Y_2Ti_2O_7$ with diamond cubic crystal structure ($Fd\bar{3}m$) having a lattice parameter of 10.1 Å. The major phases observed by X–ray diffraction were also confirmed by electron microscopic studies.

References

[1] C. Suryanarayana, Mechanical alloying and milling, *Progress in Material Science*, 46 (2001) 1–184.

[2] B.S. Murty, S. Ranganathan, Novel materials synthesis by mechanical alloying/milling, *International Materials Reviews*, 43 (1998) 101–144.

[3] R. Vijay, M. Nagini, J. Joardar, M. Ramakrishna, A.V. Reddy, G. Sundararajan, Strengthening mechanisms in mechanically milled oxide dispersed iron powders, *Metallurgical and Materials Transactions A*, 44A, (2013) 1611–1620.

[4] H. Zhang, M.J. Gorley, K.B. Chong, M.E. Fitzpatrick, S.G. Roberts, P.S. Grant, An in situ powder neutron diffraction study of nano precipitate formation during processing of oxide dispersion strengthened ferritic steels, *Journal of Alloys and Compounds*, 582 (2014) 769–773.

[5] B. Dousti, R. Mojaver, H.R. Shahverdi, R.S. Mamoory(2013) Microstructural evolution and chemical redistribution in Fe–Cr–W–Ti–Y_2O_3 nanostructured powders prepared by ball milling, *Journal of Alloys and Compounds*, 577 (2013) 409–416.

[6] J. Gil Sevillano, P. van Houtte, and E. Aernoudt, Large strain work hardening and textures, *Progressive Material Science*, 25 (1981) 69–412.

[7] G. Ressel, S. Primig, H. Leitner, The evolution of Y distribution during the processing route of mechanically alloyed iron studied by means of atom probe tomography, International *Journal of Material Research*, 104 (2013) 1088–1095.

[8] C.A. Williams, P. Unifantowicz, N. Baluc, G.D.W. Smith, E.A. Marquis, The formation and evolution of oxide particles in oxide–dispersion–strengthened ferritic steels during processing, *Acta Materialia*, 61 (2013) 2219–2235.

[9] M.L. Brocq, F. Legendre, M.–H. Mathon, A. Mascaro, S. Poissonnet, B. Radiguet, P. Pareige, M. Loyer, O. Leseigneur, Influence of ball–milling and annealing conditions on nanocluster characteristics in oxide dispersion strengthened steels, *Acta Materialia*, 60 (2012) 7150–7159.

[10] M.C. Brandes, L. Kovarik, M.K. Miller, M.J. Mills, Morphology, structure and chemistry of nanoclusters in a mechanically alloyed nanostructured ferritic steel, *Journal of Materials Science*, 47 (2012) 3913–3923.

[11] C.A. Williams, G.D.W. Smith, E.A. Marquis, The effect of Ti on the coarsening behavior of oxygen–rich nanoparticles in oxide–dispersion–strengthened steels after annealing at 1200 °C, *Scripta Materialia*, 67 (2012)108–111.

[12] Z. Oksiuta, P. Kozikowski, M. Lewandowska, M. Ohnuma, K. Suresh, K.J. Kurzydlowski, Microstructural changes upon annealing in ODS–strengthened ultrafine grained ferritic steel, *Journal of Materials Science*, 48 (2013) 4620–4625.

[13] J. Ribis, Y. de Carlan, Interfacial strained structure and orientation relationships of the nano–sized oxide particles deduced from elasticity–driven morphology in oxide dispersion strengthened materials, *Acta Materialia*, 60 (2012) 238–252.

[14] S. Ukai, Oxide dispersion strengthened steels, *Comprehensive Nuclear Materials*, 4 (2012) 241–271.

[15] S. Ohtsuka, S. Ukai, M. Fujiwara, T. Kaito, T. Narita, Nano–structure control in ODS martensitic steels by means of selecting titanium and oxygen contents, *Journal of Physics and Chemistry of Solids*, 66 (2005) 571–575.

[16] S. Ohtsuka, S. Ukai, M. Fujiwara, T. Kaito, T. Narita, Improvement of 9Cr–ODS martensitic steel properties by controlling excess oxygen and titanium contents, *Journal of Nuclear Materials*, 329–333 (2004) 372–376.

[17] A. Hirata, T. Fujita, Y.R. Wen, J.H. Schneibel, C.T. Liu, M.W. Chen, Atomic structure of nanoclusters in oxide–dispersion–strengthened steels, *Nature Materials*, 10 (2011) 922–926.

[18] P. Olier, J. Malaplate, M.H. Mathon, D. Nunes, D. Hamon, L. Toualbi, Y. de Carlan, L. Chaffron, Chemical and microstructural evolution on ODS Fe–14CrWTi steel during manufacturing stages, *Journal of Nuclear Materials*, 428 (2012) 40–46.

[19] J. Ribis, M.–L. Lescoat, S.Y. Zhong, M.–H. Mathon, Y. de Carlan, Influence of the low interfacial density energy on the coarsening resistivity of the nano–oxide particles in Ti–added ODS material, *Journal of Nuclear Materials*, 442 (2013) S101–S105.

[20] Z. Oksiuta, M. Lewandowska, K.J. Kurzydłowski, Mechanical properties and thermal stability of nanostructured ODS RAF steels, *Mechanics of Materials*, 67 (2013) 15–24.

4.2 Tensile Deformation and Fracture Behavior of Oxide Dispersion Strengthened 18Cr Ferritic Steel

4.2.1 Introduction

The process parameters employed in the manufacture of ODS steels have strong influence on the development of microstructure of the matrix and the size and number density of dispersoids. The literature available on the high temperature deformation behavior of ODS–18Cr ferritic steels is scanty, when compared to the ODS–14Cr ferritic steels. Considering the possibility of usage of ODS–18Cr steels for high temperature applications, there is a distinct need to understand the deformation behavior at different temperatures. The plastic deformation behavior of ODS steels at different temperatures and strain rates depends on the complex interrelationship between the deformation characteristics of individual phases. It is shown that ODS–18Cr steel made from powder milled up to steady–state conditions, consists of a ferritic matrix with bimodal grain structure, the average grain size being 480 nm and large number density of cuboidal $Y_2Ti_2O_7$ (2–7 nm) oxide dispersoids. The strength of this material should therefore, consist of contributions from the solid solution strength of the matrix, the strengthening effect of ultra–fine grain structure and the dispersoid strengthening induced by the oxide particles. The strain hardening behavior and the relative role of athermal and thermal deformation mechanisms vary with the temperature of deformation. In this chapter, the influence of powder milling time (microstructural changes depend on milling time) on the tensile deformation and fracture behavior of ODS–18Cr steel at different temperatures and compared with oxide–free 18Cr steel. The experimental strength values were rationalized using appropriate model.

4.2.2 Microhardness of milled powders

The effect of milling time on the microhardness of 18Cr and ODS–18Cr steel powders is shown in Fig. 4.2.1. The hardness of both steel powders was found to increase with milling time sharply at lower milling times, at reduced rate at higher milling times and finally reached a nearly steady state beyond 5 h of milling. Progressive increase in strain accumulation with increasing milling time accounts for the initial sharp rise in hardness, whereas the attainment of stabilized cell structure at higher milling times leads to saturation in hardness. The difference between the hardness of 18Cr and ODS–18Cr steel powders is nearly constant (≈30 HV) at all milling times. The reason for this behaviour

can be assessed by careful examination of the variation of projected area hardness (PAH) of 18Cr and ODS–18Cr steel powders as a function of crystallite size, which is dependent on milling time. The variation of PAH of 18Cr and ODS–18Cr steel powders with crystallite size is shown in Fig. 4.2.2. At any given crystallite size and milling time, hardness of ODS–18Cr steel powder is higher than the 18Cr steel powder. It is evident from the data presented in Fig. 4.2.2 that a) the hardness difference between 18Cr and ODS–18Cr steel powders at any given crystallite size is probably due to the contribution from the Orowan stress (presence of dispersoids) and b) at lower crystallite sizes (higher milling times), the hardness difference is lower because of reduced Orowan contribution due to dissolution of Y_2O_3 particles. It was observed that progressive milling refines the grain size, reduces the number density of Y_2O_3 particles and increases the concentration of Y and O in matrix. The increase in hardness of ODS–18Cr steel powders with milling time is due to the combined effect of all the parameters mentioned above.

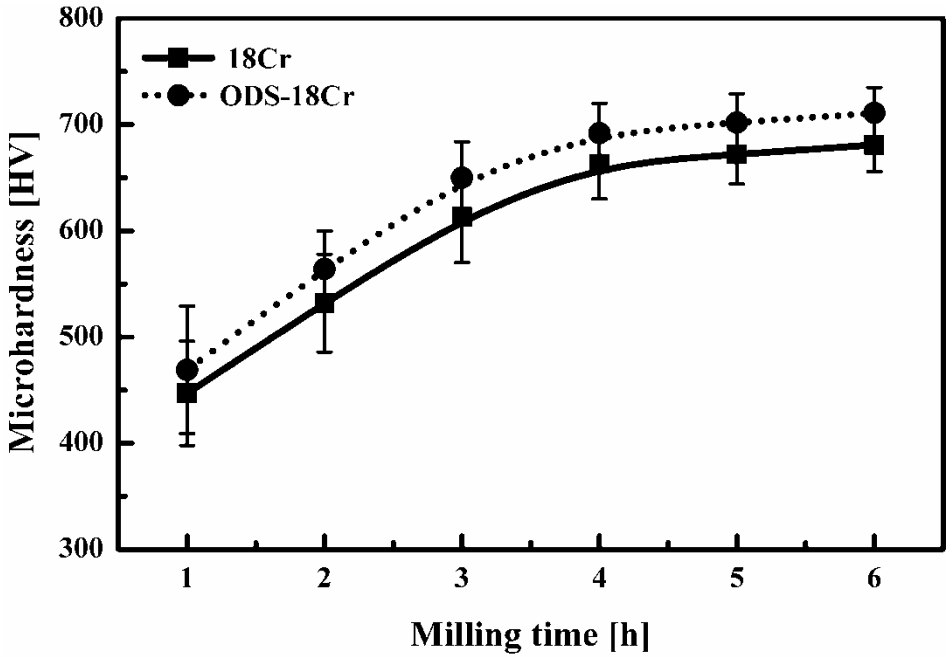

Fig. 4.2.1 Effect of milling time on hardness of 18Cr and ODS–18Cr steel powders.

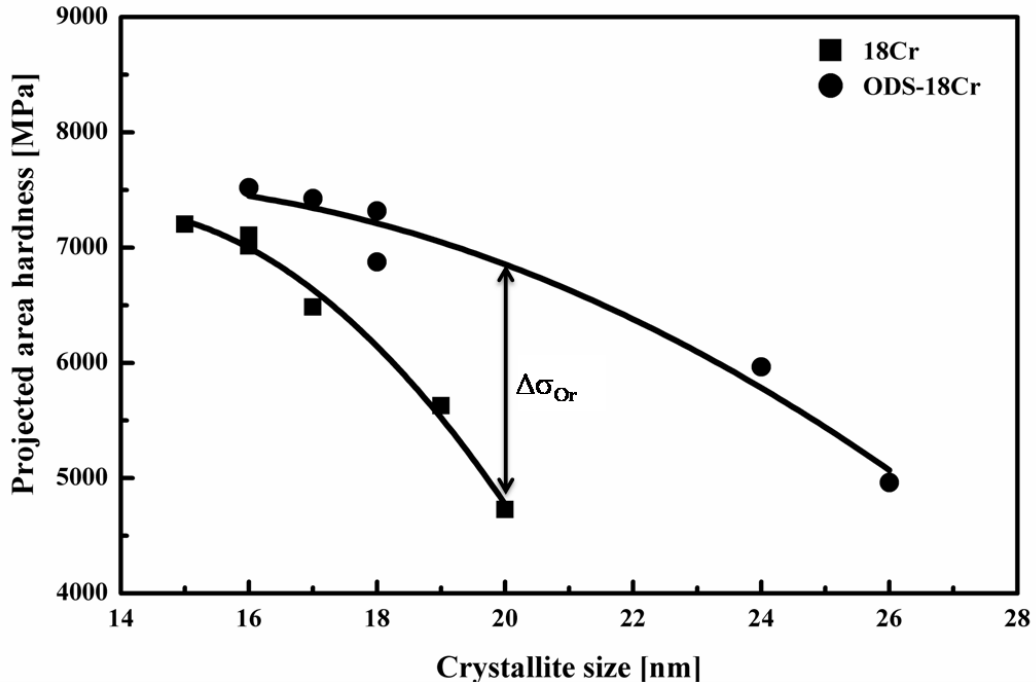

Fig. 4.2.2 Variation of hardness of 18Cr and ODS–18Cr steel powders with crystallite size.

4.2.3 Bulk hardness of consolidated samples

4.2.3.1 Upset forged samples

The hardness of upset forged ODS6 (404 HV) and NODS (201 HV) decreased by about 300 and 480 HV respectively when compared to the respective powders in milled condition. While decrease in dislocation density due to thermally assisted annihilation processes is primarily responsible for the hardness drop in both the steels (Fig. 4.1.9), the relatively lesser drop in upset forged ODS6 is due to the fact that the hardness drop due to recovery processes is partly offset by the increase in hardness due to precipitation of Y–Ti–O oxides (Fig. 4.1.12)

4.2.3.2 Extruded and annealed samples

The PAH of ODS1, ODS3 and ODS6 along with NODS with milling time is shown in Fig. 4.2.3. The hardness of ODS steel is higher than NODS (1608 MPa) and increases from ODS1 (2073 MPa) to ODS6 (3184 MPa). The progressive increase of hardness in ODS steel is due to decrease in size and increase in number density of dispersoids.

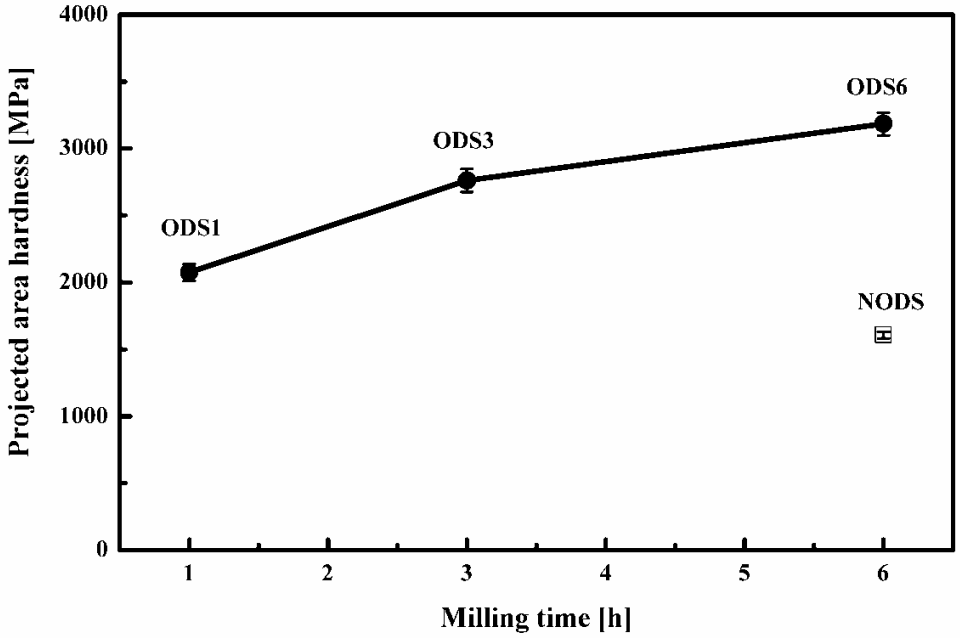

Fig. 4.2.3 Variation of hardness of annealed NODS and ODS–18Cr steels with milling time.

4.2.4 Tensile properties

Tensile tests were carried out on ODS1, ODS3 and ODS6 at room temperature (RT (25)), 200, 400, 600 and 800 °C to assess the effect of milling time and temperature dependence on tensile deformation behavior. The tests were also carried out on NODS samples to examine the role of dispersoids during deformation at different temperatures. The 0.2 % offset yield strength (σ_y), ultimate tensile strength (σ_u), percentage elongation (*% E_l*) and percentage reduction in area (*% R.A*) for the entire test matrix involving variations in milling time and test temperature are presented in Table 4.2.1.

Table 4.2.1 Tensile properties of NODS and ODS–18Cr samples.

	NODS				ODS1				ODS3				ODS6			
Temp [°C]	**YS [MPa]**	**UTS [MPa]**	**% E_l**	**% RA**	**YS [MPa]**	**UTS [MPa]**	**% E_l**	**% RA**	**YS [MPa]**	**UTS [MPa]**	**% E_l**	**% RA**	**YS [MPa]**	**UTS [MPa]**	**% E_l**	**% RA**
25	316 (±2)	526 (±3)	44.00 (±1)	83 (±1)	459 (±1)	687 (±1)	35.00 (±6)	68 (±3)	701 (±4)	889 (±5)	26.55 (±2)	69 (±2)	810 (±18)	967 (±1)	26.30 (±4)	69 (±4)
200	235 (0)	434 (±21)	41.50 (±1)	82 (±0)	391 (±3)	605 (±3)	32.75 (±1)	67 (±2)	622 (±9)	791 (±11)	24.60 (±1)	66 (±1)	743 (±4)	858 (±2)	23.35 (±3)	69 (±2)
400	217 (±1)	370 (±1)	36.50 (±2)	84 (±1)	377 (±17)	511 (±1)	26.60 (±1)	65 (±1)	549 (±15)	648 (±18)	19.20 (±1)	66 (±3)	662 (±23)	729 (±23)	21.30 (±1)	66 (±3)
600	149 (±1)	211 (±5)	41.50 (±3)	84 (±4)	244 (±4)	286 (±11)	27.35 (±4)	69 (±1)	375 (±30)	400 (±34)	20.25 (±1)	68 (0)	453 (±10)	470 (±5)	18.55 (±1)	61 (±1)
800	58 (±13)	62 (±11)	82.00 (±6)	98 (±1)	116 (0)	124 (±4)	27.00 (±2)	66 (±1)	192 (±7)	201 (±6)	20.75 (±4)	59 (±1)	232 (±3)	238 (±4)	18.85 (±2)	48 (±1)

4.2.4.1 Influence of milling time

Typical engineering stress–strain curves for NODS, ODS1, ODS3 and ODS6 at different test temperatures (RT to 800 °C) are shown in Figs. 4.2.4 (a–e). The overall tensile deformation behaviour varied significantly with milling time, but, was similar up to test temperatures below 400 °C. Beyond 400 °C, the deformation trend varied significantly, even though the general trend of increase in strength parameters (σ_y and σ_u) with milling time was retained up to the maximum test temperature of 800 °C used in this study. The variation of ductility indices (uniform strain (e_u) and total strain at fracture (e_t)) with milling time at all test temperatures are shown in Figs. 4.2.5 (a–b).

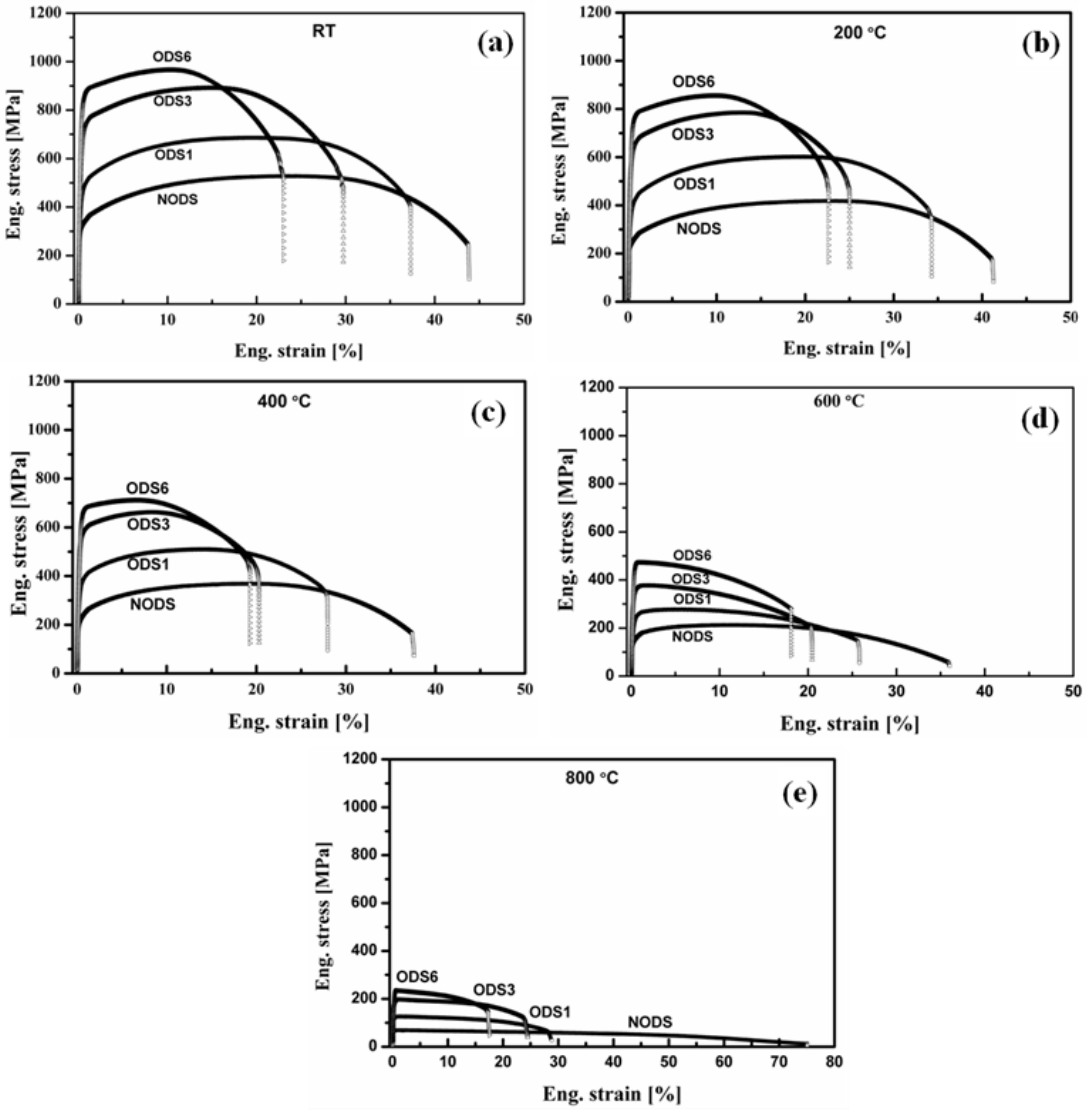

Fig. 4.2.4 Engineering stress–strain curves of NODS, ODS1, ODS3 and ODS6 samples at a) RT, b) 200 °C, c) 400 °C, d) 600 °C and e) 800 °C, respectively.

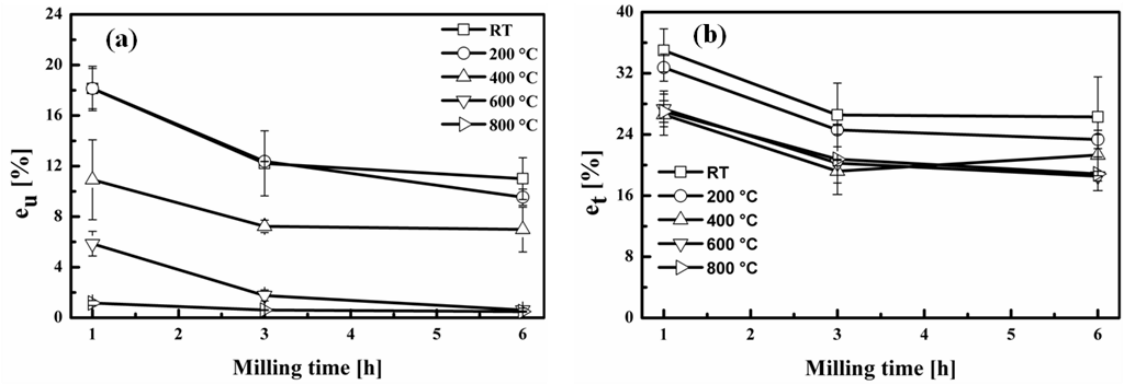

Fig. 4.2.5 Variation of ductility indices (a) e_u and (b) e_t with milling time at all test temperatures.

From the experimental results presented in Figs. 4.2.4, 4.2.5 and Table 4.2.1, it is evident that (a) at any test temperature, the tensile flow behaviour is dependent on milling time, (b) the strength (σ_y and σ_u) increased and ductility (e_u and e_t) decreased marginally with increasing milling time, (c) e_u and e_t of ODS–18Cr steels are lower than those of NODS at identical milling time, (d) the severity of parabolic hardening and the strain up to which parabolic hardening occurs and geometrical softening sets in is maximum for NODS. Both these parameters decreased with increasing milling time up to 400 °C and (e) the parabolic hardening gets restricted significantly to lower strains at temperatures above 400 °C.

4.2.4.2 Influence of temperature

The engineering stress–strain curves of NODS and ODS–18Cr steels at different test temperatures are shown in Figs. 4.2.6 (a–d). The uniform (e_u) and fracture strains (e_t) for NODS and ODS–18Cr steels are shown in Figs. 4.2.7 (a–b).

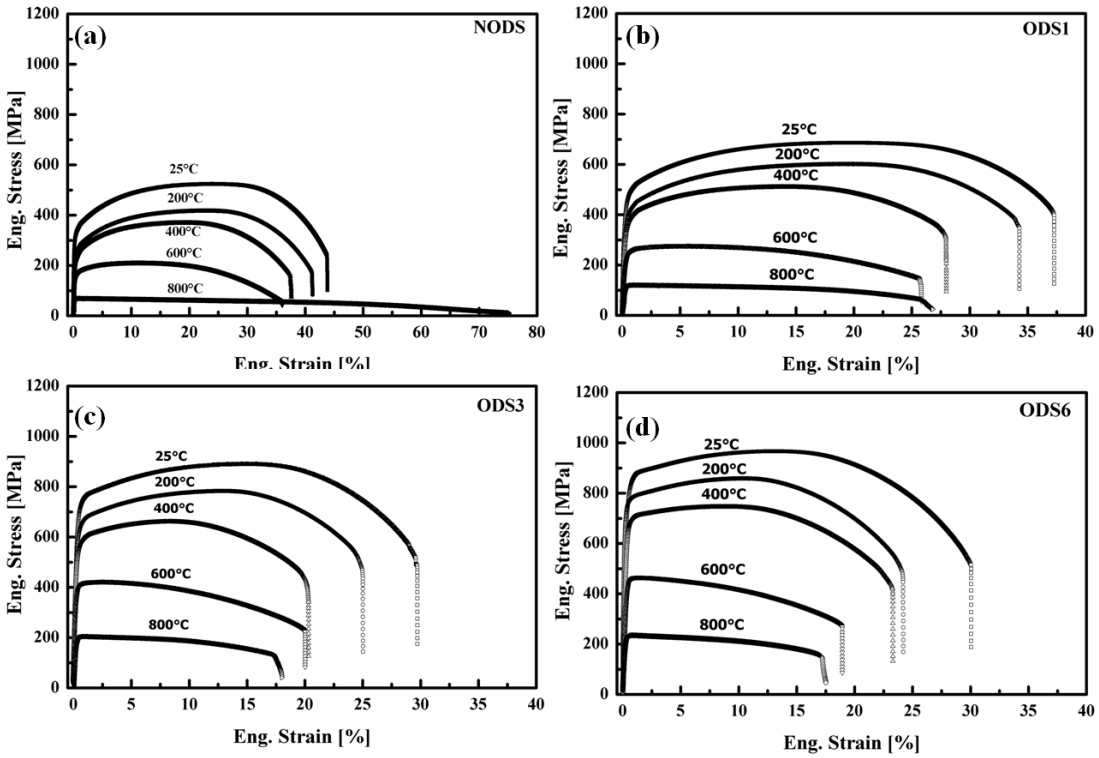

Fig. 4.2.6 Engineering stress–strain curves at different test temperatures of (a) NODS (b) ODS1, (c) ODS3 and (d) ODS6

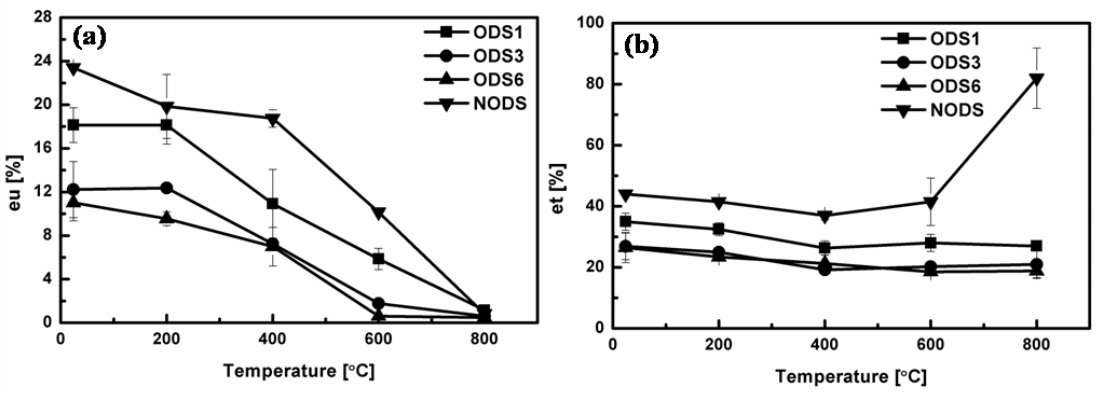

Fig. 4.2.7 Variation of ductility indices (a) e_u and (b) e_t of NODS and ODS samples with test temperature.

The combined effect of milling time and temperature on the tensile properties was analysed. The variation of σ_y and σ_u of ODS1, ODS3 and ODS6 along with NODS with temperature is shown in Figs. 4.2.8 (a–b) respectively.

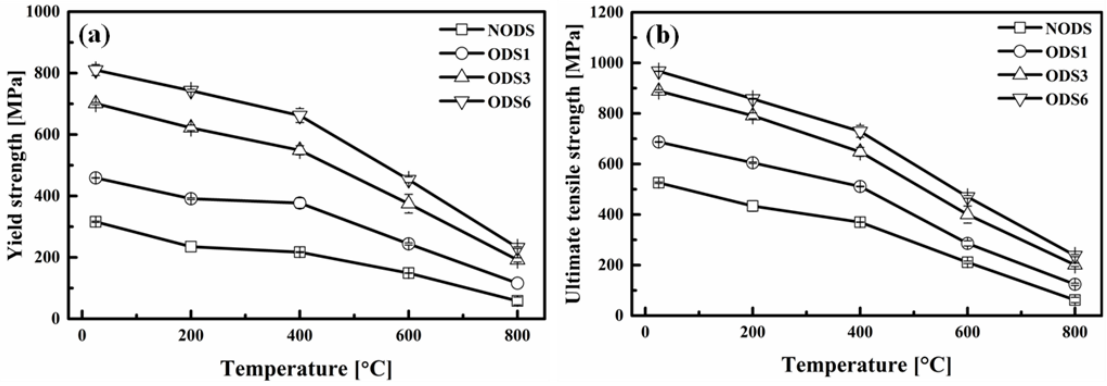

Fig. 4.2.8 Variation of (a) σ_y and (b) σ_u with test temperature of ODS1, ODS3 and ODS6 along with NODS.

Strain hardening exponent (n), was obtained from the empirical relationship, $\sigma = k\varepsilon^n$ (Ludwik–Hollomon) using the true stress (σ)–true strain (ε) data. The variation of 'n' estimated over the strain range of 0.2 % to uniform strain with milling time and test temperature is shown in Fig. 4.2.9.

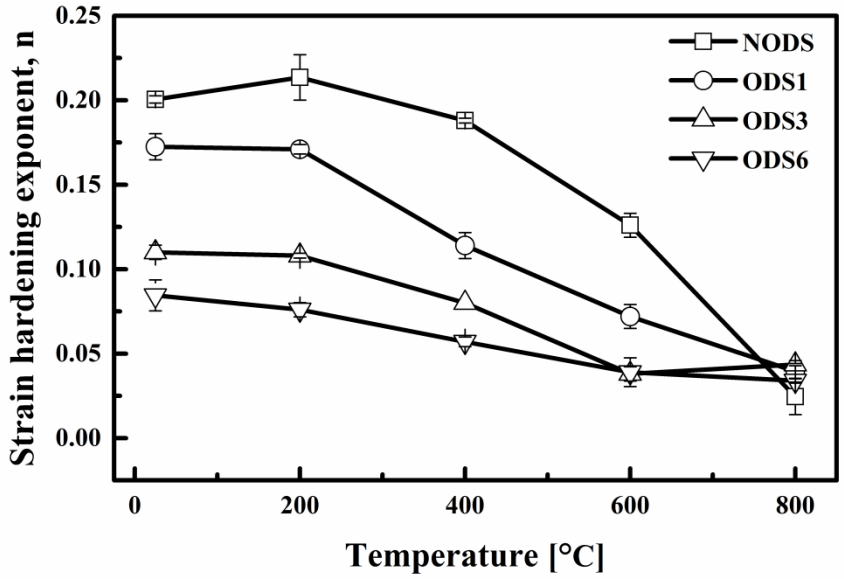

Fig. 4.2.9 Variation of strain hardening exponent with milling time and test temperature.

From the tensile data presented in Figs. 4.2.6–4.2.9 and Table 4.2.1, it is clear that the test temperature has significant effect on the flow behaviour of both ODS–18Cr and NODS

samples. The results indicate that (a) with increasing temperature, the shape of tensile curves of both ODS–18Cr and NODS samples changed from the characteristic yielding→work hardening→necking→fracture mode below 400 °C to yielding→necking→fracture mode at higher temperatures, (b) all the ODS–18Cr samples, showed higher σ_y and σ_u than NODS at all test temperatures, (c) both σ_y and σ_u decreased with increasing temperature: the decrease being relatively smaller in ODS–18Cr steel, (d) the intensity of work hardening and the strain at which geometrical softening occurs decrease with increasing temperature: both the parameters being lower in ODS–18Cr when compared to NODS steel, (e) '*n*' of NODS and ODS–18Cr samples decreases with temperature reaching an insignificant value at 800 °C and it is higher for NODS than all the ODS–18Cr samples up to 600 °C, (f) '*n*' of ODS steels decreases with increasing milling time at all test temperatures, (g) e_t decreased with increasing milling time in ODS steels at all temperatures, (h) while e_u decreased continuously with increasing temperature in both the steels, e_t remained nearly the same up to 600 °C and increased dramatically beyond 600 °C in NODS steel sample and (i) e_u of NODS is higher than that of ODS–18Cr steel with similar milling time and at all temperatures.

The strength values of all the ODS–18Cr steels are higher than those of NODS steel and the strength increases with increasing milling time. This behaviour is due to the decreased grain and dispersoid sizes with milling time resulting in enhanced contributions from grain boundary and dispersoid strengthening to the total strength. The progressive decrease in grain size leading to the formation of ultrafine grain structure results in the initial increase in strain hardening at extremely low strains. Strain hardening rate in ultrafine grained materials is increased due to increased density of geometrically necessary dislocations [1]. The strain hardening reduces at higher strains due primarily to reduced number of dislocations stored in the grain interiors, because of the enhanced annihilation of moving dislocations at the abundantly available grain boundaries. Further, if the dispersoid size is smaller, recovery is easier and hence the work hardening is reduced as was experimentally observed [1]. The decreasing dispersoid size with milling time pins the statistically stored dislocations promoting the formation of cell structure. Smaller the dispersoid size, easier the dynamic recovery and lower the strain hardening. The gradual decrease in strain hardening during the tensile flow behaviour of ODS–18Cr steels with milling time can thus be attributed to continued decrease in grain size and dispersoid size.

The influence of temperature and milling time on the tensile deformation behaviour can also be explained in terms of the strain hardening, onset of dynamic and thermal recoveries, the effectiveness of dispersoids in dislocation pinning and the grain refinement. The high strength of ODS–18Cr steels when compared to NODS at all temperatures can be attributed to the refinement in dispersoid size. The decrease in strain hardening with increasing temperature at all milling times (Figs. 4.2.6 and 4.2.9) is the result of the increased dynamic/thermal recovery caused by enhanced mobility of dislocations in nanocrystalline materials and the reduced efficacy of dispersoids in pinning dislocations. The gradual decrease in uniform and fracture strains with milling time (Fig. 4.2.7) in all ODS–18Cr steels is caused by decreasing strain hardening. Further refinement in grain size and dispersoid size limits the ductility due to inhomogeneous deformation. The NODS steel shows drastic increase in fracture strain beyond 600 °C. The superplastic behaviour of NODS can be attributed near zero strain hardening exponent, favorable temperature, grain structure and strain rate hardening exponent. The ODS–18Cr steels on the other hand showed decrease in fracture strain due to the stability of microstructure which promotes inhomogeneous deformation and pinning of grain boundaries by oxide particles inhibiting grain boundary sliding even at high temperatures.

Flow stress was found to decrease in both NODS and ODS–18Cr steels up to 800 °C. The relative drop in strength with temperature was low up to 400 °C beyond which the strength drops rapidly (Fig. 4.2.8). At temperatures below 400 °C, athermal mechanisms dominate plastic deformation. The drop in flow stress with temperature has been attributed to decrease in Peierls stress [2] and elastic modulus [3] with temperature. The stress drop is also attributed to the formation of micro cracks [4] during deformation. At high temperatures (>400 °C), thermally activated mechanisms control plastic flow [2, 5]. The sharp decrease in flow stress with temperature is considered to be due to the increased ease with which dislocations can climb and detach from the particles and strain softening caused by dislocation annihilation [6]. In the absence of dispersoids, the drop of flow stress in NODS can be attributed to thermal recovery.

4.2.5 Prediction of flow stress

An attempt was made to predict the various strengthening mechanisms operating in ODS1, ODS3 and ODS6 alloys. It is well known that the dominant mechanisms for the improved strength of ODS steels are grain boundary strengthening (Hall–Petch) and dispersion hardening. The hardening effect due to dispersoids is because of dislocations cutting the dispersoids or due to bowing around the dispersoids (Orowan strengthening). Whether the dislocation cuts or bows around the dispersoid depends on the hardness, size of the dispersoids and the coherency of dispersoid–matrix interface. Dislocations cannot cut the incoherent dispersoids and hence Orowan bowing is the only possible mechanism. Recent work suggests that in case of $Y_2Ti_2O_7$ dispersoids, these are semicoherent in nature [7] and thus, in principle, dislocations can cut through the dispersoids. However, if the dispersoids are non–deformable due to their high hardness, then also Orowan bowing is the preferred mechanism. In the present study, the hardness of $Y_2Ti_2O_7$ (12.1 ± 0.1 GPa) is much higher than that of Y_2O_3 (6.9 to 9 GPa) [8] and thus cutting of $Y_2Ti_2O_7$ dispersoid is quite unlikely. Thus the yield strength of ODS steels is due to the combination of the inherent matrix strength (σ_m), grain size strengthening ($\Delta\sigma_{H-P}$) as per Hall–Petch relationship and Orowan strengthening due to bowing of dislocations around dispersoids ($\Delta\sigma_{Or}$).

4.2.4.1 Based on hardness data

The room temperature strengths (PAH=$3\sigma_y$) of NODS (σ_{yNODS}) and ODS–18Cr (σ_{yODS}) steels are given by the following equations [9–11]:

$$\sigma_{yNODS} = \sigma_m + \Delta\sigma_{H-P}, \tag{4.2.1}$$

$$\sigma_{yODS} = \sigma_m + \Delta\sigma_{H-P} + \Delta\sigma_{Or}, \tag{4.2.2}$$

The matrix strength includes Peierls stress and strengths due to solid solution and residual dislocations in the matrix. Since the compositions are similar, it is assumed that the matrix strength is constant for both NODS and ODS–18Cr steels. The strength contributions due to grain size and dispersoid can be calculated using the equations given below [10, 11]:

$$\Delta\sigma_{H-P} = K_{H-P} d_g^{-1/2}, \tag{4.2.3}$$

$$\Delta\sigma_{Or} = A\left(\frac{Gb}{S}\right)\ln\left(\frac{d_p}{2b}\right), \tag{4.2.4}$$

$$S = \frac{d_p}{2}\left\{(2\pi/3f)^{1/2} - 2(2/3)^{1/2}\right\}, \qquad (4.2.5)$$

where K_{H-P} is the Hall–Petch constant, d_g is the average grain size, A is a numerical constant [9], G is the matrix shear modulus, b is a matrix Burgers vector, d_p is the measured average dispersoid size, f is the volume fraction of dispersoids and S is the inter–dispersoid spacing. Initially, matrix strength is calculated using Eq. (4.2.1) in which σ_{yNODS} is experimentally measured value and $\Delta\sigma_{H-P}$ is calculated using Eq. (4.2.3) with measured grain size of NODS (Table 4.2.2) and K_{H-P} of 338 MPa.μm$^{1/2}$ [12]. The calculated matrix strength (σ_m) of 222 MPa is used subsequently along with $\Delta\sigma_{H-P}$ and $\Delta\sigma_{Or}$ to predict the strengths of ODS1, ODS3 and ODS6. $\Delta\sigma_{H-P}$ and $\Delta\sigma_{Or}$ are calculated using equations (4.2.3)–(4.2.5) with the data given in Table 4.2.2. The calculated individual strength contribution along with the experimentally obtained strength values are given in Fig. 4.2.10. The values predicted by the model are in close agreement with the experimental values.

Table 4.2.2 Average dispersoid size, number density and volume fraction of dispersoids in extruded+annealed ODS–18Cr steel along with the values of the various parameters used in equations (4.2.1)–(4.2.5).

S. No	Property	NODS	ODS1	ODS3	ODS6
1	Average dispersoid size (d_p), [nm]	–	15	10	5
2	Number density of dispersoids, [no/m^3]	–	6.21x10^{21}	1.82x10^{22}	1.24x10^{23}
3	Volume fraction of dispersoids (f)	–	0.0092	0.0094	0.0096
4	Average grain size (d_g), [μm]	13	1.17	0.73	0.48
5	Numerical constant (A) (Eq. 4)	–	0.3	0.3	0.3
6	Burgers vector (b), [nm]	–	0.25	0.25	0.25
7	Shear modulus (G), [GPa]	–	82	82	82
8	Hall–Petch constant for yield strength (K_{H-P}), [MPa.μm$^{1/2}$]	338	338	338	338
9	Matrix strength (σ_m), [MPa]$^{\#}$	222	222	222	222
10	Inter–dispersoid spacing (S), [nm]	–	101	66	33

$^{\#}$ Calculated using Eq. (4.2.3) with measured yield strength value of NODS [316 MPa] at room temperature.

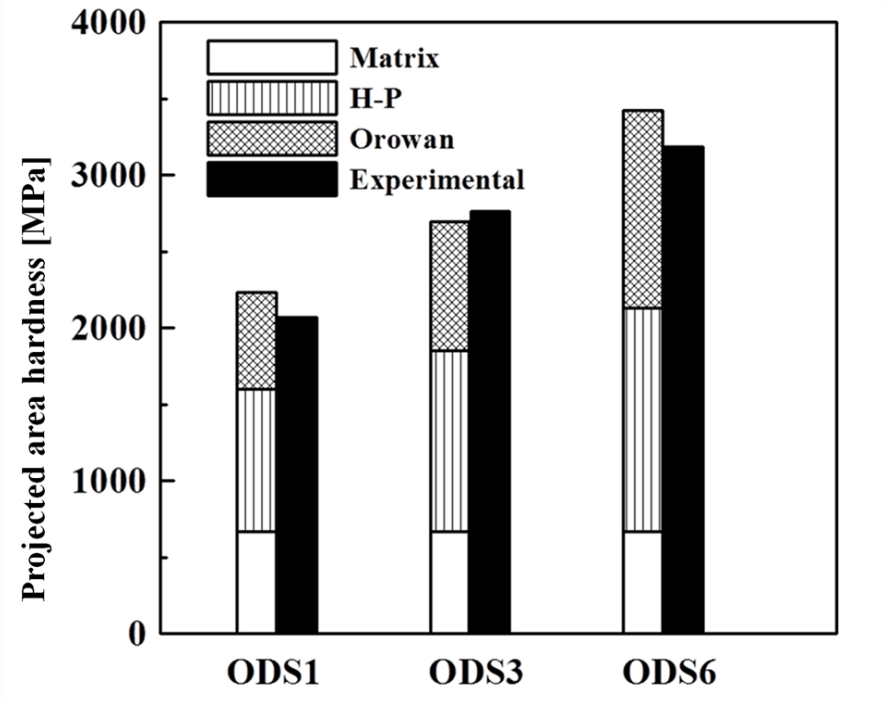

Fig. 4.2.10 Calculated strengthening values of ODS–18Cr steels along with experimental values.

4.2.4.2 Based on tensile data

The temperature dependence of various strengthening parameters that contribute to the strength of ODS–18Cr steels was analyzed.

The structure–property correlations of ODS steels do not always follow the linear superposition model due to the complexity of microstructures [13]. Even though, there is no model which is universally accepted to predict flow stress, rule of mixtures of different forms as given in Eq. (4.2.6) are available [13–15].

$$\sigma_y^k = \sigma_m^k + \Delta\sigma_{H-P}^k + \Delta\sigma_{dis}^k, \qquad (4.2.6)$$

The value of parameter ‘k’ was established to be in the range of 1–2 on considerations of the properties of second phase particles [16–18]. The value of the parameter ‘k’ is taken as 2 for the present case where the types of obstacles are same but the number density is different [18]. Hence the Eq. (4.2.6) becomes, root of sum of squares of matrix strength ($\Delta\sigma_m$), grain size strengthening ($\Delta\sigma_{H-P)}$ and dispersion strengthening ($\Delta\sigma_{Or}$) due to Orowan mechanism; which is given below:

$$\sigma_{rss} = \sqrt{\sigma_m^2 + \Delta\sigma_{H-P}^2 + \Delta\sigma_{Or}^2} \tag{4.2.7}$$

The grain size and dispersoid size were estimated by TEM on samples fractured at RT and 800 °C. The requisite sample was taken from about 1 mm below the fracture surface to account for the effect of strain and temperature. As per the observations made on tensile deformed sample at RT and 800 °C, it is found that the microstructure was stable even at the highest test temperature thus ruling out the possibility of grain and dispersoid coarsening. Hence, the relevant data given in Table 4.2.2 are used to predict the matrix, Hall–Petch and Orowan strengths of ODS steels at all the test temperatures using the equations (4.2.3)–(4.2.5).

The values of K_{H-P} as a function of temperature were taken from Kim *et al* [12]. The matrix strength at each temperature was calculated using Eq. (4.2.1) in which σ_{yNODS} is experimentally measured yield strength value of NODS at that temperature and $\Delta\sigma_{H-P}$ was computed using Eq. (4.2.3) with the measured grain size of NODS (Table 4.2.2) and the reported K_{H-P} value at that temperature (Table 4.2.3). Shear modulus (G, GPa) was calculated as a function of temperature using the equation given below [12]:

$$G = 93.2(1 - 4.368 \times 10^{-4} T), \tag{4.2.8}$$

The calculated individual strength contributions along with the experimentally measured strength values at different temperatures are given in Table 4.2.3. The flow stress values predicted by the root of the sum of squares model along with experimentally measured values at different temperatures for ODS1, ODS3 and ODS6 are shown in Figs. 4.2.11 (a–c) respectively. The model predicts the strength values very well at high temperatures and reasonably well at room temperature.

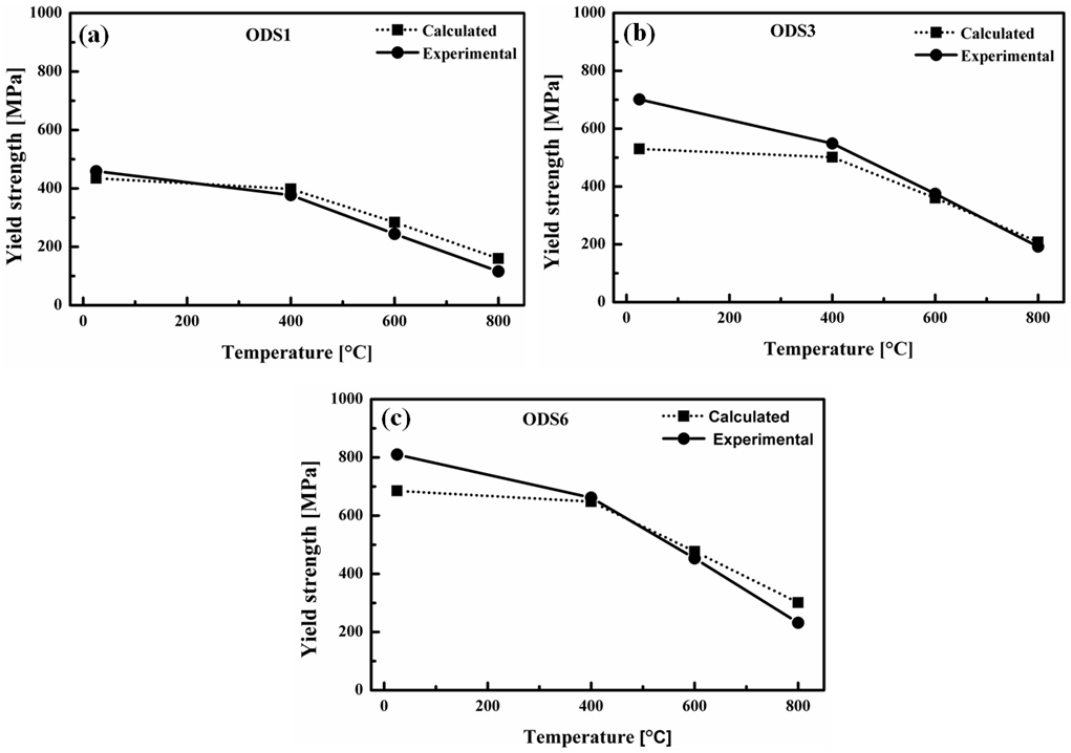

Fig. 4.2.11 Comparison of calculated strength values along with experimental values of ODS–18Cr steels: (a) ODS1, (b) ODS3 and (c) ODS6.

Table 4.2.3 The calculated strength values including σ_m, $\Delta\sigma_{H-P}$ and $\Delta\sigma_{Or}$ along with experimental values of ODS1, ODS3 and ODS6 at various temperatures.

Temperature [°C]	K_{H-P} [MPa.μm$^{1/2}$]	G [GPa]	σ_m [MPa]	Strength [MPa]											
				ODS1				ODS3				ODS6			
				$\Delta\sigma_{H-P}$	$\Delta\sigma_{Or}$	**cal**	**Exp**	$\Delta\sigma_{H-P}$	$\Delta\sigma_{Or}$	**cal**	**exp**	$\Delta\sigma_{H-P}$	$\Delta\sigma_{Or}$	**cal**	**exp**
25	338	81	222	312	205	435	459	396	274	530	701	488	427	685	810
400	371	66	114	343	166	398	377	434	222	501	549	535	346	648	662
600	249	58	80	230	146	284	244	291	195	360	375	359	303	477	453
800	103	50	29	95	125	160	116	121	167	208	192	149	260	301	232

4.2.5 Fractographic examination

In order to understand the influence of microstructure on the deformation and fracture behavior, detailed examination was carried out on fractured tensile specimens made of ODS–18Cr steel powders milled for different milling times and tested at different temperatures. Fracture surfaces of NODS tested at different temperatures were also examined. The fracture features observed at the central (non–shear lip) region of the fracture surfaces of ODS1, ODS3, ODS6 and NODS at RT along with the corresponding macro fractographs are presented in Figs. 4.2.12 (a–d).

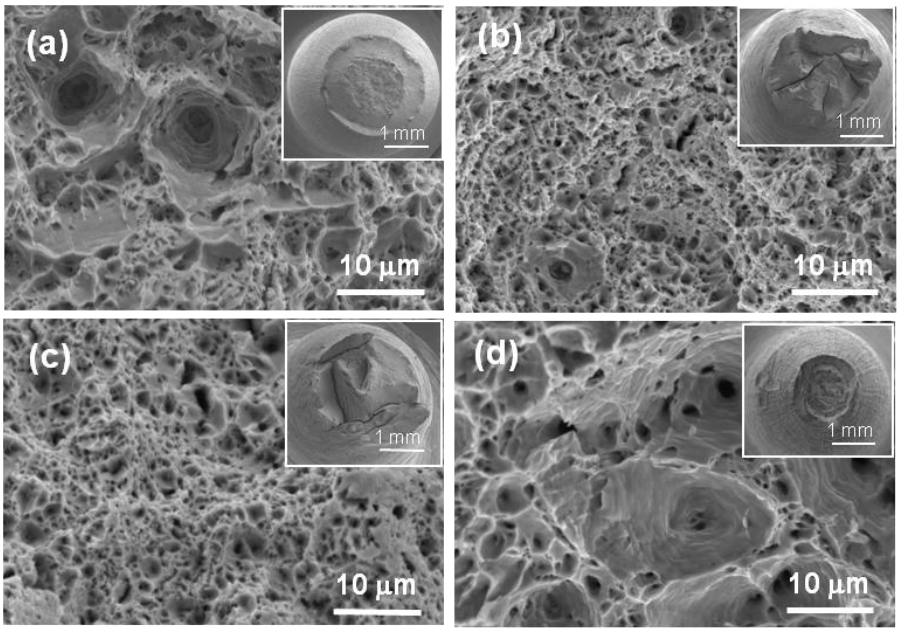

Fig. 4.2.12 Fractographs of ODS–18Cr and 18Cr steels at RT along with the corresponding macro fractographs: (a) ODS1, (b) ODS3, (c) ODS6 and (d) NODS.

The fracture features indicated that the failure was in a ductile mode with distinct neck and shear lip formation. All the samples revealed equiaxed dimples at the central region and elongated dimples in the shear lip region. The area occupied by shear lip decreased with increasing milling time in ODS samples and NODS had a shear lip area similar to ODS6. The increasing incidence of secondary cracks was observed on the fracture surfaces with increasing milling time and NODS did not reveal the presence of such cracks. While NODS showed bimodal dimples with stretch marks on larger dimple walls, the proportion of large dimples and the size of dimples decreased with increasing milling time in ODS samples with ODS6 showing uniform fine equiaxed dimple fracture. Some of the large dimples contained sub–micrometer sized Cr–rich particles and no particles

could be identified in the smaller dimples at magnifications commonly employed for fractography.

The fracture features observed in ODS6 and NODS at different test temperatures are shown in Fig. 4.2.13 and Fig. 4.2.14 respectively. The corresponding macro fractographs of tensile fracture surfaces are embedded in Figs. 4.2.13 and 4.2.14 respectively.

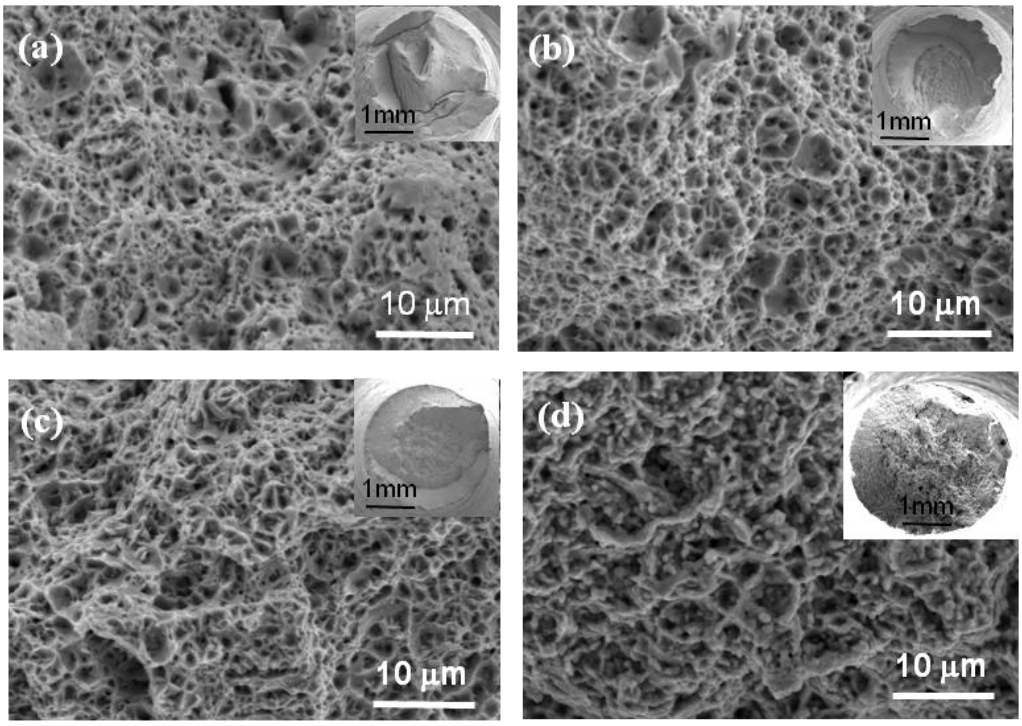

Fig. 4.2.13 Fractographs of ODS6 at different test temperatures: (a) RT, (b) 400, (c) 600 and (d) 800 °C. Inset shows the corresponding macro fractographs.

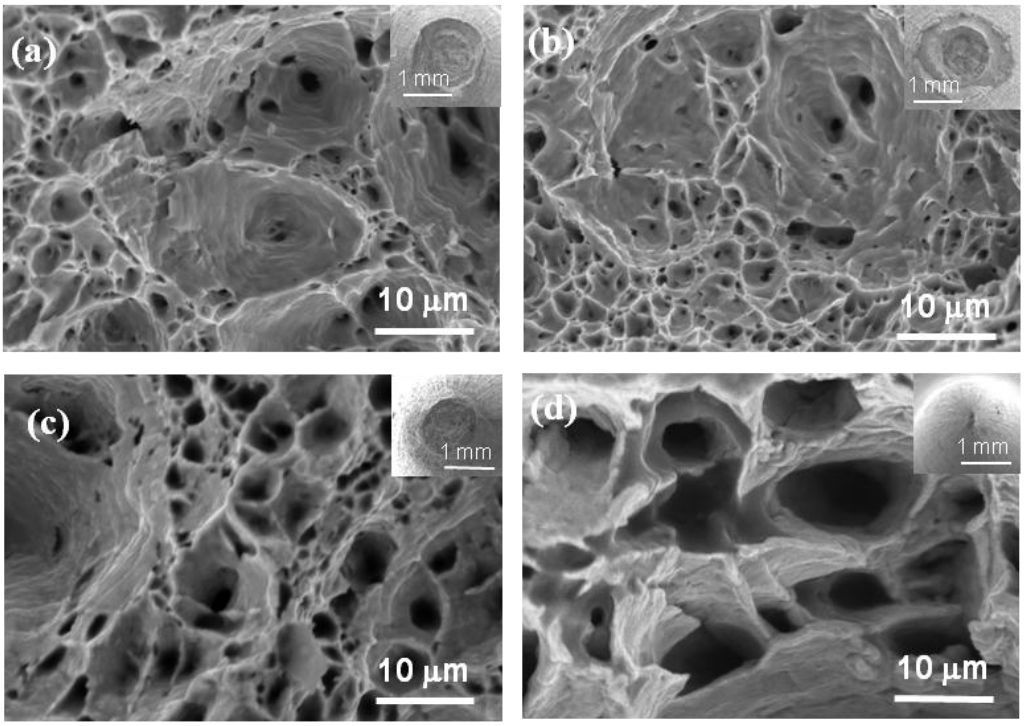

Fig. 4.2.14 Fractographs of NODS at different test temperatures: (a) RT, (b) 400, (c) 600 and (d) 800 °C. Inset shows the corresponding macro fractographs.

Both ODS6 and NODS fractured samples showed the typical cup–and–cone type fracture with a central flat region surrounded by shear lip. The extent of necking prior to fracture was nearly similar up to test temperatures of 400 °C for both the materials. At higher temperatures, the reduction in area decreased in ODS6 and increased in NODS samples. Fractographic examination revealed both large and small equiaxed dimples. While ODS6 showed predominantly finer dimples, NODS showed a significantly larger population of larger dimples. The size and depth of the dimples increased with increasing test temperature. A few Ti– and Cr–rich particles were observed in the larger dimples. The samples tested at 800 °C were heavily masked by oxide layer which was removed by a combination of replica technique and by ultrasonic cleaning in an oxide remover solution. However, some oxide debris was still present in ODS6. The fine particles observed on the fracture surface of ODS6 tested at 800 °C (Fig. 4.2.13 (d)) were the reminiscences of oxide debris and not related to the Y–Ti–O dispersoids which are an order of magnitude finer.

The milling time and temperature dependent tensile fracture features observed in ODS–18Cr steels are relatable to the presence of second phase particles and matrix strength. It

is well known that during tensile deformation micro voids nucleate at second phase particles. The plastic strain at which void nucleation initiates decreases with increasing second phase particle size and matrix yield strength. It is also well established that void growth occurs due to localized strain (serpentine glide) in ductile matrix or by decohesion at the interfaces of smaller second phase particles. Increasing milling time results in decrease in the size of both dispersoids and other particles resulting in increased matrix strength and decreased ductility. Consequently, as was experimentally observed, the number, size and depth of larger dimples decreased and the number of smaller dimples increased from ODS1 to ODS6. The cracking finally appears to have occurred by the coalescence of growing larger voids as in ODS1 or by the joining of a few larger voids via a number of smaller voids formed at dispersoids as in ODS3 or by the nucleation, growth and coalescence of voids at nano sized dispersoids as in ODS6 [19, 20].

The tensile deformation and fracture behavior of ODS–18Cr steels at elevated temperatures also depend on the relative roles played by different microstructural features like inclusions, carbides, dispersoids and grain boundaries, *etc.* in the fracture process. The deformation behavior presented in earlier sections indicated that, both the strain at which strain localization occurs (e_u) and the fracture strain (e_t) decrease with increasing temperature in all ODS–18Cr samples up to 800 °C. All the test samples showed dimpled rupture even at 800 °C. Once larger particles like inclusions and carbides trigger micro void nucleation as in NODS and ODS1, fracture occurs by joining of growing voids in NODS and assisted by voids nucleated at coarser dispersoids in ODS1 at all test temperatures. However, at larger milling times, the size of second phase particles is greatly reduced leading to nucleation of a large number of fine micro voids. The growth of micro voids is expected to be enhanced at higher temperatures due to the increased matrix ductility and the ease with each the voids coalesce. The progressive decrease in dimple size with increasing temperature up to 600 °C is due to micro void coalescence by impingement of numerous voids nucleated at large dispersoid population. This type of coalescence (void sheet formation) before the initial voids grow is responsible for the observed decrease in ductility. The slightly coarser dimples in ODS6 at 800 °C, which are still finer than those in NODS, are due to the enhanced matrix ductility and relative dominance of void growth. In the case of NODS void coalescence occurs by growth of large voids and void sheet formation by nucleation of voids at finer particles, probably of

$M_{23}C_6$ type carbides and a few oxides formed due to milling contamination. While linking of voids with void sheets appears to be responsible for the fracture up to 400 °C, void growth seems to be the dominating factor beyond 600 °C. Both the dimple size and depth increased dramatically at 800 °C in NODS. The lower strain rate, higher temperature and relatively fine grained structure together are responsible for the super plastic behavior of NODS steel. Neither the ODS–18Cr nor NODS samples showed intergranular fracture at ant test temperature, thus discounting the possibility of the operation of grain boundary sliding or diffusion creep in the fracture process.

4.2.6 Summary

Pre–alloyed 18Cr ferritic steel powder was milled with and without yttria in high energy mill for various durations till steady–state condition is reached. The powders were then consolidated by hot extrusion followed by annealing. The hardness of both 18Cr and ODS–18Cr steel powders was found to increase with milling time and finally reached a steady state beyond 5 h of milling. The hardness of ODS–18Cr steel is higher than NODS and increases from ODS1 to ODS6. The progressive increase of hardness in ODS–18Cr steel is due to decrease in size and increase in the number density of dispersoids. The tensile deformation and fracture behavior of ODS–18Cr steel over a wide temperature range of 25–800 °C were studied as a function of milling time along with NODS steel. Yttria containing steels developed an ultra–fine grained structure along with fine dispersion of complex oxide particles that enhance the strength levels in comparison to the yttria–free steel. Both yield and tensile strengths of ODS–18Cr steels increased with milling time at all the test temperatures. The overall tensile deformation behavior varied significantly with milling time, but, was similar up to test temperatures below 400 °C. Beyond 400 °C, the deformation trend varied significantly, even though the general trend of increase in strength with milling time was retained up to the maximum test temperature of 800 °C. The experimental strength values were compared with the values predicted by an appropriate model. Fractographic examination was carried out on ODS–18Cr and NODS fractured tensile samples, revealed that the failure was in ductile fracture mode with distinct neck and shear lip formation for all milling times and test temperatures.

References

[1] M.F. Ashby, The deformation of plastically non–homogeneous alloys, in: A. Kelly, R.B. Nicholson (Eds.), Strengthening methods in crystals, Wiley, New York, 1971, pp. 137–190.

[2] R. Rahmanifard, H. Farhangi, A.J. Novinrooz, S. Moniri, Development of a high–strength ultrafine–grained ferritic steel nanocomposite, *Metallurgical and Materials Transactions A*, 44A (2013) 990–998.

[3] S. Li, Z. Zhou, J. Jang, M. Wang, H. Hu, H. Sun, L. Zou, G. Zhang, L. Zhang, The influence of Cr content on the mechanical properties of ODS ferritic steels, *Journal of Nuclear Materials*, 455 (2014) 194–200.

[4] J.H. Kim, T.S. Byun, D.T. Hoelzer, Tensile fracture characteristics of nanostructured ferritic alloy 14YWT, *Journal of Nuclear Materials*, 407 (2010) 143–150.

[5] W. Blum, X.H. Zeng, A simple dislocation model of deformation resistance of ultrafine–grained materials explaining Hall–Petch strengthening and enhanced strain rate sensitivity, *Acta Materialia*, 57 (2009) 1966–1974.

[6] F. Tang, J.M. Schoenung, Strain softening in nanocrystalline or ultrafine–grained metals: A mechanistic explanation, *Materials Science & Engineering A*, 493 (2008) 101–103.

[7] J. Ribis, Y. de Carlan, Interfacial strained structure and orientation relationships of the nanosized oxide particles deduced from elasticity–driven morphology in oxide dispersion strengthened materials, *Acta Materialia*, 60 (2012) 238–252.

[8] L.F. He, J. Shirahata, T. Nakayama, T. Suzuki, H. Suematsu, I. Ihara, Y.W. Bao, T. Komatsu, K. Niihara, Mechnical properties of $Y_2Ti_2O_7$, *Scripta Materialia*, 64 (2011) 548–551.

[9] R. Vijay, M. Nagini, J. Joardar, M. Ramakrishna, A.V. Reddy, G. Sundararajan, Strengthening mechanisms in mechanically milled oxide–dispersed iron powders, *Metallurgical and Materials Transactions A*, 44A (2013) 1611–1620.

[10] M. Nagini, R. Vijay, M. Ramakrishna, A.V. Reddy, G. Sundararajan, Influence of the duration of high energy ball milling on the microstructure and mechanical properties of a 9Cr oxide dispersion strengthened ferritic–martensitic steel, *Materials Science & Engineering A*, 620 (2015) 490–499.

[11] R. Vijay, M. Nagini, S.S. Sarma, M. Ramakrishna, A.V. Reddy, G. Sundararajan, Structure and properties of nano–scale oxide dispersed iron, *Metallurgical and Materials Transactions A*, 45A (2014) 777–784.

[12] J.H. Kim, T.S Byun, D.T. Hoelzer, C.H. Park, J.T. Yeom, J.K. Hong, Temperature dependence of strengthening mechanisms in the nanostructured ferritic alloy 14YWT: Part II–Mechanistic models and predictions, *Materials Science & Engineering A*, 559 (2013) 111–118.

[13] E. Nembach, Particle Strengthening of Metals and Alloys, Wiley, New York, 1996.

[14] B. Reppich, in: R.W. Cahn, P. Haasen, E.J. Kramer (Eds.), *Materials Science and Technology*, Wiley, Germany, 1993, pp. 311.

[15] A.J. Ardell, in: J.H. Westbrock, R.L. Fleischer (Eds.), *Intermetallic Compounds*, Wiley, New York, 1994, pp. 257.

[16] U.F. Kocks, A.S. Argon, M.F. Ashby, Thermodynamics and kinetics of slip, *Progressive Material Science*, 19 (1975) 1–288.

[17] L.M. Brown, R.K. Ham, In: A. Kelly, R.B. Nicholson, Strengthening methods in solids, Applied Science Publishers, Barking, 1971.

[18] T.J. Koppenaal, D. Kuhlmann–Wilsdorf, The effect of pre stressing on the strength of neutron–irradiated copper single crystals, *Applied Physics Letters*, 4 (1964) 59–61.

[19] C.D. Beachem, The effects of crack tip plastic flow directions upon microscopic dimple shapes, *Materials Transactions A*, 6 (1975) 377–383.

[20] R.H. Van Stone, T.B. Cox, J.R. Low, J.A. Psioda, Microstructural aspects of fracture by dimpled rupture, *International Jounal of Materilas Reviews*, 30 (1985) 157–179.

4.3 Influence of Dispersoids on Corrosion Behavior of Oxide Dispersion Strengthened 18Cr Steels

4.3.1 Introduction

Corrosion resistance in various media and environment is an important functional consideration while selecting steels for applications involving corrosion. The corrosion resistance of steels can be enhanced by increasing Cr content beyond 12 %. Correct compositional optimization is needed to balance between increased corrosion resistance and the formation of deleterious intermetallic phases with increasing Cr content. The high temperature properties are enhanced by the dispersion of stable oxide particles in high Cr steels as in oxide dispersion strengthened steels. Although, the corrosion behavior of ODS steels at high temperatures is well studied in super critical pressurized water (SCPW), liquid lead, lead–bismuth eutectic (LBE), sodium and molten fluoride salts, the general corrosion behavior of these steels at room temperature is not fully evaluated. Corrosion behavior of ODS steels in the marine environment is of importance because the components made from ODS steels in systems like nuclear reactors, turbines and heat exchangers, *etc.* are likely to be exposed to aqueous NaCl environment at room temperature during transportation, storage, and maintenance. As yet, electrochemical corrosion studies in aqueous chloride medium are not carried out on ODS–18Cr ferritic steels. The systematic evaluation of the influence of milling time on the electrochemical corrosion behavior of 18Cr ferritic steels with and without dispersoids in 3.5 % NaCl solution at room temperature are presented in this chapter.

4.3.2 Electrochemical studies

4.3.2.1 Cyclic polarization

Cyclic polarization (CP) studies were carried out on ODS1 and ODS6 along with NODS samples in 3.5 % NaCl solution after pre–immersion (0.5 h) to stabilize OCP. Typical CP curves of the experimental samples described with relevant parameters are shown in Fig. 4.3.1.

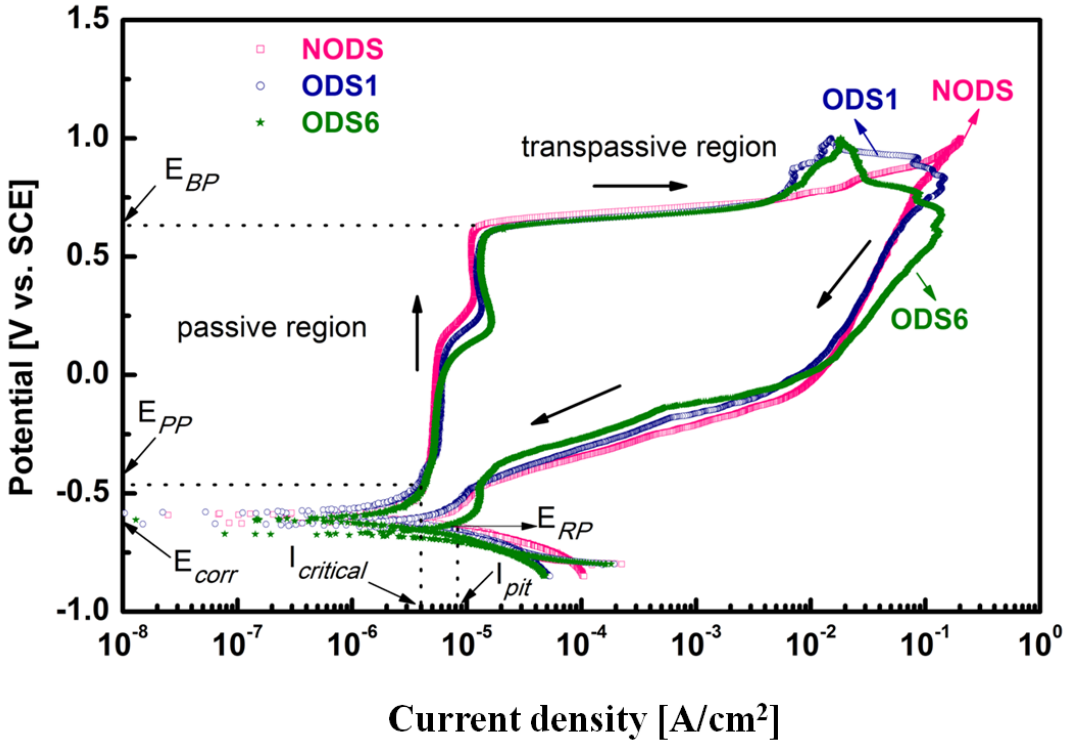

Fig. 4.3.1 CP curves of ODS–18Cr samples along with NODS sample.

To determine the pitting tendencies (passivation breakdown and repassivation behavior) of the active–passive alloys which undergo localized (pitting) corrosion in the metal–solution system, CP measurements were carried out. In the CP curve, potential is increased from cathodic to anodic direction until the current density reached the given magnitude, then the potential is decreased in the reverse direction. Here the anodic branch extends to a wider potential range reaching up to 1 V with OCP, then the potential decreased towards OCP. Pitting phenomenon can be explained with the nature of hysteresis loop formed with forward and reverse scans. Positive hysteresis indicates (loop is on the right) the localized corrosion susceptibility and the amount of the localized corrosion incurred by the material and is represented by the area under the hysteresis loop [1, 2]. The presence of huge positive hysteresis loop is an indication of the nucleation and growth of pits. Negative hysteresis (loop is on the left) indicates the formation of passive film which is protective and self–healing. In other words, it indicates that the damaged passive film repairs by itself [3, 4]. No hysteresis also indicates high resistance to localized corrosion [5].

Since the localized (pitting) corrosion was observed to be the dominant mode of damage in the steels studied, pitting rate (MPY_{pit}) was calculated using the following equation [5]:

$$MPY_{pit} \cong 20(I_{pit})(\Lambda)\left(\frac{1}{\rho}\right)(\varepsilon), \qquad (4.3.1)$$

where, I_{pit} is the pitting current density [A/cm^2], Λ is the combination of several conversion terms and is 1.2866×10^5 [equivalents. sec. mils/coulombs. cm. years], ρ is the metal density [g/cc] and ε is equivalent weight [grams/equivalent].

The shapes of CP curves are broadly similar for both ODS samples with different milling times and NODS sample. From the obtained CP curves, it is evident that a) distinct active, passive and transpassive regions exist, b) current density increases slightly in the passive region with increasing potential, c) transition from passive to transpassive state is sharp, d) current density increased significantly in transpassive region with a small increase in potential, e) potential reversal resulted in positive hysteresis, f) the passive region width is high and g) the repassivation potential (E_{RP}) is lower than the corrosion potential (E_{corr}).

Important parameters like corrosion potential (E_{corr}), corrosion current density (I_{corr}), primary passive potential (E_{pp}), critical current density (I_{crit}), passive current density (I_{pass}), breakdown/pitting potential (E_{BP}), potential range of passive region E_{BP}–E_{corr} (ΔV), repassivation potential (E_{RP}), pitting current density (I_{pit}), pitting rate and the area under hysteresis loop were derived from the CP curves and are presented in Table 4.3.1.

Table 4.3.1 Data obtained from analysis of CP hysteresis curves of NODS and ODS samples.

Sample Name	Corrosion potential (E_{corr}) [mV]	Corrosion current density (I_{corr}) [μA/cm^2]	Primary passive potential (E_{PP}) [mV]	Critical current density (I_{crit}) [μA/cm^2]	Passive current density (I_{pass}) [μA/cm^2]	Breakdown potential (E_{BP}) [mV]	$E_B - E_{corr}$ ΔV[mV]	Repassivation potential [E_{RP}][mV]	Pitting current density (I_{pit}) [μA/cm^2]	Pitting rate [MPY]	Area of hysteresis Loop [I×V]
NODS	–583	1.717	–526	3.110	5.425	607	1190	–607	2.961	25.00	40
ODS1	–577	1.777	–444	4.025	6.127	600	1177	–610	3.152	26.89	48
ODS3	–565	2.201	–509	3.154	6.593	615	1180	–607	3.847	32.48	47
ODS6	–604	2.694	–450	4.435	8.688	608	1212	–651	3.951	33.35	54

The corrosion potentials (E_{corr}) are almost similar for all the samples studied. Corrosion current density (I_{corr}) values are higher for ODS samples than the NODS sample and it is higher for ODS6 than ODS1. In all the samples, passive region has started immediately after E_{corr} showing the formation of a protective barrier oxide layer on the surface of the sample and the extent of the passive region is similar. The primary passivation potential (E_{pp}) is more negative in NODS which shows the early formation of passive layer compared to ODS–18Cr samples. The critical current density (I_{crit}) and passive current density (I_{pass}) provide information on the nucleation and growth of the passive oxide layer and the nature of the passive oxide layer formed on surface of the sample, respectively. There is a variation in both of these values from NODS to ODS–18Cr and higher in ODS samples which is due to the porosity generation through the passive oxide layer. All the samples exhibited well defined passive region with $\Delta V \approx 1200$ mV. The more extended the passive region (difference between E_{BP} and E_{corr}), the better the resistance to pitting corrosion with better passivation characteristics [6]. For all the samples, this passive region ends at the breakdown potential (E_{BP}) and pitting corrosion starts beyond E_{BP}. The reason for corrosion of passive materials is the damage of the passive oxide layer on the metal surface because of the existence of chloride or other aggressive anions [1, 4, 7]. The higher the value of E_{BP}, the greater is the resistance to the initiation of pitting corrosion. The sudden increase in the passive current density (i_{pass}) at E_{BP} shows the breakdown of the passive oxide film formed and initiation of the pit [1].

In CP curve, the presence of the hysteresis loop also represents a delay in repassivation of an existing pit, when the scan is reversed. If the hysteresis loop is larger, then repassivation of the pit becomes difficult [7]. Repassivation potential (E_{RP}) represents the potential where the reverse scan intersects the forward scan (loop closes on the reverse scan). At this potential, pit growth is arrested and current decreases drastically. If the E_{RP} is more negative than the E_{BP}, susceptibility to the pitting corrosion is high. At the potentials between the pitting and repassivation potential ($E_{RP} < E < E_{BP}$), new pits will not form, but existing pits will develop into bigger pits [8]. In the present study, E_{RP} is more negative for ODS6 compared to ODS1 and NODS steels. The experimental results also indicate that the area under the loop which represents the amount of pitting corrosion was higher for ODS than NODS. Pitting current density (I_{pit}) and pitting rate values are higher in ODS–18Cr than NODS and also increases with milling time.

4.3.2.2 Electrochemical impedance spectroscopy

Impedance analysis was carried out in order to study the properties of electric double layer formed at the interface of the sample and electrolyte at different exposure times. The impedance test results of ODS1, ODS6 and NODS samples at exposure times of 1 and 48 h plotted in the form of Nyquist and Bode plots are shown in Fig. 4.3.2. Similarly Nyquist and Bode plots of ODS1, ODS6 and NODS samples as a function of exposure time are shown in Fig. 4.3.3. The Nyquist plot shows real and imaginary components of impedance which is expressed in $\Omega.cm^2$ and in the Bode plot, the frequency dependence of the phase angle θ and modulus are plotted. The frequency dependence of the phase angle θ and modulus of impedance indicate whether one or more time constants are present in the system. Examination of different equivalent electric circuit models has been carried out to fit the plots using the Z–view software. An equivalent circuit with two time constants was found to be suitable for fitting the data at OCP and is shown in Fig. 4.3.4. The χ^2 value less than '1' is considered as good fit and the obtained χ^2 values (Table 4.3.2) showed a good fit of experimental data. The Bode plots of (Figs. 4.3.2 and 4.3.3) all the samples show the existence of two time constants, where the time constant at higher frequencies attributes to the resistance and capacitance values of a very thin oxide film formed on the sample substrate along with the uncompensated solution resistance (R_s). The other time constant at lower frequencies shows the capacitance of electric double layer (C_{dl}) formed at the interface of test sample and electrolyte and charge transfer resistance (R_{ct}) of the test sample. The numerical values of EIS parameters obtained from the fitted circuit are summarized in Table 4.3.2.

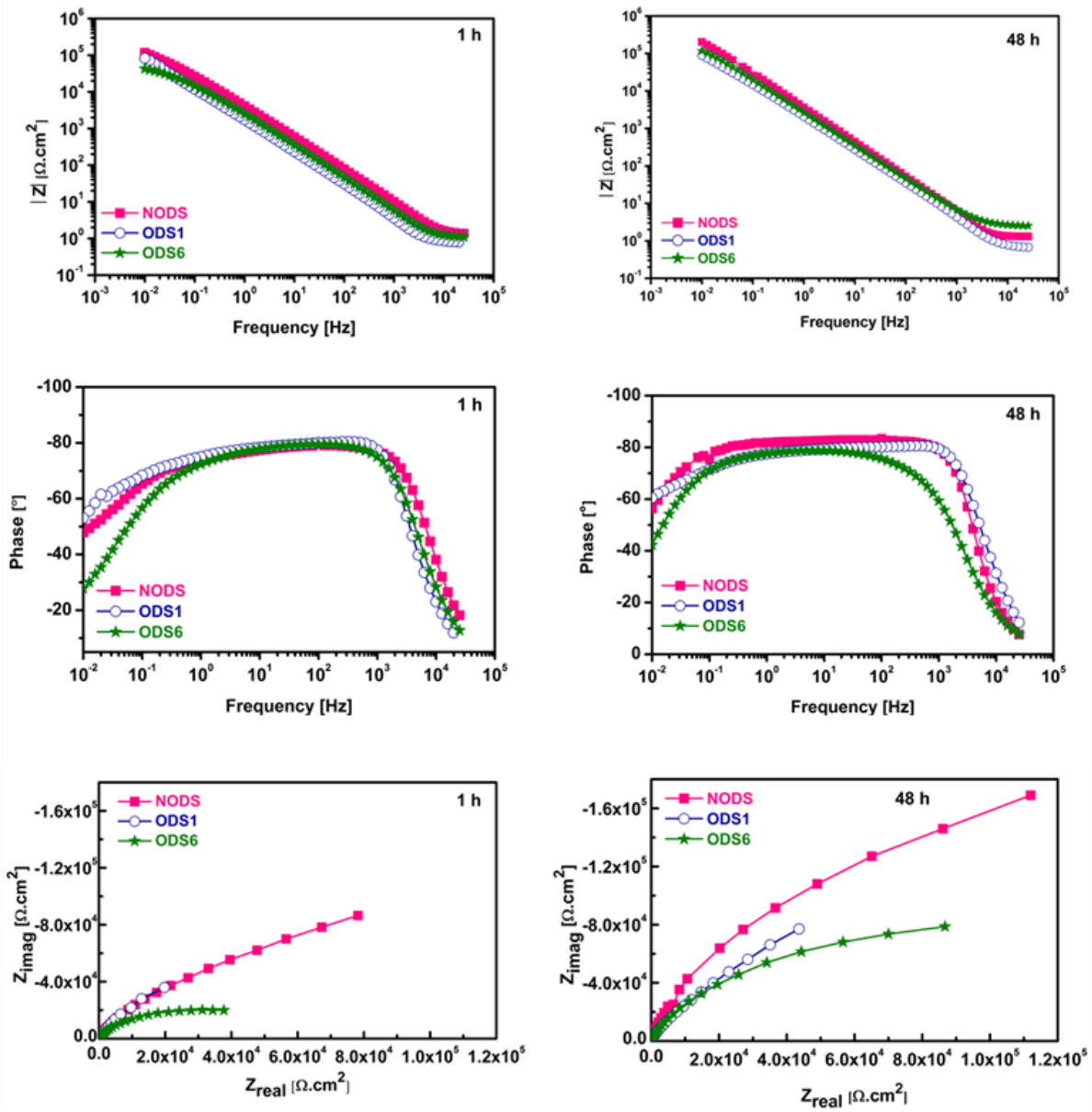

Fig. 4.3.2 Nyquist and Bode plots of ODS and NODS samples for exposure times of 1 and 48 h.

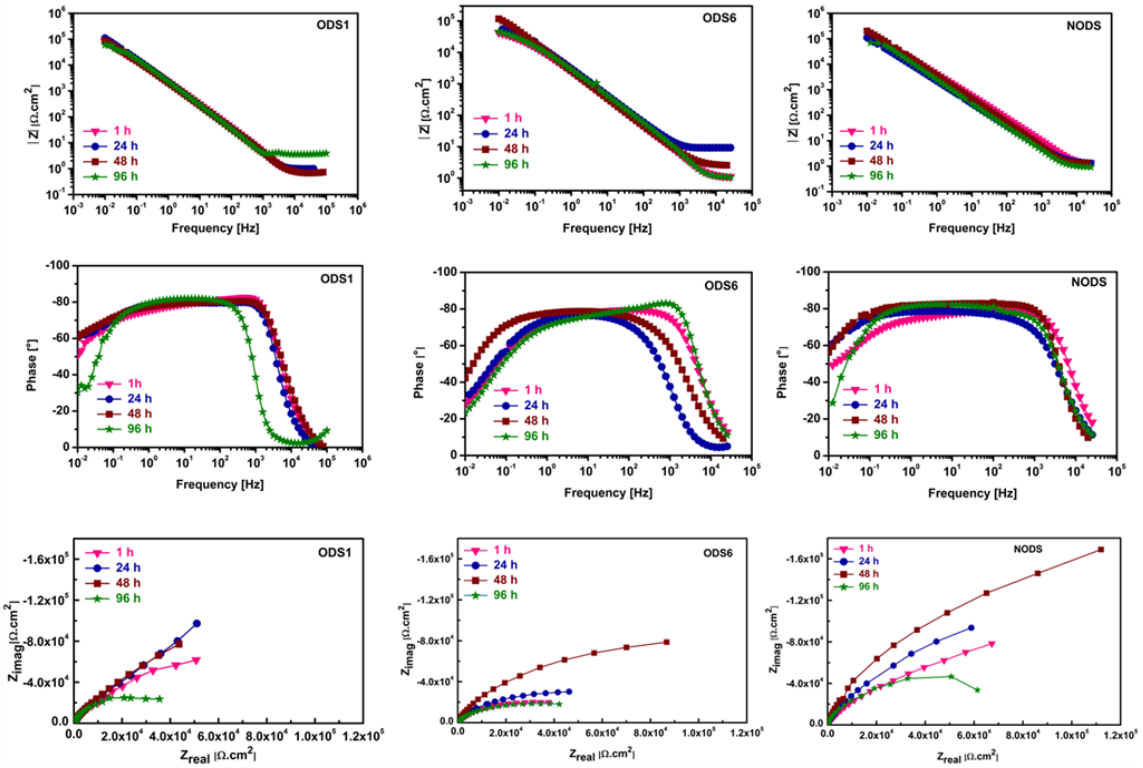

Fig. 4.3.3 Nyquist and Bode plots of ODS and NODS samples with different exposure times of 1, 24, 48 and 96 h.

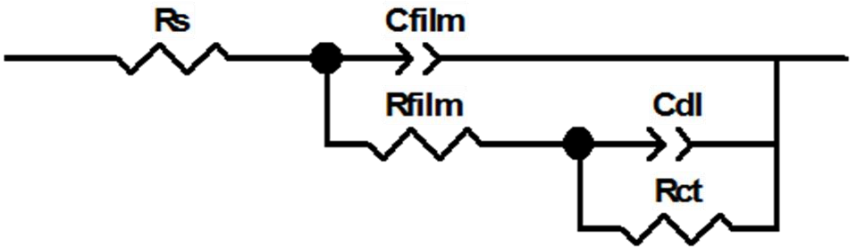

Fig. 4.3.4 Equivalent circuit used to fit the EIS data.

Table 4.3.2 Parameters obtained from the impedance circuit and corrosion rate calculated from potentiodynamic polarization data for ODS and NODS samples

Exposure time [h]	Sample name								
	R_s [$\Omega.cm^2$]	C_{film} [F/cm^2] $*10^{-5}$	R_{film} [$\Omega.cm^2$]	n_1	C_{dl} [F/cm^2] $*10^{-5}$	R_{ct} [$\Omega.cm^2$] $*10^5$	n_2	$\chi 2$	Corrosion rate from polarization data [MPY]
	NODS								
1	1.279	1.36	52.39	0.97	4.179	2.564	0.73	0.0006	0.438±0.0.29
24	1.252	5.667	79.41	0.98	3.402	3.249	0.76	0.0057	0.291±0.029
48	1.322	1.198	55.16	0.97	3.934	5.347	0.84	0.0021	0.27±0.037
96	0.899	4.498	98.91	0.98	2.769	0.951	0.87	0.0038	0.508±0.025
	ODS1								
1	0.807	1.900	40.63	0.97	7.982	2.258	0.76	0.009	0.589±0.042
24	0.676	2.695	42.11	0.98	7.431	3.169	0.77	0.0004	0.522±0.051
48	0.606	3.428	53.12	0.98	7.097	3.438	0.77	0.0007	0.434±0.031
96	3.896	0.973	43.73	0.97	7.644	0.734	0.84	0.0071	0.592±0.061
	ODS6								
1	1.078	2.885	53.69	0.99	6.198	0.583	0.70	0.0003	0.864±0.061
24	9.13	1.644	69.92	0.97	5.45	0.781	0.76	0.0017	0.74±0.049
48	2.446	6.534	41.85	0.98	7.871	1.73	0.83	0.0014	0.683±0.049
96	1.094	0.86	34.13	0.99	7.253	0.551	0.75	0.0057	0.823±0.064

A careful review of electrochemical impedance results shows the following:

The film resistance (R_{film}) is less in ODS–18Cr steels compared to that of NODS steel. This is due to the presence of dispersoids, which act as discontinuities in the oxide layer. The oxide layer formed on the surface of ODS–18Cr steels due to corrosion is thus not uniform and hence is not very effective in offering protection unlike an effective continuous passive film formed on NODS steel surface. As the area of the oxide layer on the surface is less, the capacitance of the passive film (C_{film}) is less in ODS–18Cr steels when compared to NODS steels. The exposed area of ODS samples increases with immersion time due to the presence of a discontinuous passive layer on the surface. As the area of interface of test sample and electrolyte increases, the double layer capacitance (C_{dl}) also increases. ODS–18Cr samples have high C_{dl} values compared to that of NODS. The charge transfer resistance (R_{ct}) is high for NODS for all exposure times than those of ODS–18Cr samples. This may be due to the presence of continuous passive film in NODS and dispersoid–induced discontinuities in the passive film of ODS–18Cr samples. ODS1 sample showed better R_{ct} values compared to ODS6 samples due to the presence of the less number of dispersoids. R_{ct} values for all samples increase up to 48 h and then decrease for 96 h of exposure which shows that the passive film is protective up to 48 h only. The factor 'n' is an empirical constant, which lies between 0 to 1 and can be related to surface roughness of the electrode [9]. The n_1 value for passive layer is closer to 1, which shows that the nature of film is like pure capacitor. The decrease of n_2 values shows the increase in surface roughness of the electrode and the values are increased with the exposure time for all the samples.

4.2.2.3 Potentiodynamic polarization

To study the corrosion behavior as a function of immersion time, the potentiodynamic polarization (PD) experiments were carried out on ODS1, ODS6 and NODS steels in 3.5 % NaCl solution after pre–immersion for different exposure times of 1, 24, 48 and 96 h. The corrosion rates of NODS and ODS–18Cr steels with exposure time calculated from the graphs are given in Table 4.3.2.

From the corrosion rate data, it is evident that, (a) the corrosion rate is higher for all ODS–18Cr steels than that of NODS at all exposure times, (b) corrosion rate increases in ODS–18Cr steels with milling time and is maximum in ODS6. The differences in the

quality of oxide film and grain size may be responsible for the higher corrosion rate in ODS–18Cr samples and (c) in both NODS and ODS–18Cr steel samples, corrosion rate decreases up to 48 h and increases thereafter. The passive layer formed on the substrate is protective up to 48 h, as the thickness of the passive layer increases; it may spall or become porous and allows easy access of the electrolyte to oxide–steel interface thereafter increasing the corrosion rate [1].

4.3.3 Immersion studies

To study the corrosion behavior of samples for longer time, immersion tests were carried out by dipping all the samples in 3.5 % NaCl solution for 365 days. The samples were examined periodically for any indications of corrosion. Initially there was no observable change, but after 6 months, small pits were formed and severe corrosion was noticed after 1 year of immersion. Fig. 4.3.5 shows the SEM images of the samples immersed for 365 days. The pit densities of ODS1, ODS6 and NODS are 261, 336 and 195 cm^{-2} respectively. Pit density increased with milling time in ODS–18Cr steels and is higher than NODS. The observed trend in this study followed well with electrochemical experiments.

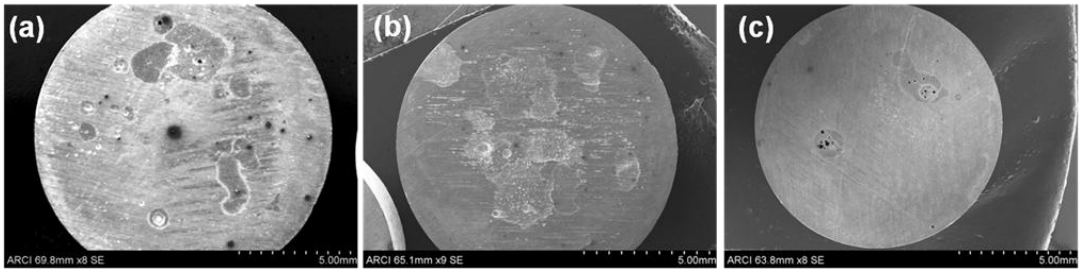

Fig. 4.3.5 SEM Morphologies of immersed samples of (a) ODS1, (b) ODS6 and (c) NODS.

4.3.4 Microstructural studies

The surface morphologies of corroded samples of ODS1, ODS6 and NODS after potentiodynamic polarization tests in 3.5 % NaCl solution after an exposure time of 48 h are shown in Fig. 4.3.6. The size, distribution and morphology of pits formed are imaged on cross–sections of corrosion tested samples after 48 h immersion of ODS 6 and NODS steels and shown in Fig. 4.3.7.

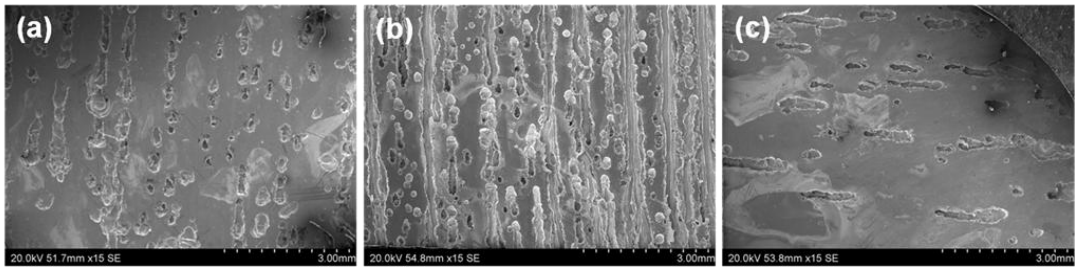

Fig. 4.3.6 The surface morphologies of PD tested samples of (a) ODS1, (b) ODS6 and (c) NODS after 48 h exposure to the 3.5 % NaCl solution.

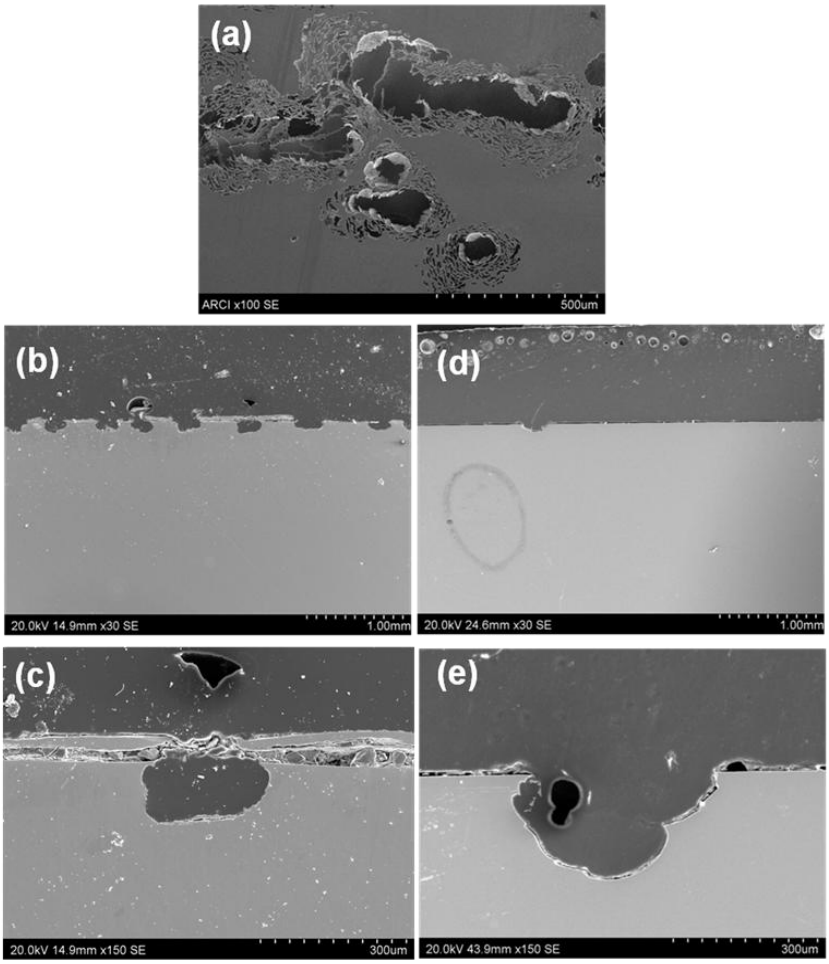

Fig. 4.3.7 The morphology of pits (a) on the surface; cross–section: (b) and (c) ODS6; (d) and (e) NODS.

The microstructures reveal the occurrence of predominantly localized (pitting) corrosion along with general corrosion in both ODS and NODS samples. In ODS samples, pits are smaller, large in number and partly covered with debris, while in NODS, pits are less, shallow and open. From the cross–sectional studies (Fig. 4.3.7), pit shapes mainly appeared to be hemi–spherical and globular. The formation of more number of pits in

ODS steels is probably due to the non–uniformity of passive layer. The pit formation in NODS is considered as a general galvanic corrosion, occurring as a small active area, which is being accelerated by the large continuous passivated area. This relative area difference causes acceleration of the corrosion, resulting in deeper penetration of the pits [10]. More rapid propagation of the pits may occur due to their initiation at metallurgical features, *e.g.*, inclusions and grain boundaries, second phase particles and solute segregated grain boundaries, *etc.* [1]. In the present study, the nucleation of pits occurs predominantly at dispersoids which in this case are Y_2O_3 and $Y_2Ti_2O_7$. Both of these oxides are noble when compared to the matrix and exhibit similar electrochemical behavior. Morphology of pits observed under SEM (Fig. 4.3.7 (a)) shows lacelike patterns with a central hole. This lacy metal structure contains white sponge portion with enrichment of Ti caused by preferential leaching of Fe from the corrosion debris.

The salient features of the corrosion studies carried out on ODS–18Cr and NODS steels using various electrochemical (CP, EIS and potentiodynamic) and immersion techniques are summarized below:

In general, the resistance to corrosion, passivation characteristics and the anodic protection ability of a material in CP studies are associated with the negative E_{pp}, lower I_{crit}, I_{pass} values, higher E_{BP}, broader passive region (ΔV) and nobler E_{RP}. NODS sample exhibited better properties amongst all. Pitting corrosion is the main corrosion occurred in all the samples and the order of pitting rate followed as NODS<ODS1<ODS6. The charge transfer resistance (R_{ct}) is inversely proportional to the pitting rate and is lowest for ODS6 which exhibited the highest pitting rate. Impedance analysis revealed a better corrosion resistance surface film for NODS than ODS–18Cr steels. The corrosion rate calculated from the PD polarization data compares well with the results of impedance data. Immersion studies also reflect the same trend for corrosion resistance as observed by electrochemical techniques. Even though all the above mentioned corrosion studies indicate that ODS–18Cr samples exhibit lower corrosion resistance than NODS samples, the difference is not very significant.

4.3.5 Summary

The corrosion behavior of ODS1 and ODS6 along with NODS steels in 3.5 % NaCl solution was investigated using CP, EIS, and potentiodynamic polarization and immersion studies. ODS–18Cr steels are more prone to pitting corrosion in comparison to the NODS. Amongst ODS–18Cr steels, pitting tendency increases with milling time. The charge transfer resistance (R_{ct}) values are less for ODS–18Cr steels when compared to NODS steel. In both ODS–18Cr and NODS steels, corrosion rate decreases up to 48 h due to formation of a protective passive layer and increases beyond due to the increase of porosity in the passive layer. Immersion studies also exhibit the same trend in corrosion behavior as observed by the electrochemical techniques. Electrochemical and immersion data results revealed that the role played by dispersoids on the corrosion behavior in steel is insignificant.

References

[1] G.S. Frankal, pitting corrosion of metals: a review of the critical factors, *Journal of Electrochemistry Society*, 145 (1998) 2186–2198.

[2] L.M. Calle, R.D Vinje, L.G. MacDowell, Electrochemical evaluation of stainless steels in acidified sodium chloride solutions, Corrosion/2004, Paper No. 04303 (Houston, TX: NACE)

[3] M. Darabara, L. Bourithis, S. Zinelis, G.D. Papadimitriou, Susceptibility to localized corrosion of stainless steel and niti endodontic instruments in irrigating solutions, *International Endodontic Journal*, 37 (2004) 705–710.

[4] A.H. Kandil, A.A. Fahmy Waheed, H.M.T. Tawfik, Water chemistry effect on corrosion of nuclear fuel cladding material, Zircaloy–4 (Zr–4), *International Journal of Advanced Research*, 2 (2014)149–162.

[5] W.S. Tait, An introduction to electrochemical corrosion testing for practicing engineers and scientists, Pair Docs Publication, Madison, 1994.

[6] E. Klar, P.K. Samal, Powder metallurgy stainless steels: processing, microstructures and properties, ASM International, Materials Park, 2007, p. 155.

[7] Z. Szklarska–Smialowska, Mechanism of pit nucleation by electrical breakdown of the passive film, Corrosion Science, 44 (2002) 1143–1149.

[8] L. Bertolini, B. Elsener, P. Pedeferri, E. Redaelli, R.B. Polder, Corrosion of steel in concrete: prevention, diagnosis, repair, Wiley– VCH, Weinheim, 2013

[9] C. Liu, Q. Bi, A. Leyland, A. Matthews, An electrochemical impedance spectroscopy study of the corrosion behaviour of PVD coated steels in 0.5 N NaCl

aqueous solutions: part II. EIS interpretation of corrosion behaviour, *Corrosion Science*, 45 (2003) 1257–1273.

[10] R.T. Loto, Pitting corrosion evaluation of austenitic stainless steel type 304 in acid chloride media, *Journal of Materials and Environmental Science*, 4 (2013) 448–459.

4.4 High Temperature Oxidation Behavior of Oxide Dispersion Strengthened 18Cr Ferritic Steel

4.4.1 Introduction

High temperature oxidation resistance in various media and environment is an important functional consideration while selecting steels for applications involving oxidation. The oxidation resistance of steels can be enhanced by increasing Cr content beyond 12 %. Correct compositional optimization is needed to balance between increased oxidation resistance and the formation of deleterious intermetallic phases with increasing Cr content. The high temperature properties are enhanced by the dispersion of stable oxide particles in high Cr steels as in ODS steels. Even though, the oxidation behavior of ODS steels at high temperatures is well studied in super critical pressurized water (SCPW), liquid lead, lead–bismuth eutectic (LBE), sodium and molten fluoride salts, the high temperature oxidation behavior of these steels is not fully evaluated. Since ODS steels are intended for operation at temperatures greater than 650 °C, the oxidation behavior of these steels has to be completely understood. The reported literature on the high temperature oxidation behavior of ODS steels is scarce. ODS steels appear to exhibit better oxidation resistance than conventional steels; however the detailed mechanisms are not yet clear. The systematic evaluation of the effect of grain size on oxidation behavior at high temperatures of 18Cr ferritic steels with and without dispersoids is presented in this chapter.

4.4.2 Oxidation kinetics

The weight change per unit surface area ($\Delta W/A$) of NODS and ODS–18Cr samples as a function of exposure time at 650, 750 and 850 °C is shown in Figs. 4.4.1 (a–c) respectively. All the samples exhibited rapid weight gain during the initial stages of oxidation (up to 100 h) and reduced weight gain beyond 100 h of exposure. The initial rate of weight gain and the overall weight gain of all the samples increased with exposure temperature. At any given exposure temperature, the weight gain by ODS–18Cr samples is lower than that of NODS (without dispersoids) sample. Amongst ODS–18Cr samples, the weight gain decreased with increase in milling time. Oxidation of both ODS–18Cr and NODS samples followed the parabolic rate law which is given below:

$$(\Delta W / A)^2 = k_p t\,, \qquad (4.4.1)$$

Where, k_p is parabolic rate constant ($g^2/cm^4/s$) and t is time (s). The parabolic rate constants for NODS and ODS–18Cr samples were estimated by plotting $(\Delta W/A)^2$ with exposure time and the k_p values obtained at each test temperature are given in Table 4.4.1. It is found that the parabolic rate constant (k_p) increased with temperature for all the samples and at each temperature, ODS–18Cr samples have significantly lower k_p values than the base material. Amongst ODS–18Cr samples, the k_p value decreased with increasing milling time. The lower k_p values of ODS–18Cr samples indicate that the resistance to oxidation is high for these steels. The activation energy for NODS and ODS–18Cr samples is obtained from the Arrhenius plot (Fig. 4.4.2) as per the equation given below using the experimental data and are tabulated in Table 4.4.1.

$$k_p = k_0 \exp(-E_A / RT), \tag{4.4.2}$$

where, k_o is the pre–exponential factor of the reaction ($g^2/cm^4/s$), R is the universal rate constant (8.314×10^{-3} kJ/mol/K), T is the temperature (K) and E_A is the activation energy (kJ/mol). The variation of parabolic rate constant with grain size of both NODS and ODS–18Cr samples and dispersoid size of ODS–18Cr samples at all the temperatures is shown in Figs. 4.4.3 (a–b) respectively. It can be seen from the graph that the parabolic rate constant at all temperatures decreased with decrease in grain size and dispersoid size. The lower grain size obtained due to the presence of fine dispersoids in ODS–18Cr samples increased the rate of formation of Cr_2O_3 layer by the enhanced grain boundary diffusion of chromium at early stages of oxidation thereby acting as an effective barrier for further oxidation.

Table 4.4.1 The values of parabolic rate constant (k_p), pre–exponential factor (k_0) and activation energy of NODS and ODS–18Cr samples.

Sample Name	Parabolic rate constant, k_p, [$g^2cm^{-4}s^{-1}$]			Pre exponential factor, k_0, [$g^2cm^{-4}s^{-1}$]			Activation energy [kJ/mol]
	650 °C	750 °C	850 °C	650 °C	750 °C	850 °C	
NODS	0.56×10^{-13}	4.88×10^{-13}	5.98×10^{-13}	8.54×10^{-08}	18.5×10^{-08}	7.12×10^{-08}	109
ODS1	0.42×10^{-13}	3.11×10^{-13}	4.60×10^{-13}	6.34×10^{-08}	11.8×10^{-08}	5.57×10^{-08}	
ODS3	0.34×10^{-13}	2.86×10^{-13}	4.18×10^{-13}	5.24×10^{-08}	10.9×10^{-08}	5.06×10^{-08}	
ODS6	0.26×10^{-13}	2.13×10^{-13}	3.81×10^{-13}	3.94×10^{-08}	8.07×10^{-08}	4.61×10^{-08}	

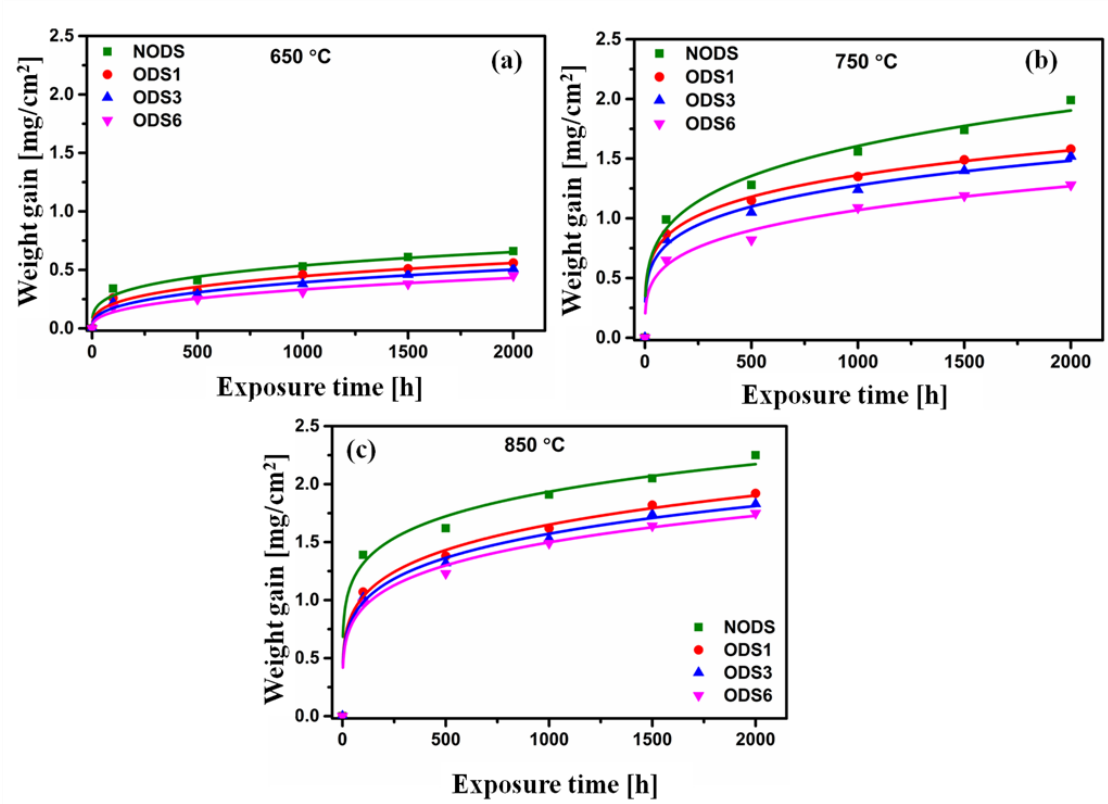

Fig. 4.4.1 Variation of weight gain as a function of exposure time: (a) 650 °C, (b) 750 °C and (c) 850 °C.

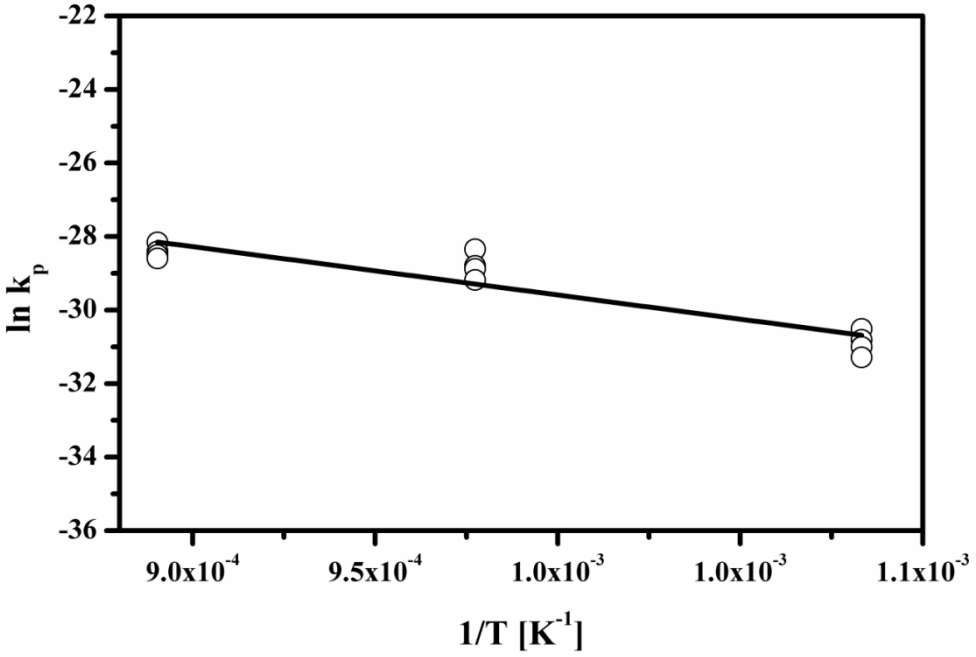

Fig. 4.4.2 Arrhenius plot of the parabolic oxidation rate constants of NODS and ODS–18Cr samples.

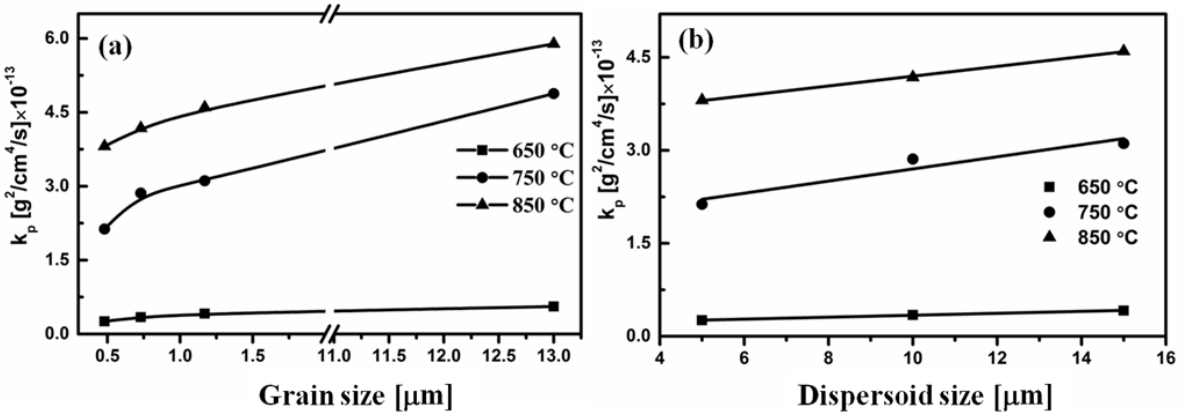

Fig. 4.4.3 Variation of parabolic rate constant with (a) grain size and (b) dispersoid size.

4.4.3 Characterization of surface oxide layer

Typical oxide morphologies of the adherent oxide scale formed on surfaces of ODS6 and NODS samples exposed at 850 °C for 500, 1000 and 2000 h are presented in Fig. 4.4.4. Similarly, the morphologies of oxide layer of the samples oxidized at 650, 750 and 850 °C for exposure time of 2000 h are shown Fig. 4.4.5. Typical oxide morphologies of the adherent oxide scale formed on the surfaces of ODS1, ODS3, ODS6 and NODS samples exposed at 850 °C for 2000 h are shown in Fig. 4.4.6. The surface morphologies of the oxidized samples at all the experimental conditions (Figs. 4.4.4–4.4.6) showed broadly similar features. In general, the oxide layer consists of fine grained matrix (marked M)

with blisters (marked B) of coarse particles distributed randomly over the entire surface. Examination of the oxidized surfaces of ODS−18Cr and NODS samples indicated that increasing time at a given temperature and increasing temperature at a given time resulted in decrease in the size and population of globular particulate clusters (blisters) leading to predominance of granular matrix oxide layer at highest temperature and largest exposure time. Increase in milling time of powder also caused refinement in globular particles (blisters) with granular matrix oxide structure dominating for longest milled sample. The granular matrix oxide structure appears to be finer in NODS when compared to ODS6 under identical exposure conditions. EDS analysis was carried out on the granular matrix oxide and blisters of all the oxidized samples. The variation of the composition of matrix and blisters of ODS6 and NODS oxidized at 850 °C for different exposure times and oxidised at different temperatures for an exposure time of 2000 h are given in Tables 4.4.2 and 4.4.3 respectively. The composition obtained on the oxidised surfaces of ODS1, ODS3, ODS6 and NODS samples oxidised at 850 °C for 2000 h is given in Table 4.4.4. The EDS results indicate that the granular matrix oxide is predominantly chromium oxide (Cr_2O_3) with small quantities of iron oxide. The globular particles (blisters) are of the type $(FeCr)_xO_y$. The EDS analysis also revealed that, at constant exposure temperature (850 °C), the Cr content of the granular matrix oxide increased with exposure time and the composition of the blisters remained unchanged for both ODS6 and NODS samples. Similarly, at constant exposure time (2000 h), the Cr content of the granular matrix oxide increased and the composition of blisters remained similar with increasing exposure temperature from 650 to 750 °C, whereas at 850 °C the Cr content of both the granular matrix oxide and the blisters increased significantly when compared to lower exposure temperatures. The time of powder milling does not seem to influence the composition of either the blisters or granular matrix oxide when the samples are exposed to the highest temperature (850 °C) and the longest exposure time (2000 h).

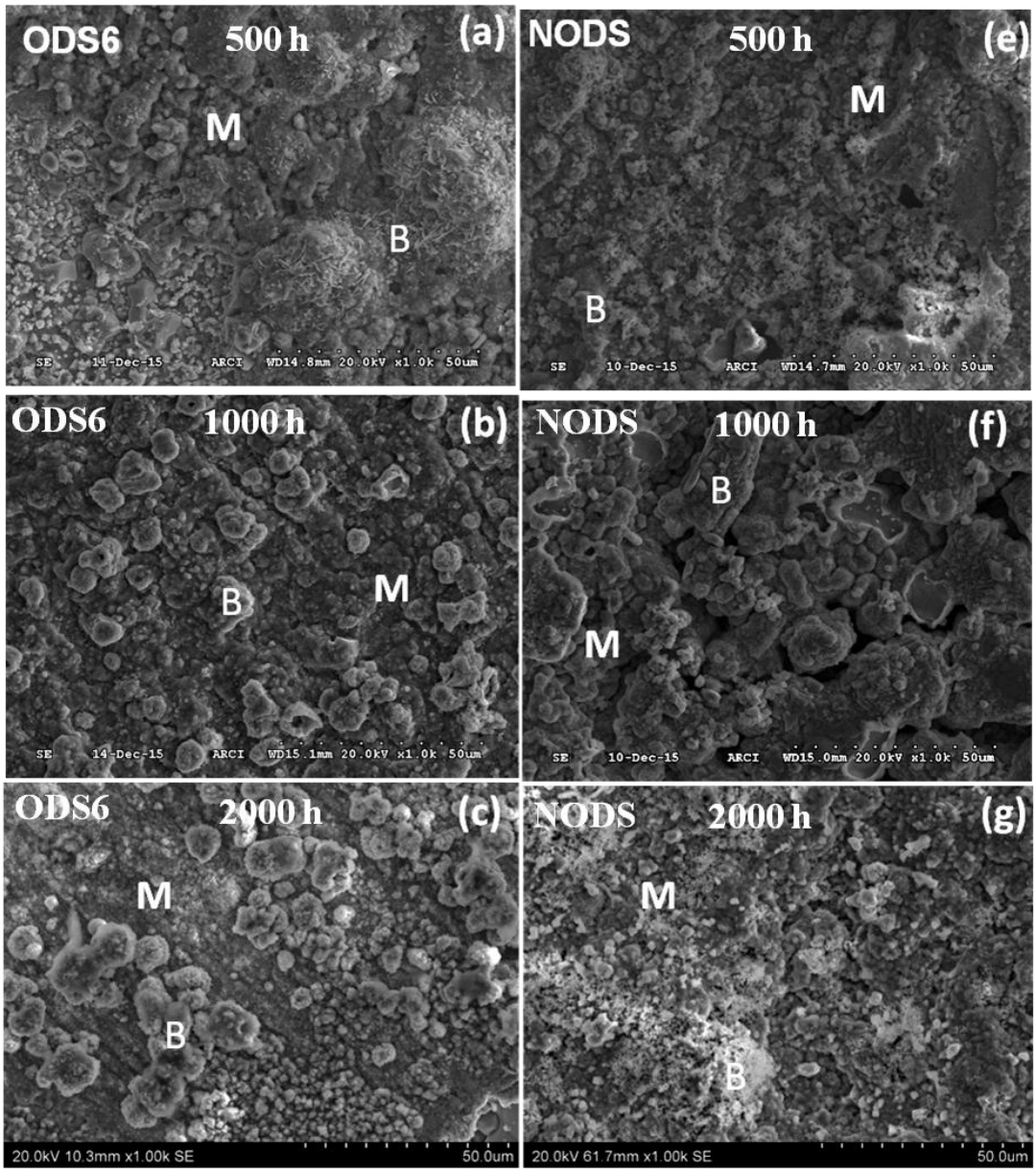

Fig. 4.4.4 SEM morphologies of ODS6 (a) 500 h, (b) 1000 h, (c) 2000 h and NODS (d) 500 h, (e) 1000 h, (f) 2000 h at 850 °C.

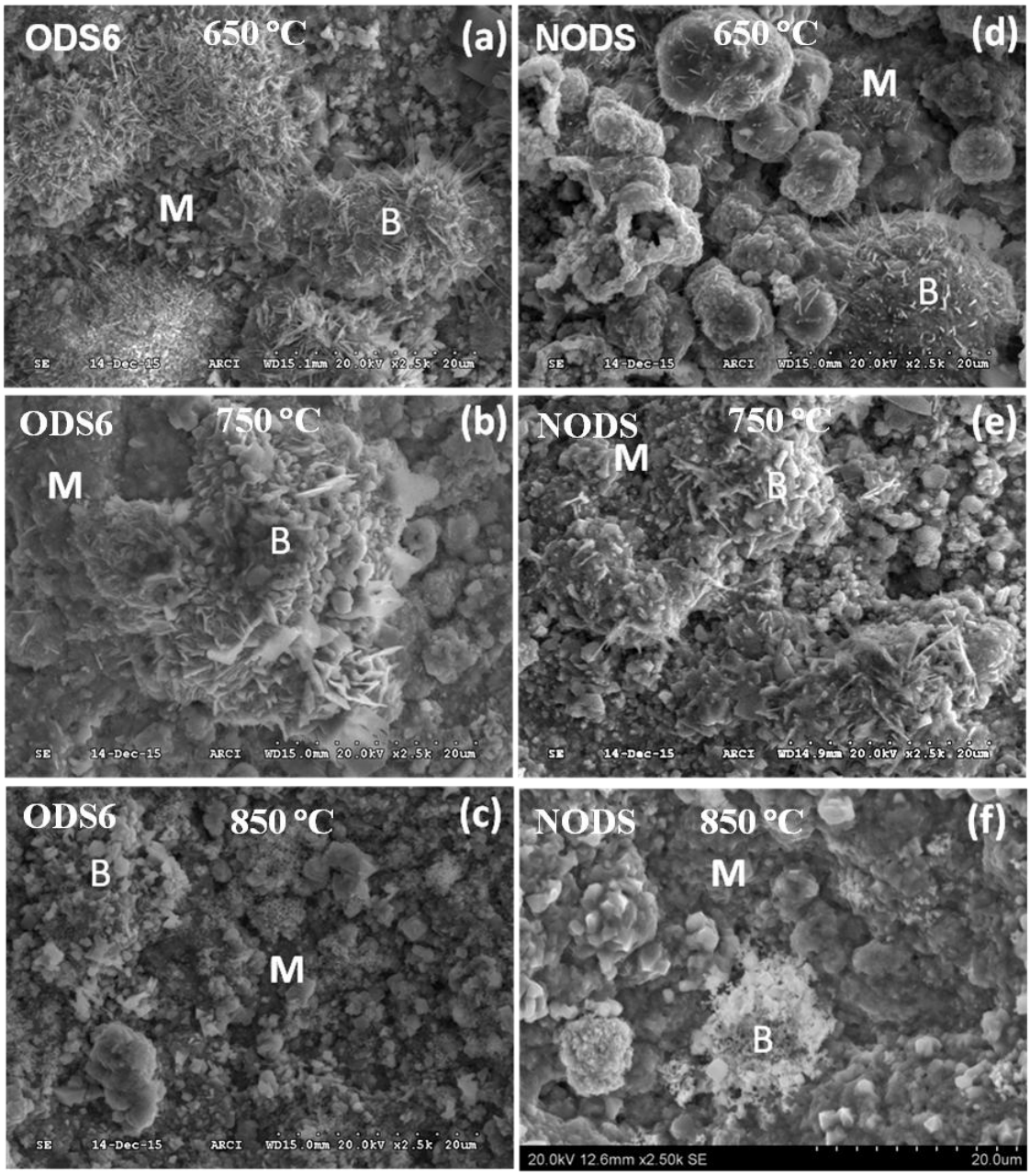

Fig. 4.4.5 SEM morphologies of ODS6 (a) 650 °C, (b) 750 °C, (c) 850 °C and NODS (d) 650 °C, (e) 750 °C, (f) 850 °C for exposure time of 2000 h.

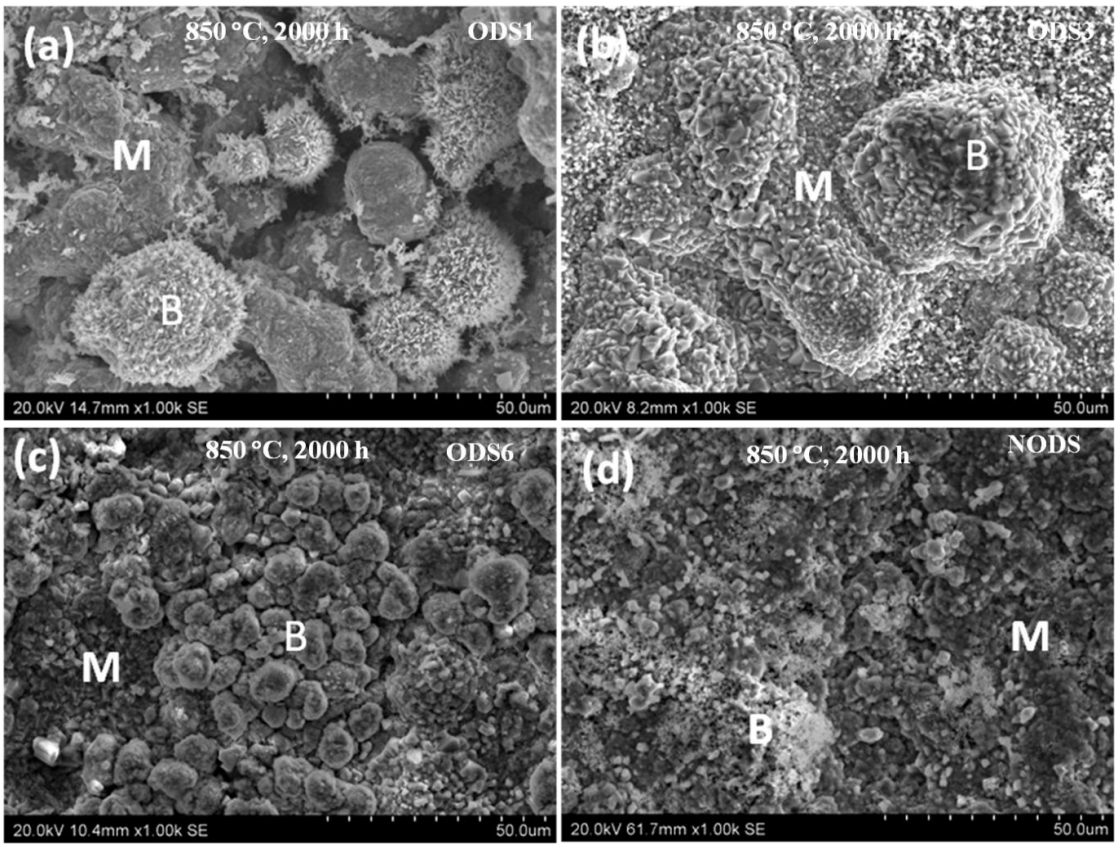

Fig. 4.4.6 SEM morphologies of (a) ODS1, (b) ODS3, (c) ODS6 and (d) NODS exposed for 850°C and 2000 h.

Table 4.4.2 Variation of composition of blisters and matrix for different exposure times at an exposure temperature of 850 °C.

Element	ODS6 at 850 °C					
	500 h		1000 h		2000 h	
(at. %)	blister	Matrix	blister	Matrix	blister	matrix
Fe	29	6	26	10	25	11
Cr	33	30	37	27	32	49
Ti	0.2	0.3	0.3	0.3	0.2	0.5
O	37	64	37	63	43	39
	NODS at 850 °C					
Fe	30	3	32	2	28	7
Cr	34	44	35	44	36	55
Ti	0.3	0.5	0.3	0.4	0.4	0.4
O	36	53	33	54	36	37

Table 4.4.3 Variation of composition of blisters and matrix at different exposure temperatures for an exposure time of 2000 h.

Element	ODS6 for 2000 h					
	650 °C		750 °C		850 °C	
(at. %)	blister	Matrix	blister	Matrix	blister	matrix
Fe	42	21	39	15	25	11
Cr	7	33	7	35	32	49
Ti	0.3	0.5	0.3	0.3	0.2	0.7
O	51	45	54	49	43	39
	NODS for 2000 h					
Fe	35	6	38	7	28	7
Cr	6	30	13	35	36	55
Ti	0.2	0.5	0.4	0.4	0.4	0.4
O	59	64	49	57	36	37

Table 4.4.4 Variation of composition of blisters and matrix for different milling times at 850 °C and 2000 h.

Element	850 °C, 2000 h							
	ODS1		ODS3		ODS6		NODS	
(at. %)	blister	matrix	Blister	matrix	Blister	matrix	blister	matrix
Fe	27	6	31	11	25	11	28	7
Cr	39	58	32	45	32	49	36	55
Ti	0.2	1.3	0.5	0.9	0.2	0.7	0.4	0.4
O	34	35	37	43	43	39	36	37

4.4.4 Raman analysis of oxides

The Raman spectra obtained from the surfaces of the ODS6 and NODS samples oxidized at 850 °C for different exposure times and oxidized at different temperatures for an exposure time of 2000 h are shown in Figs. 4.4.7(a–b) and Figs. 4.4.7(c–d) respectively. The Raman spectra obtained on the surfaces of ODS1, ODS3, ODS6 and NODS samples oxidized at 850 °C for 2000 h are shown in Fig. 4.4.7(e). Analysis of oxidized surfaces by Raman spectroscopy indicated that the oxide layers of all the experimental samples consist of Cr_2O_3, Fe_2O_3, Fe_3O_4 and $FeCr_2O_4$ in varying proportions. The Raman frequencies of these oxides from the present work are presented in Table 4.4.5 along with the reported values in the literature [1–3].

Table 4.4.5 Raman frequencies (cm^{-1}) of oxides from present work along with the reported data.

Oxide	Raman shift [cm^{-1}]		
	Present work	Ref [1,2]	Ref [3]
$FeCr_2O_4$	684	685	685
Cr_2O_3	306	303	306
	352	352	353
	395	397	397
	531	530	528
	537	532	538
	544	541	540
	555	554	552
Fe_3O_4	672	667	670
	680	680	676
Fe_2O_3	228	227	227
	246	245	243
	297	299	298
	413	412	414
	506	501	506

The results of Raman spectroscopic examination revealed that the oxides in both ODS6 and NODS (Figs. 4.4.7 (a–b)) are found to be Cr_2O_3 and $FeCr_2O_4$ at all exposure times for a constant exposure temperature of 850 °C and the intensity of Cr_2O_3 increased with exposure time. The presence of Cr_2O_3 was relatively less dominant in NODS at identical conditions. At constant exposure time (2000 h), the oxide layer in ODS6 consists of Fe_3O_4 and Cr_2O_3 at 650 °C. At higher temperature (850 °C), Fe_3O_4 changed to $FeCr_2O_4$ and the dominance of Cr_2O_3 increased (Fig. 4.4.7 (c)). Where as in NODS sample, Fe_2O_3 and Fe_3O_4 were noticed at lower exposure temperatures and the composition changed to

predominantly Cr_2O_3 and $FeCr_2O_4$ at higher exposure temperature (Fig. 4.4.7 (d)). At all milling times, the oxide layers consist of Cr_2O_3 and $FeCr_2O_4$ at 850 °C and 2000 h. The dominance of Cr_2O_3 was found to increase with increasing milling time (Fig. 4.4.7 (e)). The Cr_2O_3 was more prominent in ODS6 than that in NODS, both of which were milled for 6 h prior to consolidation.

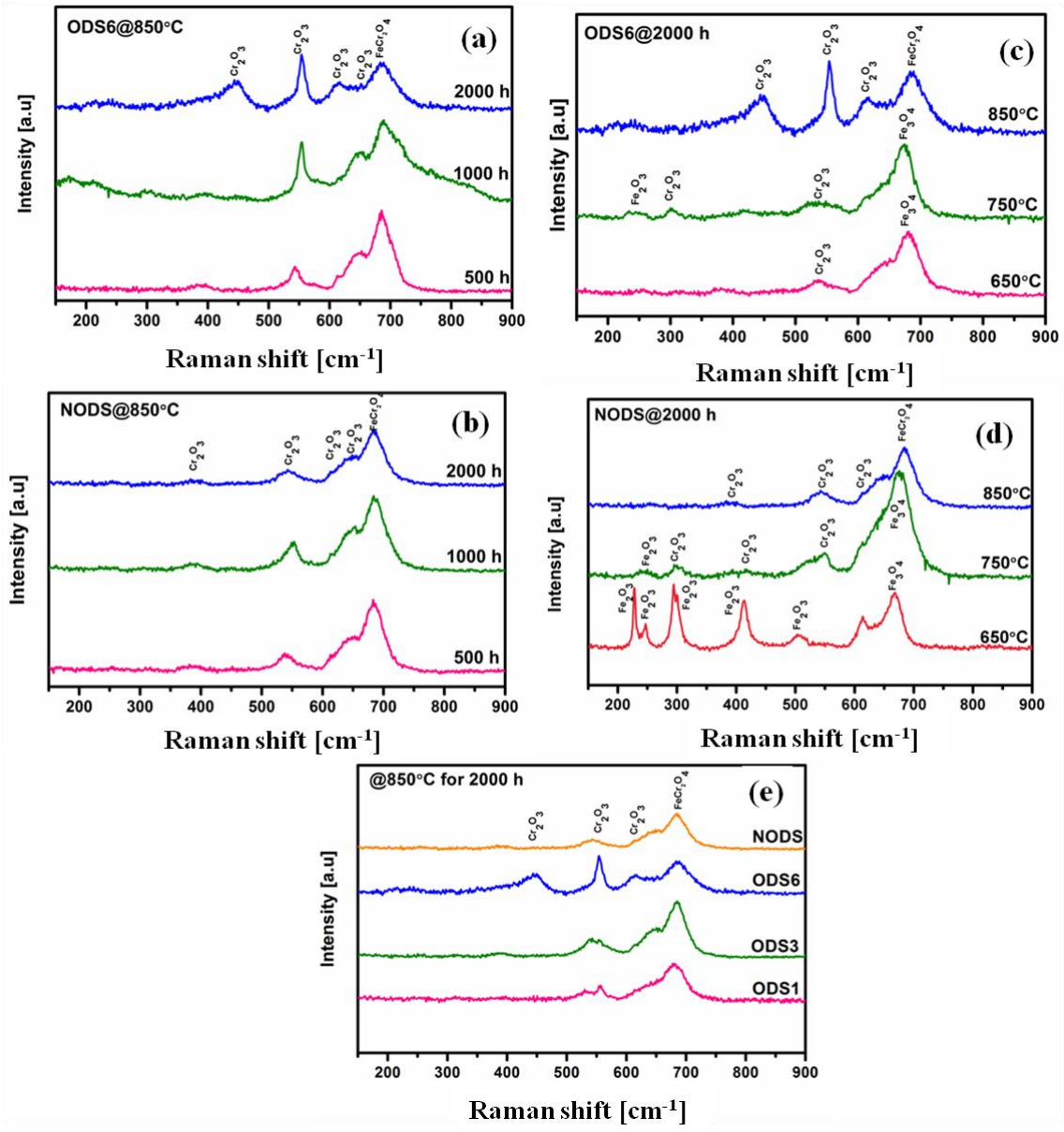

Fig. 4.4.7 Raman spectra of NODS and ODS–18Cr samples (a, b) as a function of exposure temperature (c, d) as a function of exposure time and (e) as a function of milling time.

4.4.5 Characterization of oxide scale

The backscattered electron images taken on the cross–section of oxide layers formed on ODS6 and NODS samples exposed at 850 °C for 2000 h are shown in Figs. 4.4.8 (a–b) respectively. The EDS line scan across the oxide scale was carried out to obtain the elemental concentration profiles in the oxide layer and adjacent matrix and are shown in Figs. 4.4.8 (c–d) respectively. The Raman spectra obtained on the surface of the NODS and ODS6 samples oxidised at 850 °C for an exposure time of 2000 h are shown in Fig. 4.4.8 (e). The oxide layer was found to be dense, continuous and showed good adherence to the matrix. The thickness of the oxide layer of ODS6 is lower (17 µm) when compared to NODS (65 µm) and are in conformity with the respective weight gains.

The Fe, Cr, O, Ti and W concentration profiles of oxidised samples from the outer surface of the oxide scale to substrate obtained by EDS line scan revealed that the concentration of Fe, Cr and O varied in the oxide scale indicating the presence of different oxide layers. The oxide scale is composed of a two layer structure. The line scan analysis of ODS6 (Fig. 4.4.8 (c)) indicate that, Fe was dominant in the outer layer and its concentration decreases significantly a few microns below the outer layer. Chromium and oxygen concentrations are higher in the inner oxide layer than the outer oxide layer. The higher O and Cr contents in the oxide layer when compared to substrate are due to the ingression of oxygen from air and diffusion of Cr from the substrate. The concentrations of Ti and W remained unchanged in the oxide–layer and substrate. At the oxide–substrate interface, the concentration of Fe increased rapidly and that of Cr and O fell drastically. The concentration profiles of Fe, Cr, O, Ti and W in the oxidised NODS sample are similar to ODS6 but the thickness of Fe–rich phase (outer layer) is higher in NODS compared to ODS6. The chemical composition of the outer layer of the scale is mainly composed of iron, chromium and oxygen suggestive of the formation of $(FeCr)_xO_y$ type oxide. The inner oxide layer of the scale in contact with substrate consists of only chromium and oxygen corresponding to Cr_xO_y. It indicates that the outer layer is formed by outwards diffusion of iron and chromium ions.

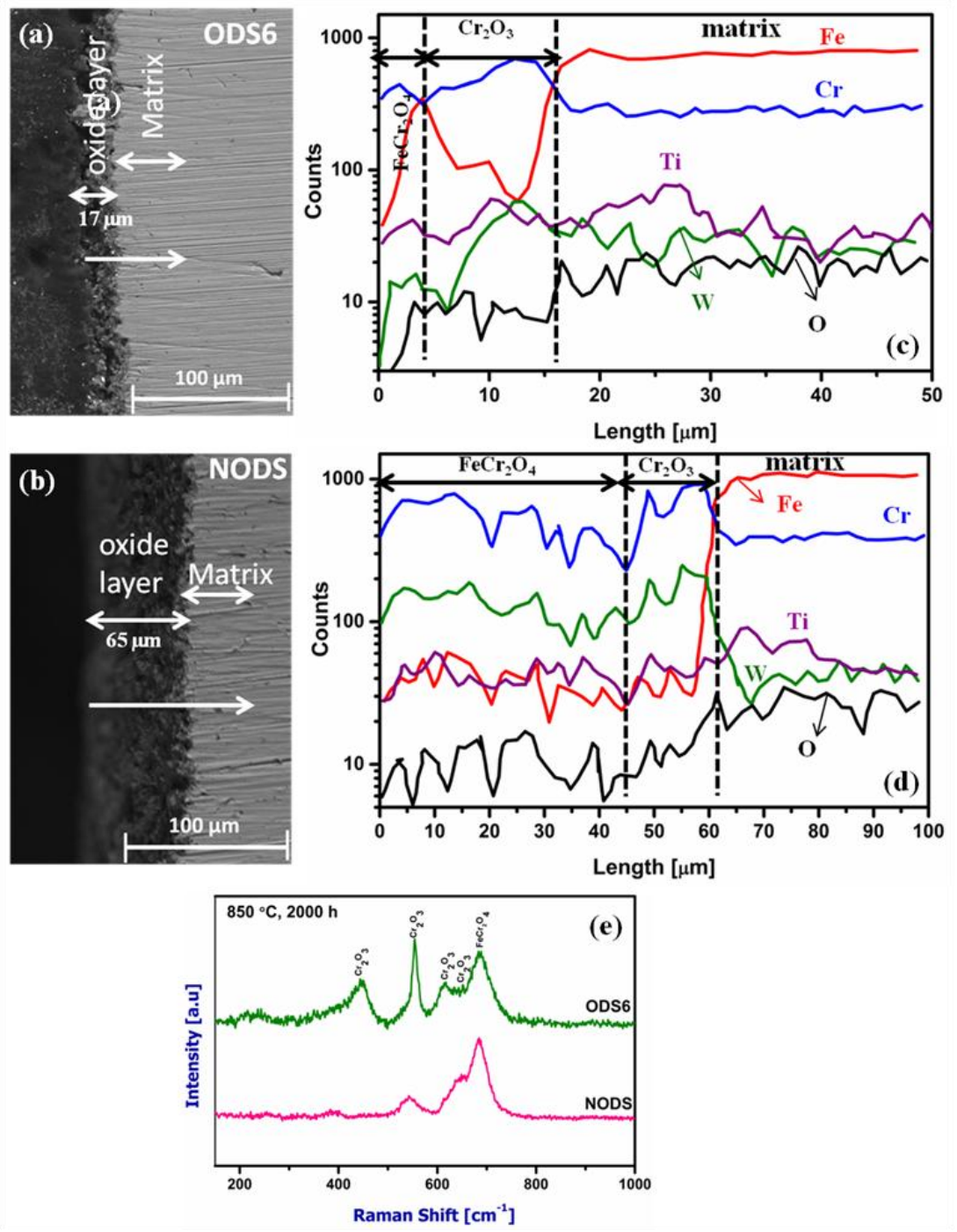

Fig. 4.4.8 (a) and (b) Cross–section images ODS6 and NODS samples exposed to 850 °C for 2000h, respectively. (c) and (d) show the EDS line–scan images of (a) and (b), respectively. (e) Raman spectra.

4.4.6 Discussion

The oxidation of Fe–18Cr alloy involves oxidation of all the oxide forming elements in the steel during the initial stages resulting in the formation of a thin oxide layer on the surface. Further exposure results in continued inflow of oxygen through the transient oxide layer and outflow of metallic ions to the oxide–substrate interface. During these stages, the oxidation mechanism is strongly dependent on the kinetic boundary conditions and thermodynamics. According to Ellingham–Richardson ($\Delta G^0 - T$) plots, the standard free energy (ΔG^0) of Cr_2O_3 formation is far more negative when compared to the other oxides over the temperature range of 650–850 °C in high Cr steels [4]. Since the formation of Cr_2O_3 layer is thermodynamically the most favored, a thin impervious Cr_2O_3 layer forms at the surface. Usually, the formation of Cr_2O_3 layer is controlled by the rate of Cr supply. The high Cr content of the steel favors increases in the diffusion of Cr through the grain boundaries and enhances the availability of Cr for the formation of Cr_2O_3 layer. Further oxide growth is controlled by the diffusivities of Fe and Cr through Cr_2O_3 layer and their interaction with oxygen [5].

The results of the oxidation studies revealed that the weight gain increased continuously at all test temperatures and times in accordance with the parabolic rate law (Eq. (4.4.1)). It is well known that, high temperature oxidation process depends on the reactions of metal ions with oxygen and kinetics of the formation of oxides. The parabolic growth rate behavior is usually controlled by the diffusion and transport of anionic or cationic species through the oxide layer [6]. Lower k_p value indicates that the activation energy needed for the formation of oxides is higher and the oxidation resistance is higher. The parabolic rate constant (k_p) was lower in ODS–18Cr steels than NODS and was found to decrease with increase in milling time.

The weight gain in all the experimental samples is found to be in the order of ODS6<ODS3<ODS1<NODS for all the oxidation conditions studied. Even though, Cr content is similar in NODS and ODS–18Cr steels, the oxidation resistance is higher in ODS–18Cr steels. Amongst the ODS–18Cr steels, the oxidation resistance increased with increasing milling time; ODS6 being the most oxidation resistant. The predominant cause for this behaviour is the refinement in grain size and the dispersoid size with increasing milling time. It is well known that for a given ratio of grain boundary diffusivity to the lattice diffusivity, the atomic flux to the oxidizing surfaces increases with reduction in

grain size [7]. Consequently, NODS being the coarse grained (13 μm) material exhibits lowest oxidation resistance when compared to ODS–18Cr samples where the grain size decreased with increasing milling time. ODS6 exhibited the highest oxidation resistance in view of its sub micron grain size (0.48 μm). Further, better oxidation resistance of ODS–18Cr steels is in part attributable to the presence of 2–7 nm size $Y_2Ti_2O_7$ dispersoids. The addition of rare earth elements (Y, Ce, La *etc*.) to Fe–Cr steels has beneficial effect on the oxidation resistance of ferritic steels [8–11]. Yttrium addition by itself is known to improve the oxidation resistance by segregating to the Cr_2O_3 grain boundaries and retarding elemental diffusion through the oxide [7]. The addition of yttrium was also found to be beneficial in enhancing the oxidation resistance of ODS steels by reducing the spallation tendency [11]. The enhanced oxidation resistance of ODS steels is attributable to the probable presence of residual Y in solid solution. Presence of Y–Ti–O dispersoids is believed to act as nucleation sites for the formation of Cr_2O_3 even during early stages of oxidation and reduce the oxide growth rate [11].

SEM examination and Raman spectra revealed the presence of different oxide layers (Fe_2O_3, Fe_3O_4, $FeCr_2O_4$ and Cr_2O_3) in different proportions depending on the experimental conditions. The oxide layer closest to the substrate is Cr_2O_3 followed by Fe_2O_3 and Fe_3O_4 or $FeCr_2O_4$.

The type and thickness of individual oxide layers depend on the relative diffusivities of Fe and Cr and inward flow of O through the initially formed Cr_2O_3 layer. The diffusivities depend on the microstructure of the substrate in the Cr_2O_3 layer and the temperature and time of exposure. The diffusion rates of metal ions decrease in the order $D_{Mn}>D_{Fe}>D_{Ni}>D_{Cr}$ [12]. In both NODS and ODS–18Cr samples, the inner most oxide layer (on the substrate) was Cr_2O_3. While the thickness of Cr_2O_3 is a significant fraction of total oxide thickness in ODS–18Cr samples, it is relatively low in NODS samples as evidenced by the elemental EDS line scan data (Fig. 4.4.8). The predominant reasons for this behaviour of ODS–18Cr steel is (a) the formation of dense Cr_2O_3 layer, due to grain refinement induced enhanced diffusivity of Cr to Cr_2O_3, (b) the increased nucleation sites caused by nano–sized $Y_2Ti_2O_7$ dispersoids and (c) reduced diffusivity of both Cr and Fe through fine grained Cr_2O_3 layer. The layer above Cr_2O_3 is either Fe_3O_4 or $FeCr_2O_4$ depending on the temperature and milling conditions of ODS–18Cr steels. At temperatures ≤750 °C, the layer mainly consists of Fe_3O_4 and at higher temperatures, it is

$FeCr_2O_4$. $FeCr_2O_4$ formation occurs due to either Cr atoms replacing Fe atoms in Fe_3O_4 or the reaction between Fe_xO_y and Cr_2O_3 [13]. Relative to ODS–18Cr samples, the thickness of $Fe_3O_4/FeCr_2O_4$ is larger in NODS sample due to extensive outward flow of Fe through the less dense Cr_2O_3 layer. At low temperatures (650 °C), Fe_2O_3 was also observed in NODS because of the lower diffusivity of Cr through the coarse grain structure of the substrate and the inherently higher Fe diffusivity than through Cr_2O_3 layer. The observed columnar growth of Fe–rich oxide crystals (Fig. 4.4.6–4.4.8) is typical of Fe–Cr alloys [14, 15, 16] and is caused by the outward flow of Fe atoms through the defects in Cr_2O_3 layer.

4.4.7 Summary

High temperature oxidation behaviour of ODS–18Cr ferritic steels along with 18Cr (NODS) steel was examined at different exposure temperatures (650–850 °C) for varying exposure times (100–2000 h). ODS–18Cr steels exhibited higher resistance to oxidation over the whole range of exposure temperature and time compared to NODS steel. The oxidation resistance of ODS–18Cr steels increased progressively with milling duration due to the gradual refinement of dispersoids and grains. The inner oxide layer is Cr_2O_3 in both NODS and ODS–18Cr steels, although its thickness fraction of total oxide thickness was different. In both NODS and ODS–18Cr steels, outer layer of oxide scale consisted of Fe_3O_4 at lower temperatures (≤ 750 °C) and $FeCr_2O_4$ at higher temperature (850 °C). The enhanced oxidation resistance of ODS–18Cr steels is due to fine grain structure and beneficial effects of fine Y–Ti–O dispersoids.

References

[1] J.H. Kim, I.S. Hwang, Development of an in situ Raman spectroscopic system for surface oxide films on metals and alloys in high temperature water, *Nuclear Engineering and Design*, 235 (2005) 1029–1040.

[2] S.C. Tjong, Laser Raman spectroscopic studies of the surface oxides formed on iron chromium alloys at elevated temperatures, *Materials Research Bulletin*, 18 (1983) 157–165.

[3] W.E. Boggs, R.H. Kachick, G.E. Pellissier, The effect of oxygen pressure on the oxidation of zone–refined iron, *Journal of Electrochemical society*, 112 (1965) 539–546.

[4] J.H. Kim, B.K. Kim, D.I. Kim, P.P. Choi, D. Raabe, K.W. Yi, The role of grain boundaries in the initial oxidation behavior of austenitic stainless steel containing

alloyed Cu at 700 °C for advanced thermal power plant applications, *Corrosion Science*, 96 (2015) 52–66.

[5] Y. Xu, X. Zhang, L. Fan, J. Li, X. Yu, X. Xiao, L. Jiang, Improved oxidation resistance of 15 wt.% Cr ferritic stainless steels containing 0.08–2.45 wt.% Al at 1000 °C in air, *Corrosion Science*, 100 (2015) 311–321.

[6] M. Sun, X. Wu, Z. Zhang, E.H. Han, Oxidation of 316 stainless steel in supercritical water, *Corrosion Science*, 51 (2009)1069–1072.

[7] S.N. Basu, G.J. Yurek, Effect of alloy grain size and silicon content on the oxidation of austenitic Fe–Cr–Ni–Mn–Si alloys in pure O_2, *Oxidation of Metals*, 36 (1991) 281–315.

[8] J.H. Kim, K.M. Kim, T.S Byun, D.W. Lee, C.H. Park, High temperature oxidation behavior of nano structured ferritic oxide dispersion strengthened alloys, *Thermochimica Acta*, 579 (2014) 1–8.

[9] Z. Oksiuta, High temperature oxidation resistance of ultrafine–grained 14%Cr ODS ferritic steel, *Journal of Materials Science*, 48 (2013) 4801–4805.

[10] H.S. Seo, G. Jin, J.H. Jun, D.H. Kim, K.Y. Kim, Effect of reactive elements on oxidation behaviour of Fe–22Cr–0.5Mn ferritic stainless steel for a solid oxide fuel cell interconnects, *Journal of Power Sources*, 178 (2008) 1–8.

[11] F. Riffard, H. Buscail, E. Caudron, R. Cueff, C. Issartel, S. Perrrier, Yttrium implantation effect on 304L stainless steel high temperature oxidation at 1000 °C, *Journal of Materials Science*, 37 (2002) 3925–3933.

[12] Y. Chen, K. Sridharan, S. Ukai, T.R. Allen, Oxidation of 9Cr oxide dispersion strengthened steel exposed in supercritical water, *Journal of Nuclear Materials*, 371 (2007) 118–128.

[13] R.E. Lobnig, H.P. Schmidt, K. Hennesen, H.J. Grabke, Diffusion of cations in chromia layers grown on iron–base alloys, *Oxidation of Metals*, 37 (1992) 81–93.

[14] L. Ehlers, D.J. Young, E.J. Smaardijk, A.K. Tyagi, H.J. Penkalla, Enhanced oxidation of the 9%Cr steel P91 in water vapor containing environments, *Corrosion Science*, 48 (2006) 3428–3454.

[15] N. Briks, G.H. Meier, F.S. Pettit, Introduction to the high temperature oxidation of metals, second edition, Cambridge University Press, 2006, Ch. 5.

[16] Q. Gao, X. Dong, C. Li, Z. Lin, X. Yang, M. Dai, Microstructure and oxidation properties of 9Cr–1.7W–0.4Mo–1Co ferritic steel after isothermal aging, *Journal of Alloys and Compounds*, 651 (2015) 537–543.

CHAPTER 5

Conclusions and suggestions for future work

The conclusions made based on the work carried out are presented in this chapter. The issues that could not be addressed in the current work are also suggested for the future work.

5.1 Conclusions

The conclusions arrived at from the detailed research study on the effect of milling time on microstructural evolution in nano ODS–18Cr ferritic steel and the resultant mechanical, corrosion and oxidation properties are given below.

5.1.1 Microstructural evolution

Influence of milling time on the microstructural changes that occur in ODS–18Cr ferritic steel (Fe–18Cr–2.33W–0.34Ti–0.36Y_2O_3) during milling and subsequent hot consolidation of the milled powders was investigated. The salient features are given below:

- Crystallite sizes of both 18Cr and ODS–18Cr steel powders decreased with milling time reaching a steady state after 5 h.
- The yttria particle size decreased during initial stages of milling and finally either dissolved or formed atomic clusters in powder milled for 6 h.
- The oxide particles were coarse and non–uniformly distributed in consolidated samples of 1 and 3 h milled powders. They were finer (2–7 nm) and uniformly distributed in samples made with 6 h milled powder.
- The dispersoids in ODS6 are cuboidal shaped semicoherent $Y_2Ti_2O_7$ particles having a crystal structure of diamond cubic ($Fd\bar{3}m$) with a lattice parameter of 1.01 nm.
- Even though there is no change in shape of the oxide particles in upset forged and extruded conditions, coarsening of particles (3 to 5 nm) was observed.
- The major phases observed by high intensity micro focus X–ray diffraction were confirmed with electron microscopic studies.

- In ODS1, the oxides of $YTiO_3$ type are predominant along with Y_2O_3 and Y_2TiO_5. As the milling time was increased to 3 h (ODS3), oxides of Y_2O_3 , Y_2TiO_5 and $Y_2Ti_2O_7$ were found.
- In ODS6, oxide particles of Y_2TiO_5 and $Y_2Ti_2O_7$ were found and these particles have finer size when compared to ODS1 and ODS3 samples.
- In all the samples, Ti–enrich (TiO) particles were also present, which has face centered cubic (FCC) crystal structure.

5.1.2 Mechanical properties

The tensile deformation and fracture behaviour of ODS–18Cr ferritic steels along with 18Cr (NODS) steel at different test temperatures were investigated. The salient features from the present study are given below:

- The microhardness of both 18Cr and ODS–18Cr steel powders was increased with milling time and finally reached a steady state beyond 5 h of milling.
- The bulk hardness of ODS–18Cr steel is higher than NODS and increases from ODS1 to ODS6. The progressive increase of hardness in ODS–18Cr steel is due to decrease in size and increase in number density of dispersoids.
- The strength of ODS–18Cr steels increased with milling duration at all the test temperatures due to the refinement of dispersoids and grains.
- All ODS–18Cr steels exhibited superior strength values over the whole range of test temperatures compared to NODS steel and the strength of both the steels decreased with temperature.
- The ductility indices of ODS–18Cr steels showed marginal decrease with milling time over the test temperature range and were lower than those of NODS steel.
- With increasing test temperature, NODS and ODS–18Cr steels exhibited continuous decrease in uniform elongation, but the fracture strain remained nearly same.
- The fractured samples of NODS and ODS–18Cr steels showed typical cup–and–cone type fracture with characteristic dimple rupture.
- The fracture features of NODS and ODS–18Cr steels were correlated to the milling time dependent microstructural features.
- The predicted hardness values of extruded+annealed samples compare well with the experimental values.

- The strength values, predicted by root of sum of squares model at higher temperatures compare well with experimental values.

5.1.3 Corrosion studies

The corrosion behavior of ODS1 and ODS6 along with NODS alloy steels in 3.5% NaCl solution was investigated using CP, EIS, potentiodynamic polarization and immersion studies. The conclusions from the study are given below:

- ODS–18Cr steels are more prone to pitting corrosion when compared to NODS and the pitting tendency increases with milling time.
- The marginally higher pitting rates in ODS–18Cr steels are due to the presence of dispersoids which act as initiating sites for the formation of pits.
- The charge transfer resistance (R_{ct}) values are less for ODS–18Cr steels when compared to NODS because of the difference in the formation of passive film.
- In both ODS–18Cr and NODS steels, corrosion rate decreases up to 48 h due to formation of protective passive layer and increases beyond due to the increase of porosity in the passive layer.
- Corrosion behavior of both ODS–18Cr and NODS steels is found to be similar in both electrochemical and immersion studies.

5.1.4 Oxidation studies

High temperature oxidation behavior of ODS–18Cr ferritic steels along with 18Cr (NODS) steel was examined at different exposure temperatures (650–850 °C) for varying exposure times (100–2000 h). The salient features from the present study are given below:

- ODS–18Cr steels exhibited higher resistance to oxidation over the whole range of exposure temperature and time compared to NODS steel.
- The oxidation resistance of ODS–18Cr steels increased progressively with milling duration due to the gradual refinement of dispersoids and grains.
- The inner oxide layer is Cr_2O_3 in both NODS and ODS–18Cr steels, although its thickness fraction of total oxide thickness was different.
- In both NODS and ODS–18Cr steels, outer layer of oxide scale consisted of Fe_3O_4 at lower temperatures (≤ 750 °C) and $FeCr_2O_4$ at higher temperature (850 °C).

- The enhanced oxidation resistance of ODS–18Cr steels is due to fine grain structure and beneficial effects of fine Y–Ti–O dispersoids.

5.1.2 Scope for the future work

The following studies could be carried out in order to gain additional understanding of the properties of ODS–18Cr ferritic steel on long term exposure to high temperature.

- Coarsening kinetics of Y–Ti–O complex dispersoids and the resultant microstructure in ODS–18Cr steels under high temperature for longer times.
- Effect of dispersoids on creep and fatigue life of ODS–18Cr ferrites steel at high temperature.